Low-THz Automotive 3D Imaging Radar

by

Dominic Phippen

A thesis submitted to the University of Birmingham
for the degree of
DOCTOR OF PHILOSOPHY

School of Engineering
College of Engineering and Physical Sciences
University of Birmingham
June 2021

To my parents, Susan & James,

and my brother, Jonathan.

Acknowledgements

This work was supported by Jaguar Land Rover and the UK-EPSRC grant EP/N012372/1 as part of the jointly funded Towards Autonomy: Smart and Connected Control (TASCC) Programme.

I would like to thank the following people:

Marina Gashinova and Mikhail Cherniakov for their guidance and supervision throughout the project. Also Liam Daniel, Scott Cassidy, Edward Hoare, Emidio Marchetti, Ana Stroescu, Alan Yates, and the rest of the MISL team for all of their help.

Our partners at the University of Edinburgh and Heriot-Watt University, led by Bernard Mulgrew and Andrew Wallace.

My industrial supervisors Thuy Yung Tran, Damien Ward, Anthony Jones, and Nigel Clarke.

Finally I would like to extend a special thanks to all of those who have supported me throughout the project. To my friends Richard, Dominic, Jack, Ellen, Kiran, and Oliver. Last but not least, to my family, Susan, James, Jonathan, Lorna, Mike, David, Verna, Jennifer, Josh and Chloe for all of their love and support.

Abstract

This thesis lays out initial investigations into the 3D imaging capabilities of low-THz radar for automotive applications. This includes a discussion of the state of the art of automotive sensors, and the need for a robust, high-resolution imaging system to compliment and address the short-comings of these sensors. The unique capabilities of low-THz radar may prove to be well-suited to meet these needs, but they require 3D imaging algorithms which can exploit these capabilities effectively. One such unique feature is the extremely wide signal bandwidth, which yields a fine range resolution. This is a feature of low-THz radar which has not been discussed or properly investigated before, particularly in the context of generating the 3D position of an object from range information. The progress and experimental verification of these algorithms with a prototype multi-receiver 300GHz radar throughout this project are described; progressing from simple position estimation to highly detailed 3D radar imaging. The system is tested in a variety of different scenarios which a vehicle must be able to navigate, and the 3D imaging radar is compared with current automotive demonstrators experimentally.

Table of contents

List of figures

List of tables

Nomenclature

Acronyms

(I)SAR	(Inverse) Synthetic Aperture radar
(L)FMCW	(Linearly) Frequency Modulated Continuous Wave
ACC	Adaptive Cruise Control
ADAS	Advanced Driver-Assistance Systems
ADS	Automated Driving Systems
AWGN	Additive White Gaussian Noise
CC	Connected Component
CFAR	Constant False Alarm Rate
CW	Continuous Wave
DBS	Doppler Beam Sharpening
DOA	Direction of Arrival
DSP	Digital Signal Processing
EM	Electromagnetic
EMW	Electromagnetic Wave

EO	Electro-optical
FFT	Fast Fourier Transform
FWHM	Full-Width Half-Maximum
GOLA	Gaussian Optics Lens Antennas
IEEE	The Institute of Electrical and Electronics Engineers
IEM	Integral-Equation Model
IF	Intermediate Frequency
ITU	International Telecommunications Union
lidar	Light Detection and Ranging
LO	Local Oscillator
MIMO	Multiple-Input Multiple-Output
MMIC	Monolithic Microwave Integrated Circuit
OMP	Orthogonal Matching Pursuit
PPI	Plan Position Indicator
radar	Radio Detection and Ranging
RF	Radio Frequency
RMS	Root mean square
Rx	Receiver
SAE	Society of Automotive Engineers
SIMO	Single-Input Multiple-Output

SNR	Signal to Noise Ratio
T(D)oA	Time (Difference) of Arrival
TRRL	Transport and Road Research Laboratory
Tx	Transmitter
TxRx	Transceiver / co-located transmitter and receiver

Symbols

α	Chirp ramp rate. Hyperparameter for tuning regularisation in Chapter 7.
$\circledast$	Convolution.
$\delta\varphi$	Finer angular estimate achieved through monopulse techniques
$\delta(...)$	Dirac delta function.
ε	Electromagnetic permitivitty.
Γ	Reflection coefficient.
$\hat{n}$	Normal unit vector.
λ	Wavelength. Hyperparameter for tuning regularisation in Chapter 7.
$^{\mathsf{T}}$	Transpose of a vector or matrix.
$\mathbf{A}$	Measurement matrix used in OMP and convex optimisation.
$\mathbf{b}$	Vector used in multilateration.
$\mathbf{E}$	Ellipse or ellipsoidal surface.
$\mathbf{H}$	Geometric transform matrix used in multilateration.
$\mathbf{p}$	3D position vector.

$\mathbf{s}$	Signal vector.
$\mathbf{y}$	Image vector.
$\mathscr{D}$	Root mean squared error operator.
$\mathscr{F}$	Fourier transform
$\mathscr{R}$	Radon transform
μ	Mutual coherence of a measurement matrix.
∇	Directional derivative.
ν	Vector of additive white Gaussian noise.
ϕ	Phase
σ	Radar cross section
τ	Time delay or time of arrival.
θ	Azimuth angle
θ_{tgt}	Rotation angle of object on a turntable.
θ_{BW}	Azimuth beamwidth
θ_R	Radar azimuth orientation. Used particularly in later chapters for a scanned Tx-Rx stack.
φ	Elevation angle
φ_{BW}	Elevation beamwidth
ζ	Numerical constraint.
A	Area of an antenna, or amplitude of a signal.
B	Sweep bandwidth.

b	Receiver baseline (separation in height).
c	The speed of light. Approximately 2.998×10^8 ms^{-1}
D	Largest dimension of the antenna.
e_{eff}	Efficiency of the antenna.
f	Frequency
f_c	Signal carrier frequency.
F_p	Propagation factor.
G	Gain or beam pattern.
$g(...)$	Height response - maximum of the image along the height axis.
h	Residuals for optimisation.
I_0	Modified Bessel function.
I_{ref}	Series of reflections.
K	Level of sparsity.
k	Wavenumber.
k_B	Boltzmann constant.
L_a	Loss due to atmospheric attenuation.
L_i	Loss due to various sources of loss in the hardware for the ith Tx-Rx pair.
L_p	Path loss.
l_{cl}	Surface correlation length.
n_c	Number of chirps per dwell.

N_F	Noise figure.
n_{tg}	Number of scattering centres.
P	Power
q_i	Amplitude correction factor.
R	Range
R_b	(Quasi-)Bistatic range.
$S(...)$	Range profile.
$s(...)$	Time series signal.
SNR	Signal to noise ratio.
T	Temperature, usually 293 K.
t	Time.
t_c	Chirp duration.
W	Window function.
$w(z)$	Correlation function of a surface.
x	Horizontal position (driver's left-right)
x'	Ground range.
y	Horizontal position (driver's forward-backward)
z	Vertical position

Chapter 1

Introduction

Radio Detection and Ranging (radar) has long been used as a robust sensing tool for a great many applications, from luggage screening to planetary imaging. As emerging high frequency radars continue to be developed, such as those in the mm-wave band, the imaging techniques created for the conventional lower-frequency radars are now being adapted and applied to higher frequencies. The properties of the mm-wave band are already being exploited in the security, healthcare, and military sectors, but recently the automotive sector has shown great interest in the band for vehicle autonomy. At even higher frequencies, the emerging low-THz or sub-THz band appears to be a promising alternative to existing vehicle sensors. Autonomous vehicles have drawn huge interest from engineers and the general public alike. Although automobile autonomy can take many forms, the desired end goal for many people is a fully autonomous self-driving car. Self-driving cars have the potential to be a near-ideal driver; a driver who never gets distracted, tired, stressed, or intoxicated, and has the possibility of super-human reaction speeds and sensing capabilities. If used correctly, autonomous vehicles could be more economical, safer, and usable by anyone regardless of age or disability. It is difficult to predict the impact of fully autonomous cars, but if it is widely adopted it could fundamentally change the way humans and vehicles interact. One of the most crucial parts of such systems are the sensors. These sensors need to be able to provide the system with all the information it needs for a wide range of applications. It is here that high resolution 3D automotive radar proves to be both useful and necessary.

The goal of this chapter is to introduce radar, automotive sensors, and the need for full 3D radar imaging.

It will examine novel high frequency radars and their applications, with a focus on short range 3D sensing and their use in self-driving cars. It is laid out as follows:

First, section 1.1 examines the state of the art of radar and autonomous vehicles to provide the context for this project. It will cover well established 3D and height-finding radar techniques, and the sensors which have been conventionally used for self-driving cars. Then section 1.2 will focus on recent developments in low-THz and 3D automotive radar, with a review of the academic literature. Section 1.3 gives the problem statement, novel contributions, and outlines the structure of the work in this thesis. Finally, this is summarised in section 1.4.

1.1 Background

This section will give the context of the research by describing radar, 3D radar, autonomous vehicles, and well-established technology and techniques within automotive sensors. Section 1.1.1 provides a brief history and introduction to radar sensors, and section 1.1.2 provides a focused look at their ability to produce height information and 3D imagery.

The focus then shifts to the context of autonomous vehicles: Section 1.1.3 defines what is meant by autonomous vehicles, lays out what the future impact of autonomous vehicles may be, and what the motivation is for them. It includes the conditions in which the sensors will have to operate, and hence their requirements. Section 1.1.4 looks at the state of the art of commercial automotive sensors. It also details the sensor systems used by existing Automated Driving Systems (ADS), Advanced Driver-Assistance Systems (ADAS), and automotive datasets. Finally section 1.1.5 gives an overview of existing automotive radar.

1.1.1 Radar

Sensing using microwave systems has existed for over 100 years. The ideas which underpin radar are widely accepted to have been proposed by John Clerk-Maxwell and Heinrich Hertz at the end of the 19th century, which led to the first recognisable radar device being demonstrated by Christian Hülsmeyer in 1903 [1]. At the most basic level, a radar is a microwave system which can detect a target, and infer information about its position and velocity. Although radar systems come in many forms, they have the same key feature at the heart of their operation. An Electromagnetic Wave (EMW) is sent from the transmitter unit and propagates through space until some fraction of the waves interact with a target [2]. Some of these microwaves are then scattered towards a receiver unit, which measures useful information about the target. [3]. Since their conception, radars have found all kinds of different applications. These include air traffic control, aircraft navigation, ship detection and tracking, weather radar, sensing from space, missile seeking and much more [4].

A major application for radar is imaging. Rather than detecting and characterising a radar target, imaging radar seeks to build up an intensity image of a scene from its radar returns [5]. 3D imaging algorithms are a subset of these, which generate height information from either scanning the radar, using time of flight information, using phase information, or through many other techniques [6].

Imaging radar falls loosely into two categories - real aperture and Synthetic Aperture radar (SAR). Real aperture radar refers to a radar generating an image from one measurement position. The image resolution is constrained by the physical aperture size of the radar system [7]. SAR refers to a family of techniques which improve the resolution of a radar image by combining the returns of multiple real aperture radar images into larger synthetic apertures [8]. Although the focus is real aperture radar, both real aperture and SAR imaging will be used in some capacity in this thesis.

In the modern day, radar systems typically operate between 1 MHz and 1 THz with designated bands from the International Telecommunications Union (ITU) and Institute of Electrical and Electronics Engineers (IEEE) spanning this frequency spectrum, as shown in Figure 1.1

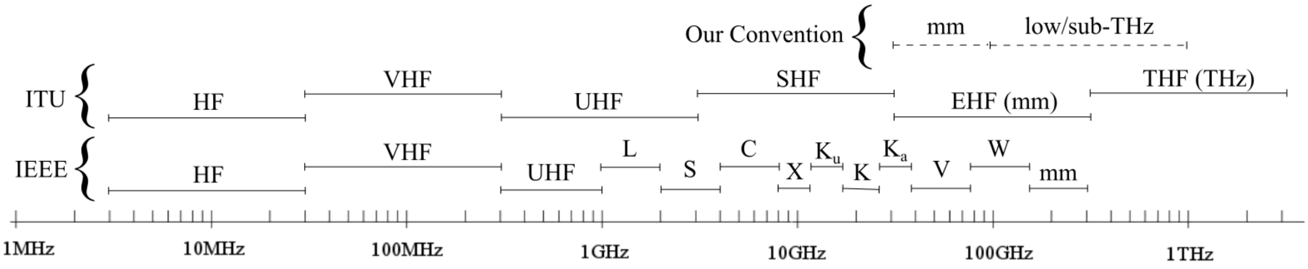

Fig. 1.1 Microwave frequency bands designated by the ITU and IEEE [3, 9]

Our research is focused on frequencies between 0.1 and 1 THz - a band which is referred to as the low-THz or sub-THz band [10]. It also deals in part with the rest of the EHF (mm-wave) band. Because of this, when the term mm-wave is used, it is commonly used to refer to the mm-wave (EHF) band which is not a part of the low-THz band, i.e. approximately 30 to 100 GHz.

Typically the higher frequency bands are used for applications at the shortest ranges, and can produce highly detailed radar imagery [10]. With this in mind, current commercial automotive radars mostly operate within the ISM 77 GHz band, and more recently in the 76-81 GHz band [11]. These higher frequencies are well suited for 3 reasons: they have a larger bandwidth for the same fractional bandwidth, the antenna aperture size scales with wavelength [12], and the higher wavenumber means that the scattering is both more diffuse and more sensitive to smaller surface detail [13]. Because of this, high frequency radar devices tend to be more compact, and better suited to measuring scenes on a smaller scale [13]. However, in the automotive context, the current resolution and information provided by mm-wave radar may not be sufficient for many applications, as will be seen in section 1.1.3.

By increasing the Radio Frequency (RF) of these devices to the low-THz band, the attributes of high frequency radar become even more distinct. One of the most useful features is a higher achievable bandwidth, which yields an even finer range resolution [14]. Furthermore, with this small a wavelength and this high a wavenumber, the Rayleigh criterion dictates that many common surfaces appear rough to low-THz radar [13]. This gives rise to diffuse surface scattering, which means that the reflection from the same surface area of a radar target can be intercepted by a number of radar positions with a relatively large variation of aspect angle [15, 16]. Low-THz radar is therefore even more sensitive to the surface texture of many road objects, and capable of creating a finer resolution radar image of them.

In summary, the low-THz band seems to be a natural choice for automotive radar, but the chosen radar imaging algorithm must be able to make the best use of the unique features of the low-THz band. Namely, the algorithm must exploit the very fine range resolution and diffuse scattering mechanisms to generate high resolution 3D imagery. In the next section a variety of well-established height-finding and 3D radar techniques will be considered.

1.1.2 Radar for Height Finding & 3D Imaging

This section provides an overview of long-existing 3D imaging and height finding radar algorithms. The goal is to introduce these algorithms in sufficient detail to discuss which are appropriate for short range low-THz automotive imaging in later sections. It will introduce target localisation using a number of different approaches, including mechanically scanning, monopulse, phased array and Multiple-Input Multiple-Output (MIMO) radar, interferometry and multilateration.

The simplest way to determine the elevation of a target is to illuminate a series of different elevation positions with a directive antenna pattern, and determine which position yields the returns from a target. This is illustrated in Figure 1.2. This style of height finding was first employed in early radars in a method known as searchlighting, where the scene was scanned with the radar beam, and the orientation with the brightest returns was taken to be the position of a target [4]. This scanning procedure was performed either through mechanically scanning the scene with a beam [17], or by switching between multiple beams with different illumination patterns [18]. 3D localisation through mechanical scanning was then sped up using nodding radars, which applied this principle to a radar which already provided 2D information to generate elevation information [4]. This process was then developed and sped up further with electro-mechanically scanned beams. Assuming the target's signal to noise ratio (SNR) is high, the accuracy and resolution of this technique in elevation is dictated by the beamwidth of the antenna pattern, φ_{BW}. Even if φ_{BW} is large, the elevation of a target can still be estimated from the angle with the brightest returns, which is height estimation rather than 3D imaging, as it estimates the elevation of a target rather than generating a radar intensity image. However, for large φ_{BW}, this technique may not resolve multiple nearby targets.

The image on the right in Figure 1.2 shows an alternative to scanning, which simultaneously uses two nearby beams to estimate the Direction of Arrival (DOA) of a target. This is the idea at the heart of monopulse radar [18]. This family of techniques improves upon the accuracy of scanning radars, φ_{BW}, by using two overlapping antenna patterns to yield a finer angular accuracy, $\delta\varphi$. By comparing the radar target's amplitude in both of the beams, the target can be localised to a narrower region of space. The resolution, $\delta\varphi$, is proportional to φ_{BW} and the inverse of the target's SNR [19]. Therefore, if the radar returns are sufficiently bright, this technique can provide a much better elevation resolution than scanning

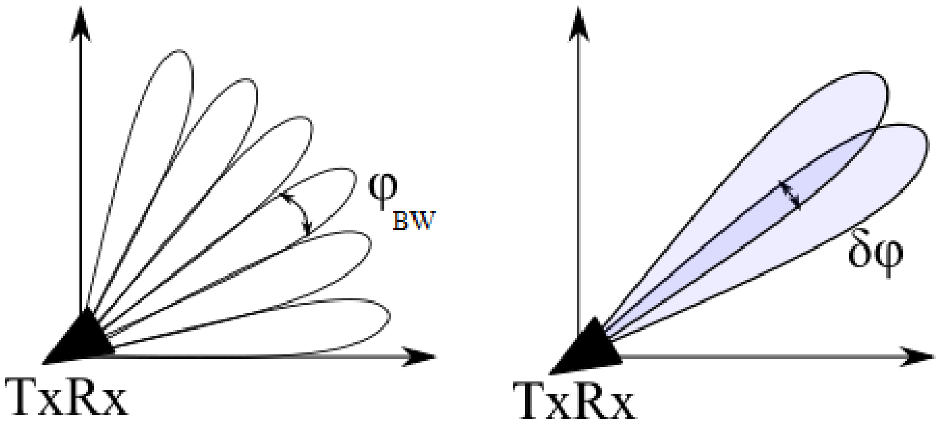

Fig. 1.2 Diagram of target localisation using: a mechanically scanned radar (left), and a monopulse radar (right).

alone. The first monopulse radar was patented in 1946 [20] and the technology has been applied to everything from localising aircraft [21] to hand gesture recognition [22]. This same idea can be extended into measuring azimuth and elevation simultaneously. Such a monopulse antenna may contain 4 or more elements, with a minimum required configuration of a 2x2 planar array for 3D radar localisation. The DOA estimation in either direction comes from considering both the sum and difference beams between each element. A unique solution to the DOA can be obtained in both azimuth and elevation by comparing these patterns [23].

An alternative approach is to consider an array of radiating or receiving elements, which gave rise to phased array radars. For a linear or planar array of transmitting elements, the combined EMW wavefront from all of these elements is directive, and can be electronically steered by applying a phase offset to the signal of each element [24], as in Figure 1.3. The directivity, gain, and the resolution of such a system is defined by the array length and the RF wavelength [25]. Rather than physically steering the beam, this idea of a steering vector can be applied in a different way digitally. Whereas an electronically steered phased array steers the transmit wavefront, a steering vector can be implemented in the signal processing of the output data. As such, a Single-Input Multiple-Output (SIMO) radar can apply a steering vector to the isotropic signals, as the single transmitter and receiver positions are known. A major breakthrough came in the form of Multiple-Input Multiple-Output (MIMO) radar, which synthesises a larger aperture and a better localisation by considering a larger number of virtual Tx-Rx pairs. This is shown in Figure 1.3 as the 2 Tx - 3Rx sites yield 6 virtual pairs, with a larger array width than the 5 elements could give

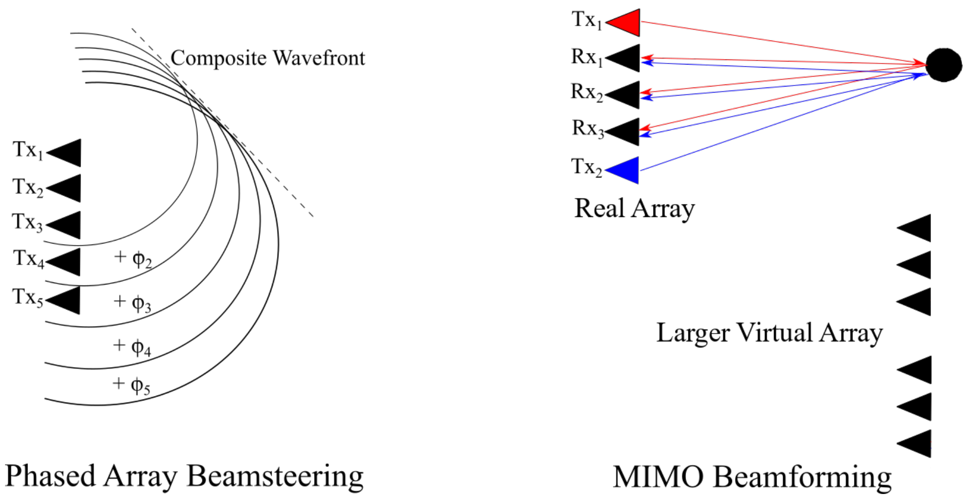

Phased Array Beamsteering MIMO Beamforming

Fig. 1.3 Diagram of target localisation using: an active electronically scanned array (left), and MIMO beamforming (right).

in a real aperture. It also has the advantage that the transmitted signal is not directive, so a MIMO array can illuminate many different directions at once rather than illuminating only one angle [26]. In this case, which transmitter is being used can be determined through time division multiplexing, or through waveform diversity [26].

Compared to scanning systems, monopulse and phased array systems have the major advantage that they do not require scanning with mechanical moving parts. These moving parts generally lead to a lower update rate and are likely to require maintenance. Perhaps more importantly, not scanning allows the radar to observe the entire scene simultaneously without shifting its field of view away from a potential target site. This allows for a long dwell time, which yields a large gain through integration and a very fine Doppler resolution [4]. As a steering vector is applied to generate the radar intensity for many positions in 3D space, this can be viewed as a form of 3D radar imaging.

The focus of the previous approaches has been to focus or steer the beam in different directions to illuminate different regions of space, but this is not the only way 3D information can be gathered. Much like the steering vectors used in array processing, many algorithms exploit the fact that the signal will propagate over a different path length depending on the Tx, Rx, and target position. This difference in path length between multiple Tx and Rx sites can be measured using range, time of arrival, or phase information. For spatially offset Tx-Rx sites, the target can be localised using this information. This is the idea behind multilateration and interferometry, which are central to the work performed during this PhD project. Time (Difference) of Arrival, T(D)oA, geometries like this underpin most of the 3D imaging techniques developed, which will be considered in greater detail in Sections 5 to 7 [27].

Multilateration is the most conceptually simple and easy to implement of these approaches. It directly converts a set of measured range values into coordinate positions in 2D or 3D space [27]. A diagram of this process can be seen in Figure 1.4 in 2D for 1 Tx and 3 Rx sites. Although this diagram shows this process for a set of bistatic radar sites in 2D, the technique is perfectly general and can be applied to monostatic configurations and in 3D [27]. A target appears in the radar signal at a range value for multiple receivers. Figure 1.4 illustrates that a given range value corresponds to an ellipse in 2D (or ellipsoid in 3D). Multilateration works by assuming that the target from each radar signal is at the same point in space, and hence the target's true position lies at the intersection of these ellipses. As highlighted in Figure 1.4, this is by no means a perfect process, with the major drawback of the technique being the presence of ghost targets. Most of these ellipses will have multiple points of intersection, and the intersections which do not correspond to targets are known as ghost targets. Multilateration therefore needs multiple extra Tx or Rx sites to confirm which sites are real targets and which are ghost targets, by considering which positions are consistent between pairs of TxRx sites. The resolution of this technique is dictated by the range resolution of the system, and the spacing of the Tx and Rx sites.

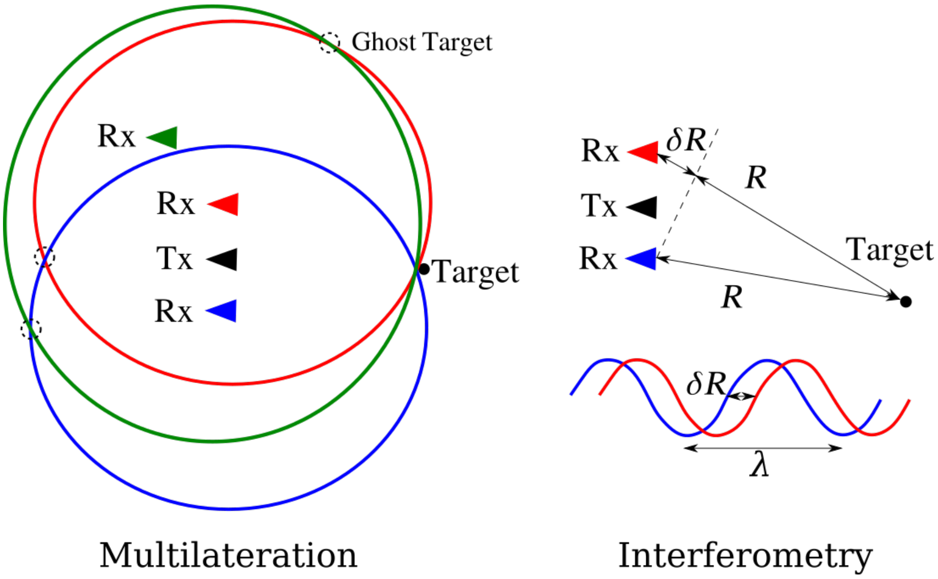

Fig. 1.4 Diagram of target localisation using: multilateration in 2D for 1 Tx and 3 Rx (left), and interferometric radar for 1 Tx and 2Rx (right).

A finer source of distance information present in radar signals is that from phase information. By comparing the difference (δR) in target path length for two height offset receivers, height information can be extracted. This is shown on the right in Figure 1.4. The process of measuring the phase difference between two height offset receivers is knows as interferometric radar [7]. This technique has been exploited for a long time for both airborne and spaceborne radar systems. A very common usage for this style of radar is topography, where the phase information is used to generate a height profile of the land which the radar is imaging. The statistics and height profile from the interferometric radar data are great tools for assessing the terrain and its composition [28]. This method has one main drawback for $\delta R > \lambda$. The effect of the phase difference caused by δR is periodic, and the interference caused by δR is the same as that caused by $\delta R + m\lambda$, where m is any integer. To accurately reconstruct δR and the target position, the unique value of δR has to be found through a process known as unwrapping the phase, which is an extremely difficult task for $\delta R >> \lambda$. This process is equivalent to multilateration, but using the much more sensitive phase information rather than range. Multilateration and interferometry are mostly position estimation techniques, but this information can be applied to generate 3D imagery.

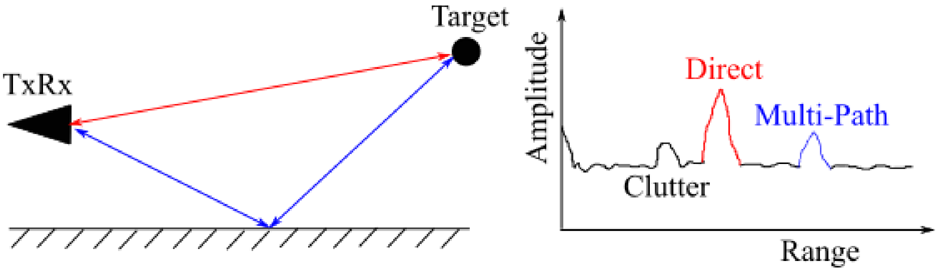

Fig. 1.5 Diagram of two-ray propagation, used for ground bounce height finding.

All of the previous approaches have required multiple Tx-Rx pairs, or measurements from multiple directive signals. However, if some information is known about the scene a priori, then height finding using range information can be performed with only one Tx-Rx pair. Two-ray or ground bounce models are a useful and simple technique for height finding when the scene can be taken to be a target over a near-flat Earth. This is shown in Figure 1.5. When the radar signal is reflected from the target, part of the signal is scattered directly back to the receiver, and part of the signal is first reflected off of the ground and then gets to the receiver. By looking at the time delay of the direct and multipath signals, one can estimate the additional distance travelled by the multipath signal and hence the target's height relative to the ground plane [29]. One of the main advantages of this technique is that it requires only one TxRx site, as opposed to the many sites of multilateration. It may prove to be a useful technique for targets in a road scene, as the road surface is usually relatively flat and predictable. However, detecting both the direct and multipath signal, and picking them out in the presence of clutter and multiple targets is not an easy task. Therefore, this technique does not have a guarantee of working every time.

In summary, there are many 3D imaging and height finding radar techniques, but those explored here can be loosely grouped into two sets. Those which find height information through selectively illuminating a certain region of space, and those which estimate the position of the target through differences in the signal propagation path length. The first group includes scanning, monopulse, and array processing, and the second group includes multilateration, interferometry, and ground bounce height finding. 3D imaging radar is a large field of research, and there are a number of other height finding techniques which have seen use but simply can not be covered by the scope of this thesis, such as Doppler Beam Sharpening (DBS) [30].

Now that a basis of traditional radar sensors and the methods they use for extracting height information have been laid out, the next section will consider the application of autonomous vehicles.

1.1.3 Autonomous Vehicles

This section defines the different levels of vehicle autonomy, and introduces the reasons why it is desirable for users, companies, and local authorities to invest in autonomous vehicles, and the impacts this may have. Although fully self-driving cars are yet to be realised, semi-autonomous vehicles have been on the road for some time. Vehicle autonomy can take many forms depending on what the manufacturer and user wish to achieve. The Society of Automotive Engineers (SAE) loosely group vehicle automation from levels 0 to 5 [31] which can be seen in Figure 1.6. For the higher levels of autonomy (4-5), the system must be in control of the vehicle for the vast majority of the journey, and must be able to perform all functions which a human driver can perform.

Level 1-2 systems are by far the simplest from an engineering perspective. Some of these systems may only take control of the acceleration and braking, and only under specific circumstances. This includes Adaptive Cruise Control (ACC) [32] and emergency braking systems [33]. Other systems may only sense road markings or vehicles around them in order to steer or to warn the human driver, such as lane keeping warning systems which activate when the driver is in danger of unknowingly departing from their lane on a motorway [34]. These are examples of very constrained vehicle autonomy, where the vehicle measures one aspect of the scene and varies a single parameter. In the case of ACC and emergency braking, the system only has to keep the vehicle speed under a measured value, and in the case of lane keeping, the system has to keep the driver's left-right position within two measured values.

In more advanced (level 3-4) cases the vehicle must plan a set of actions, and then take control of both the speed and steering to move the vehicle to a known position. Some good examples of this are self-parking systems, which require much more processing than level 1-2 systems. These systems have the additional tasks of path planning, dynamic 3D scene monitoring, and full adaptive vehicle control. However, in this situation the driver is initiating a set procedure to move the vehicle to a known position in its immediate vicinity over a short time span. A more complex example is current Autopilot systems, which combine lane-keeping, ACC, overtaking, and emergency braking to autonomously drive the vehicle along a road [36] (though the abilities of these processes are continually being updated). Most of these systems can only be applied to a very particular situation, and still require human intervention, and as such they are a

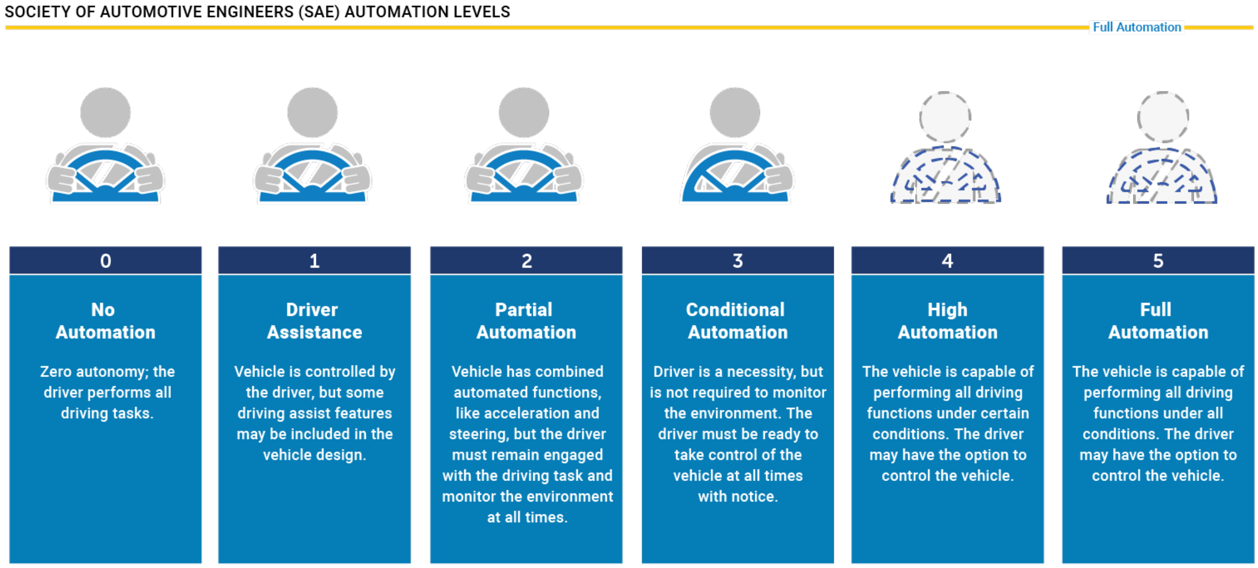

SOCIETY OF AUTOMOTIVE ENGINEERS (SAE) AUTOMATION LEVELS

0 **No Automation**
Zero autonomy; the driver performs all driving tasks.

1 **Driver Assistance**
Vehicle is controlled by the driver, but some driving assist features may be included in the vehicle design.

2 **Partial Automation**
Vehicle has combined automated functions, like acceleration and steering, but the driver must remain engaged with the driving task and monitor the environment at all times.

3 **Conditional Automation**
Driver is a necessity, but is not required to monitor the environment. The driver must be ready to take control of the vehicle at all times with notice.

4 **High Automation**
The vehicle is capable of performing all driving functions under certain conditions. The driver may have the option to control the vehicle.

5 **Full Automation**
The vehicle is capable of performing all driving functions under all conditions. The driver may have the option to control the vehicle.

Fig. 1.6 Levels of vehicle autonomy defined by the SAE [35]

far cry from the level 5 all-conditions fully self-driving vehicle.

The motivation for each of the users vary depending on the level of autonomy. Level 1-2 ADAS systems exist as a method to enhance the safety and usability of the vehicle. For example, the ACC systems allow a better traffic flow and a larger safety margin in mild and moderate braking events [37]. According to Mercedez-Benz, employing enhanced braking systems could mitigate 53% of rear-end collisions, and avoid 35% entirely [38]. According to the American Automobile Association, self-parking systems result in 81% fewer curb strikes, 10% faster parking, and parking 37% closer to the curb [39]. Lane departure warning systems have been shown to reduce the number of road accidents by keeping drivers in their correct lanes on the motorway [40]. Although these systems are invaluable, they do not represent a seismic shift in the way vehicles are used. On the other hand, level 4-5 ADS systems have this potential.

Level 5 ADS systems are equivalent to having a separate driver in the vehicle. This in itself introduces interesting ethical and legal questions in terms of who is responsible for the actions taken by the vehicle, but this is outside the scope of this thesis. The first interesting consideration for these systems is how it will affect the car user-base. Unlike level 4, level 5 systems do not expect the driver to take control of the vehicle in any circumstances, and in theory the user does not need to have a driver's license or be able to operate the vehicle. It is predicted that autonomous vehicles will first be expensive, and as the technology matures and more second-hand vehicles are introduced they will become cheaper and more widely adopted. As such, initially they are likely to exist as a status symbol [41] and a way to achieve a comfortable ride such that the driver does not have to perform tasks such as long motorway driving or finding a parking space [42]. At all stages, autonomous vehicles are expected to see use as taxi-like services owned by private companies [43]. Currently, young, disabled, or elderly people may have to use public transport to get around, but automated vehicles could fill this role - either as a taxi-like service, or as the technology becomes cheaper, as privately owned vehicles [43].

Because of this wider user-base it is expected that the number of road users will increase, but that does not necessarily mean more traffic congestion, collisions, or longer journeys. The traffic flow is likely to be improved through the use of cloud-connected vehicles, with knowledge of the intentions and states of other vehicles improving traffic congestion [44], which can be implemented with systems as simple as cooperative ACC [45]. [46] and [47] both predict a total collision reduction of 90% with large scale adoption of autonomous vehicles. A similar study found even braking assist systems which work cooperatively can reduce collisions in hard braking vehicles by up to 50% if they are widely adopted [48], (though may in fact degrade performance if not widely adopted). Finally, [49] concluded that in some cities that as few as 10% of the original vehicles could provide all of the transportation needs met by the original vehicles.

When compared to humans, even if the system only pilots the vehicle as well as an alert human driver, this is still a significant safety increase for most vehicles - as human drivers often drive while being distracted, tired, or intoxicated. A UK governmental study found that 27% of fatal crashes were caused by failure to look and 10% were caused by distracted drivers [50]. A review paper on accidents related to sleep found it was essential that road users and employers are educated about the risks of driving while tired, and outlined many studies which show how dangerous it is [51]. Drink driving has caused approximately six thousand accidents and nine thousand casualties in the UK alone in the last decade [52]. All of these factors mean that autonomous vehicles are likely to provide faster journeys for all, with less congested cities, and fewer collisions.

Finally, let us briefly consider the challenges associated with designing an autonomous vehicle. To do this, it is essential to identify the conditions in which the host vehicle exists, and what the vehicle is expected to do. To help frame this discussion, a summary of these conditions are shown in Table 1.1, and an example road scene is shown in Figure 1.7. Table 1.1 is by no means a definitive list of the full variety of conditions the vehicle will encounter, but serves as a rough summary of the conditions of everyday driving. These conditions describe a rapidly changing dynamic scene, with variable atmospheric and lighting conditions. On top of this, the vehicle is a relatively small platform, and the sensor system has to be adapted to this. It is desirable to minimise the size of the sensors, their associated processing load and processing (reaction) time, and the power consumption of the system. This variety of conditions and requirements demonstrates that vehicle autonomy should not be the task for a single automotive sensor, but rather a combination of different sensors.

Parameter	**Consideration**	**Conditions**
Maximum Target Range	ITU long-range radar range [53]	150 - 250 m
Vehicle Speed	UK 70 mph speed limit [54]	0 - 31 ms^{-1}
Platform Size	Size of large passenger car [55]	5 x 2 x 2 m^3 (l w h)
Azimuth FOV	Possible angle of collisions	360 °
Height FOV	Prevention of bridge strikes [56]	0 - 5 m above ground
Reaction Time	Under human reaction time [54]	< 0.7 s
Lighting Conditions	Overcast night - direct sunlight [57]	0.0001 - 130000 lux
Atmospheric Conditions	Typical conditions	Clear air, rain, fog, snow, sand
Sensor Coverings / Contaminants	Typical conditions	Water, ice, mud, dirt, sand, leaves

Table 1.1 Typical road conditions in which a vehicle is expected to operate.

Figure 1.7 is designed to illustrate how diverse the response from the vehicle should be depending on the object in the scene is. For a speed-bump (a), the vehicle is expected to reduce its speed and continue straight ahead, whereas for an arm barrier (b) the vehicle must come to a stop until the barrier has been lifted. For overhead objects such as branches (c) and a bridge (e), the vehicle must correctly identify if the vehicle can safely pass underneath this object. Finally with other road users, such as the pedestrian (d), the vehicle must estimate what the road user is going to do next and take measures to avoid them and follow the highway code. Behind all of these behaviours are a great number of signal processing and control systems problems, and the sensor suite of these vehicles must be able to handle all of these situations to inform the vehicle not only where all of these objects are, but also what they are and what they may do next.

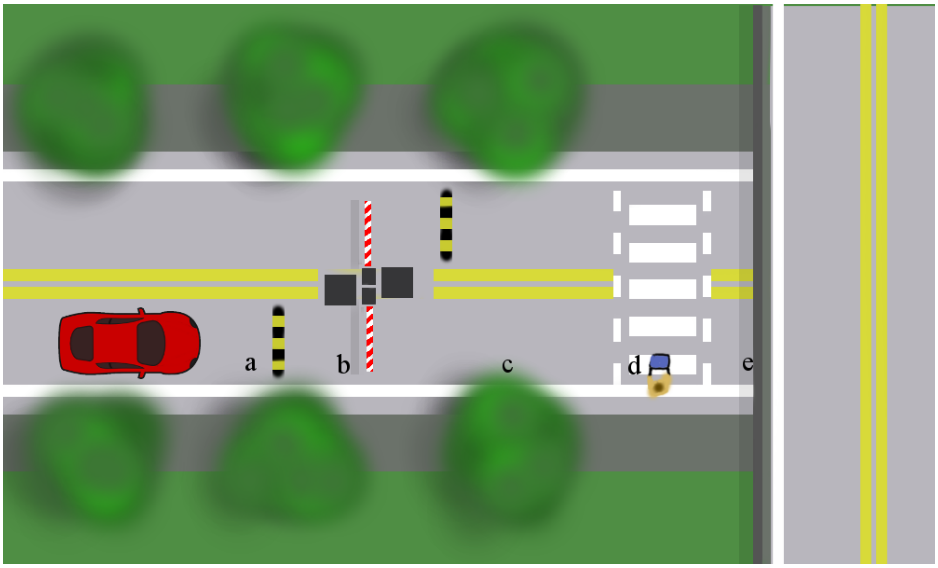

Fig. 1.7 Bird's-eye view of an example automotive scene. Objects shown include a speed-bump (a), arm-barrier (b), overhanging tree branches (c), a pedestrian stepping off of the curb (d), and a bridge (e).

In conclusion, the higher levels of automation may prove to be a completely transformative technology with a great number of benefits. However, the vehicle must be able to perform all of the operations which a human driver performs in everyday operation of the vehicle. Therefore the sensors of the vehicle must be able to provide highly detailed, dynamic, and robust 3D information of the world around the vehicle, and operate in highly variable conditions. The following section will explore which sensors are being employed to meet these challenges.

1.1.4 Automotive Sensors & Their Applications

This section will explore the state of the art automotive sensors used in industry. The industry standard of high resolution automotive sensors for 3D reconstruction is a combination of stereo video and Light Detection and Ranging (lidar) systems [58]. Stereo video systems can be thought of much like human binocular vision, with two (or more) separated cameras measuring a scene. For stereo video systems, the height and cross-range information is given by the pixel position of the target in the camera image, and the depth is generated from differences in the images of multiple cameras [59, 60]. This depth map generation is a computationally intensive process which looks at the position and size of common features, keypoints, or landmarks in the images between multiple cameras to estimate their depth [60]. Typically this process generates a 2D RGB + depth image of the scene, though more complex algorithms may stitch together a 3D reconstruction from many images.

Lidar systems come in many forms, but have the same general principle; range information is generated from the time of flight of coherent light from an emitter to a receiver. These lidar beams are typically very highly directive, and the 3D azimuth and elevation maps are generated from the orientation of the scanning pencil beam, much like scanned radar in section 1.1.2. Current demonstrators achieve this through either mechanically scanning the lidar emitters and receivers [61], reflecting the beam off of a mirror which rotates mechanically or microelectromechanically ([62] and [63] respectively), or more recently solid state lidars have been developed which electronically steer the beam using phased arrays [64].

There are a number of limitations for both types of electrooptical system. As in most cameras, the images used by stereo-video systems are saturated when directly illuminated by direct sunlight or bright lights, and are under-illuminated and noisy in the dark. For a vehicle driving with direct sunlight illuminating the camera, or at night time (a dark scene with bright lights illuminating the camera), the stereo video system cannot exploit the camera's full dynamic range [65]. This makes detecting common features between cameras, and hence depth estimation, much more challenging [59].

Most lidar systems used in automotive demonstrators [66, 67] only offer a point cloud of reflected positions, as opposed to dense range-profiling which can deliver surface texture information. While full waveform lidar exists, which is akin to range profiling, it has a large data rate. This means that existing systems can only process the data from a single beam for full waveform lidar, which needs mechanical scanning to form a full 3D image [68]. Lighting conditions also adversely affect lidar systems, where direct illumination from the sun will saturate the receiver elements [69], and the extra scene illumination greatly increases the noise floor and false positive detections [70]. Both stereo video and lidar have high levels of attenuation in adverse weather conditions and stop functioning altogether if the sensor is covered [71, 72]. There is also no way to directly measure the velocity of an object, and instead they must make use of frame-to-frame association and tracking to measure the velocity of the target by considering its change in position over time.

As the more mature automotive sensor systems for autonomous driving, lidar and video are the primary sensors of the most widely used datasets. These datasets are the starting point of the development of vehicle autonomy, as they can be used as training data for algorithms without operating a vehicle. Table 1.2 shows a list of widely used general purpose datasets. There are a number of datasets which have been published, each with slight differences in sensors and applications. Among the most popular are the KITTI [66], Ford Campus [67], Oxbotica [73], and ApolloScape (Baidu) [74] datasets. The focus of the majority of these datasets is lidar and stereo vision data, though datasets which have automotive imaging radars are now being published by the Oxford team [75] and 3D radar imaging from Astyx [76]. Although arguably the most widely used source of automotive scene data is Google Maps' StreetView [77] and Baidu's Panorama [78], these have limited utility due to the lack of labelled data and ground truth data. There are, however, some datasets which take this data and label and augment it, such as the Toronto City dataset [79], which are popular because of the large quantities of data provided which just has to be labelled. The datasets in Table 1.2 represent the benchmark datasets which industry and academia use to test their deep learning and machine learning algorithms. The trend in these datasets appear to be that cameras are mounted all around the vehicle, with one or more dual-return lidars. Now that automotive radar is maturing as a technology, Oxbotica has been updated to include a FMCW mm-wave radar and Astyx have produced a dataset to showcase their new 3D radar.

The wealth of information provided by these datasets are often used to train algorithms for the more advanced actions, such as object identification, surface identification, occupancy mapping, and operating in a variety of real world weather and lighting conditions. In fact, there are already a number of prototype

Dataset	**Year**	**Video**	**Lidar**	**radar**	**IMU/GPS**
Ford [67]	2011	Point Grey Ladybug3	Velodyne 64E,	-	Applanix POS-LV 420 INS,
KITTI [66]	2013	PointGray Flea BW & colour	Velodyne 64E	-	GPS & OXTS RT3003
			Riegl LMS-Q120		Trimble GPS, Xsens MTi-G
Toronto City [79]	2016	PointGray Bumblebee 3	Velodyne HDL-64E	-	Applanix POS LV
Oxbotica [73]	2017	Point Grey Bumblebee XB3	SICK LMS-151, SICK LD-MRS	-	NovAtel SPAN-CPT
Apolloscape [74]	2019	VMX-CS6	Riegl VMX-1HA, VUX-1HA	-	Not Detailed
Oxbotica radar [75]	2019	Point Grey Bumblebee XB3 Point Grey Grasshopper 2	Velodyne HDL-32E, SICK LMS-151	Navtech CTS350-X	NovAtel SPAN-CPT
Astyx [76]	2019	Point Grey Blackfly	Velodyne VLP-16	Astyx 6455 HiRes	Not Detailed

Table 1.2 Widely used datasets for autonomous vehicle development, including the sensors used.

level 4 vehicles which have been on the roads. There are too many to detail each of them here, but a complete list of the largest technology companies and their efforts into self-driving cars can be found in [80].

Based on Table 1.2, automotive radar has only recently been added to datasets for self-driving cars. As such, it appears that many companies have been slow to adopt radar as a primary sensor until now. One of the companies which is at the forefront of autonomous vehicles is Tesla [80], who have launched many cars with auto-pilot features onto public highways. It is fair to say that the sensor layout of the Tesla Model X, which can be seen in Figure 1.8, represents at least a part of what the automotive industry thinks the layout of automotive sensors should be. The following passage taken from a recent Tesla article [36], explains their recent decision to adopt automotive radar as a primary sensor.

" After careful consideration, we now believe it (radar) can be used as a primary control sensor without requiring the camera to confirm visual image recognition. This is a non-trivial and counter-intuitive problem, because of how strange the world looks in radar. Photons of that wavelength travel easily through fog, dust, rain and snow, but anything metallic looks like a mirror. ... Therefore, the big problem in using radar to stop the car is avoiding false alarms. Slamming on the brakes is critical if you are about to hit something large and solid, but not if you are merely about to run over a soda can. Having lots of unnecessary braking events would at best be very annoying and at worst cause injury. ... When the car is approaching an overhead highway road sign positioned on a rise in the road or a bridge where the road dips underneath, this often looks like a collision course. The navigation data and height accuracy of the GPS are not enough to know whether the car will pass under the object or not. By the time the car is close

and the road pitch changes, it is too late to brake."

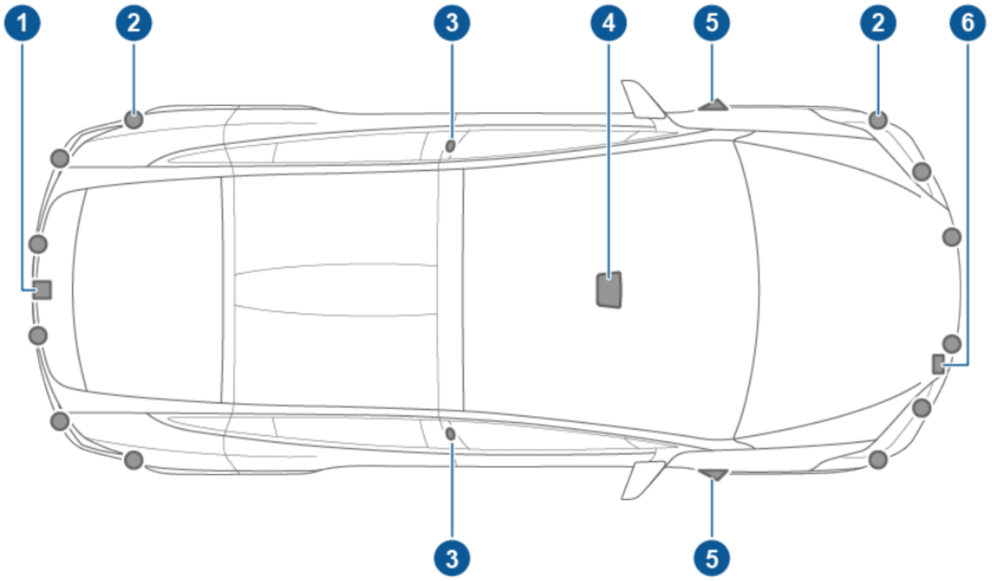

1. A camera is mounted above the rear license plate.
2. Ultrasonic sensors are located in the front and rear bumpers.
3. A camera is mounted in each door pillar.
4. Three cameras are mounted to the windshield above the rear view mirror.
5. A camera is mounted to each front fender.
6. Radar is mounted behind the front bumper.

Fig. 1.8 Diagram of the sensor layout of a Tesla Model X [81]

They recognise that although radar is indeed a robust sensor, the actions that the vehicle will take using only a radar may be difficult to predict and explain compared to optical systems. This confirms that the automotive industry also recognises the need for height information for route guidance, and are concerned that radar does not currently offer this capability.

This section has outlined existing stereo video and lidar systems which have seen extensive use for the development of autonomous driving. It has also outlined the existing sensor datasets which are being used to train various algorithms, and the inclusion of radar into these datasets. It has highlighted potential weaknesses of electro-optical sensors, and the fact that industry has noticed this and is considering automotive radar to address these weaknesses. The next section will shift focus to automotive radar.

1.1.5 The Development of Automotive radar

The goal of this section is to provide an overview of the history and development of automotive radar systems, as well as the industry standard today. Automotive radar was first experimented with in the 1950s at the Transport and Road Research Laboratory (TRRL) [82]. These earliest prototypes were existing radars at lower frequencies, such as X band, which were mounted onto the roof of a vehicle. In fact, in their early stages of development, automotive radar was tested at many frequencies from 10 to 94 GHz by companies such as VDO, Standard Electric Lorenz, and AEG- Telefunken [83]. Although the need for robust sensors were well founded, the early lower frequency radars were very large compared to the vehicle. Realistically, smaller radars would be needed if they were ever to be taken seriously as an automotive sensor. It was not until the 90s that 24GHz anti-collision systems were introduced by Greyhound thanks to advancements in semiconductor technology [84]. Since then, automotive radar has been pushed into the ITU EHF band [3], and has been applied to a variety of ADAS systems for some time [85].

Automotive radar has been widely adopted in ACC and collision avoidance systems [85]. They have two major advantages which make them well suited to such systems. First, the velocity of road objects relative to the host car can be determined directly from the Doppler information [4], as opposed to the change in position of a target at each time step (as in stereo video systems [59]), although frame-to-frame association can still be a useful tool for the evaluation of these parameters. The second is that such radars are more flexible with respect to where and how they can be mounted, with 79 GHz radar being able to be mounted behind the vehicle's bumper [86] and being relatively unaffected by radome contaminants, such as leaves, water or dirt covering the sensor which would completely occlude electrooptical (EO) sensors [10]. Indeed, one of radar's most useful feature is that it is robust to many conditions which limit use of EO sensors [87]. Because of this, the radar used by the majority of existing ACC systems is a 24 or 77 GHz radar which is mounted behind the bumper of the vehicle to measure the relative velocity of the vehicle ahead, and hence whether the host vehicle needs to reduce its speed.

These kinds of automotive radars are usually classed as either short range radar (SRR) or long range radar (LRR) [83]. A diagram of this is shown in Figure 1.9. Often one radar of each type is combined, with the goal of being able to monitor 3 lanes of a motorway, with SRR focusing on ranges up to 30 m, and LRR with ranges typically up to 150 m [88]. The earliest production vehicle with such a setup was the Mercedes S class in 2005, which made use of a 24 GHz SSR and 77 GHz LRR [88].

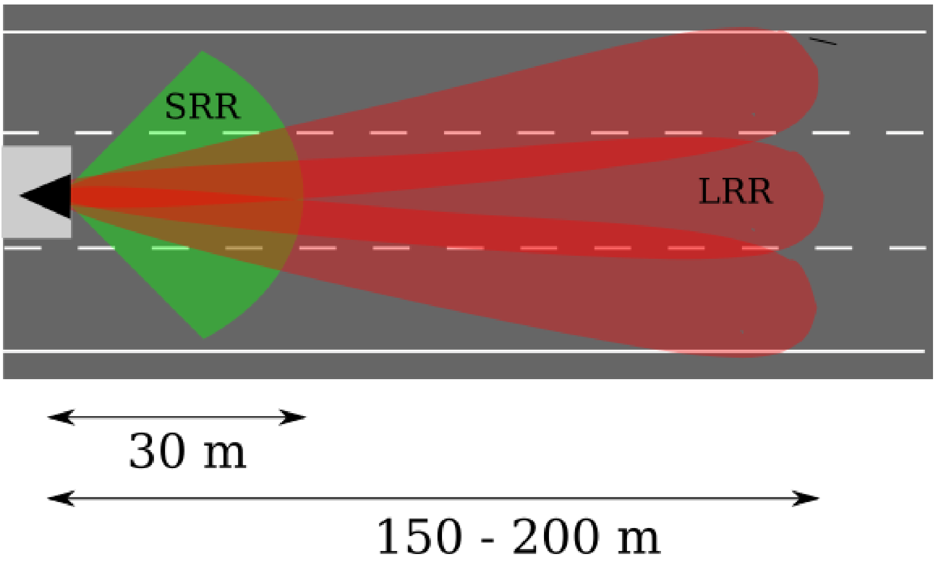

Fig. 1.9 Illustration of long range radar and short range radar.

By developing ADS and ADAS systems from level 0-2 to the higher levels, the focus of the radar has become less about characterising a single target and has moved towards imaging and dynamic scene monitoring. Essentially, the radars which have been previously discussed were not designed to be the primary means of controlling the vehicle. They exist as a means of assisting the driver to create a safer and more comfortable experience. The human driver is still entirely in the loop, and is performing the vast majority of the driving tasks. For autonomous driving, these systems could still be implemented like this as a means to assist stereo video and lidar systems. However, as discussed in section 1.1.3, the development of higher levels of automation means that the sensors must be able to perform robustly in all conditions, and still be able to deliver high resolution imagery. Stereo video and lidar systems assisted by an ACC radar or collision mitigation system does not provide this capability. Instead, automotive radar must be adapted to respond to these new demands, and provide new imaging capabilities which they currently do not deliver. With this in mind, the imaging techniques from the lower radar frequency bands are being adapted to automotive radars.

Digitally beamformed 77 GHz automotive radars have existed since 2003 [89], but with somewhat limited azimuth resolution. As in Figure 1.9, for many LRR this angular localisation only had to be good enough to determine which lane the vehicle ahead occupies. In modern radars, the system is being used to generate a range-azimuth image which appears somewhat like a bird's eye view of the scene. One popular system is the Navtech ORI radar used in [73]. This system creates such an image by rapidly scanning the radar system in azimuth. Another popular approach has been to perform 1D MIMO beamforming. Examples of these commercially available radars include NXP [90], Inras [91], and Texas Instruments [92], and many current automotive chip-sets are already based on 1D MIMO. Although the exact application depends on the radar, the focus of many of these new radars is more like SRR imaging systems - to generate a high resolution range azimuth image of the scene close to the vehicle.

In short, the history of automotive radar has involved testing radar frequencies up to 100GHz, before settling upon the 24 GHz and 79 GHz bands as the main operating frequencies. The specific radar system used depends on the application, but typically multiple radars are used to monitor at short range (SRR) and long range (LRR). More mature technologies such as ACC may only use a radar to measure the speed of the car ahead, whereas emerging systems with higher levels of autonomy are likely to require full imaging radar.

This section has given the background of radar, autonomous vehicles, and automotive sensors. The following section will look specifically at recent developments both in industry and the academic literature, focusing on low-THz radar and 3D automotive radar.

1.2 Literature Review

This section will look at recent advances in low-THz radar, and 3D and height-finding automotive radar in industry and the academic literature. It is split into two sections. Section 1.2.1 examines the emerging low-THz band and the way it is being used. Section 1.2.2 looks at how height-finding and 3D imaging techniques have been applied to automotive radars.

1.2.1 Low-THz radar

This section will explore the current uses of and recent developments in the low-THz band, and why the literature suggests that it has the potential to be used as an alternative to current automotive radars.

Frequencies between 0.1 and 10 THz have long been known as the THz frequency gap - a region between Microwave and Infrared radiation which has yet to be fully exploited [93]. Microwave frequencies can be generated and detected by electronic oscillators, while infrared frequencies may use semiconductor band gaps [94]. However, the THz gap is a region where the power output of both the microwave electronics and infrared photonics approaches are not sufficient for most sensing applications. It is only recently that these frequencies have started to be explored, due to advances in frequency multipliers and Monolithic Microwave Integrated Circuit (MMIC) devices.

A number of studies and demonstrators have shown that radars in the low-THz band can be used for short-range, highly-detailed, 3D imagery. As it is still an emerging technology, low-THz 3D imaging radars have (until very recently) been constrained to very short-range sensing, such as personnel and luggage screening because of their low transmit power. Examples of this kind of 3D imaging on the scale of metres using FMCW radars can be found at 150GHz [95], 300GHz [96], and 670GHz [97]. These setups achieve 3D imaging through mechanically scanning in multiple directions using a mirror or linear positioners, as in Figure 1.2. For a slightly larger target range of 8m, [98] applied a similar idea at 300GHz to for personnel screening. The high resolution 3D images produced here demonstrate the sub-cm resolution and the wealth of information available to such radar systems, but the application here relaxes many constraints on these sensors. The systems are static and can be precision mounted, the target exists in a fixed (relatively small) imaging volume, and a long processing time with multiple observations can be used to obtain the necessary level of detail. Furthermore, although [96] demonstrated a sub-cm cross range resolution at 300 GHz, this was performed at a range of 1 m. The cross-range error and extent is expected to increase radially, and it is the short range which gives these images their fine cross-range resolution. Therefore the systems and techniques proposed here may only have limited utility for automotive uses which have longer ranges, larger fields of view, and shorter processing times.

There are now examples of radar in the low-THz band using MIMO techniques, illustrated in Figure 1.3. MIMO setups are now being implemented at 120 GHz [99, 100], though low-THz MIMO systems are still in their early stages of development and have not seen much use in 3D imaging. The angular resolution of MIMO setups are dictated by the number and spacing of TxRx pairs (for example the 2 Tx - 6 Rx 120 GHz system [99] only has an angular resolution of 3.5 °). To beamsteer and beamform efficiently without generating grating lobes, the spacing between antenna elements should be half-wavelength or less [101]. A further consideration is that it is desirable to integrate over a large number of elements to obtain a high gain and narrow beamwidth [25]. To do this requires manufacturing many elements with a separation of less than wavelength, which is particularly difficult when this wavelength is on the scale of a mm. Moreover, to make use of the desired finer range resolution for the same imaging scene requires even faster sampling, putting higher demands on the data rate, especially with a large number of elements. Therefore, although MIMO may prove to be invaluable in future low-THz radars, the technology is still emerging.

Currently, the low-THz band is not widely thought of as automotive radar. This is most likely due to the lack of an assigned frequency band for automotive radars here [102]. Current demonstrators have a low transmit power, and for road conditions (see Table 1.1), a concern about low-THz radar was that the propagation loss and attenuation through different media would be too high. Therefore investigations were made into the absorption due to rain [103], snow [104], ice [105], sand [106], leaves [107], radome contaminants [108, 109], and the bumper of a vehicle itself [86]. These studies of attenuation were taken a step further by creating multi-sensor images which show that these radars are much more penetrative than existing EO sensors through obscurants [72]. Although the attenuation was in general slightly higher for low-THz radar compared with 79 GHz, each of the studies found that these levels were reasonably similar and acceptable. Specifically, the loss caused by the atmospheric absorption from water and oxygen is shown in Figure 1.10. Although in general the absorption is larger for higher frequencies, there are a number of peaks and troughs present in the absorption spectrum. This means that the atmospheric attenuation can be kept to an acceptable level if the RF frequency lies within one of these windows of lower absorption, such as those centred at approximately 100 GHz and 250 GHz. Therefore, the literature demonstrates that it is feasible to use low-THz radar in road conditions.

The next major step in assessing the usability of this band for automotive radar is to characterise the appearance of automotive objects to this kind of radar. There is a large literature of the RCS of different targets in commonly used radar bands, and it is needed to properly characterise and predict the abilities of radar sensors for manufacturers. This has been started by establishing a body of low-THz radar parameters for a wide variety of common road objects [111–114]. Many common automotive objects have a larger RCS in the low-THz band, such as a passenger car, where the RCS had a mean of 3.5 dBsm at 24 GHz and 6.8 dBsm at 300 GHz [111]. For some of the most crucial targets such as a pedestrian, the more diffuse nature of EMW scattering means that the RCS is more uniform and predictable, meaning the target can be detected regardless of what aspect angle it makes with the host vehicle [112].

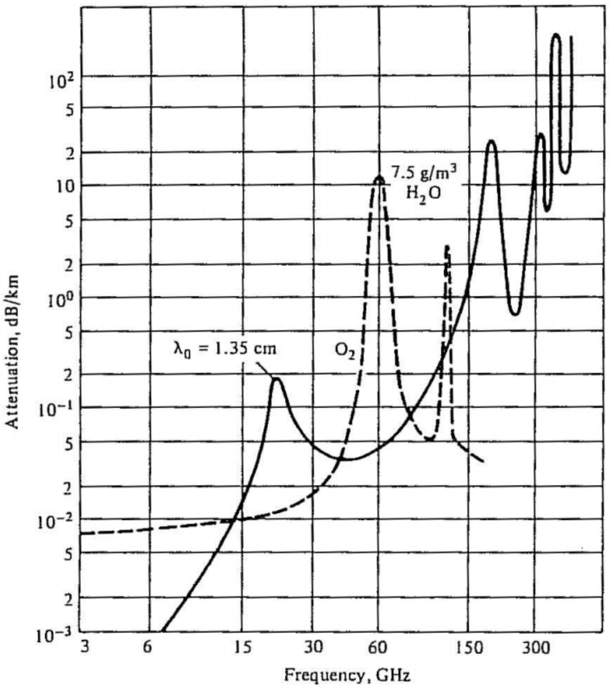

Fig. 1.10 Microwave attenuation due to atmospheric oxygen and water vapour [110].

The next stage in this development was to mount these kind of radars into a vehicle and to take measurements of automotive scenes. This was performed on both complex road scenes [16, 115], and off-road scenes [116]. One such example is shown in Figure 1.11. The resolution provided by these systems is very fine, such that one can reliably tell not only the position of a target, but what the road surface may be - such as the gulley (G) compared to the track regions (T). In fact, some academic papers are now applying surface classification techniques to these images [117].

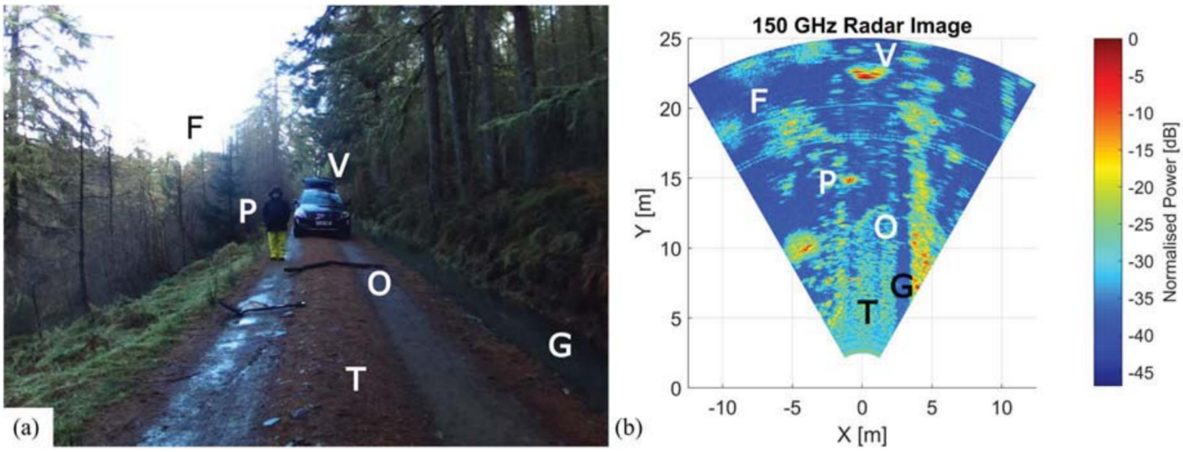

Fig. 1.11 Low-THz radar image of an off-road scene, taken from [116]. (a) video ground truth, (b) 150 GHz scanned radar image. The scene includes foliage (F), a pedestrian (P), a vehicle (V), a fallen branch (O), the track (T), and a water-filled gulley (G).

This section has overviewed the existing development of short-range low-THz radar, its potential issues, and the way in which it could be applied to address the shortcomings of automotive mm-wave radar. The next section will focus on the height-finding and 3D imaging aspects of both mm-wave and low-THz automotive radar.

1.2.2 3D Automotive radar

This section provides a literature review of height-finding and 3D automotive radar. From the discussions in sections 1.1.3 and 1.1.4, the aim of height-finding and 3D radar is to provide an extra degree of freedom of positional information to existing 2D imaging radar. Whether this is a height estimate of one target, a 2D + height image, or a full 3D image is entirely a matter of the application, system, and signal processing techniques. For the goal of distinguishing between overhead bridges, speed bumps, and walls, a height estimate or 2D + height may be sufficient. For 3D occupancy mapping, height profiling, and identifying complex targets, a full 3D image may be more appropriate. All 3 cases are discussed here.

Height estimation for automotive radar has existed for some time in the academic literature. Using the multipath ground-bounce technique, (see Figure 1.5), [118] applied this method to estimate the height of objects while using only 1 Tx - 1 Rx in the 76-81 GHz band. To improve the TOA estimate of the direct and multipath signal, which is used to generate the target height, the team developed on this using the RELAX and MODE algorithms [119]. As shown in these papers, these techniques rely on the ability of the system to reliably identify a direct and multipath signal, and the resolution in height is ultimately determined by the range resolution of the system, which is why resolution enhancement techniques needed to be used to improve this height estimate. Similarly, at 76-81 GHz [120] used the interference patterns of direct and multipath signals to identify and estimate the height of an overhanging bridge as the vehicle drove towards it. This is similar to the ground bounce technique, but looking at the variation in signal amplitude due to two-ray interference of the direct and ground-reflected signals. What is interesting about this technique is that it only requires 1 Tx - 1 Rx, and does not rely on detecting and estimating the direct and multipath TOA, however it does require the signal to be observed at a series of platform positions, and for the target to be static. In [121], Doppler Beam Sharpening (DBS) was applied to perform height-finding for an overhanging gate when the vehicle was travelling at a speed between 11-13ms^{-1}. This has very similar advantages and disadvantages as [120] above, but with the added complication that the platform must be moving. Therefore DBS and this form of multipath interference cannot work when the car is stationary. Although DBS can be used to generate a 3D image, the authors only demonstrate the ability of these techniques to estimate the height of one target rather than providing a 3D image. These techniques may prove to be useful for the height estimation of an object of interest in a scene, but they each have constraints on when and how they can be used, and so they could be best used alongside more general 3D imaging strategies.

Interferometry is now being applied to automotive imaging radar to provide a height value for each pixel in the range-azimuth image. This generates a 2D plus height image, with both an intensity value and height estimate for every pixel in the 2D radar image. Astyx [76] are using a combination of 1D MIMO to provide the azimuth information, and interferometry to generate the height information for 2D plus height imagery. Astyx have demonstrated the ability of this system to detect and estimate the height of an overhead bridge, which is one of the critical use cases for height-finding radar. There are also a number of research papers reporting interferometric imaging in this way. However, the majority of car-borne interferometric SAR papers are chiefly interested in topography, such as the measurements in [122, 123] which look at valley and slope deformation. For autonomous vehicles, [124] demonstrated the capabilities of a 24 GHz interferometric radar to detect speed bumps using interferometry. However, a major issue with 2D plus height radar images is that it does not necessarily provide the 3D shape and extent of a target, but rather it is a topographic map of a scene.

In commercial research, MIMO techniques are now being employed in some demonstrators to provide a full 3D image of the scene, such as the radars of Texas Instruments [125] and Arbe [126]. Currently, Texas Instruments [125] only achieve a range resolution of 0.6m and an elevation resolution of 18° using their MIMO setup, though MIMO demonstrators are such a large area of development that this is likely to improve. One way to improve the angular directivity and gain is through synthesising a larger virtual array, as in Figure 1.3. There are trade-offs in each method of generating a larger virtual array. Introducing more Rx elements would greatly increase the data rate, introducing more time-multiplexed Tx elements would lower the pulse cycle repetition frequency decreasing the update rate and the Doppler resolution, and introducing more Tx elements with frequency-multiplexed signals over the same available frequency support would decrease the bandwidth for each Tx signal which decreases the range resolution [101]. With current demonstrators, the images formed with the resolution from current demonstrators are incomparable to the detail of lidar or stereo video systems. To provide the extent, shape, pose, and height of a target (which is needed for target identification and many forms of sensor fusion with lidar and cameras), one must move towards higher resolution 3D imaging, which is where low-THz radar offers a promising alternative.

The literature in section 1.2.1 show highly detailed images, which demonstrate the wealth of information available in low-THz imagery and the sensitivity to surface detail. This is most notable in the interferometry in the low-THz band shown in [127], which has an incredible level of 3D information compared with existing automotive interferometry [124]. There are some papers which have demonstrated the ability of low-THz radar to perform very high resolution 3D SAR imaging of typical road scenes, using multilook side-looking SAR to reconstruct a plane defined by other sensors. Most notably, Fraunhofer have used their Miranda 300 GHz radar to reconstruct the facade of a row of buildings [128], and mapped a road surface [129]. The images produced are very highly detailed, but the system is not designed to be used for autonomous vehicle guidance unlike most automotive radars. While it is possible to know the radar's position to the scale of a wavelength (1 cm at 24 GHz), this kind of precision is very difficult for systems operating at 300 GHz or higher (<1 mm), meaning this highly detailed interferometry is likely to not be possible currently on a moving vehicle.

It is here that Time of Arrival (ToA) may provide an alternative for low-THz radar. The range resolution for many low-THz radars have been shown to be sub-cm [130, 131], which means that the height resolution generated by low-THz radars using ToA information has the potential to be similar to that generated by interferometric techniques in current automotive radars. In fact, there are already height-finding papers in the academic literature which report this [132]. The work of this thesis is designed to extend this idea, to generate not only ToA height finding techniques in the low-THz band, but to create full 3D imagery using ToA information. It is hoped that the techniques developed throughout this project will be able to generate not only 2D + height imagery, but to be able to provide a rudimentary height profile or extent information for complex radar targets, while keeping the robustness required for automotive applications.

1.3 Problem Statement, Contribution & Thesis Outline

Autonomous vehicles have a clear need for a robust, high resolution, 3D sensor which can compliment existing lidar and stereo video systems. Automotive radar is being developed to provide these capabilities in designated bands around 24 and 79 GHz, but the emerging low-THz band has not been properly investigated for this application.

The aim of this work is to test the ability of low-THz radar to perform height finding and generate 3D imagery, and to design appropriate algorithms which best make use of the strengths of the radar (fine range resolution, unique scattering mechanisms, aperture size), while mitigating its shortcomings (low transmit power, low SNR, limited coherency). This will be validated experimentally in a variety of different scenarios by using a prototype 300 GHz multi-receiver radar.

The novel contributions of this project are the development of new 3D imaging algorithms using ToA information which are optimised for low-THz radar, and their validation in a variety of scenarios through a combination of theory, simulations, and experiments. The earlier chapters focus on what the best sensor layout and localisation strategy may be. Therefore, although the specific application of 3D scanning and multilateration is novel, the algorithms outlined in earlier chapters are similar to those in the literature [96, 97, 132]. Once the configuration has been optimised, the modified forms of backprojection, basis pursuit, and compressive sensing imaging algorithms in later chapters are the main novel contributions to the state of the art.

The thesis is structured as follows: Chapter 2 gives a mathematical model for the system. Chapter 3 performs investigations into the prototype system, experimentally confirming its performance and system parameters. Chapter 4 looks at the imagery formed by mechanically scanning the system. Chapter 5 performs target localisation through time of arrival in multiple configurations. Chapter 6 generates 3D imagery from the range profiles of multiple Rx modules using a modified form of backprojection. Then chapter 7 attempts to improve upon the resolution of these images using compressive sensing and basis pursuit algorithms. Finally in chapter 8, conclusions are drawn and future plans are laid out.

1.4 Conclusion

Autonomous vehicles are a topic of great interest, with the potential to transform the way in which humans and vehicles interact for the better. However, the pursuit of higher levels of vehicle autonomy put increased demands on the vehicle's sensors. To create a level 5 autonomous car, the system needs to drive with a human driver entirely out of the loop, with safety levels greater than a typical human driver. Therefore the vehicle requires sensors which are robust enough to function in a number of atmospheric, lighting, and road conditions. Currently, the main sensors used by industry are a combination of lidar, stereo video, and 24-79 GHz radar systems. While the lidar and stereo video systems offer a highly detailed 3D view of the world, they do not offer the same levels of robustness as radar does. On the other hand, although radar is a very robust sensor, it does not provide a high resolution 3D image of the world around it. Therefore, if the lidar or stereo video systems were to fail, the vehicle is left with the radar as its primary sensor, and would have to rely on the radar's 2D lower resolution scene map. The vehicle will not only lose detail of the scene, but will lose height information. For example, the system will be unable to tell if the object ahead is clearable, such as a speed-bump or overhead bridge, or if it is on a collision course with a wall. This demonstrates the need for a robust, high resolution 3D sensor. Compared to more mature lower frequency radar bands, there are many useful physical properties created by working at such high frequencies, but also constraints from the technology readiness level of the hardware. The focus of the research presented here is to design 3D localisation and imaging algorithms which best exploit the high bandwidth, robustness, and quasi-optical properties of the low-THz band to generate high resolution 3D images of the road scene.

Chapter 2

System Model

This section aims to introduce the underlying theory and physics which are needed to support the 3D imaging algorithms. This includes a description of the coordinate systems, the imaging spaces, and the signal model for the low-THz radar. It is also necessary to detail all of the mechanisms effecting the power link budget of the system, including path loss and propagation effects, and scattering mechanisms from radar targets. It is laid out as follows; section 2.1 defines the coordinate systems used, section 2.2 defines the signal model. Then the signal power is considered: section 2.3.1 looks at the antenna gain, section 2.3.2 examines the losses of the signal due to propagation, including path loss and atmospheric attenuation, and section 2.3.3 looks at the scattering from road objects in the low-THz band. Finally, section 2.4 considers the discrete imaging grids on which the reconstructions of a scene are based.

2.1 Geometry

This section will lay out a mathematical description of the 3D space surrounding the vehicle. In most cases the coordinate system used will be sensor-centric as opposed to platform-centric or geographic. The coordinate frame is defined in general terms for a finite set of n_{Tx} Transmitters (Tx) and n_{Rx} Receivers (Rx). The equations in this section are given for the i^{th} transmitter (Tx_{i}) and receiver (Rx_{i}), where i is a positive integer counter which specifies a particular Tx-Rx pair. A single Tx or Rx may be used in multiple pairs. Coordinates in Cartesian $\mathbb{R}^3$ space are denoted as (x,y,z), those in spherical polar coordinates are denoted as $(R_{\mathrm{Tx_i}}, \theta, \phi)$, and cylindrical polar coordinates are denoted as (x', θ, z).

The conversion between these coordinate systems is given by (2.1), and is illustrated in Figure 2.1. The experimental setups will deal both with general Tx-Rx configurations and with the specific case shown in Figure 2.1b which is referred to as a TxRx stack.

$$\begin{bmatrix} x \\ y \\ z \end{bmatrix} = \begin{bmatrix} R_{\mathrm{Tx_i}} cos(\varphi) cos(\theta) + x_{\mathrm{Tx_i}} \\ R_{\mathrm{Tx_i}} cos(\varphi) sin(\theta) + y_{\mathrm{Tx_i}} \\ R_{\mathrm{Tx_i}} sin(\varphi) + z_{\mathrm{Tx_i}} \end{bmatrix} = \begin{bmatrix} x' cos(\theta) + x_{\mathrm{Tx_i}} \\ x' sin(\theta) + y_{\mathrm{Tx_i}} \\ z \end{bmatrix} \tag{2.1}$$

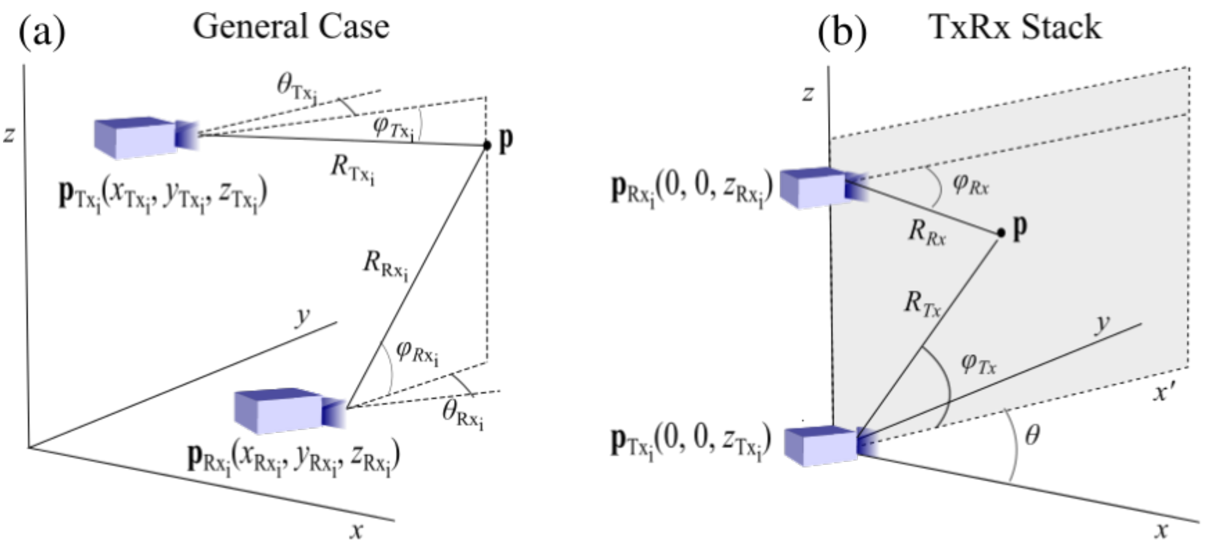

Fig. 2.1 Geometric model of the radar and the field of view of 3D space. (a) General case. (b) Specific case where the Tx and Rx are colocated in the ground plane at (x, y) = (0,0), and are coaligned in azimuth.

The cylindrical polar and Cartesian coordinate frames have their origin at ground height directly below the Tx. The Cartesian coordinate system is a left-handed coordinate system, where the positive z direction is directly upwards, the positive y direction is the bisector of the radar field of view, and the positive x direction is orthogonal to x and y. When the equipment is used in a vehicle, the positive y direction is the vehicle's nose-to-tail (rear-facing), and the positive x direction is the vehicle's right-to-left. This can be considered to be a platform-centric coordinate system, but the radar will be set up in later sections such that it still meets the definitions from the sensor-centric frame. The spherical polar coordinates, on the other hand, are only used for power link budgets and antenna patterns. Hence, for some measurements which are used to characterise the equipment, the origin may be redefined to be a specific Tx or Rx site. The transmitter position vector is $\mathbf{p}_{\mathrm{Tx_i}} = (x_{\mathrm{Tx_i}}, y_{\mathrm{Tx_i}}, z_{\mathrm{Tx_i}})$, and $\mathbf{p}_{\mathrm{Rx_i}} = (x_{\mathrm{Rx_i}}, y_{\mathrm{Rx_i}}, z_{\mathrm{Rx_i}})$ is the receiver position vector. It is often helpful to define their height separation as $b_i = z_{\mathrm{Rx_i}} - z_{\mathrm{Tx_i}}$. For an observation point $\mathbf{p}$, the (quasi-)bistatic range is given by (2.2). The monostatic range corresponds to the specific case where $\mathbf{p}_{\mathrm{Tx_i}} = \mathbf{p}_{\mathrm{Rx_i}}$. This bistatic range can be evaluated by the time-of-arrival (ToA), τ_{i}, which is the time taken for a signal propagating at the speed of light, c, to pass from $\mathbf{p}_{\mathrm{Tx_i}}$ to a point $\mathbf{p}$ and then back to the receiver $\mathbf{p}_{\mathrm{Rx_i}}$.

$$R_{\mathrm{b_i}}(\tau_{\mathrm{i}}) = \frac{c\tau_{\mathrm{i}}}{2} = \frac{R_{\mathrm{Tx_i}} + R_{\mathrm{Rx_i}}}{2} = \frac{||\mathbf{p} - \mathbf{p}_{\mathrm{Tx_i}}|| + ||\mathbf{p} - \mathbf{p}_{\mathrm{Rx_i}}||}{2} \tag{2.2}$$

All of the points which give the same ToA (and hence, the same bistatic range) lie on an ellipsoid with foci $\mathbf{p}_{\mathrm{Tx_i}}$ and $\mathbf{p}_{\mathrm{Rx_i}}$. The exact expression for these ellipses will be given depending on the setup. Due to the rotational symmetry of the TxRx stack in Figure 2.1b it is useful to define the ground-range, x' (2.3), as in Figure 2.1b.

$$x' = \sqrt{x^2 + y^2} = R_{\mathrm{Tx_i}} cos(\varphi) \tag{2.3}$$

Now that a treatment of the 3D space surrounding the vehicle has been established in this section, the following section will discuss a model of the radar signal.

2.2 Signal Model

This section lays out an ideal general signal model for the radars used in this thesis. For the experiments performed for 3D imaging, a linearly frequency modulated continuous wave (LFMCW) multi-receiver radar is used. The transmitted signal is comprised of a series of consecutive up chirps - signals with a linearly increasing frequency which has the form of (2.4) [14], illustrated in Figure 2.2a.

$$s_{\mathrm{Tx_i}}(t) = A_{\mathrm{Tx_i}} \exp\left(2\pi j\left(f_c t + \frac{1}{2}\alpha t^2\right)\right) \tag{2.4}$$

where f_c is the carrier frequency of the radar, t is time, $A_{\mathrm{Tx_i}}$ is the signal amplitude (defined as the square root of the transmitted power $\sqrt{P_{\mathrm{Tx_i}}}$), and α is the chirp ramp rate. The transmitted signal is a single channel, $\mathrm{Re}\left(s_{\mathrm{Tx_i}}(t)\right)$, but this complex exponential form is useful for later equations, where one can specify whether the real component, complex component, or envelope of the signal is being taken. It is assumed that $A_{\mathrm{Tx_i}}$ is approximately constant across the sweep bandwidth. The chirp is defined for a set sweep duration $t \in [0, t_c]$, during which it sweeps over a bandwidth, B, such that $\alpha t_c = B$. In a single dwell, the radar will transmit a train of n_c chirps. For this thesis, (2.4) is a sufficient description for each chirp of the train, as the targets are taken to be stationary throughout a dwell, and so the scene is static between $t = 0$ and $t = n_c t_c$.

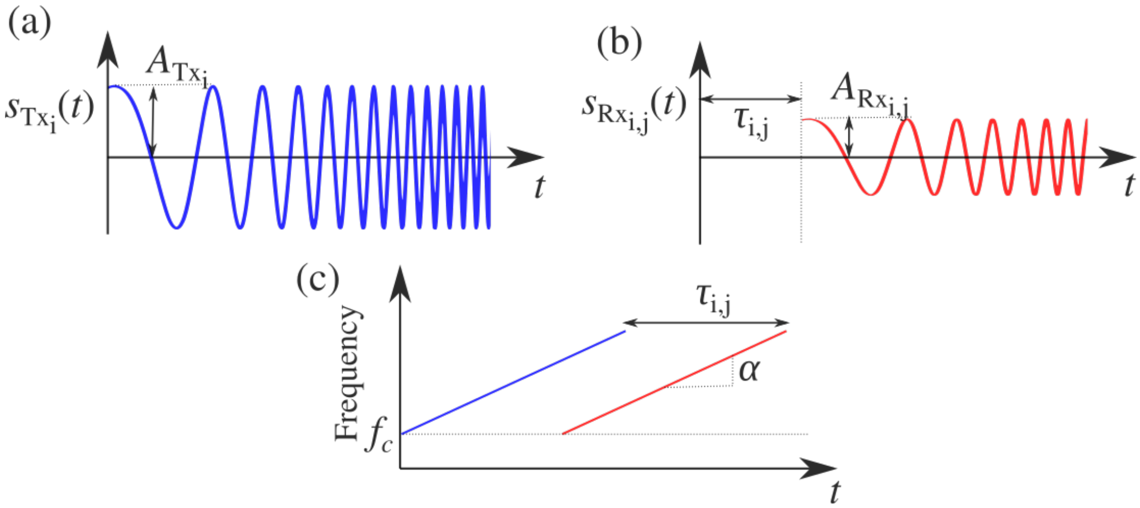

Fig. 2.2 Diagram of the transmitted and received signals. (a) Real component of the transmitted chirp (2.4). (b) Real component of the received signal for a single point target (2.5). (c) Frequency to time plot of both the signals in (a) (2.4) and (b) (2.5).

Let us consider a scene with n_{tg} scattering centres present. These are small objects within the scene which generate a noticeable reflection of the Tx signal (2.4). Most road objects are considered to be made up of multiple scattering centres along their surfaces. For the j^{th} scattering centre which is at a position of $\mathbf{p}_{\mathrm{j}} = (x_{\mathrm{j}}, y_{\mathrm{j}}, z_{\mathrm{j}}) = (R_{\mathrm{j}}, \theta_{\mathrm{j}}, \varphi_{\mathrm{j}})$, where j= $1, \ldots, n_{tg}$ is an integer counter, some fraction of the signal is scattered and arrives at Rx_{i} with some time delay $\tau_{\mathrm{i,j}}$. This is evaluated as τ_{i} in (2.2), for $\mathbf{p} = \mathbf{p}_{\mathrm{j}}$. $\tau_{\mathrm{i,j}}$ is different for each Tx Rx pair provided that the combination of $\mathbf{p}_{\mathrm{Tx_i}}$ and $\mathbf{p}_{\mathrm{Rx_i}}$ is unique for that Tx Rx pair. The value of $\tau_{\mathrm{i,j}}$ for each Tx Rx pair is the ToA which will be used to yield the height information in later sections. The received signal has the form of (2.5), illustrated in Figure 2.2b. The amplitude of the received signal, $A_{\mathrm{Rx_{i,j}}}$ (defined as the square root of the received power $\sqrt{P_{\mathrm{Rx_{i,j}}}}$), is a function of a number of effects which will be discussed in greater detail in section 2.3.

$$s_{\mathrm{Rx_{i,j}}}(t) = A_{\mathrm{Rx_{i,j}}} \exp\left(2\pi j\left(f_c\left(t - \frac{2R_{\mathrm{b_{i,j}}}}{c}\right) + \frac{\alpha}{2}\left(t - \frac{2R_{\mathrm{b_{i,j}}}}{c}\right)^2\right)\right) \tag{2.5}$$

Note that while the signals shown in this section are complex, there is only one output channel (not I and Q). (2.5) is the signal which is collected over the antenna aperture and passes into the hardware, and the real and complex components are not considered independently in the observable output of the hardware. The measurable Rx signal is the combination of the received signal of every one of the n_{tg} scattering centres (2.5), which are summed as in (2.6).

$$s_{\mathrm{Rx_i}}(t) = \sum_{\mathrm{j=1}}^{n_{\mathrm{tg}}} s_{\mathrm{Rx_{i,j}}}(t) \tag{2.6}$$

This treatment may seem perfectly general, as n_{tg} scattering centres can be distributed to describe any scene, but it has one minor drawback. In this linear formulation, (2.6) only accounts for signals passing from Tx_i to a scattering centre and then to Rx_i. It cannot account for a signal which has been scattered more than once, e.g. passing from one scattering centre to another. This means that the model does not account for shadowing or multi-path signals [4]. The applicability of this model will be revisited in later sections.

Following standard stretch processing [14], this signal (2.6) is then dechirped in the Rx module, a process which removes the carrier frequency by mixing the signal with the reference transmitted signal (2.4). This means that the output of the hardware is of the form of (2.7). The constant of proportionality here, A_{IF_i}, is directly proportional to $A_{\mathrm{Rx}_{\mathrm{i,j}}}$, as it is the amplitude of the signal (2.6) after dechirping and sampling.

$$s_{\mathrm{IF_i}}(t) = \sum_{\mathrm{j=1}}^{n_{\mathrm{tg}}} A_{\mathrm{IF_{i,j}}} \exp\left(\frac{4\pi j}{c^2}\left(cf_c R_{\mathrm{b_{i,j}}} + \alpha ct R_{\mathrm{b_{i,j}}} + \alpha R^2_{\mathrm{b_{i,j}}}\right)\right) \tag{2.7}$$

A point of note here is that the chirped signals (2.4-2.7) have a finite chirp duration, t_c, which can be expressed using a rectangle function. This is introduced in (2.8). As a LFMCW radar, the system is constantly transmitting and receiving a chirp over $t \in [0, t_c]$, after which the measurement stops.

$$s_{\mathrm{IF_i}}(t) = \sum_{\mathrm{j=1}}^{n_{\mathrm{tg}}} A_{\mathrm{IF_{i,j}}} rect\left(\frac{ct - R_{\mathrm{b_{i,j}}}}{ct_c}\right) \exp\left(\frac{4\pi j}{c^2}\left(cf_c R_{\mathrm{b_{i,j}}} + \alpha ct R_{\mathrm{b_{i,j}}} + \alpha R^2_{\mathrm{b_{i,j}}}\right)\right) \tag{2.8}$$

Finally, to generate a range profile, the signal must be converted from the time domain to the frequency domain. This generates the spectral content of different range beat frequencies, generating a distribution of signal amplitude to bistatic range (a range profile) [14]. The conversion between domains is done by performing a Fourier Transform ($\mathscr{F}$) on the signal.

$$\begin{gathered}\mathscr{F}\Big(s_{\mathrm{IF_i}}(t)\Big) = \int_{-\infty}^{\infty} s_{\mathrm{IF_i}}(t) \exp(2\pi jft)dt = \\ \sum_{\mathrm{j=1}}^{n_{\mathrm{tg}}} A_{\mathrm{IF_{i,j}}} t_c \mathrm{sinc}\Big(t_c(f - \alpha\tau_{\mathrm{i,j}})\Big) \exp\Big(2\pi f_c \tau_{\mathrm{i,j}}\Big) \exp\Big(-j\pi\alpha\tau^2_{\mathrm{i,j}}\Big)\end{gathered} \tag{2.9}$$

where f is the frequency axis over which the Fourier transform is applied. As t_c and $A_{\mathrm{IF_{i,j}}} \propto A_{\mathrm{Rx_{i,j}}}$ are both constants, for later system calibrations, when estimating $A_{\mathrm{Rx_{i,j}}}$ from the sampled signal (2.9), $A_{\mathrm{IF_{i,j}}}$ is used as a general placeholder for the amplitude of the digitised output (2.9).

In a dwell of n_c chirps, the scene is stationary for this dwell and this is the same sinc function and exponentials for each pulse. When this is summed, the resultant function (2.10) has a gain of n_c in amplitude or n_c^2 in power.

$$\mathscr{F}\Big(s_{\mathrm{IF_i}}(t)\Big) = n_c \sum_{\mathrm{j=1}}^{n_{\mathrm{tg}}} A_{\mathrm{IF_{i,j}}} t_c \operatorname{sinc}\Big(t_c(f-\alpha\tau_{\mathrm{i,j}})\Big) \exp\Big(2\pi f_c \tau_{\mathrm{i,j}}\Big) \exp\Big(-j\pi\alpha\tau_{\mathrm{i,j}}^2\Big) \tag{2.10}$$

At the same time, a window function, W, is applied to the signal. The use of a window function is to combat artefacts in the signal which emerge from performing a Fourier Transform over a signal with finite duration and bandwidth, which generates a sinc function with undesirable sidelobes [4]. The window function chosen will be trade-off between suppressing these sidelobes and defocusing the signal [133]. The final range profile has the form of (2.11). This signal is then sampled in $R_{\mathrm{b_i}}$, where the length of each range bin is the range resolution, R_{res}.

$$S(R_{\mathrm{b_i}}) = \mathscr{F}(W s_{IF}(t)) \tag{2.11}$$

Although this is the ideal signal for a set of scattering centres, in reality this signal will be corrupted by noise. The performance of radar systems are often determined by the signal to noise ratio (SNR). Each radar will have an associated noise corrupting the signal, which originates from various points in the hardware. It is assumed that this noise will be additive, white, and Gaussian. The noise power for this type of noise is given by (2.12).

$$P_n = n_c k_b B_{\mathrm{Rx}} T N_f \tag{2.12}$$

where k_b is the Boltzmann constant, B_{Rx} is the receiver bandwidth, T is the temperature of the equipment, and N_f is the noise figure, which is assumed to be similar for each Tx Rx pair. The assumption that the noise has this form will again be tested in the system characterisation. The usual rule of non-coherent integration is used here, such that when n_c noise realisations are summed, there is a resultant gain of $\sqrt{n_c}$ in amplitude or n_c in power [4].

This section has laid out the form of the radar signals, and the way in which the position of a target relates to the observed signal. However, as it is such a complex topic, a specific discussion of the power budgets and amplitudes have been saved for the following section.

2.3 The Radar Equation

This section will cover a number of effects which govern the Rx signal amplitude described in section 2.2. Here one can use the definition from before that the amplitude of the signal for the i$^{\text{th}}$ Tx Rx pair, and the j$^{\text{th}}$ scattering centre is the square root of the corresponding received power; $A_{\mathrm{Rx_{i,j}}} = \sqrt{P_{\mathrm{Rx_{i,j}}}}$ (2.5). The equation which determines the overall received power is the Radar equation [4], which is presented in general terms in (2.13).

$$P_{\mathrm{Rx_i}}(\mathbf{p}_\mathrm{i},\mathbf{p}_\mathrm{j}) = \frac{n_c^2 P_{\mathrm{Tx_i}} \sigma(\mathbf{p}_\mathrm{i},\mathbf{p}_\mathrm{j}) G_{\mathrm{Tx_i}}(\mathbf{p}_\mathrm{i},\mathbf{p}_\mathrm{j}) G_{\mathrm{Rx_i}}(\mathbf{p}_\mathrm{i},\mathbf{p}_\mathrm{j})}{L_p(\mathbf{p}_\mathrm{i},\mathbf{p}_\mathrm{j}) L_a(\mathbf{p}_\mathrm{i},\mathbf{p}_\mathrm{j}) L_i} \tag{2.13}$$

where $P_{\mathrm{Tx_i}}$ is both the peak and average transmitted power, as $|s_{\mathrm{Tx}_i}(t)|^2 = A^2_{\mathrm{Tx}_i}$ is a constant for $t \in [0, t_c]$. $G_{\mathrm{Tx_i}}(\mathbf{p}_\mathrm{i},\mathbf{p}_\mathrm{j})$ and $G_{\mathrm{Rx_i}}(\mathbf{p}_\mathrm{i},\mathbf{p}_\mathrm{j})$ are the Tx and Rx gain of the j$^{\text{th}}$ scattering centre observed by the i$^{\text{th}}$ Tx Rx pair. $\sigma(\mathbf{p}_\mathrm{i},\mathbf{p}_\mathrm{j})$ is the RCS of the j$^{\text{th}}$ scattering centre, which is also dependant on the aspect angle made by the Tx and Rx modules. The total loss is described in terms of a path loss L_p, an atmospheric loss L_a, and various other sources of loss which is unique to the i$^{\text{th}}$ Tx Rx pair L_i.

At this stage it is useful to define the SNR of the system, which are given in (2.14). Where P_n is the power of the noise corrupting the signal (2.12).

$$SNR_{\mathrm{i,j}} = \frac{P_{\mathrm{Rx_{i,j}}}}{P_n} \tag{2.14}$$

such that the SNR scales with n_c. This section will break down the effects on the received power from each stage of interaction, grouping the quantities in (2.13) into the three areas in Figure 2.3.

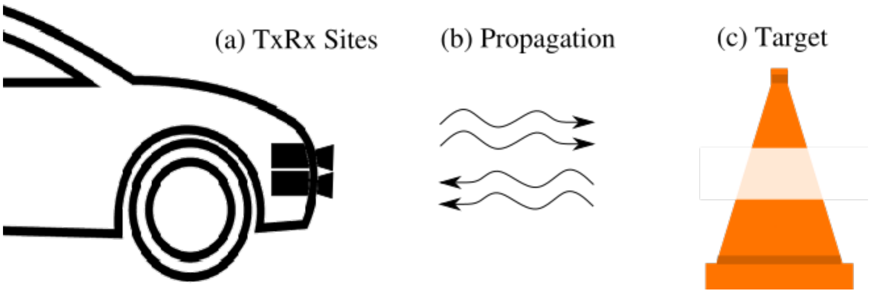

Fig. 2.3 Diagram breaking down the radar equation into three parts; the radar, propagation, and scattering from the target.

Section 2.3.1 details the effects which occur at the radar site and inside the hardware, which includes the transmitted power and the gain of the antennas. Section 2.3.2 details the various losses which occur while the signal propagates from the Tx to a target, and then from the target to the Rx. Finally section 2.3.3 examines what defines the RCS of a target and of individual scattering centres, which is ultimately what is reconstructed by most imaging algorithms.

2.3.1 Tx Rx Sites

This section will examine the transmitted power and the gain of the antennas.

First, let us consider P_{Tx} (2.4). If the hardware, the setup, and the output frequency are constant (a narrow band signal), it is reasonable to assume P_{Tx} is constant throughout a chirp. The output power of radar systems is, however, linked to their transmitted frequency [93]. Therefore for the LFMCW radar signal (2.4) which linearly modulates the signal's frequency, it is likely that there will be some low-level variation in the output power of the system if the sweep bandwidth ($B = \alpha t_c$) is sufficiently large. In section 3.2, the effect of sweep bandwidth on the range response will be investigated.

Let us now consider how the system focuses this transmitted power in a certain direction. This section introduces an antenna pattern and its key features, leaving a more detailed investigation in sections 3.3 and 4. G_{Tx} and $G_{\mathrm{Rx_i}}$ are the maximum gain of the signal caused by the antennas focusing the energy in a particular direction. In the case of an isotropic antenna, this gain is uniform for all values of θ and φ. The gain of a antenna is a well known quantity given by (2.15). This is defined by the ratio of the maximum transmitted power of the radar (as a function of angle), to that of a isotropic transmitter with the same total output power.

$$G = \frac{4\pi A e_{\mathrm{eff}}}{\lambda^2} \tag{2.15}$$

where A is the area of the antenna aperture, and e_{eff} is the efficiency of the antenna (usually ≈ 0.5). This expression (2.15) predicts the maximum gain of the Tx and Rx antenna. The beam pattern as a function of angle will be derived from measurement.

Antenna beam patterns are usually described in terms of a periodic lobe structure as shown in Figure 2.4.

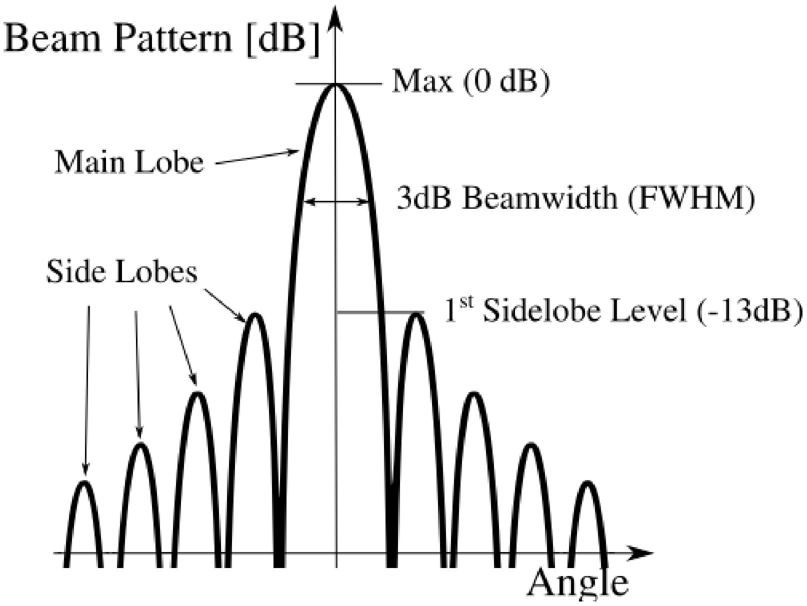

Fig. 2.4 Diagram of the antenna beam pattern, showing the antenna gain as a function of aspect angle.

This pattern has a beamwidth defined by the dimensions of the antenna [134]. These beam patterns are usually quantified by their gain (2.15), the 3dB beamwidth of the beam pattern which is the Full Width Half-Maximum (FWHM) of the main lobe, and the side-lobe levels - the maximum amplitude of each of the sidelobes.

2.3.2 Propagation

This section will consider the loss in signal power as it propagates through the space surrounding the vehicle. As the signal propagates through space, a number of factors will effect how the microwaves are reflected, refracted, and absorbed by the medium. This section is designed to describe the theoretical models of propagation loss.

The transmitted wavefront propagates radially away from the Tx, and then propagtes similarly back from a scattering centre. For the case of a Tx in free space transmitting a wavefront at $t = 0$, at a given time (t_0) the wavefront would occupy the space defined by $R_{\mathrm{Tx}_i} = ||\mathbf{p} - \mathbf{p}_{\mathrm{Tx_i}}|| = ct_0$ (2.2). The signal is spread out over a spherical wavefront, and so the energy of the wave is distributed over an area of $4\pi R^2_{\mathrm{Tx_i}}$. Because of this, in free space the power illuminating a unit area of this sphere decreases in accordance with the inverse square law, $R^{-2}_{\mathrm{Tx_i}}$. The exact same process occurs for the backscattered signal from a point of reflection to the receiver, which gives an additional path loss which scales with $R^{-2}_{\mathrm{Rx_i}}$. This combined process is the free space path loss of a signal, as in equation (2.16) [4]. This includes a factor of λ^2 from the area of the antenna from (2.15) intercepting the second sphere.

$$L_p = 16\pi^2\lambda^{-2}R^2_{\mathrm{Tx_i}}R^2_{\mathrm{Rx_i}} \tag{2.16}$$

In reality the signal does not propagate through ideal free space, and as such there are mutually interfering reflections occurring in the scene. One of the most notable sources of interference is the ground plane [135]. Note that this model is not dependant on the amplitude of the returns from the scattering centres along the ground-plane, and so does not invalidate the linear signal model (2.6) of section 2.2. In this case, part of the signal backscattered from the target is reflected from the ground-plane, with a reflection coefficient Γ. This reflected signal has additional phase due to the additional path length travelled, and interferes with the received signal. This information is modelled by a propagation factor, F_{p} (2.17) [135]. Although most highways are flat asphalt, there is no guarantee that the ground ahead of the radar will be flat with a uniform reflection coefficient. Therefore one must be careful to model and image the 3D scene without making potentially incorrect a priori assumptions. It is worth noting that $F_p = 1$ is the free space path loss case.

$$F_{\mathrm{p}} = \left| 1 + \Gamma \exp\left(\frac{4\pi j z_{\mathrm{Tx}} z_j}{\lambda R_{\mathrm{Tx}_i}} \right) \right| \tag{2.17}$$

The environment through which the signal propagates is mainly air above a near-planar Earth, which at short range is largely devoid of additional scattering objects between a target and the Tx-Rx sites. Therefore it is most likely unnecessary to use statistically fit distributions of path loss, such as mean area models which are used to model complicated scenes [135]. In many cases the multipath signal will be mitigated by putting absorber on the ground, setting $\Gamma \approx 0$ and $F_p \approx 1$.

As the signal is propagating through air, this itself has some associated attenuation which are shown in Figure 2.5. This is the atmospheric loss, L_a in (2.13).

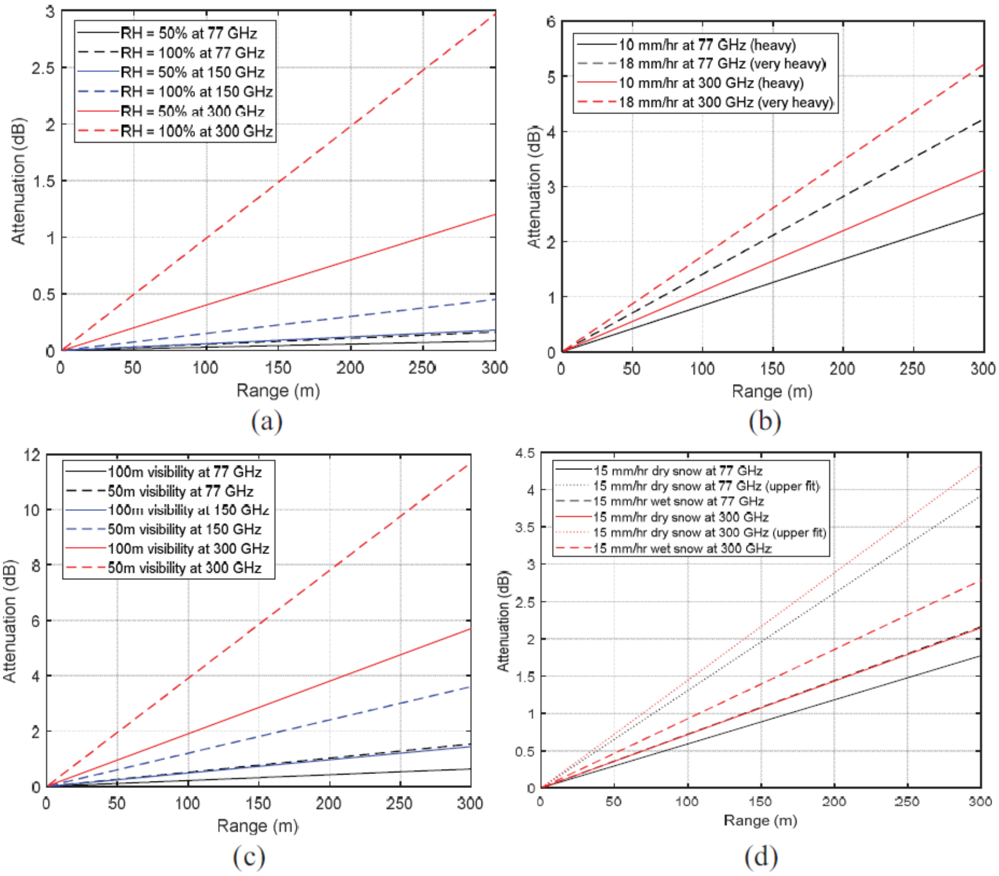

(a) (b) (c) (d)

Fig. 2.5 Loss due to attenuation from atmospheric gases in the low-THz band, taken from [10]. (a) clear air, (b) rain, (c) fog, and (d) snow.

It is very difficult to derive an analytical expression for the scattering and absorption of gaseous molecules in the atmosphere, and as such it is common practice to instead use expressions derived from measurement, which is L_a in Figure 2.5. This attenuation is mostly due to the water content of the atmosphere, as can be seen in the relative differences in attenuation between 50% and 100% humidity air in graph (a). In addition, the presence of hydro-meteors such as rain, fog, and snow only worsens these effects, though it is still much more robust to these effects compared to electro-optical systems. On average this attenuation is not range dependant - the same proportion of radiation is absorbed per metre at one range as another. Because of this, the attenuation for any target range is some attenuation constant multiplied by the target range. When considering SRR, the range is less than 30 m, and $L_a \leq 0.3$ dB in clear air, and is at most around 1 dB in fog. It can therefore largely be considered negligible.

There are various other sources of loss which will occur from between the radar site, and the target, (as well as losses in the hardware). These have been grouped together into a combined a combined loss term, L_o. One major source of loss which most automotive radars will have to deal with is the radome, such as mounting the radar behind the bumper of the vehicle. In this thesis, a radome will not be used, and so the additional attenuation caused by radomes and their contaminants are largely outside of the scope of this thesis. That being said, there is likely to be other various sources of loss present. Combining the expressions for the path loss (2.16,2.17), the atmospheric attenuation (2.5) along with the discussion of antenna patterns in the previous section; a combined expression for the power of a receiver is given by (2.18).

$$P_{\mathrm{Rx_i}}(\mathbf{p}) = \frac{n_c^2 P_{\mathrm{Tx}} \sigma(\mathbf{p}) G_{\mathrm{Tx}}(\mathbf{p}) G_{\mathrm{Rx_i}}(\mathbf{p}) F_p}{(4\pi)^3 R_{\mathrm{Tx_i}}^2(\mathbf{p}) R_{\mathrm{Rx_i}}^2(\mathbf{p}) L_a L_i} \tag{2.18}$$

(2.18) is sufficient to describe the amplitude of the Rx signal (2.6) yielded for a certain RCS value, σ. However, what is missing is a complete description of σ, which is what the next section will provide.

2.3.3 Scattering

This section will examine the RCS of targets in the low-THz band. Namely, the quantity σ in (2.13). σ defines an effective area intercepting the spherical transmitted wavefront (2.2), which scatters the energy towards the Rx site. The RCS of a real world object is dependant on a great many things, including the Radar's frequency, the object's material composition, and the aspect angle the object's surface makes with the radar's orientation. The way in which Electromagnetic (EM) radiation scatters at the boundary of surfaces is dependant on its wavenumber ($k = 2\pi\lambda^{-1}$) and the surface roughness. Because of this, the low-THz band which has a very high k has a very different sensitivity to the surface texture of many common objects compared to other radar bands.

The RCS of an object is the sum of all of the returns from every scattering centre making up an object. For a radar with a low range resolution (or to a Doppler radar), all of these scattering centres may not be resolvable in range. If they exist in very few range cells, and the object appears point-like, the RCS defining the sum of all of these returns is sufficient to define the returns from the object as a whole. I.e. there is functionally no difference between (2.6), and (2.5) with $A_{\mathrm{Rx}_i} = \sum_j A_{\mathrm{Rx}_{i,j}}$ if $R_{b_{i,j}}$ is indistinguishable for all j. However, for a high resolution imaging radar, the target will be spread across many range cells. Higher resolution radars typically split an extended target up into constituent scattering centres, and aim to reconstruct the distribution of scattering centres in space [136]. The first description is useful for detection and categorising a single target, whereas the latter is more relevant for radar imaging.

To generate an RCS distribution, one has to consider that the Rx signal is the combined returns of every facet of a target's surface. Real world objects are complicated structures. They have a geometric structure on a larger scale, and random deformations according to their surface roughness on a smaller scale. There are two main approaches to calculating the RCS distribution of such objects; models based on a canonical distribution and ensemble averaging, and computational geometric optics methods. The first approach assumes that the macroscopic structure of an object is canonical (such as a plane or a sphere), and that a statistical method can be used to describe the rough surface deformations on a smaller scale [13]. On the other hand, geometrical optics methods instead split the object up into a mesh of scattering centres, and solve for the combined returns computationally. Both of these descriptions will be considered in the remainder of this section.

Here let us consider the effect of surface roughness on the backscattered radar signal.

The first step in examining the scattering from a rough surface is to define a statistical treatment of a random rough surface. An example rough surface is shown in Figure 2.6. Here a surface is considered with zero-mean height, and a RMS deviation around this of (z_{rms}) [13] As illustrated in the height profile of the surface, although the distribution of the height of a surface is random, the undulations have characteristic frequencies to their structure which are parameterised by a correlation length (l_{cl}). The surface deformations are still random, but through ensemble averaging these small deformations can be described on a macroscopic scale by a statistical distribution which is known as a correlation function. The most commonly used is the correlation function given by (2.19).

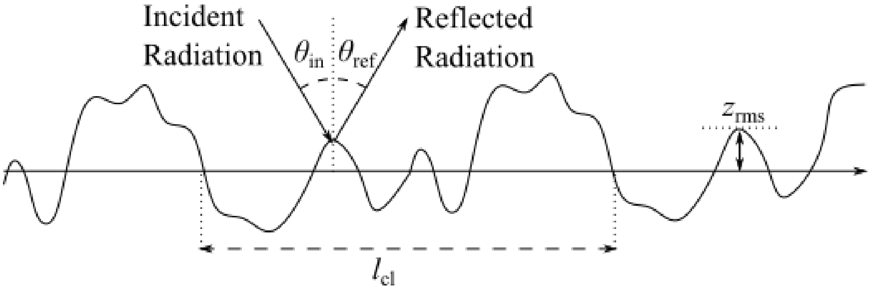

Fig. 2.6 Diagram showing electromagnetic scattering from a cross-section of a rough surface.

$$w(z) = \frac{1}{l_{cl}\sqrt{2\pi}} \exp\left(\frac{-z^2}{2l_{cl}^2}\right) \tag{2.19}$$

One can define the Rayleigh roughness parameter, ρ [15], which is the root mean square (RMS/rms) phase variation between incident and reflected radiation, and it is used to define the EM roughness of a surface. A mirror-like smooth surface will yield $\delta\phi_{rms} \to 0$, whereas a very rough surface yields $\delta\phi_{rms} \to \pi$. This behaviour has been simplified into two main criteria which dictate if a surface is rough or smooth. These are the Rayleigh criterion $\delta\phi_{rms} \leq \pi/2$, and the Fraunhöfer criterion $\delta\phi_{rms} \leq \pi/4$.

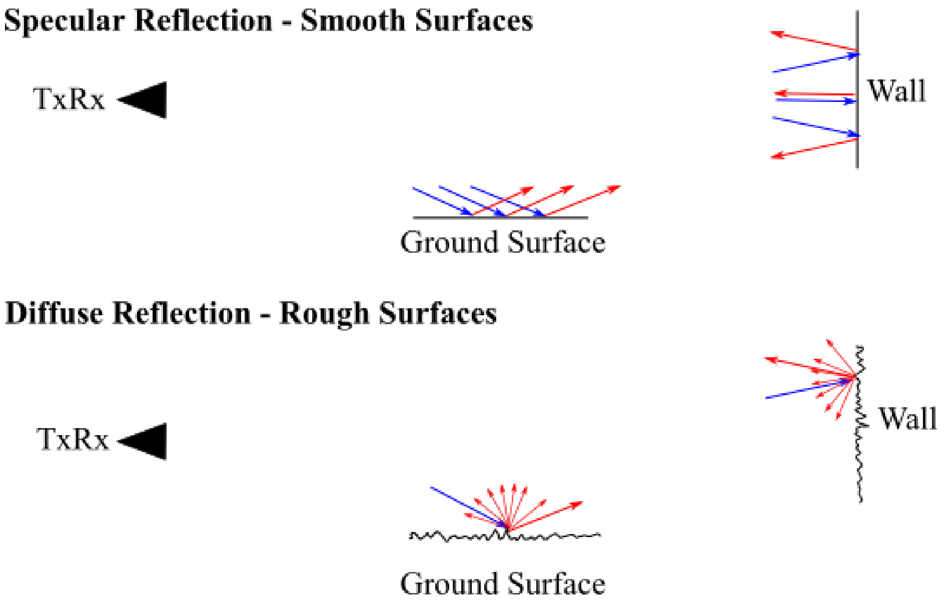

Fig. 2.7 Example of specular and diffuse scattering for automotive radar. Where blue arrows are radiation incident on the surfaces, and red arrows are reflected radiation.

$$\rho = kz_{rms}\cos(\theta_{in}) = \frac{\delta\phi_{rms}}{2} \tag{2.20}$$

A purely smooth ($\delta\phi_{rms} = 0$) surface causes the reflection to be entirely specular, a focused beam of reflected radiation in the direction $\theta_{in} = \theta_{ref}$. On the other hand, a rough surface creates a combination of specular reflection and diffuse reflection, which scatters the radiation in an unfocused way in many directions. Usually specular reflections are brighter as all of the reflected energy is focused in one direction. This is illustrated in Figure 2.7 for an automotive environment with the ground below and a wall ahead of a vehicle. (2.20) shows that a smaller z_{rms} is required to appear electromagnetically rough for higher k, so low-THz radiation with a higher k yields more diffuse scattering.

Crucially, if the reflection were purely specular, very little of the transmitted radiation from the ground or from the top and bottom of the wall are reflected back towards the vehicle. Only a specular reflection is present at TxRx height. This means that the signal may not be detectable and very little information can be gained as so little energy is backscattered towards the TxRx site when these surfaces are electromagnetically smooth.

Let us consider the road surface now. In terms of the geometry laid out in section 2.1, one can parametrise the Rayleigh criterion as follows in (2.21).

$$z_{rms} \geq \frac{\pi R_{\mathrm{Tx_i}}}{4kz} \tag{2.21}$$

This means that the further away from the vehicle the surface is, the higher the RMS surface roughness needs to be before it can be considered rough. Similarly, a smaller wavelength decreases the required RMS height needed for the surface to appear electromagnetically rough. Therefore it is only at these higher frequencies, and at closer ranges that one can expect diffuse scattering from road surfaces.

There are a number of long-existing models which describe the way radiation is backscattered from a random rough surface according to its parameters [13], such as the Kirchoff model. Most models predict a bright lobe due to specular reflection in the direction $\theta_{\mathrm{ref}} = \theta_{\mathrm{in}}$, and diffuse reflection in other directions which is highly dependant on surface roughness. However, many do not account for shadowing, multi-path, or depolarization well [137]. All of these factors are important when dealing with radiation propagating close to the $\theta_{in} \rightarrow \pi/2$. A widely used type of model which is far better suited to account for these effects is a computational or integral-equation based surface scattering model (IEM) [138]. Using the model put forward in [139], Figure 2.8a shows what the backscatter coefficient should be for an asphalt surface ahead of a monostatic radar mounted in a vehicle at multiple different frequencies [139].

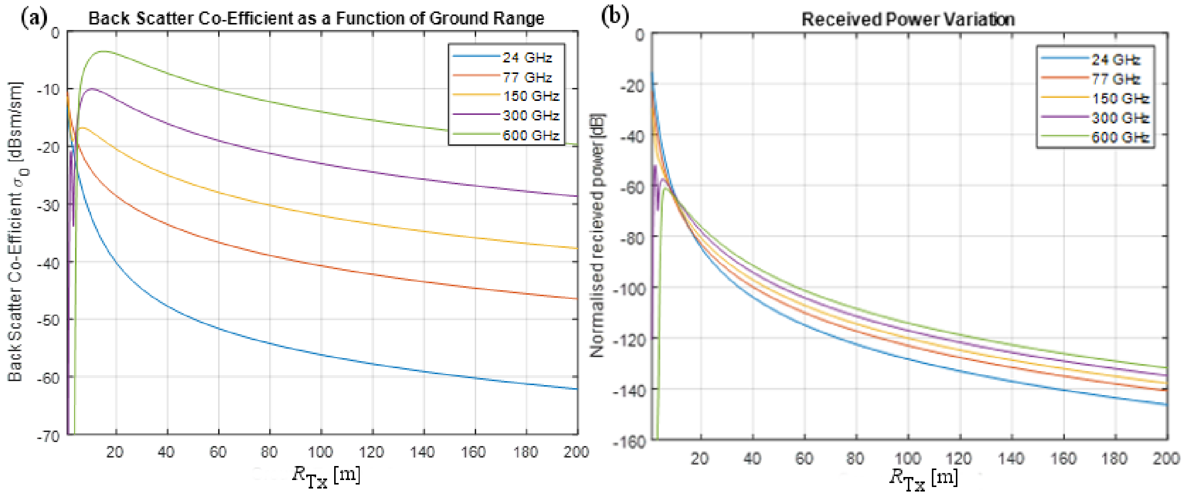

Fig. 2.8 Rough surface scattering of tarmac from different frequency bands using a model taken from [139]. (a) Backscatter from the ground. (b) Received power of this backscatter.

From Figure 2.8a, one might infer that the asphalt ahead of the vehicle appears many 10s of dB brighter in the low-THz band as opposed to 24GHz, but in reality Figure 2.8b shows the predicted received power (5-20dB higher than 24GHz). The reason for this can be seen in equation (2.18), as the received power scales with wavelength. Therefore, although there is not a hugely significant improvement in received power, there is still a significant increase in diffuse scattering from ground surfaces, giving significant returns at a larger variation in aspect angle.

The previous discussion has considered averaging over a surface, but now let us focus on individual scattering centres, like an IEM does. A scattering centre or scatterer is usually defined in terms of a pixel or cluster of pixels in a radar image [140]. For high resolution radars a wall or a patch of a tarmac occupies many pixels in a radar image. Because of this, they are considered as extended objects and are made up of many scattering centres. In fact, most road objects have many corners and surface elements which are all scattering centres. Highly detailed 3D imagery requires an algorithm which can estimate the returns of each individual scattering centre to the desired resolution. These algorithms must estimate the height profile, the response of the target as a function of height, like the distributions illustrated in Figure 2.9 for a TxRx stack.

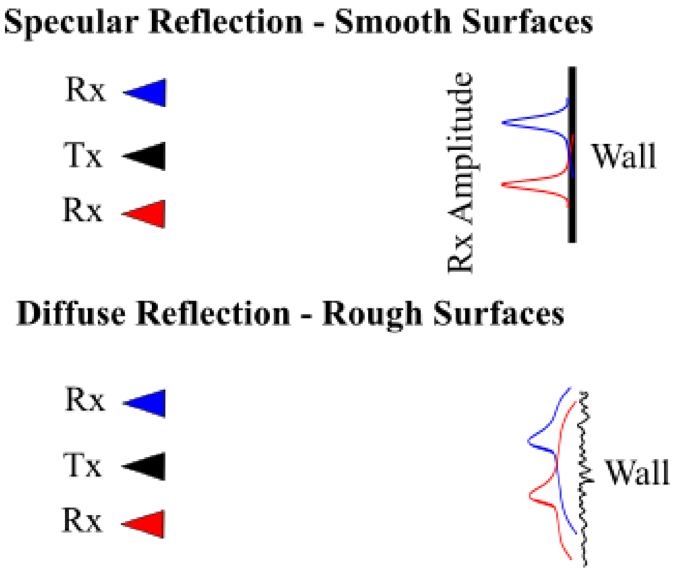

Fig. 2.9 Illustration of the backscattered Rx amplitude across a smooth and rough extended surface.

The returns are likely to be a combination of specular and diffuse scattering being scattered in different directions. When considering a small section of a surface with relatively few facets, models which use ensemble averaging may no longer be appropriate. If the scale is small enough, many simulations make use of only specular reflection from each individual facet which sums together to create a combined total reflection pattern which may be diffuse. The next effect which one must consider is that of shadowing. These facets will be obscured by other physical objects in the real world, even from the same surface or object.

Figure 2.9 shows a situation with a large variation in the wall's height profile based on the Rx used. To perform height finding using the methods which use the geometry of multilateration (section 5 onwards), multiple receivers needs to detect a signal from the same scattering centre. This is where the diffuse and specular scattering becomes important. For a smooth mirror-like surface directly in front of the TxRx stack, the reflection looks exactly like the mirror image of the radar equipment itself. Even for a rough wall ahead of the equipment, the specular returns will most likely be the brightest (2.20). Crucially, the brightest points of reflection are not the same for each Tx-Rx pair for an extended surface such as a wall, so each Rx is not detecting the same n_{tg} scattering centres (2.8). This is an interesting fundamental restriction to ToA algorithms which must be discussed further in later chapters.

Imaging algorithms for multiple receivers require the combination or integration of the signal of multiple receivers. One of the most commonly used metrics used in Radar is the coherent integration angle. This defines the maximum possible separation of the Tx-Rx sites where the coherently integrated SNR still increases [140]. In this region the assumption that the Rx sites are receiving the signal from the same scattering centre holds. In the low-THz band a study [141] found that the coherent integration angle was 2-3° for a real metal sphere, and 1.3 ° for a complex real world object with many scattering centres. The main criticism with using this criterion is that this thesis seeks to deliberately use non-coherent imaging techniques, and the coherent integration angle may not inform the margins of applicability for this technique. In theory, all that is required is that the returns from a scattering centre are sufficiently bright to be detectable after image formation.

2.4 Image Grids

This section looks at how the 3D space around the sensors will be discretized. Namely, the imaging grids which can be used for the imaging algorithms will be laid out.

First let us discuss the radar, which uses a mixture of 1D, 2D polar, 3D spherical polar, and 3D cylindrical polar image grids. For a set position, the radar generates a range profile (2.11). This is a 1D signal with range cell size of R_{res}. To generate 2D positional information, this setup is scanned in azimuth, generating a 2D polar (PPI) radar image. This can be done in both θ and ϕ simultaneously, to generate a 3D spherical polar image, which is explored in section 4. In later sections, ToA information will be used to augment a set of 2D PPI radar images into a 3D cylindrical polar image.

In most cases, a natural choice for the origin of a sensor's coordinate system is the position of the sensor. Usually spatially aligning the multi-sensor data is just a matter of translating the image coordinates from the sensor's position to a common origin. Translation in 3D space is most easily done using Cartesian coordinates, and also produces easily visually understandable imagery. Because of this, most 3D plotting will be done in Cartesian 3D space. When 2D PPI radar imagery is going to be shown alongside this, 2D images are shown as a projection in the ground plane ($z = 0$ m).

Two kinds of 2D radar images will be used in this thesis. First, scanned polar images in $(R_{\mathrm{b_i}}, \theta)$, similar to traditional Plan Position Indicator (PPI) radar images [4], which are often displayed as projections in the xy plane ($z = 0$). It is usually a quasi-monostatic image which is being shown in these cases, so $\mathbf{p}_{\mathrm{Tx_i}} \approx \mathbf{p}_{\mathrm{Rx_i}}$ and $R_{\mathrm{b_i}} \approx R_{\mathrm{Tx_i}}$. Second, a ground-range-height (x', z) image which may be the most relevant for 3D height profiling. In both cases it will be specified which is being shown. Most of the procedures generated are for a TxRx stack as in Figure 2.1 which is scanned in azimuth. Scanned 2D radar data is in a 2D polar coordinate frame, and is sampled in constant range cells of size R_{res}, and constant azimuth cells of size, θ_s. When transformed into Cartesian space, the physical area occupied by a single range-azimuth cell increases radially. Although the radial length of the range cell (R_{res}) is fixed, the cross-range (tangent) length occupied by this cell increases radially. This is shown in Figure 2.10 as the green and red sections on the 2D polar grid (blue).

The 3D ToA imaging algorithms work by augmenting a set of range profiles into a 3D cylindrical polar

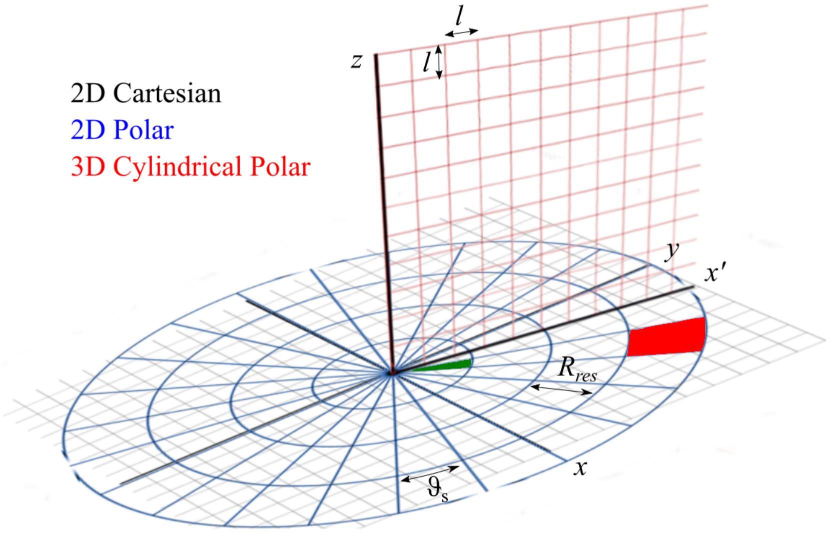

Fig. 2.10 Diagram of the Cartesian, polar, and cylindrical grids on which an image will be generated.

image. The ToA algorithms are used to create a ground-range height image ($x'z$) from the range profiles (2.11) of multiple receivers at a single given azimuth bin. This is used to transform a set of 2D polar images into a single 3D cylindrical polar image. In doing so, the requirement on the cylindrical polar grid is that an increment in the $x'z$ plane does not undersample the range profile from any receiver. To achieve this, the criterion for a grid step is l is that the difference in $R_{\mathrm{b_i}}$ from the positions (x', z) to $(x'+l, z+l)$ is less than R_{res}, i.e. $l \leq \frac{R_{res}}{2\sqrt{2}}$. A single voxel in this cylindrical polar imaging space has side lengths of l by θ_s by l in x', θ and z respectively. In the xy ground plane, the resolution of the 3D cylindrical polar grid is the same as the 2D polar case.

To provide a ground-truth of the scene using high resolution commercially available sensors, a photo and a lidar scan is taken of the scene. The rotating array of lasers naturally generate a 3D spherical polar point cloud, but are output as points in 3D Cartesian space.

2.5 Conclusion

This section has introduced the geometry, theory, and mathematical notation necessary to describe measurements and 3D imaging using a low-THz LFMCW radar system. First it detailed the different coordinate systems which will be used, then the signal model of a FMCW radar. Then followed a brief discussion of the radar equation to define the amplitudes of the signal model, including the gain of the antennas, the losses from propagation, and the RCS and scattering mechanism of targets. Finally, the image grids based on the different coordinate systems were laid out.

The next section will use these descriptions to parametrise the low-THZ multi-receiver radar system which will be used in the vast majority of experiments.

Chapter 3

System Characterisation

The vast majority of experiments performed make use of a bespoke 300GHz 1Tx-3Rx LFMCW radar system designed at the University of Birmingham and manufactured by ELVA-1 [142]. Because it is a prototype system, it is expected that some parameters may not exactly match those quoted by the manufacturer, and it is essential to fully characterise this system. These results will be used to quantify its performance in later experiments, design the constraints for algorithms, and determine the margins of applicability for each technique. This chapter seeks to fully parametrise this radar in terms of its antenna patterns, noise characteristics, the system point response in range, and the path loss of the system.

It is laid out as follows: Section 3.1 provides an overview of the operational parameters and the way in which the radar system can be used. Section 3.2 looks at the response of the system in range. Section 3.3 similarly examines the response of the system in elevation and azimuth. Section 3.4 will look at the noise characteristics of the system. Finally, section 3.5 will use a combination of the results of measurement and the academic literature to provide link budget calculations to determine how this system can be used.

3.1 Operation

The system is comprised of 1 Tx module, 3 Rx module, and a control box. These units are separable and can be configured as desired. Photographs of the system can be seen in Figure 3.1. Each of the Tx and Rx units are connected to the control box which supplies them with power, a strobe signal to trigger the Tx to transmit a chirp, and a reference local oscillator (LO) signal, which is used to generate the output intermediate frequency (IF) signal of each Rx (2.7). This control box connects directly to a computer via an ethernet connection, so that the desired parameters and signal can be configured. The signal (2.7) is digitised at a rate which produces 4096 samples. When the Fourier transform is performed on this (2.10), it produces 2048 range samples (without oversampling). The specific operational parameters of the signal can be seen in Table 3.1. These parameters were confirmed experimentally, and a number of technical issues were overcome with this equipment.

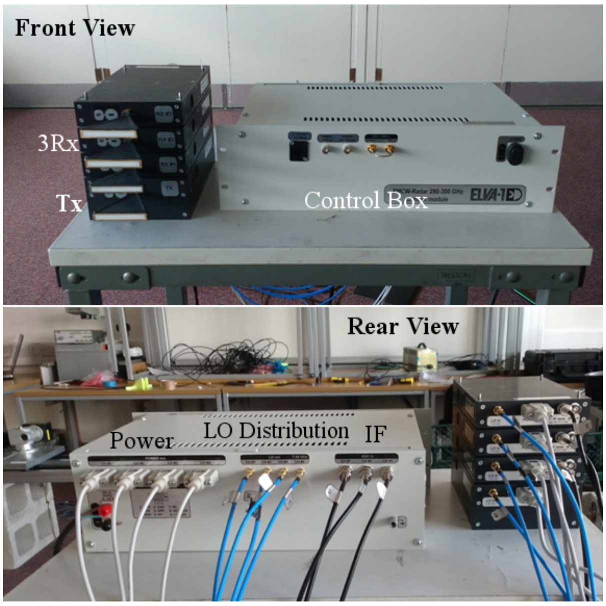

Fig. 3.1 Photographs of the multi-receiver 300GHz radar: front view (top), and rear view (bottom).

The most unique feature of the parameters in Table 3.1 is the available bandwidth of the FMCW system. The 20GHz (280-300 GHz) bandwidth affords the system a very fine range resolution, which will be discussed in the following section.

Parameter	Value
Frequency Output	280-300 GHz
Power Output	0.5-1.5 mW
Modulation	Linear Up/Down Chirp
Sweep time	1-10ms with 1ms step
IF Bandwidth	10kHz - 10MHz
Data Output	FFT 2048 harmonics x 3
LO Reference	10MHz , 0dBm

Table 3.1 Available operational parameters of the prototype 300GHz radar.

3.2 Range Point Response

This section will consider how a target will appear in range based on the instrument and measurement technique, which is known as the point response, or instrument response in range. Specifically, this function examines the point response of this radar in range with varying bandwidth.

Theoretically, the point response of the system in range is given by the ideal sinc function in (2.10). The range resolution comes from the 3dB width (3.1) of such a sinc function, which is defined by its bandwidth as in (2.7) [14].

$$R_{\text{res}} = \frac{c}{2B} \tag{3.1}$$

This resolution is based on the case of (2.10) for $n_{tg} = 2$ and $A_{\text{IF}_{i,1}} = A_{\text{IF}_{i,2}}$. The sinc functions from the two scattering centres are resolvable in range to within 3 dB (2.10), when $c|\tau_{i,1} - \tau_{i,2}| \geq R_{res}$. Therefore, one would predict that the maximum bandwidth of 20 GHz yields a range resolution of 7.5 mm. To generate the range response, one can measure the range profile of a canonical target, with $n_{tg} = 1$ bright scattering centres. Examples of this could be a corner reflector [143], or a finely milled smooth metallic plate which yields only one point of specular reflection [13] which is illustrated in Figure 2.9. To do this, each Rx was tested individually in a quasi-monostatic configuration where the Rx unit was placed directly on top of the Tx in turn. This is shown in Figure 3.2. Each of these Rx units were used to measure a 0.5 m by 0.5 m flat metallic plate which was placed 6.0 m from the Tx-Rx site.

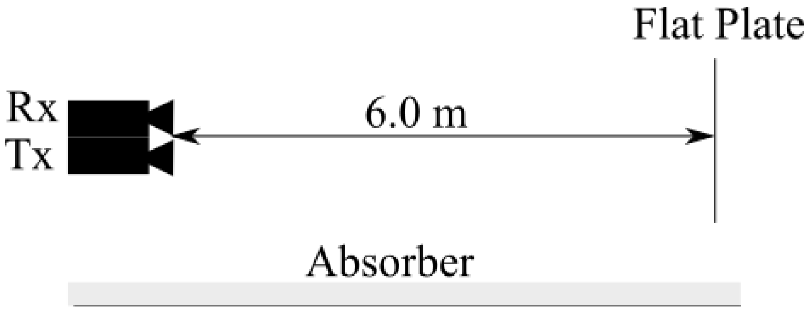

Fig. 3.2 Diagram of the experimental setup for measuring the range response of a flat plate.

Based on the discussion in section 2.3.3, with the setup geometry in Figure 3.2 and the fact that this plate was milled to have a surface roughness well below the signal's 1 mm wavelength, one can predict that the only reflection will be the specular point-like reflection at the Tx-Rx height on the flat plate based on (2.20). A bright specular reflection from a single point means that this measurement should isolate the point response of the system in range, while being easily distinguishable from the noise floor. In theory this should give a single sinc function (2.10) centred at $R_\mathrm{b} = 6.0$ m, whose width scales with the sweep bandwidth according to (3.1). This measured response is shown below in Figure 3.3.

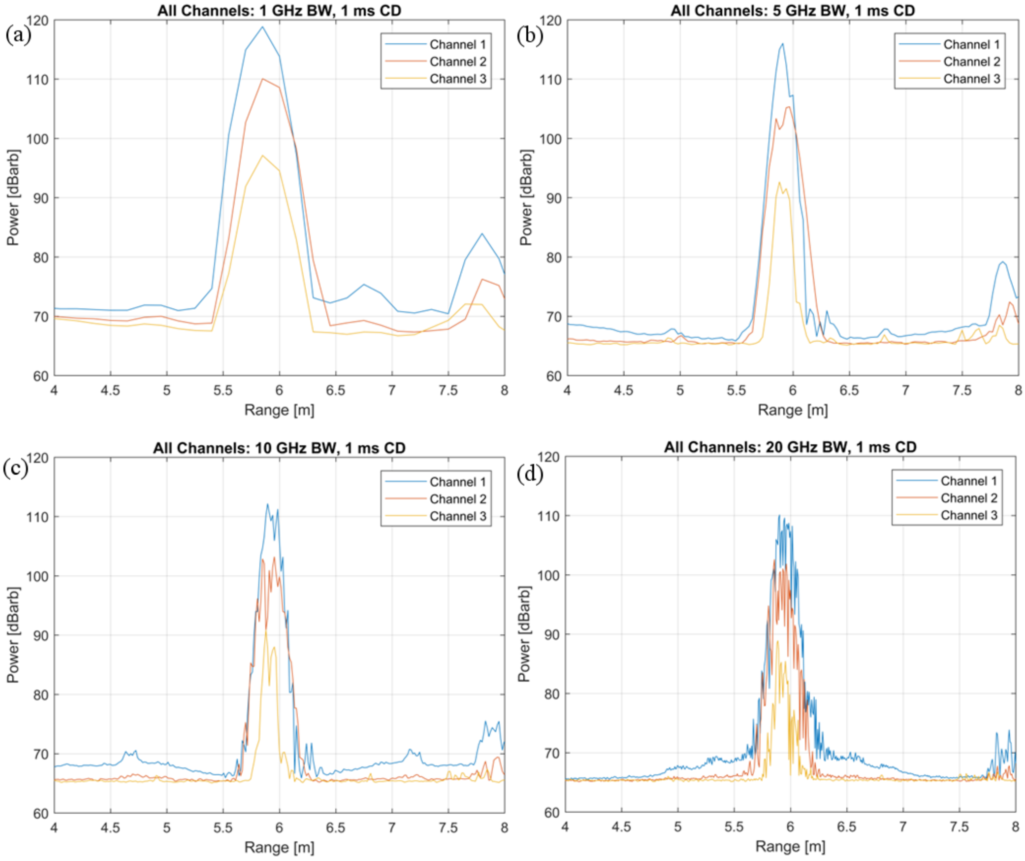

Fig. 3.3 Range profile of a flat plate for different sweep bandwidths. Responses are shown in arbitrary decibel units (dBarb), which is 20 $\log_{10}$ the raw digitised output. (a) 1GHz, (b) 5 GHz, (c) 10GHz, and (d) 20GHz.

The range profile (2.11) for each Rx at different bandwidths can be seen in Figure 3.3. The peak power varies dramatically between each channel. As all aspects of the radar equation (2.13) were kept constant between measurements, the only difference between channels is L_i. In Figure 3.3a, the peak power of channel 2 (i=2) is 8 dB lower than channel 1, and channel 3 is 21 dB lower. Therefore $L_2 L_1^{-1} = 8$ dB, and $L_3 L_1^{-1} = 21$ dB. This loss does not seem to affect the noise floor, though it will affect the SNR of the system and hence its performance.

The point response of B=1GHz appears far broader than that of the other bandwidths, as one would expect. Due to the sampling rate, it appears as a single peak rather than a well defined lobe structure of a sinc function (2.10). Beyond B=5GHz the point response does not appear to be a single peak with one monotonic ascending and descending limb any more. Instead it appears to be made up of many constituent peaks, but again, not in the distinctive sinc pattern. Although it is a little difficult to quantify the width of the peaks in Figure 3.3, it is certainly larger than the predicted range resolution (3.1), and so this degradation of the point response needed to be accounted for before ToA information could be extracted. Although it was possible that there was some additional scattering occurring within the scene which gave rise to these range profiles ($n_{tg} > 1$), it was unlikely. The plate was milled to a very fine tolerance, carpet which was previously found to be a good absorber was used to limit other sources of reflection [144], and otherwise there were no other sources of reflection due the simplicity of the setup. Instead, investigation focused on the hardware of the LFMCW radar. One major contributing factor to the degraded point response at higher frequencies appeared to be the coaxial LO cables which were used to separate the Tx-Rx units and connect them to the control box. The effects of these specific cables, and details of how to compensate it are laid out in [145].

The cables between the control box and the Tx, and the Rx and the control box are both transmission lines with multiple sources of internal reflection present. As is common in transmission line theory, multiple sources of internal reflections in series introduce an infinite set of reflections to the original input signal [146]. While typically one might generate a lattice diagram of these reflections to characterise them, the individual sources of reflection are not of interest, and indeed may be too numerous. Only the resultant series is of interest, and how to mitigate these effects to recover the ideal point response (2.10).

The method can be thought of as follows. The signal reflected from the scene enters the transmission line (2.6), and is split into a series of signals by a set of internal reflections [146]. Each of the resultant signals reaches the control box with some additional delay and attenuation which pertains to the specific set of reflections it has undergone. Therefore with no loss in generality, for an LFMCW radar [14] one can consider the signal to be approximately the ideal signal (2.6), convolved with an infinite series of many different internal reflections, I_{ref} in (3.2). For the signal from a reference target, s_{ref}, which is the observed Rx signal for $n_{tg} = 1$ and a high SNR, and an ideal radar signal with a linear phase fit to this, s_{ideal}, this series can be evaluated as follows.

$$s_{\text{ref}}(t) = s_{\text{ideal}}(t) \circledast I_{\text{ref}} \tag{3.2}$$

where $\circledast$ denotes convolution. From this, one can define the inverse of the series as $\tilde{I}_{\text{ref}}$, such that $s_{\text{ideal}}(t) = s_{\text{ref}}(t) \circledast \tilde{I}_{\text{ref}}$. Therefore one can evaluate this series by fitting a signal with linear phase to a reference target which is known to both have a large SNR and be point-like, as in [145], to find s_{ideal}. This must be done independently for each receiver which each have a unique transmission line and hence a unique set of internal reflections.

This transmission will introduce some loss to the system from these reflections, which means that $|I_{\text{ref}}|^2 < 1$. This method does not compensate for these losses, but instead removes the additional delay to form the set of reflections into one coherent signal. It has three main useful features. First, it focuses the energy of the point response into a narrower peak, increasing the peak amplitude of the point response, and hence increasing the SNR. Secondly, this allows for a better estimate of the TOA by focusing this peak to have a narrower spread in range. Finally, and maybe most importantly, it sets the maximum amplitude of the point response to be at the target's bistatic range, which is a feature of a sinc function $S(R_b)$ (2.10) but which is not true in general for the degraded sinc function, $\mathscr{F}(s(t) \circledast I_{\text{ref}})$. Because of this, the TOA of the target can be found by finding a local maximum in the range profile. A more detailed explanation of how the target's TOA value is estimated is discussed in section 5.

To demonstrate the effect of internal reflections within the cables, the response of the plate for the same configuration is shown in three cases in Figure 3.4.

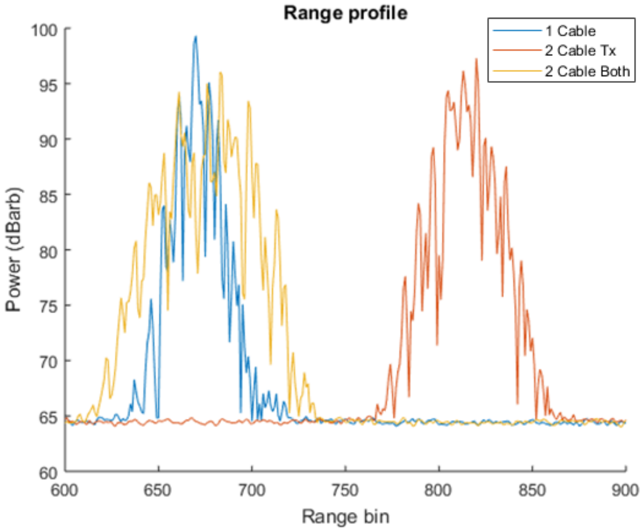

Fig. 3.4 Range profile of a flat plate with cables of different lengths connecting the Tx and Rx units to the control box.

The first case (blue) is with the standard 1.5m long coaxial cable from the control box to the Tx, and the same from theRx to the control box. The second (orange) has an additional 1.5m long cable attached from the control box to the Tx. Since mixing is performed in the Rx module, the effect of increasing the Tx cable length is to increase the apparent target range. Finally (yellow) both the Tx and Rx connections were both 3m of coaxial cable. As predicted, the effect of increasing the cable length was to introduce more internal reflections, which degrades and spreads the point response of the system.

An example of this technique is shown in Figure 3.5, for the flat plate at a slightly closer range of 5.8 m. The method laid out in [145] has been applied to generate the ideal sinc function in blue. As predicted, this process focuses the energy of the peak into a much finer extent in range, which increases the peak SNR. This is shown by the increase of 9dB in Figure 3.5, for approximately the same noise floor. The response of the flat plate is now a single peak rather than a collection of multiple reflections. Therefore one now observes a single peak with the characteristic sinc function in range, with the predicted 3 dB extent of approximately the range resolution, 7.5 mm (3.1), with peak amplitude at the target range of 5.8 m. Of course, as this is the reference target used in the point response correction process, it by definition will generate an ideal point sinc function for this target [145]. The true test is to see how the point response of non-calibration targets in the image are focused using this process, which can be seen in later sections.

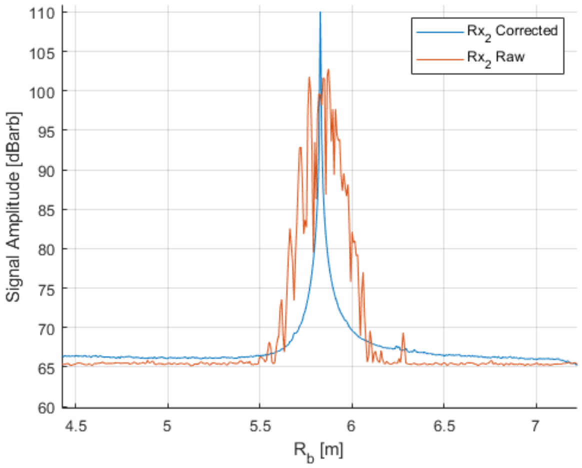

Fig. 3.5 Range response of a flat plate before and after correction, following [145]

With a detailed discussion of the point response of the target in range in place, the focus will now shift to the angular response of the radar in the next section.

3.3 Antenna Patterns

This section investigates the response of the antennas in both azimuth and elevation. Specifically, the aim of this section is to experimentally evaluate the antenna parameters laid out in section 2.3.1, including the 3 and 6 dB beam widths, and sidelobe levels. These tests made use of the same configuration as section 3.2, but with the Tx-Rx units in a monostatic configuration, mounted on a pan-tilt head (2D angular positioner) which can be seen in Figure 3.6. By measuring the reflection from the precision milled flat plate at a series of different aspect angles, one can measure the two-way beam pattern of the antennas.
The first factor to consider is the far field (Fraunhofer) distance, given by (3.3) [134].

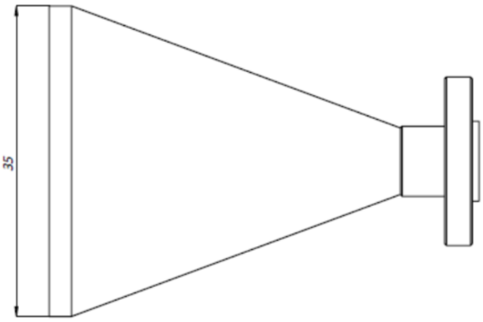

(a) Top-Down View

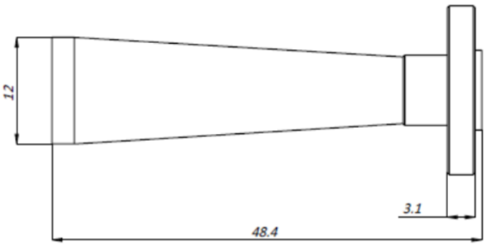

(b) Side View

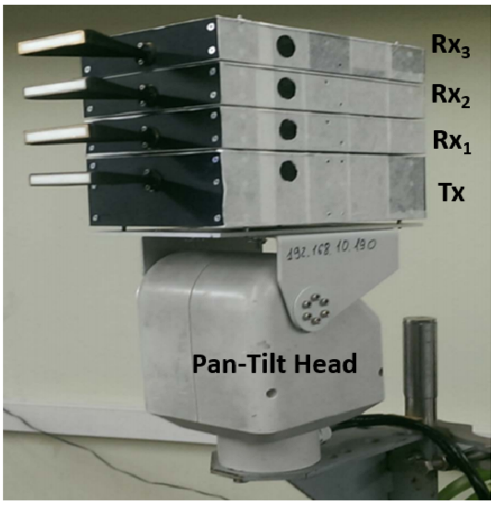

(c) Photograph

Fig. 3.6 The 300 GHz fan beam antennas. Top-Down (a) and side view (b) diagrams of the antennas with distances in mm, and a photograph of the Tx and Rx units mounted on a pan-tilt head (c).

$$R_f = \frac{2D^2}{\lambda} \tag{3.3}$$

Where D is the length of the antenna along the longest distance. Beyond this distance, the radiation pattern as a function of angle has minimal changes in amplitude. For the diagonal of the antenna shown in

Figure 3.6, this far field distance is 2.7 m. This is only the case for a monostatic transceiver (TxRx) using one antenna. It may be more accurate to factor in the Tx-Rx separation, using the description of a two element array, $D = \sqrt{(|z_{Tx} - z_{Rx}| + 2z_a)^2 + y_a^2}$, where y_a is the antenna width, and z_a is the antenna height. Now, $D = 7.3$ cm, and $R_f = 10.6$ m (3.3). Given that this is the smallest Tx-Rx separation possible, one can conclude that the target range of 5.9 m, as well as the majority of short range experiments ($R_{Tx} \in [3, 15]$ m), will be in the far-field region for a given antenna, and the near-field region of the combined Tx-Rx stack.

As introduced in section 2.3.1 the beam patterns of the antennas form a sinc function in azimuth and elevation, with periodic lobe structures [134]. Using (2.15), one would predict the gain of these antennas to be approximately 34 dB. In theory, to evaluate this antenna pattern one should place the target in the far field region. However, given that the majority of later short range imaging will be performed in the Tx-Rx stack's near field, it seemed more useful to put the plate at a typical target range of 5.9 m.

The two-way antenna patterns measured from a flat metal plate are shown below in azimuth (Figure 3.7) and elevation (Figure 3.8). One feature of these plots is that the antennas have different angles when the response of the antenna disappears into the noise floor, which is discussed in greater detail in section 3.4. Based on these distributions the beamwidths can be extracted, which are shown in Table 3.2. Although the data is not a perfect sinc function, the 3dB and 6dB beamwidths of the antennas are in line with those given by the manufacturer. The azimuthal pattern is much narrower than the elevation pattern. Therefore these antennas appear suitable for a system configuration which is mechanically scanned in azimuth to only illuminate a small cross-range extent at a time, while illuminating a large extent in height.

Parameter	Rx_1	Rx_2	Rx_3
Azimuth Beamwidth (3dB) [°]	1.1	1.0	1.1
Azimuth Beamwidth (6dB) [°]	1.5	1.4	1.5
Elevation Beamwidth (3dB) [°]	7.0	6.2	6.4
Elevation Beamwidth (6dB) [°]	9.1	8.8	8.9

Table 3.2 Two-way beamwidths of each Rx unit, measured from the Tx antenna to the antenna of each Rx.

It's not immediately obvious that these distributions correspond to the predicted patterns in Figure 2.4. Arguably, in azimuth the first null can be seen at just under $\theta = \pm 2^\circ$, and in elevation the first can be seen at $\varphi = -4^\circ$ and the second at $\varphi = -8^\circ$. Assuming that the antenna pattern is of the form $\text{sinc}^2(kx)$, one

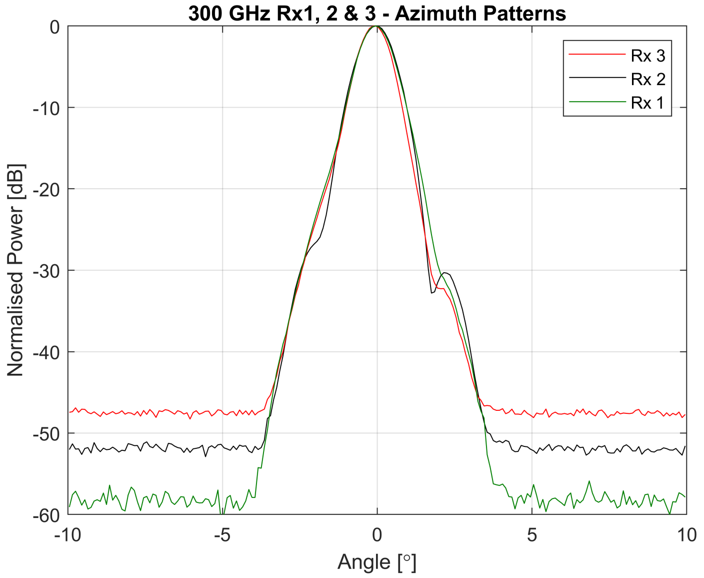

Fig. 3.7 Two-way normalised monostatic azimuthal beam patterns of each Rx.

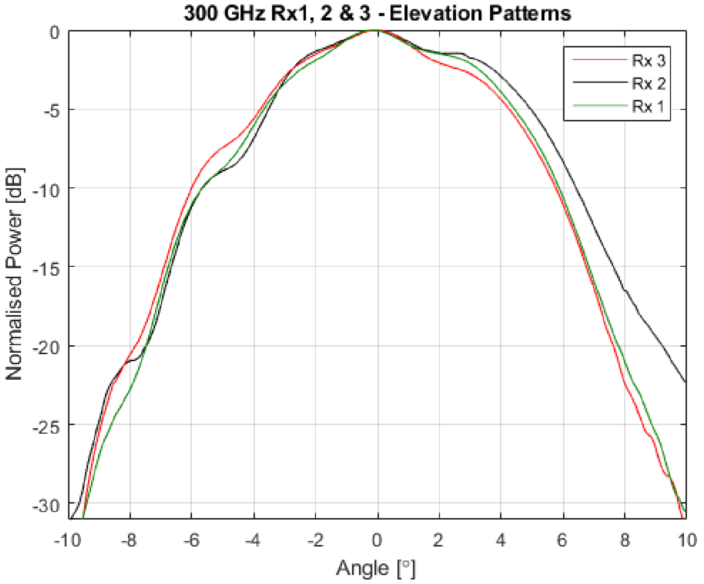

Fig. 3.8 Two-way normalised monostatic elevation beam patterns of each Rx.

would predict that the maximum of the first sidelobe in the antenna pattern occurs at $2kx = 3\pi$. This can be used to estimate the point where $\mathrm{sinc}^2(kx) = 0.5$ or 0.25, which are the 3dB and 6dB beam widths. For the position of the first sidelobe maximum being 2.1° in azimuth, this predicts a 3 dB width of 1.2 ° and a 6 dB width of 1.6 °, which are only a small overestimate of the measured values in Table 3.2.

The measured distributions in Figures 3.7 and 3.8 do not quite capture a sinc function for multiple reasons. First is that the amplitude of these sidelobes should be predictable as -13 dB for the first, and -18 dB for the second sidelobe maxima (-26 and -36 for this two-way pattern) [147]. The whole sidelobe structure is poorly defined. The nulls of theoretical antenna pattern are narrow, and it is true that in reality the null of an antenna pattern will appear smoother rather than a steep trough as the energy is distributed over the total area of the target and the antenna. However, this does not explain this level of asymmetry and aperiodicity. It is likely that there is a combination of effects of non-uniform amplitude distribution due to the lens and near field effects from an extended target. In some cases, Gaussian Optics Lens Antennas (GOLA) were used to illuminate a narrow region in both azimuth and elevation. A picture of these antennas and the antenna pattern provided by the manufacturer are shown in Figure 3.9 [142].

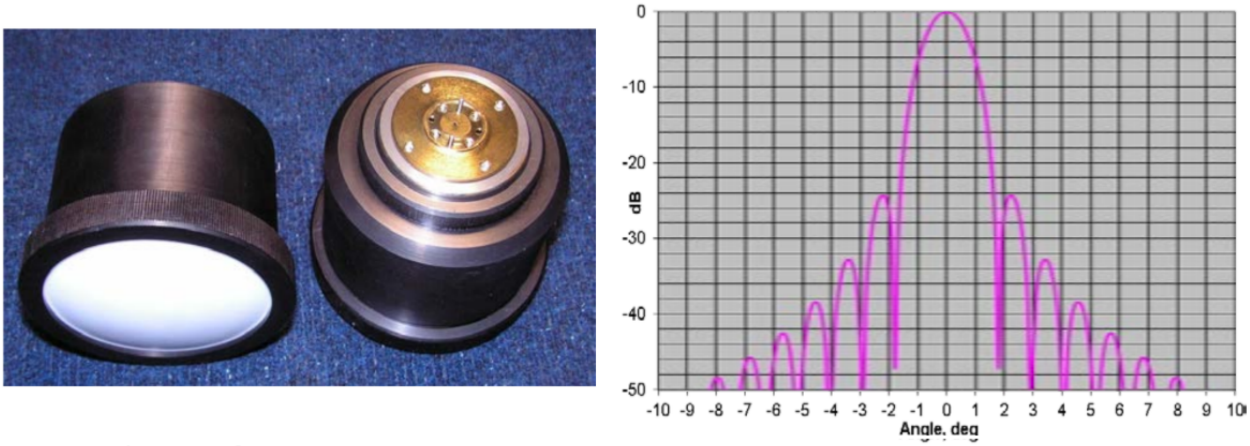

(a) Picture of GOLA Antennas

(b) Antenna Pattern of GOLA Antennas

Fig. 3.9 The GOLA antennas. (a) photograph and (b) antenna pattern.

These antennas are rotationally symmetric, and so the elevation pattern in azimuth and elevation is the same. Compared to the fan beam antennas previously measured, these GOLA antennas were used in very few experiments. Because of this, and the fact that the fan beam antenna parameters were in line with those provided by the manufacturer, the provided antenna pattern and parameters were used. Namely, a 1.3 ° 3dB two-way beamwidth in both azimuth and elevation.

In this section the antenna patterns have been measured. Where tested, the beamwidths of the antennas are consistent with those provided by the manufacturer, however, the predicted sidelobe structure was not observed to the expected levels.

3.4 Noise

In this section the background noise level of the radars will be characterised. This is important information to determine the maximum range of the radar system, and to inform the imaging algorithms of later chapters.

In section 3.2, it was observed that channel 2 and 3 had an additional loss of 8 dB and 21 dB respectively compared to channel 1. This means that in Figure 3.7, when the channels have been normalised to have a maximum power of 0 dB, it appears as if they have a different mean noise power. Following on from measurements of the point response, the connections were repaired inside the hardware in an effort to minimise losses. Because of this, the SNR in Figure 3.7 does not appear consistant with section 3.2, as the relative loss has been decreased to 3 dB and 9 dB instead. As before, each measurement had an identical setup, save for the Rx unit used, and so the peak IF amplitudes, A_{IF} (2.7), correspond to the same scattered power in (2.18).

In most experiments in this thesis, the range profiles will be calibrated to the calculated power of a known reference target. Much like Figure 3.7, this means that the apparent noise floor is larger due to L_i. The quoted noise figure from the manufacturer is N_F =13 dB, however, this does not account for the differences between $\mathrm{Rx}_{1/2/3}$. To estimate the apparent noise floor, $L_i N_F$, the calibration data from section 3.2 was used. The point response correction in range was first applied to focus the energy into a peak [145]. The flat plate was taken to be within the main lobe of the beam pattern, and so was beam-filling. Using (2.18) to calculate the received power. The average noise amplitude was the mean value of a region of the range profile which was known not to contain any scattering centres. This procedure was performed for the full range of available bandwidths and sweep times for each Rx.

Table 3.3 shows the mean apparent noise figures for each Rx. This procedure is by no means perfect. The commonly defined value of N_F may match the quoted values much more closely, and the noise floor is likely to be subject to change based on the correction process outlined in [145]. This is a potential issue for this system, given that I_{ref} (3.2) and hence L_i (2.13) are likely to be unique for each configuration. If the configuration of the cables is changed throughout the measurement, for example, through bending and flexing the LO cables, then I_{ref} and L_i no longer match the set of internal reflections inside the cable. If used incorrectly, this introduces many kinds of distortions into the range profile. Although strictly speaking this is not noise, an incorrect point response correction can decrease the SNR, degrade the point response, and introduce periodic patterns into the background noise.

Parameter	Rx_1 [dB]	Rx_2 [dB]	Rx_3 [dB]
L_i	0	3.1	9.2
L_iN_F	13.6	16.7	22.8

Table 3.3 Apparent noise figure of each receiver, with loss relative to Rx_1.

3.5 Power Link Budget

Using the system parameters from throughout section 3, this section lays out power link budget calculations based on literature values of common and important automotive targets. This is done to assess how this prototype radar system can be used in an automotive context.

In all of these calculations the following assumptions are made. First, the target is assumed to be beamfilling, such that the full extent of the target is captured within the main lobe of the antennas in both azimuth and elevation. Second, for the purposes of link budget calculations, the targets occupy distances where R_b is far greater than the Tx-Rx height separation, b, meaning that the system is in a quasi-monostatic configuration such that $R_b \approx R_{Tx} \approx R_{Rx} = R$ (2.1). Third, although the targets being considered are complex structures with many constituent scattering centres, they are treated here as Swerling 0 idealised targets with a constant RCS which corresponds to the literature value of their mean RCS. For the purposes of a link budget, the RCS of an object as a whole is used to estimate $A_{Rx} = \sqrt{P_{Rx}}$ (2.18), such that $n_{tg} = 1$. Finally, the common boundary condition that a target can be detected if the target's SNR is greater than 10 dB is employed.

Table 3.4 RCS values of common automotive objects at 300GHz taken from the academic literature.

Object	Child	Adult	Bike	Car
σ [dBsm]	-9.0 [112]	-8.6 [113]	-2.3 [112]	6.8 [111]

Using these assumptions, power link budget calculations are performed to estimate the maximum distance where the system can detect some of the most common (and important) automotive targets; a car, a pedestrian, a child pedestrian, and a bike. The RCS values presented in Table 3.4 are those from the literature at 300 GHz. To obtain an expression for the maximum range, (2.18) is rearranged, with a minimum desired signal to noise ratio (SNR). Let us consider that the atmospheric loss, L_a is negligible, with a free space path loss (2.16). This maximum range is shown below (3.4) [4]. The signal of a single Rx is being coherently integrated over n_c chirps, and it is taken such that the gain in SNR from these chirps is exactly n_c [148], (a n_c^2 gain in power, and n_c gain in noise power).

$$R_{max} = \left(\frac{P_T G_{Tx} G_{Rx} \lambda^2 \sigma n_c}{(4\pi)^3 k_b T B L_i N_F (SNR)_{min}} \right)^{\frac{1}{4}} \tag{3.4}$$

The integration of signals from multiple Rx sites is not explicitly considered here, but what is most likely is that the chirps of a single Rx will be coherently integrated, while the signals of multiple receivers will be combined through ToA methods which will generate a gain somewhere between $n_{Rx}^{0.5}$ (non-coherent) and n_{Rx} (fully coherent). Even for the non-coherent case of signal integration, the amplitude gain can be as high as $n_{Rx}^{0.7}$ or $n_{Rx}^{0.8}$ [148]. This is perhaps a little pessimistic, as these signals are not non-coherent, but their signal envelopes are being summed, which may be a gain closer to n_{Rx}. When considering the maximum range, the minimum noise figures calculated in section 3.4 are used, which predict a different sensitivity for each Rx.

First, let us examine the minimum detectable RCS as a function of target range using a single chirp. In this calculation let us consider the case of a wideband LFMCW signal which is being used for ranging with the maximum available bandwidth. After dechirping, this is an IF bandwidth of 10 MHz for this system [142]. The result of this calculation is shown in Figure 3.10. This predicts that for the most sensitive Rx, a pedestrian will be detectable for ranges up to 20m, and a typical passenger car will be detectable for ranges up to 50m. For the least sensitive Rx this instead becomes 10m and 30 m respectively. Automotive SRR is defined to have an operational range of up to 30 m [83].

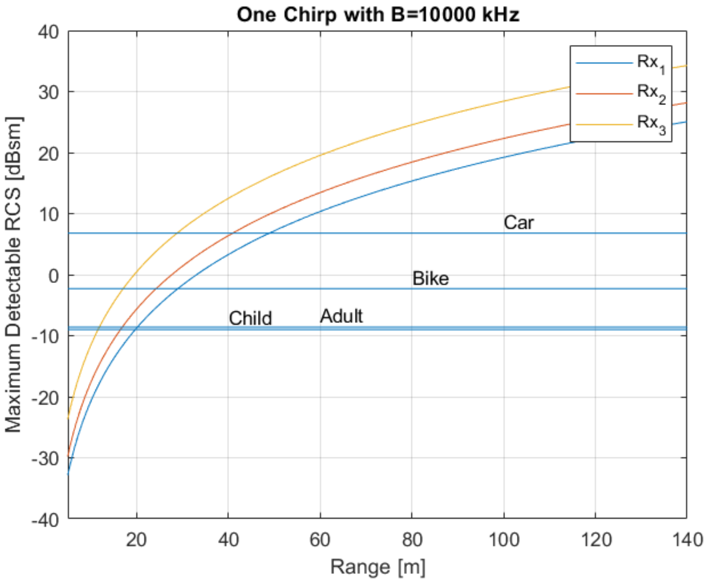

Fig. 3.10 Estimate of the minimum detectable RCS measured for each Rx for a dwell of 1 chirp.

Something which has not been properly considered yet is the sampling and digitisation of the signal. The sampling of the range profile is output as a signal of 2048 range cells, with each range cell length being the range resolution (3.1). Therefore the maximum range position along the range axis is $2048R_{res}$, which is just over 15 m for a sweep bandwidth of 20 GHz. Indeed these estimates are more pertinent for the system when using a lower sweep bandwidth, where the target may appear as a single peak and the system can observe a larger range. Therefore, whether or not a target is detectable at a range of 30 m for $B = 20$ GHz is somewhat of a moot point.

Let us now consider a smaller sweep bandwidth of 5 GHz. The vehicle is stationary, and takes a Radar measurement of the scene with a dwell time of 0.1 s before moving. The pulse repetition period of this radar is 1.1 ms, and therefore the radar can execute 91 chirps in this dwell time. For this bandwidth, the maximum range set by the sampling frequency is just over 60 m. The results for the same targets as before are shown in Figure 3.11. The detectable ranges of each of the targets are now all larger than the maximum measurable range of 60 m, except for the pedestrians for Rx_3, which can be detected up to a range of 50 m. Although this is an encouraging result, one must bear in mind that this does not account for a dynamic scene or a moving Radar platform. During the dwell time of 0.1 ms, it is highly likely that each of these targets would execute a range walk from one range cell to another. Unless some kind of mitigation is employed, this means that the integration gain from these n_c chirps is far less than n_c, and the target could appear spread in range. This is even more significant if the host vehicle is in motion.

The final consideration for these calculations is the integration of multiple chirps with a pulse repetition interval, PRI, when the vehicle is in motion with a constant speed, v. This calculation considers a stationary target directly ahead of the moving vehicle. Very similar considerations could be made to a moving target, but with v instead being the relative velocity between the target and the host car. The system parameters are the same as before, with a sweep bandwidth of 5 GHz. This time, the number of chirps used is defined by the motion of the vehicle. The dwell time of the Radar is defined to be the time taken for the vehicle to move the distance of one range cell. This was chosen as it is an indication of the maximum dwell time that can be used without incurring a large loss through range migration. This gives an expression for the number of chirps which can be used (3.5). Using this expression for n_c, the minimum detectable RCS as a function of range and the speed of the host vehicle is shown in Figure 3.12. As one would expect, lower values of v gave the Radar a longer dwell time to measure the target, and hence the targets can be detected further from the host vehicle. When the vehicle is travelling at 60 mph, the Radar can only complete one

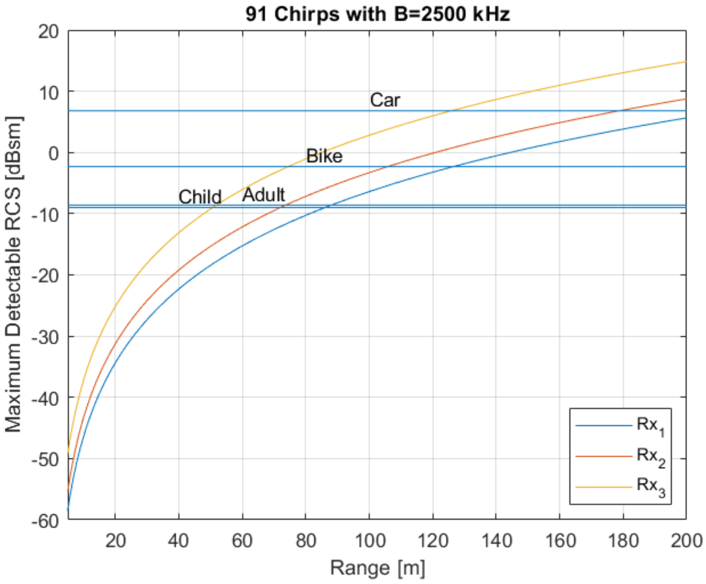

Fig. 3.11 Estimate of the minimum detectable RCS measured for each Rx for a dwell of 91 chirps.

chirp without incurring a significant range migration for a 5 GHz sweep bandwidth (3.5).

$$n_c = \frac{R_{res}}{(\mathrm{PRI})v} \tag{3.5}$$

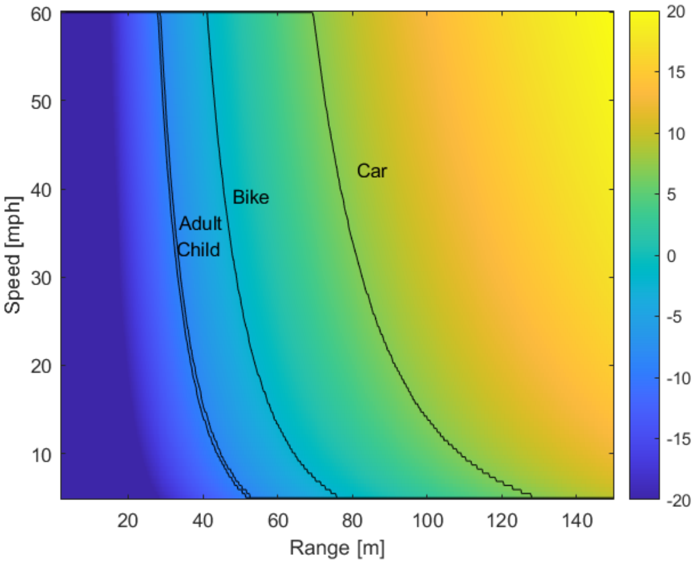

Fig. 3.12 Estimate of the minimum detectable RCS with a variable dwell time based on the speed of the host vehicle.

In general the maximum range values are lower than those required by most automotive radars, and are instead closer to those of short range radars or proximity sensors. This is particularly true for the larger bandwidths. This is not a fundamental drawback of low-THz radar, but is because of the current technology readiness level. These link budget calculations are a little simplistic for many reasons, and are only designed to provide an estimate of the limiting use cases of the system.

One of the largest shortcomings of these calculations is the assumption of free space path loss. The range predicted in (3.4) may not be indicative of what would occur for a signal with a multipath reflection from the asphalt ahead of the vehicle, using the model put forward in section 2.3.2. One can define which propagation model needs to be used by the cross-over points and break-points of the distributions in range. The cross-over point being where two-ray path propagation predicts the same received power as the free-space case (3.6) [147]. Beyond this point, the two-ray propagation model no longer predicts the received power well.

$$d_c = \frac{4\pi z_{\mathrm{Rx}} z_j}{\lambda} \tag{3.6}$$

However, even for a $z_{\mathrm{Rx}} = 0.5\mathrm{m}$ and $z_j = 0.5\mathrm{m}$, equation (3.6) predicts that this will not occur until the target range reaches 3 km. This means that the received power from the target will be subject to constructive and destructive interference from the ground reflections of the signal. This can be seen in Figure 3.13, which shows the patterns for a passenger car in 3 cases; where there is no reflection from the ground (free-space), when the radar height and target height are 0.5m and 0.5m, and then 1m and 1m respectively. It is calculated using (2.17), where the reflection coefficient Γ is calculated from (3.7) [111]. Where I_0 is a modified Bessel function of zero order, z_{rms} is the rms surface roughness of the ground, and ε is the permitivitty of the surface. The values used are $\varepsilon = 3.18$ and $z_{\mathrm{rms}} = 0.5$ mm which are taken from the literature [149, 150]. As can be seen in Figure 3.13, while the free space model predicts a R^{-4} decrease in signal power, the two-ray pattern has peaks and trough in interference which vary above and below this.

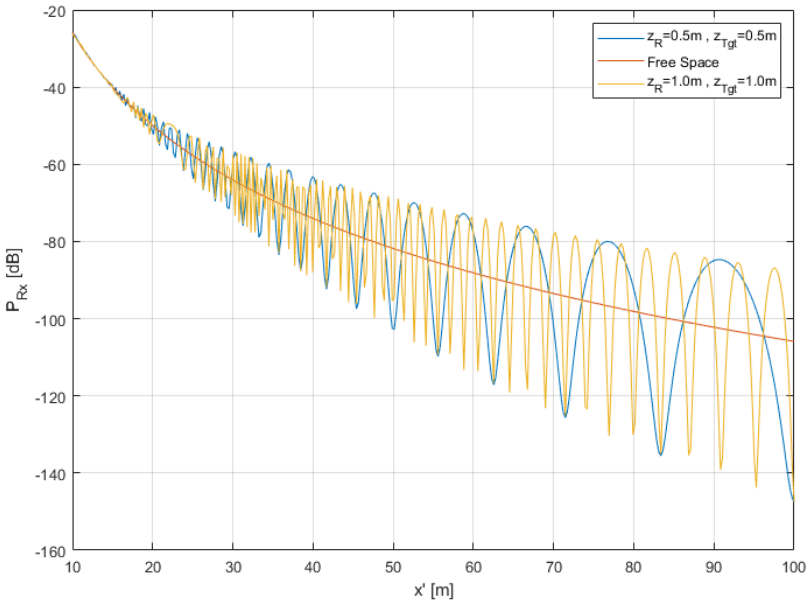

Fig. 3.13 Estimate of the received power to range using a free space or flat earth propagation model.

$$\Gamma = \frac{\varepsilon \sin(\psi_g) - \sqrt{\varepsilon - \varepsilon \cos^2(\psi_g)}}{\varepsilon \sin(\psi_g) + \sqrt{\varepsilon - \varepsilon \cos^2(\psi_g)}} \exp\left(\frac{-4\pi z_{\mathrm{rms}} \sin \psi_g}{\lambda}\right) I_0\left(\frac{-4\pi z_{\mathrm{rms}} \sin \psi_g}{\lambda}\right) \tag{3.7}$$

While this distribution appears to oscillate around the free space path loss, it does not provide a fixed single distance where the target is likely to be undetectable. Instead, it predicts that even past the values predicted above, the target will disappear and reappear above the noise floor in the range profile at different target ranges. The interference behind this is defined by a number of parameters, including the heights of the radar and target, the presence and geometry of the ground surface, and scattering characteristics of the ground surface. Therefore the link budget calculations serve as more of a mean estimate of where the target is no longer visible, rather than a definitive limit on the bounds of detection.

3.6 Conclusion

This section has laid out a characterisation of the radar system which was used in the vast majority of experiments.

In range, the range resolution of the system is very fine due to the large bandwidth of the FMCW radar system. However, it was found that the signal cables degraded the range response of the system, and each Rx module has a different loss due to components. A method which is used to address this was laid out, so that the ideal range response can be recovered.

In azimuth and elevation, two types of antenna were discussed. A fan beam which focuses the beam into a narrow azimuth beam and a wide elevation beam, and a GOLA which produces a narrow beam in both azimuth and elevation.

Although the noise was relatively similar between Rx units, the additional loss in each unit means that the sensitivity of the system varies between the Rx unit used. Although Rx_1 was found to match the manufacturer's value, the SNR of the other receivers were noticeably lower.

Finally, using the parameters from this characterisation, a power link budget calculation was performed which found that this radar system is generally acceptable for short range use, but that the sensitivity of the system was insufficient for longer range applications, such as LRR.

The following section will perform 3D imaging using mechanical scanning. This will be performed using the narrow beam antennas laid out in section 3.3, to isolate a narrow region of space, and then using an angular positioner to isolate different regions of space at a time in 3D.

Chapter 4

Mechanically Scanned Imagery

This chapter examines 3D mechanically raster scanned radar imagery, which is a well established technique to generate highly detailed 3D imagery. The aim of this chapter is to provide a benchmark for the 3D imagery generated later in this thesis, to be a starting point for algorithm development and the system imaging layout, and to experimentally verify that this system can detect returns from the entire extent of the object rather than a specular point, consistent with the discussion of scattering in section 2.3.3. Although the application is new, this section does not seek to provide a particularly novel method of raster scanned radar imagery.

This section is laid out as follows: section 4.1 examines the concept and theory of raster scanning with a radar system, then section 4.2 applies this experimentally to the 300GHz LFMCW radar system outlined in section 3. Finally these results will be discussed in section 4.3, and in section 4.4 conclusions will be drawn and further plans will be formulated.

4.1 Background

There is a large body of existing radar imagery which makes use of mechanically scanned systems. This section is concerned with systems which are mechanically raster scanned in both azimuth and elevation to produce 3D radar imagery. Examples of mechanically scanned radar systems can be found in the low-THz band in 2D [16, 72, 115], and in 3D [95–97]. Some automotive demonstrators obtain a highly detailed

2D image in this way, such as Navtech [75], but typically mechanically scanned radar systems tend to be phased out as a radar frequency band matures. This is because the moving parts usually require the most maintenance, and by definition, if the radar is only illuminating a certain region of space, it is not monitoring all other regions of space.

This section considers targets to be in the far field, using the definition of the far field distance given in (3.3), and considering $R_b \approx R_{Tx} \approx R_{Rx} = R$ (2.1). Only 1 Tx and 1 Rx is required to produce these images. Mathematically, in this region the beam pattern is taken to be a function of azimuth and elevation, but not range. The basic idea underlying this method of localisation is that the radar returns (2.11) are the product of a sinc function in range, azimuth, and elevation respectively. The range response is given by (2.8). The amplitude of (2.8) is determined by the beam pattern of the radar (2.18). As shown in section 3.3, the beam pattern of the antennas along the azimuth and elevation axes are each given by a sinc function, $\text{sinc}^2(k_\theta \theta)$ and $\text{sinc}^2(k_\varphi \varphi)$, where k_θ and k_φ are constants defining the width of the beam patterns. These can be related to the half beamwidths, as $\text{sinc}^2(k_\theta \theta_{BW}) = \frac{1}{2}$ when $k_\theta \theta_{BW} = \pm 1.392$, and equivalently in φ.

With the description of $j = 1, \ldots, n_{tg}$ (2.7), the jth scattering centre occupies a position of $\mathbf{p}_j = (R_j, \theta_j, \varphi_j)$. The antenna gain $G_i = G_{\text{Tx}_i} G_{\text{Rx}_i}$ (2.18) has the form of (4.1), which is directly proportional to the received power, P_{Rx} (2.18).

$$G_i(\theta, \varphi) \propto \text{sinc}^2\big(k_\theta(\theta - \theta_j)\big)\text{sinc}^2\big(k_\varphi(\varphi - \varphi_j)\big) \tag{4.1}$$

For $s_{\text{Rx}_{i,j}}$ (2.5), the maximum value of G_i is found at (θ_j, φ_j). Provided these n_{tg} scatterers are resolvable and brighter than the noise floor, by scanning the radar in θ and φ, θ_j and φ_j can be estimated as an angle which maximises P_{Rx_i}. For a bright point-like target, ($n_{tg} = 1$), this is a single global maximum. As this function is just the beam pattern of the radar, but shifted by (θ_j, φ_j), the shape and sidelobe parameters which define the quality of the reconstruction are the same as the antenna pattern. Therefore the 3 dB width of the antenna pattern should be the 3 dB width of the target in the (θ, φ) distribution.

The raw output is a range profile at a series of θ and φ positions, which is a 3D spherical polar image matrix $S(R, \theta, \varphi)$. All voxels will have non-zero power due to the presence of noise, but there are only n_{tg} voxels which physically correspond to scattering centres. Applying a threshold to filter out the noise is a simple yet effective method of dealing with this, but the width of the beam pattern and range response can leave the 3D image as a cluster of points around the peak of interest, making the image difficult to visually interpret. Instead, to combat this one can consider the brightest return at each azimuth and elevation position. To generate an easily interpretable 3D image with useful range information, reconstructions in this section are the positions corresponding to the maximum return of the range profile at a specific position in azimuth and elevation (4.2). The 3D reconstructions are pointclouds generated from (4.2), which are converted from spherical polar coordinates into 3D Cartesian coordinates (2.1).

$$\begin{aligned} P(\theta, \varphi) &= \max_{R} |S(R, \theta, \varphi)|^2 \\ R(\theta, \varphi) &= \operatorname*{argmax}_{R} |S(R, \theta, \varphi)|^2 \end{aligned} \tag{4.2}$$

The beamwidth and gain of the antenna patterns determine both the SNR (2.14), and angular point spread function and resolution of this procedure. For a narrow beam, the signal propagates from the Tx to the jth scattering centre at R_j and back to the Rx, giving a single dominant return at R_j, and shadowing the region with $R > R_j$. Theoretically, this is true in general in the limit that k_θ and k_φ tend to infinity, and the beam patterns tend towards a Dirac delta function. In reality, there should be no disadvantage in using this assumption if the beamwidths deliver the desired angular resolution of the surface of a target, and the first target occludes all targets behind it in the beam. In the case that there is no detectable target present, (4.2) selects the voxel with the highest noise power.

The extent of the beam in cross-range increases radially, and so the further the target is from the radar system the quality of the reconstruction will degrade, and the beam can no longer be considered narrow. Therefore there is a compromise between being in the far field region, while being as close as possible to get as fine a cross-range resolution as possible.

Using this approach, the following section will experimentally verify that a 3D radar pointcloud can be generated in this way.

4.2 Experimental Validation

In these experiments, both the Tx and Rx units of the 300 GHz LFMCW system were equipped with Gaussian Optical lens Antennas, which can be seen in Figure 3.9. These have a narrow beamwidth in both azimuth and elevation. These units were then mounted on a pan-tilt 2D positioner, to rotate this narrow beam in both azimuth and elevation. This allowed the Radar system to isolate a very narrow region of space at a time, and to build up a 3D image of the world around the system, $S(R,\theta,\varphi)$ (4.2). A diagram of this process and a photograph of the setup used can be seen in Figure 4.1. In this case, the monostatic radar is mechanically scanned in steps of θ_s and φ_s in azimuth and elevation respectively. Although the ideal monostatic case would have the Tx and Rx units being in the same position, the size of the antennas are larger than the size of the Tx-Rx heads. This required the units to have small metal spacers placed between them so that the antennas could be attached. The exact values of the parameters used in this experimental setup are given in Table 4.1. The dB units in this section are uncalibrated and are $20\log_{10}$ of the raw output of the Rx modules.

Parameter	z_{Tx}	B	n_C	φ_s	θ_s	$z_{\mathrm{Rx}_{1,2,3}}$	θ_{BW} (3dB)	φ_{BW} (3dB)
Value	1.20 m	20 GHz	10	0.5°	0.5°	1.08, 1.27, 1.31 m	1.3 °	1.3 °

Table 4.1 Parameters used in raster scanning experiments.

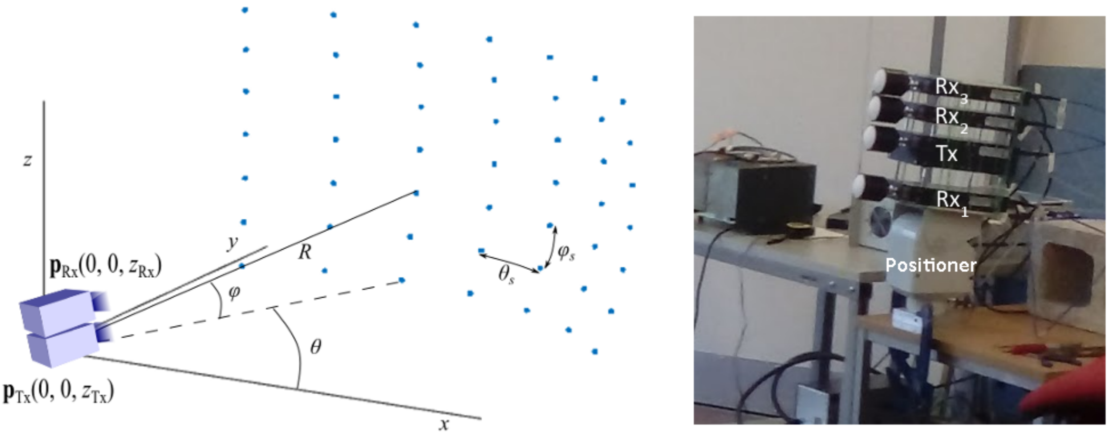

Fig. 4.1 Experimental setup of the 300 GHz radar in a raster scan configuration: diagram (left) and photograph (right).

To test the antenna pattern on a calibration target, a trihedral corner reflector of side length 4 cm was placed at a position of (R,θ,φ) = (4.0 m , 184 °, 86 °). This target was chosen because it has a large RCS while having a small extent in both azimuth and elevation of 0.6 °. The measured amplitude response of the target is shown in Figure 4.2. The response in azimuth and elevation is the range slice of $S(R = 4.0\ \mathrm{m},\theta,\varphi)$, which is the scanned image measured at the target range. The 3dB width of the response in both azimuth and elevation is 1.25 ° (a FWHM of 2.5 °), which matches the expected value of 1.3 ° to within the 0.5° resolution of the grid. The first sidelobe of the antenna pattern would be expected to be at an amplitude of -13 dB from the peak, which is below the noise floor. As predicted in (4.1), the shape of the observed antenna pattern is consistent with the measured beam pattern.

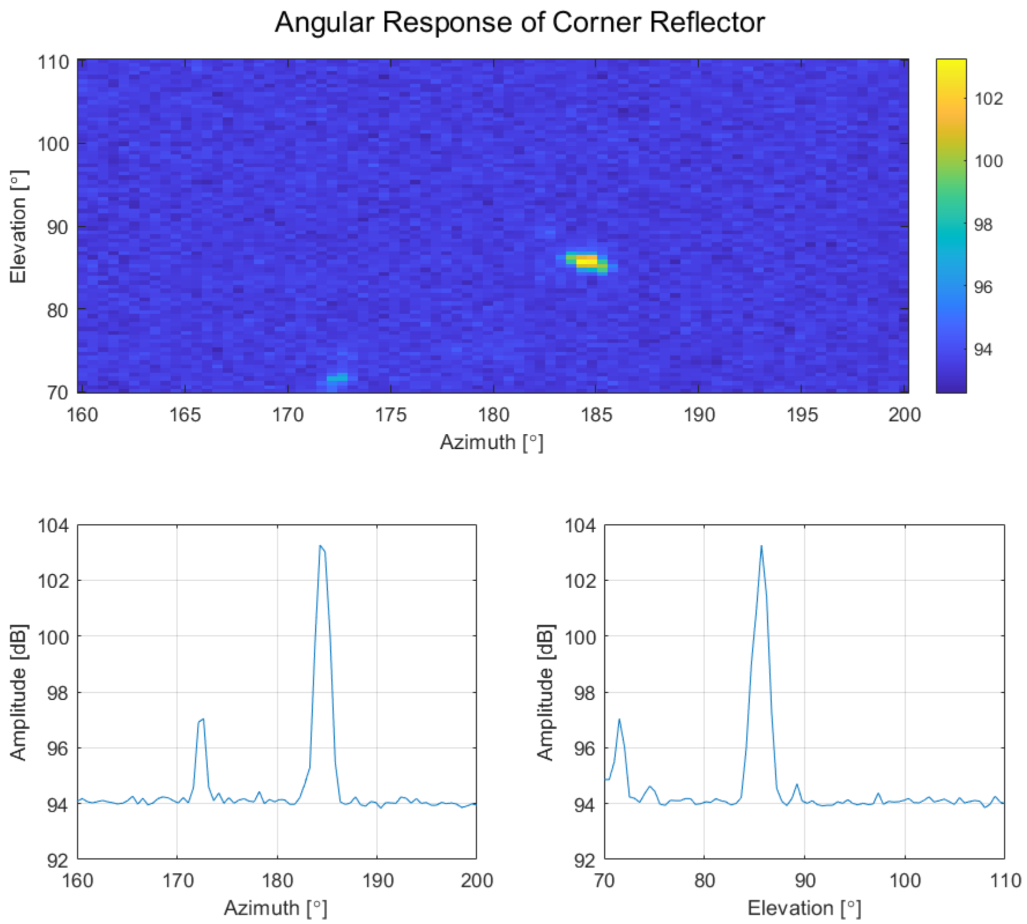

Fig. 4.2 Cross section of the raster scanned image of a corner reflector taken at $R = 4.0$ m: Azimuth elevation plot (top), with 1D azimuth (left) and elevation slices (right). Units are $20\log_{10}$ the raw uncalibrated range profile.

The first extended target which was considered was a 2.7 m by 1.5 m section of rebar which is used to reinforce concrete. This is a grid of steel with a regular square grid with side length of 0.25 m. This was positioned at an incline of 22 °, resting just above the floor at one end and on a stack of concrete breeze blocks at the other. This can be seen in Figure 4.3. Looking at the reconstruction in the xz projection, it is clear that there is the floor in the line $z = 0$ m, the breeze blocks in the line $x = 4.3$ m, and the rebar in the line from (x,z) = (2.0,0.0) m to (4.5,1.0) m. The cross-range extent of the 3 dB beamwidth is 0.05 m at the shortest range, and 0.10m at the far end of the target. What is particularly encouraging from the xy projection is that there is an repeating grid pattern, which is indicative of the spacing of the rebar grid in increments of 0.25 m in y.

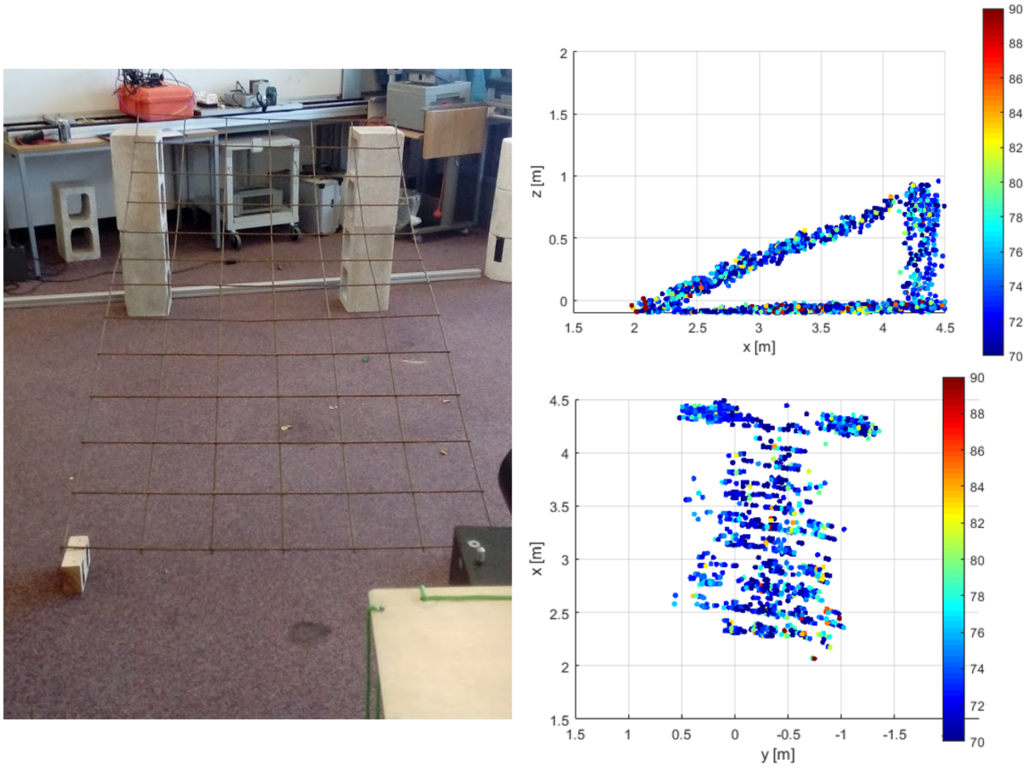

Fig. 4.3 Raster Scanned image of a section of rebar at an incline. (left) photograph, (top right) xz side-view of the radar image, (bottom right) xy top-down view of the radar image.

Next, a 1.8 m tall mannequin was considered, with a reference corner reflector. The corner reflector was placed on top of a 0.6m tall stack of polystyrene foam which was found to be non-reflective at 300GHz. Figure 4.4 shows $P(\theta,\varphi)$ (4.2), with the mannequin on the left, and corner reflector on the right of the image. The image shows a great deal of reflections from the torso and head of the mannequin, with the greatest intensity coming from the section covered by the reflective jacket. The greatest intensity from the concave of the reflective jacket is around 3 dB brighter than the small reference corner reflector. Conversely, the head and legs of the mannequin which is smooth plastic is barely visible above the noise floor. The 3D Cartesian image is shown in Figure 4.5. Both figures show the presence of the ground in the plane $z = 0$ m as expected. This method also successfully reconstructed the height of the corner reflector at $z = 0.6$ m.

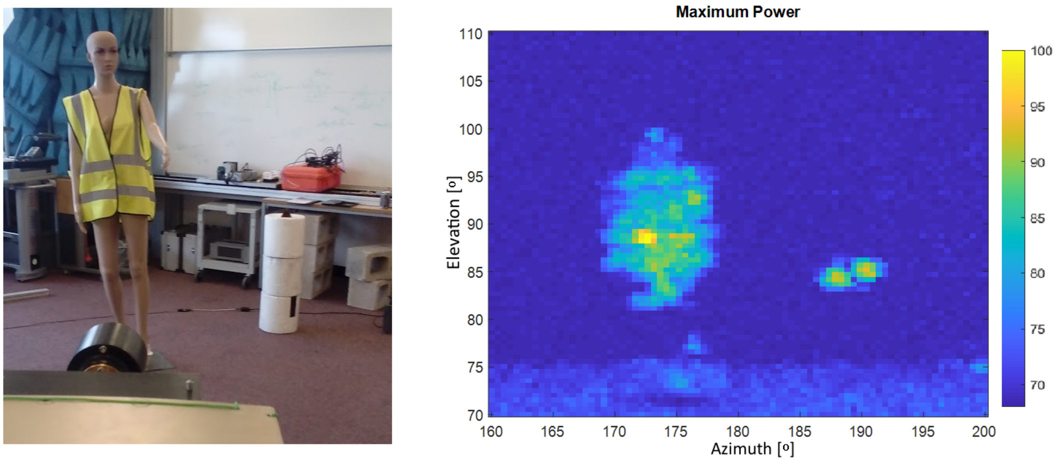

Fig. 4.4 Raster Scanned image of an adult mannequin with a corner reflector. (left) photograph, and (right) maximum amplitude at each azimuth and elevation position in the radar image. Power is in dBarb - $20\log_{10}$ the raw uncalibrated range profile.

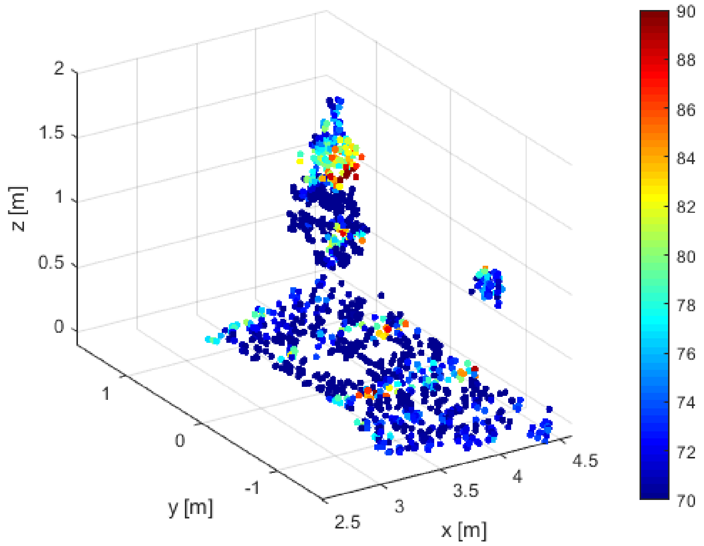

Fig. 4.5 3D Raster Scanned image of an adult mannequin with a corner reflector. Power is in dBarb - $20\log_{10}$ the raw uncalibrated range profile.

In the next measurement, objects made of 3 different materials were positioned on the floor as shown in Figure 4.6. This scene includes a corner reflector, a flat metal plate, a number of breeze blocks were places in the formation, and a section of a wooden pallette on one side.

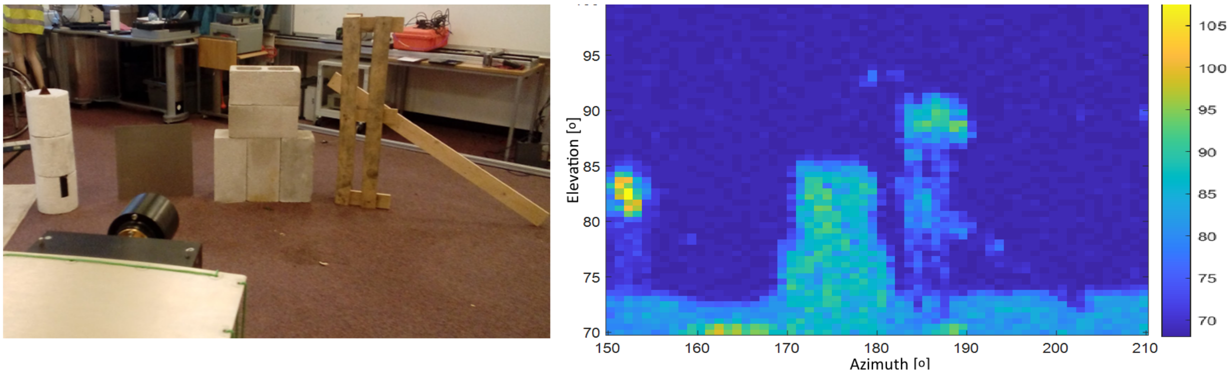

Fig. 4.6 Raster Scanned image of breeze blocks, a pallette, and a corner reflector. (left) photograph, and (right) maximum amplitude in the radar image at each azimuth and elevation position. Power is in dBarb - $20\log_{10}$ the raw uncalibrated range profile.

The 3D Cartesian point cloud of this image can be seen in Figure 4.7. As before, the corner reflector appears as a bright point-like target at a height of 0.6 m, with a barely visible polystyrene stack underneath it. The shape of the formation of breeze blocks was reconstructed successfully, with the lower 3 blocks forming a 0.6 m by 0.4 m extent in the y and z directions respectively, and the upper blocks occupying 0.4 m by 0.4 m. The side lengths of the blocks are consistent with each other, with a width of 0.4m and a height of 0.2m. The plate, on the other hand, is expected to give a specular reflection, meaning that the vast majority of the transmitted signal is scattered in a direction away from the receiver. For the palette, there are a number of corners present at the top of the palette and where the palette and plank intercept. What's more, the surface at the top of the palette is at normal incidence to the radar, and so a bright specular reflection can be observed at the top. The rest of the plank is present in the radar image, but is far dimmer than the corner sections, or the breeze blocks. Even if the plank is barely visible above the noise floor the planks cast a linear shaped shadow upon the ground.

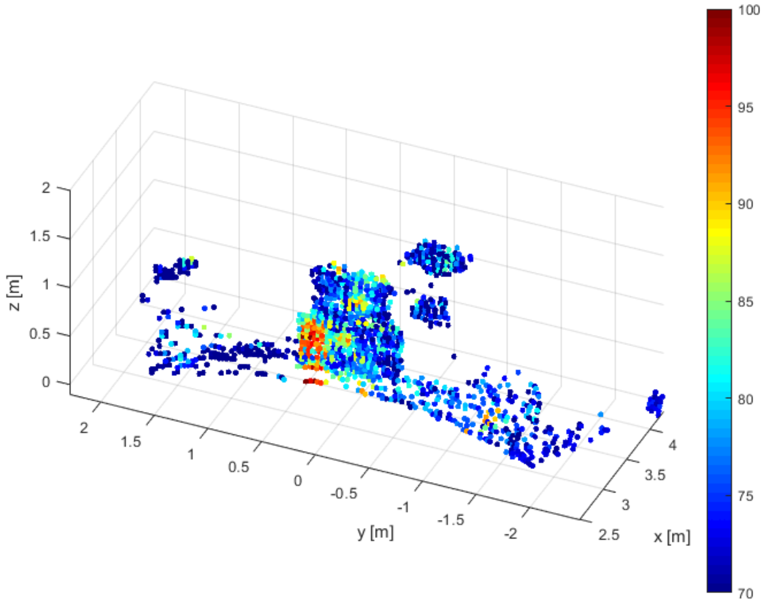

Fig. 4.7 3D Raster Scanned image of breeze blocks and pallette with a corner reflector.

Finally, a bicycle was considered. The bicycle had to be leaned over onto a stand at a slight incline to stop it from falling over. The 3D reconstruction of the bike can be seen in Figure 4.8. In the *xz* projection of the 3D image, the frame and wheels of the bike lie in the line from (3.3,0.0) m to (3.5,1.0)m. There is also a handlebar present at the position (3.2,0.9) m, and a metal stand behind the bike at (3.6,0.3) m. The 3D reconstruction reconstructes the full length of the bike, giving a length of 2m in *y* and a height of 1 m in *z*. The bike is a complex target made up of many constituent scattering centres, some of which are bright, such as the chain link at (3.4,0.0,0.3)m, or the bike seat which is held up by metal clips at (3.4,-0.3,0.8)m. On the other hand, some of the finer detail, such as the thin metal spokes of the wheel, are not captured in the 3D reconstruction.

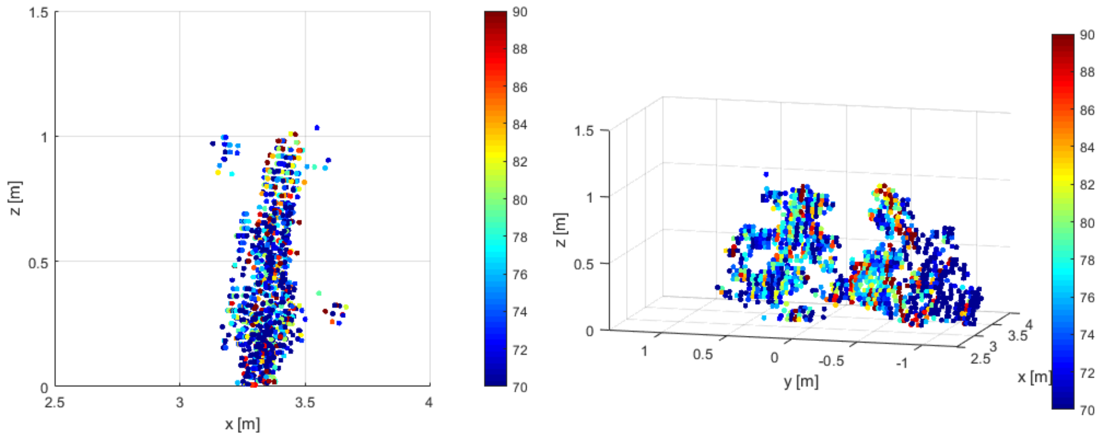

Fig. 4.8 3D raster scanned image of a bike. (left) *xy* side view, and (right) front view of the bike.

4.3 Discussion

In this section, a number of targets were considered and highly detailed 3D images were produced by equipping the radar with a narrow beam antenna and mounting it on a pan and tilt head. As predicted, the instrument response of the system in azimuth and elevation was essentially the antenna pattern, which sampled the space in azimuth and elevation through raster scanning. The width of the peak in azimuth and elevation was consistent with the antenna patterns from section 3.3. As such, both the resolution and gain of the system was improved by focusing the energy into a narrow beam. Based on the definition of R_F (3.3), the measured response of the antennas do not corresponded to the far field response of the system, because the antennas were separated in z. However, in azimuth this is unlikely to be an issue, as the Tx and Rx units are locked in position and are coaligned in azimuth to illuminate the same position. This did not appear to effect the ability of this technique to produce 3D imagery significantly.

Each of the images were able to reconstruct the full extent and shape of realistic targets, from pedestrians, bicycles, metal grids, and extended surfaces. The only exception to this were electromagnetically smooth surfaces (2.20) such as a flat metal plate or smooth plastic limbs of a mannequin, where most of the radiation was scattered away from the Tx-Rx site.

There is one key fact which makes this method with this layout unusable for automotive radar. Although the processing is very fast, the measurement time required to produce these images by raster scanning the radar is of order of 1-2 minutes per scan. In this configuration, this is a completely unacceptable amount of time to produce a 3D image of the target for an autonomous vehicle - not to mention the fact that at each dwell, the radar is only monitoring and illuminating less than 2 ° in both azimuth and elevation, and by definition the radar is not monitoring any other direction. This is not to say that this could not be improved using array processing, electronic beamsteering, or increasing the number of Tx and Rx modules to selectively illuminate many directions at once. It is, instead, a limitation of the hardware with this number of Tx and Rx modules.

4.4 Conclusion

This chapter presented high resolution 3D imagery produced through raster scanning a 300 GHz LFMCW radar system. The level of detail produced with a 1.3° 3 dB beamwidth in both azimuth and elevation, and an 8 mm range resolution means that these are very high resolution real aperture radar images. Unfortunately, the long measurement time needed to complete a full raster scan means that the technique outlined here cannot currently be used for an autonomous car.

What these measurements do is to confirm the observations from the literature that low-THz radar can produce these kinds of images through scanning in both directions. The fact that the full extent of the target could be seen confirms that radiation is backscattered from the full extent of the object, and that this information is present in the received radar signal. It also highlights the fact that an alternative method needs to be employed to reduce the measurement time, while still providing an estimate of the location and extent of the target.

Therefore, alternative methods will be investigated which allow localisation within a larger radar field of view. One way of doing this is to exploit the fine range resolution of the system. In the subsequent sections, the focus of the thesis will shift from localising the target with the antenna beam patterns to localising the targets using ToA and TDoA information between Tx-Rx pairs.

The following section will investigate converting range information to 3D positional information for multiple Tx and Rx pairs.

Chapter 5

Multilateration

This chapter demonstrates the mathematical foundation which the rest of this thesis is built upon; namely that a low-THz radar is able to perform localisation in multiple dimensions by using ToA information due to its large bandwidth. The imaging techniques developed in later chapters all fundamentally work using the geometry of these techniques. First, section 5.1 discusses how ToA information can be extracted from a radar range profile. Then multilateration is broken down into two cases; trilateration which finds a 3D position using 3 or more Tx-Rx pairs, and bilateration which performs 2D localisation using 2 Tx-Rx pairs at a time. Section 5.2 details the first trilateration experiments performed using time multiplexed signals on a large linear positioner, localising the target purely from ToA information. Section 5.3 improves upon this by employing mechanical scanning to localise the target in azimuth, and using ToA information to localise the target in range and height. Finally these results are discussed in section 5.4.
The results of section 5.2 were previously published in [151].

5.1 Estimating Time of Arrival

A block diagram outlining the process of multilateration is shown below in Figure 5.1. The diagram shows that the process of generating a range profile is much the same as in previous sections. The starting point for multilateration is the Time of Arrival (ToA) estimation. This section aims to lay out how a time of arrival or corresponding range value, $R_{\mathrm{b_i}} = \frac{1}{2}c\tau_i$ (2.2), is extracted from a range profile for the system described in chapter 2. These ToA or range values then inform the 3D localisation processes later in this chapter.

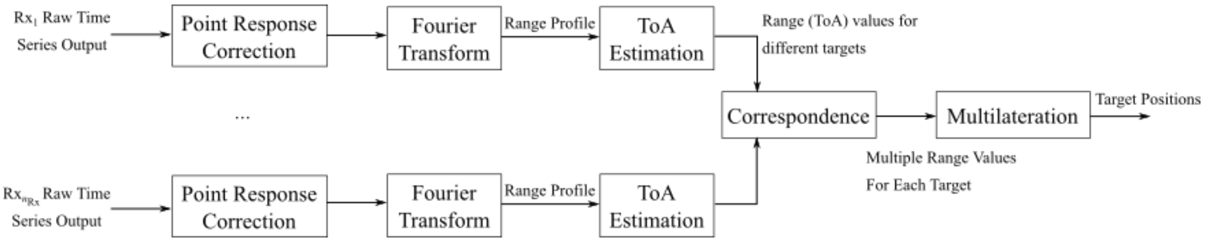

Fig. 5.1 Block diagram of multilateration.

Let us consider a scenario where there are n_{tg} point-like scattering centres present (2.10). For a high resolution radar system such as this one, it is common practice to decompose extended targets into a series of point-like scattering centres [136]. Therefore one can consider a scene to be composed of multiple scattering centres, regardless of the kind of targets present. So specifically, this section considers how to estimate the $R_{\mathrm{b_{i,j}}}$ values for each of these scattering centres in the presence of noise, for the i^{th} Tx-Rx pair, where $i = 1, \ldots, n_{Tx}n_{Rx}$.

This process is laid out for a one-dimensional range profile such as (2.11), which has noise present in the signal. It is assumed in this section that there is a sufficient SNR present that the backscattered signal from a target is distinguishable from the noise floor of a signal.

For a 1D signal with additive white Gaussian noise (AWGN), the observed signal is the sum of the returns of $j = 1, \ldots, n_{tg}$ targets and this noise. Here, (2.10) is reformulated in (5.1) to explicitly consider the noise. In chapter 3, it was confirmed that using a point correction process, the point response of the system is a sinc function (2.7) and the background noise appears as AWGN, (or at least colourless). The total signal $S(R_b)$, is the sum of the point response ($S_{\mathrm{IF}_{i,j}}$) of n_{tg} points corrupted with a AWGN noise signal ν. This range axis has been sampled uniformly in units of R_s, where typically $R_s \approx R_{res}$. This results in a 1D discrete signal of length n_s,

$$S(R_b) = \nu + \sum_{j=1}^{n_{tg}} S_{\mathrm{IF}_{i,j}}(R_b; R_{b_{i,j}}, A_{\mathrm{IF}_{i,j}}) \tag{5.1}$$

There are a few useful features of a sinc function (2.7) which allow us to extract $R_{b_{i,j}}$. First, the maximum of (2.7) occurs at $R_b = R_{b_{i,j}}$. However, the target range value often will not lie exactly at the centre of a cell, $mod(R_{b_{i,j}}, R_s) \neq 0$. Second, the function is symmetric around $R_b = R_{b_{i,j}}$. Then, the centre of mass of this function also occurs at the central maximum value of $R_b = R_{b_{i,j}}$. Finally, there is a predictable and linear point response, with a known width and range sidelobe pattern.

The remainder of this section will examine three general approaches of how to estimate $R_{b_{i,j}}$ from $S(R_b)$. Namely, it looks at the achievable resolution of a detector, maxima selection, and peak or distribution fitting, and which of the three is best for extracting $R_{b_{i,j}}$. This is important, firstly because in the presence of noise, the system needs to distinguish a real target from noise, and secondly because the system needs to precisely determine the signal amplitude and ToA or $R_{\mathrm{b_i}}$ of a target.

To illustrate each of the three approaches, an example is shown in Figure 5.2. This signal is the Fast Fourier Transform (FFT) of $2\sin(31.4x) + \sin(51.2x)$ with low-level AWGN and $R_s = 1$. The distribution in Figure 5.2 is a series with two peaks with maximum values at the cell positions 31.4 and 51.2 with low level AWGN.

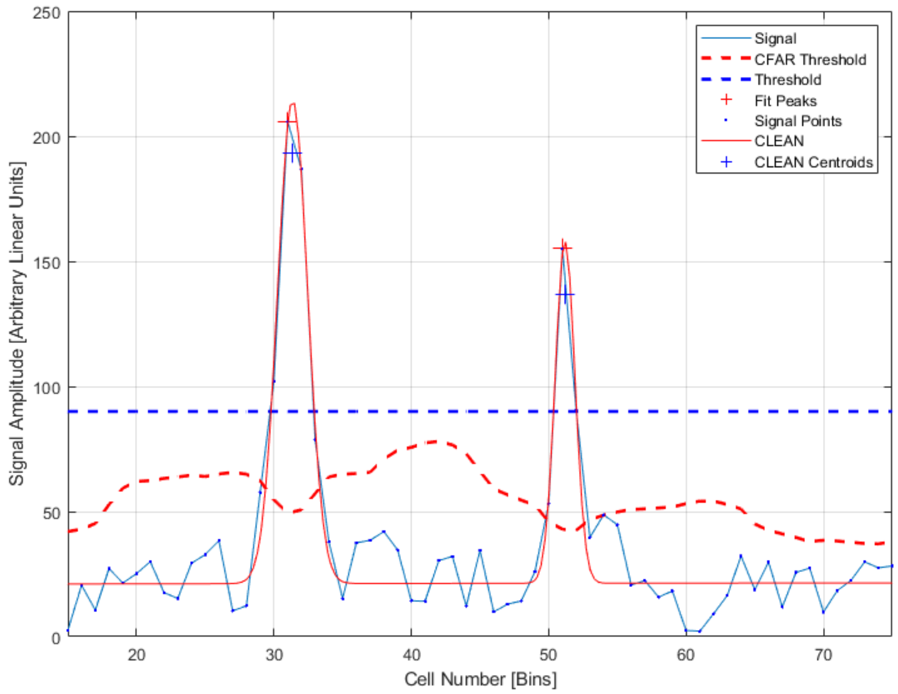

Fig. 5.2 Detection and peak selection in the presence of AWGN. The example signal is the FFT of $2\sin(31.4x)+\sin(51.2x)$.

Detector: Detectors are more focused on whether there is a target present in a set of cells under test, rather than estimating $R_{b_{i,j}}$. But by definition, if there is a target present in the cells under test, a target has been localised to be within the range cells. Some of the most simple detectors for a radar include a threshold or a constant false alarm rate (CFAR) detector [152], however more recently neural networks have been applied [153]. For these thresholding techniques and CFAR suppose that a subset of these points which have a higher amplitude correspond to targets, and the remainder correspond to noise. By applying a threshold or an adaptive threshold such as in CFAR, these set of noise and target points can be distinguished. In Figure 5.2, for both the threshold and the adaptive CFAR threshold, the cells with amplitude above the threshold line are target detections, and those below are noise. CFAR algorithms typically outperform applying a chosen threshold, as they are a computationally fast method of thresholding with a lower rate of missed detections with few false positive detections [4]. Once the noise has been removed, then a region of cells with sufficient $|S(R_b)|^2$ remain, and $R_{b_{i,j}}$ lies within this region. The estimate of $R_{b_{i,j}}$ is accurate to within multiple range cells, so the range error of this approach is greater than R_s.

Maxima Selection: Let us consider selecting a range cell corresponding to a stationary point, like (4.2), using the assumption that $|S(R_{b_{i,j}})|^2$ will be a local maximum. Therefore, a local maximum in the signal corresponds to the target position within the accuracy of one range cell. In the case of the 3D images in section 4 (4.2), one global maximum was taken at each angular position because it was assumed that there was one dominant target at each angle. For multiple targets, one can simply select the maxima which meet a constraint, such as the N brightest targets, or maxima with amplitude above a particular threshold. This is computationally very simple and is the approach behind most peak finding tools, such as Matlab's find peaks function [154]. Provided the SNR is sufficiently large, this approach is accurate to the nearest range cell, and the range error of this approach will be R_s and will be quantised in units of R_s. This thesis does not go into zero padding or oversampling, and so usually $R_s = R_{res}$.

Peak Fitting: Peak fitting presupposes that there are a set of signals present in a model, and uses some metric to find the best fit to the n_s measurements of $S(R_b)$. For example, one might use a computational solver to fit N sinc functions to $S(R_b)$, selecting the N values of $R_{b_{i,j}}$ and $A_{\mathrm{IF}_{i,j}}$ which minimise the least squares error between the fit sinc functions and $S(R_b)$. One of the most widely used examples of peak fitting is the CLEAN algorithm, which fits a series of Gaussian signals to a 1D range profile [155]. For both a Gaussian and the sinc function, the amplitude of many nearby cells can be considered together to estimate $R_{\mathrm{b_{i,j}}}$, which is the maximum and centre of mass. The range error of such an approach can be sub-R_s, though this depends heavily on the SNR and algorithm parameter choices. The specifics of super-resolution techniques, and techniques which are better applicable to this radar system will be discussed in greater detail in later sections.

In Figure 5.2, the peaks at frequencies of 31.4 and 51.2 were deliberately chosen as they are in between the centre of each frequency bin, much in the same way that it is improbable that each target position will lie exactly at the centre of a range cell. Although it is much faster, the peak detection algorithm is quantised to the nearest cell. It will select the neighbouring range cell with the largest amplitude, and offers no finer resolution. Additional information is available here by looking at where the centre of the peak is, which is information which the CLEAN algorithm exploits. While fitpeaks located the peaks at frequencies of 31 and 51, the centroid values of the CLEAN Gaussians were 31.36 and 51.19 which are much closer to the true values.

So in summary, a threshold or CFAR detector localised the target to multiple neighbouring cells, the maximum localised the target to the nearest cell, and estimating the centre of a distribution (such as a Gaussian) may localise the target to sub-range cell resolution.

The remainder of this chapter will therefore use the maxima selection approach, with $R_{\mathrm{b_i}}$ values selected through Matlab's find peaks. This is because it is a computationally simple approach, with a predictable and fine range resolution of R_s. Additional performance may be possible using super-resolution techniques, but this section seeks to estimate the 3D localisation performance of these techniques subject to the range resolution of the system, and find 3D position in a computationally simple and fast way. The next section will focus on how multiple values of $R_{\mathrm{b_i}}$ from many Tx-Rx pairs can be used to estimate the position of scattering centres.

5.2 Trilateration

5.2.1 Geometry of Trilateration

The bulk of this topic is concerned with trilateration through the conversion of 3 or more range measurements, $R_{\mathrm{b_i}}$, to a 3D position. The previous section covered how a value of $R_{\mathrm{b_i}}$ is selected from a range profile, and it is assumed that these $R_{\mathrm{b_i}}$ values from multiple unique Tx and Rx positions are known to correspond to approximately the same jth scattering centre. This section will seek to convert these range values to a position in 3D Cartesian space.

The Cartesian coordinate system used here is the one defined in section 2.1. Although strictly speaking these methods estimate the jth target position, $\mathbf{p}_j(x_j, y_j, z_j)$, multilateration is introduced here as a coordinate transform from multiple R_{b_i} values to an (x, y, z) position. Geometrically, what this range value corresponds to is dependant on the layout of the Tx and Rx sites. There are 3 main methods of range finding which correspond to 3D analogues of conic sections – Spherical, Ellipsoidal and Hyperbolic as defined in [156]:

Spherical : The monostatic case, which is a specific case of (2.2) where $\mathbf{p}_{\mathrm{Tx_i}} \approx \mathbf{p}_{\mathrm{Rx_i}}$. The surface which is defined by a given value of $R_{\mathrm{b_i}}$ is a sphere whose centre is the Tx-Rx site.

Ellipsoidal : The general bistatic case, (2.2), which does not require $\mathbf{p}_{\mathrm{Tx_i}} = \mathbf{p}_{\mathrm{Rx_i}}$. The surface which is defined by a given value of $R_{\mathrm{b_i}}$ is an ellipsoid with foci $\mathbf{p}_{\mathrm{Tx_i}}$ and $\mathbf{p}_{\mathrm{Rx_i}}$.

Hyperbolic : The time difference of arrival (TDoA) case, which requires the use of two receivers to yield a TDoA between them, $\Delta R_{\mathrm{b_i}}$. The surface which is defined by a given value of $\Delta R_{\mathrm{b_i}}$ is a hyperboloid. Although the hyperbolic case is included for completeness, it will not see use here due to the larger number of required Tx-Rx pairs.

Any of these may be used elsewhere, but this thesis is primarily interested in systems distributed over the body of a vehicle, with a greater number of Rx sites than Tx sites, so the ellipsoidal case is the most important here. Note that the spherical case is a specific case of the more general ellipsoidal case, so considering the ellipsoidal case also implicitly includes the spherical case. Specifically the focus will be a one Tx to many Rx setup. With no loss in generality, the Tx position can be used as the origin of the 3D coordinate frame. As such one can use the following definition of a bistatic range ellipsoid for a Tx at $\mathbf{p}_{\mathrm{Tx_i}} = (0,0,0)$ and a Rx at $\mathbf{p}_{\mathrm{Rx_i}} = (x_{\mathrm{Rx_i}}, y_{\mathrm{Rx_i}}, z_{\mathrm{Rx_i}})$ which is $\mathbf{E}(R_{\mathrm{b_i}}, \mathbf{p}_{\mathrm{Rx_i}})$ given by (5.2).

$$\frac{(x-\frac{x_{\mathrm{Rx_i}}}{2})^2}{R_{\mathrm{b_i}}^2+\frac{x_{\mathrm{Rx_i}}^2}{4}}+\frac{(y-\frac{y_{\mathrm{Rx_i}}}{2})^2}{R_{\mathrm{b_i}}^2+\frac{y_{\mathrm{Rx_i}}^2}{4}}+\frac{(z-\frac{z_{\mathrm{Rx_i}}}{2})^2}{R_{\mathrm{b_i}}^2+\frac{z_{\mathrm{Rx_i}}^2}{4}}=1 \tag{5.2}$$

Using the maximum in a range profile as the target position, as in section 5.1, a single measurement localises the position of a target to be between the bounds of a range cell, i.e. between the surfaces $\mathbf{E}(R_{\mathrm{b_i}}, \mathbf{p}_{\mathrm{Rx_i}})$ and $\mathbf{E}(R_{\mathrm{b_i}} + R_{res}, \mathbf{p}_{\mathrm{Rx_i}})$. Using this form of position estimation to localise a target in a given coordinate requires there to be Tx-Rx site at multiple positions in this direction. To directly estimate the target's x position, for example, one cannot have the case where $x_{\mathrm{Rx_1}} = x_{\mathrm{Rx_2}} = ... = x_{\mathrm{Rx}_{\mathrm{N}_{Rx}}}$. However, this position can be estimated from $||\mathbf{p} - \mathbf{p}_{Rx_i}|| + ||\mathbf{p} - \mathbf{p}_{Tx_i}|| = R_{\mathrm{b_i}}$ if all other positions are known. Doing so introduces a sign ambiguity in x [27]. This sign ambiguity can be combated if a priori knowledge is available, such as the fact that the target lies in the positive or x negative direction.

To localise a target in 3D with no geometric ambiguity using this method requires the use of 4 TxRx pairs to generate a unique solution to the position of the target. As will be seen, this can be reduced to 3 measurements if some a priori knowledge of the scene is known (such as the target has to be ahead of the radar setup so $y > 0$). It is possible to directly solve multiple range measurements (5.2) as a set of simultaneous equations for (x, y, z), though this is not a particularly elegant or effective way of using many Tx Rx sites in one equation. For the more general case, it is more useful to set the problem up as one linear equation.

As shown for the monostatic case in [157] and the bistatic case in [158], the problem of trilateration can be formed into a linear equation as in (5.3) using the formulation below (5.4-5.6).

$$\mathbf{b} = \mathbf{H}\mathbf{p} \Longleftrightarrow \mathbf{p} = \mathbf{H}^{-1}\mathbf{b} \tag{5.3}$$

$$\mathbf{H} = \begin{bmatrix} x_{Rx_1} & y_{Rx_1} & z_{Rx_1} & -R_{b_1} \\ x_{Rx_2} & y_{Rx_2} & z_{Rx_2} & -R_{b_2} \\ x_{Rx_3} & y_{Rx_3} & z_{Rx_3} & -R_{b_3} \\ \dots & \dots & \dots & \dots \end{bmatrix} \tag{5.4}$$

$$\mathbf{p} = \begin{bmatrix} x & y & z & R_{\mathrm{Tx_i}} \end{bmatrix}^{\mathbf{T}} \tag{5.5}$$

$$\mathbf{b} = \frac{1}{2}\begin{bmatrix} ||\mathbf{p}_{Rx_1}||^2 - R_{b_1}^2 & ||\mathbf{p}_{Rx_2}||^2 - R_{b_2}^2 & ||\mathbf{p}_{Rx_3}||^2 - R_{b_3}^2 & \dots \end{bmatrix}^{\mathbf{T}} \tag{5.6}$$

Where $^{\mathbf{T}}$ is the transpose of a vector, **p** is a variant of the position vector of a target shown above, **b** is a vector formed from the measured bistatic range, and **H** is a matrix mapping between the two vectors. The equations shown here are a specific case of [158] for a single Tx.

If the Tx-Rx sites are co-linear or co-planar, the coordinates can be redefined (rotated and translated) such that there is a column of **H** where all elements are 0. Therefore the determinant, $\det(\mathbf{H}) = 0$, and $\mathbf{H}^{-1} \propto \frac{1}{\det(\mathbf{H})}$ is undefined. Therefore, unless the Tx-Rx sites are non-colinear or non-coplanar, the matrix **H** may not be directly invertible. This is slightly problematic, as the system only has $n_{Tx} = 1$ and $n_{Rx} = 3$, and it is often convenient to lay these out in a plane. To overcome this, one can use matrix pseudo-inversion to generate a 3D position estimate. In particular, Moore-Penrose inversion was used. In practice, this returns invalid solutions to one of the coordinates for a planar setup, but it is still possible to infer one missing coordinate if all other positions in **p** are known, with use of the fact that $\sqrt{x^2+y^2+z^2} = R_{\mathrm{Tx_i}}$ as discussed. However, geometrically, this introduces a sign ambiguity.

Figure 5.3 illustrates a specific case of trilateration where the Tx and Rx units are all coplanar. In the case of automotive radar, this could correspond to a specific case where the units are mounted at the very front of the car, or along the side face of the car. In reality, the sensors may be mounted in any position along

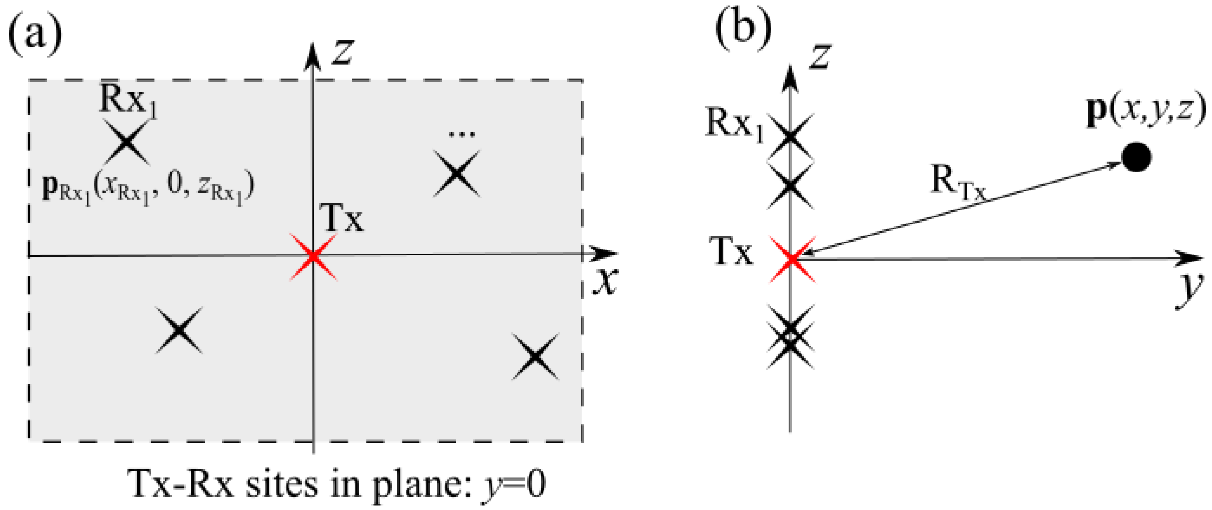

Fig. 5.3 Diagram of trilateration from Tx-Rx sites in the plane $y = 0$. (a) xz cross-section, (b) yz cross-section.

the body of the vehicle which the manufacturers see fit. The reason for this focus is that it delivers enough ways to distribute the Tx and Rx units to deliver 3D target localisation, while being able to easily set the system up experimentally with an error in positioning $\mathbf{p}_{Rx_i}$ less than the range resolution.

In the following section this formulation is going to be tested at short range, using triplets of bistatic range measurements using this formulation. It will test its applicability to the automotive target localisation problem.

5.2.2 Experimental Validation

In this section, the theory of trilateration from section 5.2.1 will be verified by short-range experiments. They are designed largely to confirm the results of [132], and extend it into 3D. The importance of the experiments is that they confirm that the technique works with acceptable accuracy and that the results are reliable. This section is laid out as follows: first this section will lay out the experimental setup used, then it will examine the predicted performance of this setup,

Experimental Setup

Based on section 5.2.1, these experiments made use of the planar setup shown in Figure 5.3. At this early stage of the project, only a separable 1Tx - 1Rx LFMCW radar was available. To measure the targets from many different Rx positions, the measurements were time multiplexed, where the Rx module was repositioned between dwells. Rather than generating 1 target position estimate, which requires 3 Rx positions, 16 different range profiles of the target were generated - each from a unique position. From these 16 measurements, triplets of Rx positions are selected to generate multiple estimates of the target position based on (5.3) with matrix pseudo-inversion.

The 300 GHz radar made use of up and down converters developed by VivaTech [159] to increase the frequency of the signals from an Agilent Fieldfox to the carrier of 290 GHz. The geometric layout of the setup is shown in Figure 5.4 and the experimental parameters used are given in Table 5.1.

System		Geometry	
Parameter	**Value**	**Parameter**	**Value**
Centre Frequency	290 GHz	$\mathbf{p}_{\mathrm{Tx_i}}$	(0, 0, 0.99) m
Sweep Bandwidth	16 GHz	$\mathbf{p}_{\mathrm{Rx_1}}$	(0, 0, 1.03) m
$\mathrm{P}_{\mathrm{Tx_i}}$	-15 dBm	$\mathbf{p}_{\mathrm{Rx_{2,3}}}$	($x_{2,3}$, 0, 0.51) m
N_F	17 dB	$x_{2,3}$	$\in$ [-0.7,0.7] m
Number of Chirps	100	R_{res}	9.4 mm
Azimuth Beamwidth	10° (3 dB)	Sphere Position	(0, 3.0, 0.5) m
Elevation Beamwidth	10° (3 dB)	Mannequin Position	(0, 4.0, 0) m

Table 5.1 Experimental parameters of the trilateration setup.

The system made use of a single transmitter at a position of $\mathbf{p}_{\mathrm{Tx_i}} = (0,0,0.99)$ m, and 3 Rx positions for a single target position estimate (denoted $\mathbf{p}_{Rx_{1,2,3}}$). Mathematically in (5.3), $\mathbf{p}_{\mathrm{Tx_i}}$ was treated as the origin of

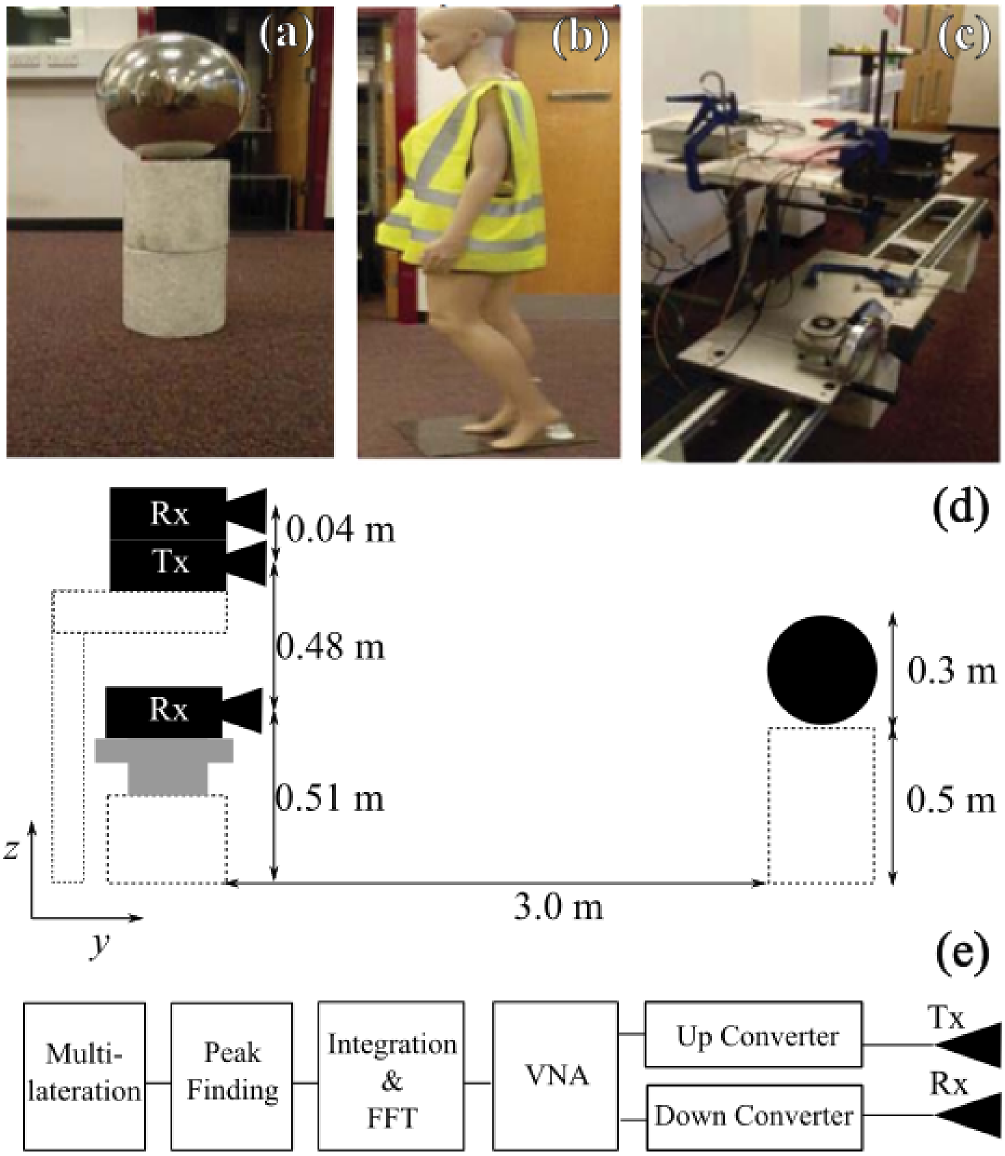

Fig. 5.4 Pictures and diagram of trilateration setup. (a) Sphere. (b) Mannequin. (c) Linear positioner. (d) Diagram of physical setup. (e) System layout.

the Cartesian coordinate system, but the ground level of the room is used as $z = 0$ in the following plots to make the position estimates easily interpretable. Using the linear formulation from section 5.2.1, the system made use of a triplets of ellipsoidal range measurements to localise the targets in 3D. The first Rx position, $\mathbf{p}_{Rx_1}$, was the same for every triplet of Rx positions. The other receivers were placed at $\mathbf{p}_{Rx_2} = (x_2, 0, 0.51)$ m and $\mathbf{p}_{Rx_3} = (x_3, 0, 0.51)$ m, where x_2 and x_3 are two values of $\{-0.7, -0.6, -0.5, \ldots, 0.7\}$ m such that $\mathbf{p}_{Rx_2} \neq \mathbf{p}_{Rx_3}$. To generate the different values of x_2 and x_3 a high precision linear positioner with a stepper was used.

In total, a range profile of the target was taken from 16 different Rx positions (2.11). From this, 105 different triplets of receiver positions ($\mathbf{p}_{Rx_1}, \mathbf{p}_{Rx_2}$, and $\mathbf{p}_{Rx_3}$) are selected. $\mathbf{p}_{Rx_1}$ was the same for each configuration and the 15 different available values of x_2 and x_3 yielded 105 (15 choose 2) possible trilateration receiver configurations, all of which were combined to create a set of 3D Cartesian positions corresponding to the position of peak received power. Therefore the plots below will show 105 different 3D position estimates.

The first experiment will be focused on the position estimate of a metal sphere with a diameter of 32cm and a measured radar cross section of - 11 dBsm. The sphere was supported on a stack of pieces of expanded polystyrene, which were found to give returns with amplitude below the noise floor. A wool carpet was used as a low-THz absorber to obscure the wall of the room. This carpet was found to have a very low RCS at 300 GHz [144]. The second experiment will attempt to reconstruct the profile of a mannequin in a high visibility jacket. This, of course, constitutes a more complex target and is more representative of many of the targets which would be seen in a real automotive radar scenario. For the target at $x = 0$, $y = 3$ m, the 10 ° transmitter beamwidth allows 0.33 m from the base of the polystyrene stack to be illuminated in the 3dB main lobe of the antenna. This encompasses the entirety of the sphere. For the 1.75 m tall mannequin, the beamwidth required it to be placed at $y = 4$ m, such that the main lobe would illuminate the entirety of the mannequin's body.

Error Analysis

Based on these system parameters and target positions one can evaluate the RMS error of multilateration along each axis. The RMS error operator for multilateration is introduced as $\mathscr{D}$ (5.7), which is used to estimate the performance of this localisation. In this analysis, it is assumed that the position of the Tx and Rx units are known to some small fraction of the range resolution, which is true given that the resolution of the linear positioner stepper motor means that the position of the Rx units is accurate to within 0.1 mm. Also, the SNR is assumed to be sufficiently high to not adversely affect this localisation. Therefore, this section is concerned with how an error in the range resolution of the system influences the error in 3D position information (5.7).

$$\mathscr{D} = R_{res}\sqrt{\sum_{i=0}^{n_{Tx}n_{Rx}}\left(\frac{\partial}{\partial R_{b_i}}\right)^2} \tag{5.7}$$

To generate the RMS error, (5.3) was solved algebraically to generate $\mathbf{p}$ (5.5) using Matlab's symbolic solver. The exact solution is too long to be useful for the reader when written out here. The solutions of x, y and z are functions of $\mathbf{p}_{Rx_1} \ldots, \mathbf{p}_{Rx_3}$ and $R_{b_1}, \ldots, R_{b_3}$, which are used in (5.7). In these experiments, there are two target positions, (0,3.0,-0.3) m and (0,4.0,0) m, and any combination of x_2 and x_3 could be used to estimate $\mathbf{p}$ (5.5). For both target positions, the RMS error in each coordinate is shown for each possible selection of x_2 and x_3. The RMS error in x, y, and z for a target at (0,3.0,-0.3) m is shown in Figure 5.5 a-c, which is the position of the sphere. Then for the mannequin, the target position is (0,4.0,0) m, which is shown in Figure 5.5 d-f. Figure 5.5 shows $\log_{10}\mathscr{D}x$, $\log_{10}\mathscr{D}y$, and $\log_{10}\mathscr{D}z$, because there is a great variation in the RMS error for different x_2 and x_3, which is easier to visualise on a log-scale.

In each case, in the line $x_2 = x_3$, the error of trilateration tends to infinity. In this line where $\mathbf{p}_{Rx_2} = \mathbf{p}_{Rx_3}$, matrix inversion does not generate a solution, and trilateration ceases to work, as there are no longer 3 unique Rx positions. These positions will not be used in the experiments. Looking at Figure 5.5 a-c, $\mathscr{D}x$ takes values from 0.12m where $x_{Rx_2} = 0.7$ m and $x_{Rx_3} = 0.7$ m to 1.35m at the smallest separation of $x_{Rx_2} = 0$ m and $x_{Rx_3} = \pm 0.1$ m. $\mathscr{D}y$ has the smallest values in the line $x_{Rx_2} = -x_{Rx_3}$, with values of between 0.05m at the furthest separation and 0.01m at the nearest separation. It is predicted that the worst

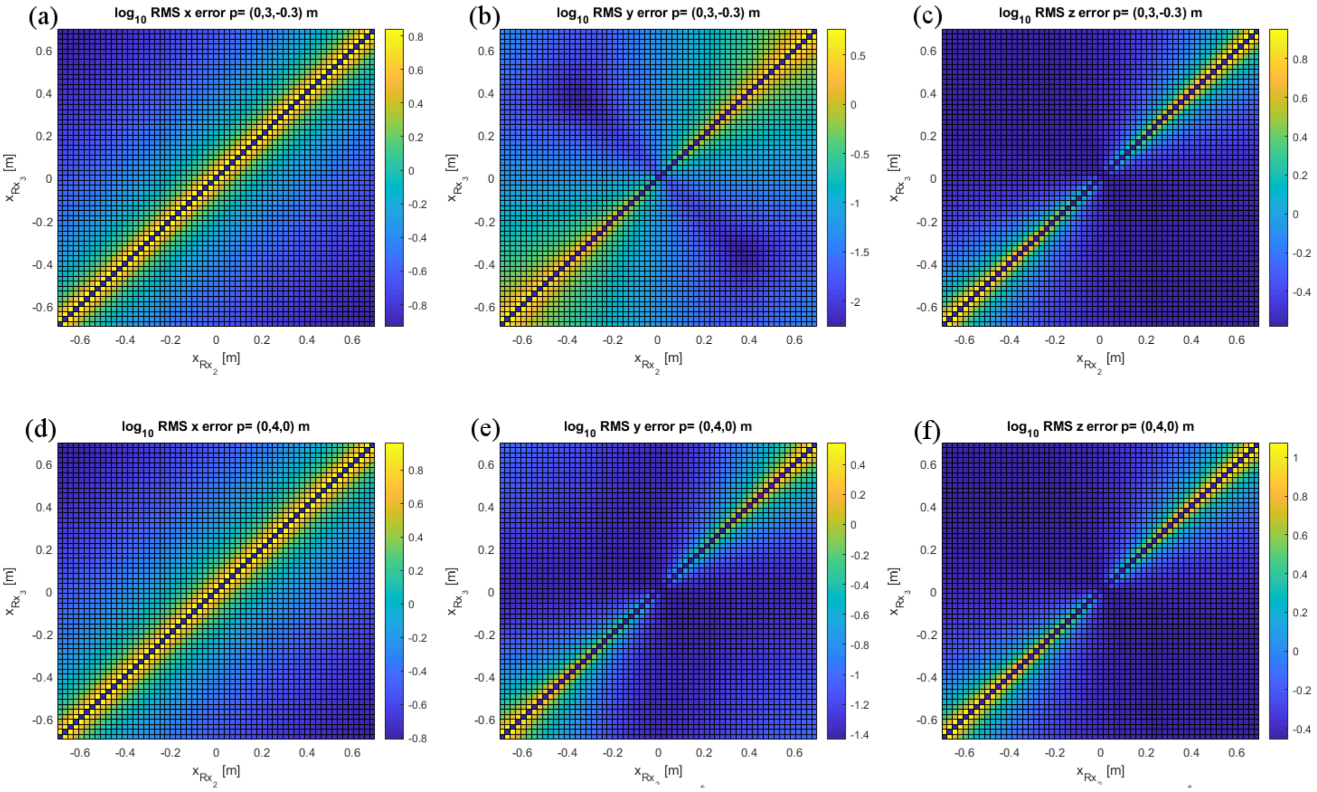
(a) $\log_{10}$ RMS x error p= (0,3,-0.3) m

(b) $\log_{10}$ RMS y error p= (0,3,-0.3) m

(c) $\log_{10}$ RMS z error p= (0,3,-0.3) m

(d) $\log_{10}$ RMS x error p= (0,4,0) m

(e) $\log_{10}$ RMS y error p= (0,4,0) m

(f) $\log_{10}$ RMS z error p= (0,4,0) m

Fig. 5.5 RMS error of trilateration for a fixed target position and variable Rx positions. Including the RMS error at the sphere's position in x (a), y (b), and z (c), and for the mannequin in the x (d), y (e), and z (f).

resolution in y will be 0.07m here. $\mathscr{D}z$ behaves similarly, but with a minimum value of 0.27m in the line $x_{Rx_2} = -x_{Rx_3}$. In Figure 5.5 d-f the same general patterns are visible for the mannequin's position too, though one would predict the resolution in each direction to degrade radially with an increase in target range. As such the minima in each direction are now 0.16 m, 0.08 m, and 0.35 m in x, y, and z respectively.

In short, the best resolution for the sphere is predicted to be ±(0.12,0.05, 0.27) m, and ±(0.16,0.08, 0.35) m for the mannequin. This is the best case scenario for when the Rx units have their maximum separation, and is highly dependant on the Rx configuration used.

Results

Using this setup, the system was used to measure the ranges to both the sphere and the mannequin. At each Rx position a range profile (2.11) was generated by coherently integrating over the 100 chirps to improve the SNR of the system [4]. Figures 5.6d and 5.7d show the range profiles plots of these targets. At some Rx positions, one can observe the direct leakage between the transmitter and receiver. This coupling was observed at a bistatic range of 0.6 m, when the receiver was just above the transmitter and at 0.8 m when the receiver was placed at 48cm directly underneath the transmitter at (0, 0, 0.51) m. The received power of these couplings decreased by -22 dB from the receiver position of (0, 0, 1.03) m to (0, 0, 0.51) m. At other receiver positions the coupling was barely distinguishable from the noise floor.

A sphere is a canonical radar target which can be treated as an ideal scatterer, with $n_{tg} = 1$. For a 32 cm diameter sphere illuminated by a 1mm RF wavelength, the radius of the sphere is far larger than the wavelength. Therefore one can assume that the RCS lies within the optical scattering regime [137]. At such close ranges, there is a significant difference in observation angle for the different Tx and Rx sites, and so one must consider the bistatic RCS here. Modelling the bistatic RCS as a perfectly conducting smooth sphere in the optical scattering regime using formulae from [160] one would predict a maximum bistatic RCS of -8 dBsm, and a minimum of approximately -34 dBsm at the greatest Tx-Rx separation. In another measurement campaign, the monostatic RCS was found to be -11 dBsm, so the observed RCS is likely to be 2-3 dB lower than the ideal case [115]. In Figure 5.6d, in a quasi-monostatic position the observed signal power of the sphere is -30 dBm, with a noise floor with power of -59 dBm. Even with the predicted decrease in RCS of -26 dB from monostatic to the furthest separated positions, the signal power should have an SNR of at least 3 dB. In practice, the power returned from the target was found to consistently be large enough to detect the target, and perform trilateration.

Using the formulation in (5.3-5.6), 105 triplets of bistatic range positions were converted into 105 position estimates, $\mathbf{p}$ in (x, y, z) (5.5). The resulting x, y and z estimates were independantly sorted into bins and displayed as histograms. Initially, the width of these bins were 1 cm for each axis for the sphere. The points in y were almost entirely distributed in the same bin, so the bin size in y was decreased to 1 mm to look more closely at the spread of points. The histograms of the reconstructed points in each direction are shown in Figure 5.6. For the sphere, the range to the peak return was 3.10 m when the receiver was directly underneath the transmitter, and the range increased to 3.15 m when the receiver was positioned at (0, -0.70, 0.51) m. This was 4cm larger than that from the range measured with the receiver at (0, 0.70, 0.51) m. Because the sphere is rotationally symmetric, the difference of 4cm between the range to peak returns suggest that the sphere was slightly misaligned relative to the central *yz* plane (i.e. from *x*=0). Figure 5.6 shows the position with the highest number of points is (0.04, 3.08, 0.45) m. Looking at the spread in (x, y, z) (5.5), the range of values are $x \in [-0.1, 0.2]$ m, $y \in [3.06, 3.1]$ m and $z \in [0.4, 0.6]$ m. This almost perfectly describes the lower hemisphere of the sphere facing the transmitter and receiver sites, however as the predicted RMS error is ±(0.12,0.05, 0.27) m it is likely that this spread is due to the uncertainty in range, rather than describing different points of reflection along the surface of the sphere. Although the range of values in *y* and *z* are a little smaller than the predicted RMS error, there appears to be an overall larger spread in target *x* values than expected. This will be discussed later in this chapter after examining the reconstruction of the mannequin.

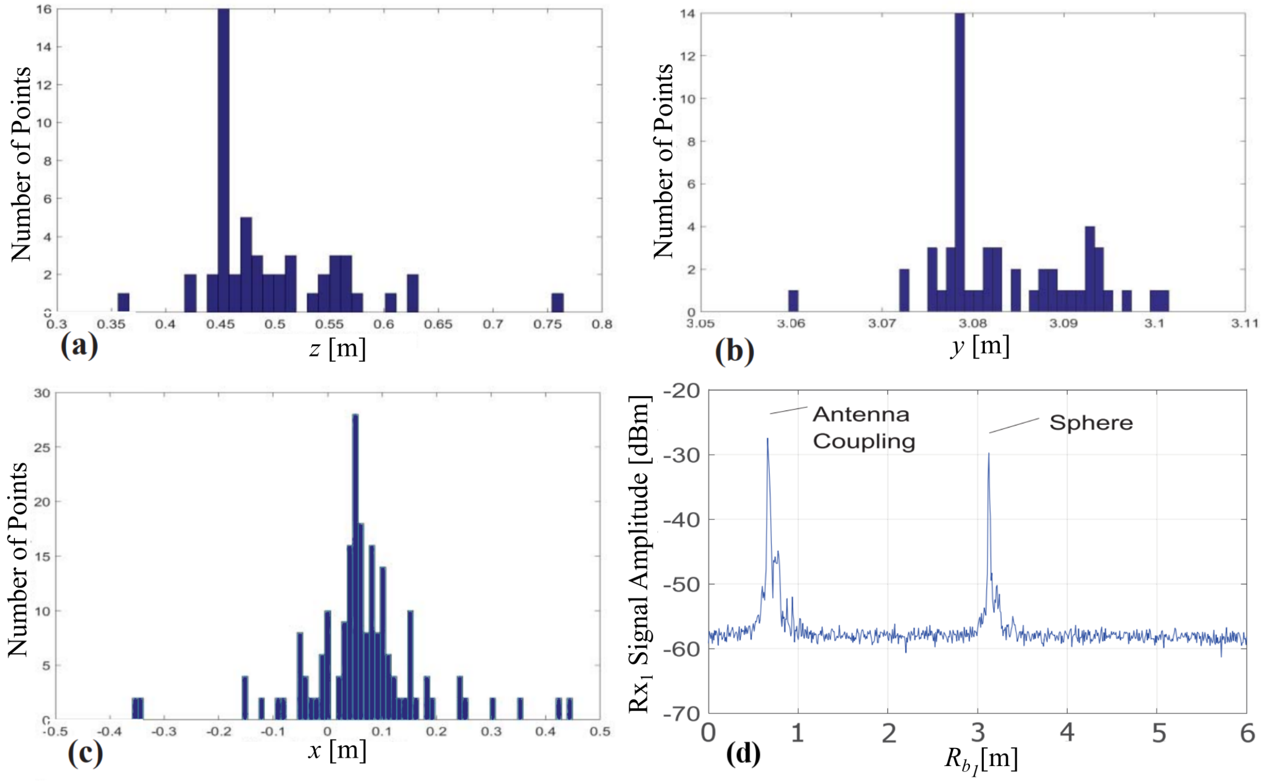

Fig. 5.6 Localisation of a sphere using through trilateration. (a) Histogram of height (z) positions from trilateration. (b) Histogram of across-room (y) positions from trilateration. (c) Histogram of along-track (x) positions from trilateration. (d) Example range profile from a monostatic position.

As was anticipated, the mannequin had a far more complex range profile than the reference sphere target. In the low-THz band, a human body is an extended target with many constituent scattering centres distributed over the body. In [114], which examined the RCS of a similar mannequin at 300GHz, the parts of the body with the largest RCS appeared to the the torso and upper legs, with monostatic RCS values of -13 dBsm and -10 dBsm respectively. Effectively, this is modelled as a target with $n_{tg} = 2$. These two sites being the dominant scattering centres is consistent with other measurements in the 77GHz band [161]. Only the range and RCS are different for the measurement of the sphere and mannequin. Because the range and RCS of the mannequin and sphere are known, this can provide an estimate of what the observed power of the mannequin should be (5.8). This is found by comparing (2.18) for the sphere and mannequin.

$$P_{mannequin} \approx P_{sphere} \frac{\sigma_{mannequin}}{\sigma_{sphere}} \left(\frac{R_{sphere}}{R_{mannequin}} \right)^4 \tag{5.8}$$

This generates a signal power of -37 dBm for the torso and -34 dBm for the legs. Although the estimate of -34 dBm for the upper legs may be accurate, the backscattered power from the torso is likely to be higher than this due to the presence of the reflective vest. That being said, in [114] this RCS value is generated by measuring only the torso or legs, and integrating the entire power returns of a range profile, and not by taking peak power values. The authors do not consider only two peaks in the returns from a mannequin, and these values should only be taken as a rough estimate.

The range profile of a mannequin from the monostatic position is shown in Figure 5.7d. Clearly there are many peaks coming from the mannequin in the region $R_{b_i} \in [4.0, 4.4]$ m, but at each Rx position it seemed that there were two dominant peaks. These peaks were typically at least 10 dB brighter that other peaks present, and so it was feasible to measure their range and correlate them in the measurements from one Rx position to another. This meant that it was always possible to make a sensible location estimate. Figure 5.7d shows a pair of peaks, the first (blue) located between $y =$3.94m and $y =$4.03m with monostatic power of -31 dBm, and the second (red) located between $y =$4.10m and $y =$4.18 m with power -34 dBm. The first major peak appeared to be comprised of multiple closely spaced maxima. In all these cases the measured range was approximately 4.01 m. The furthest measured range was with the receiver at (0, 0.70, 0.51) m where the peak was at 4.05 m. The second major peak, in contrast, appeared to be a single peak.

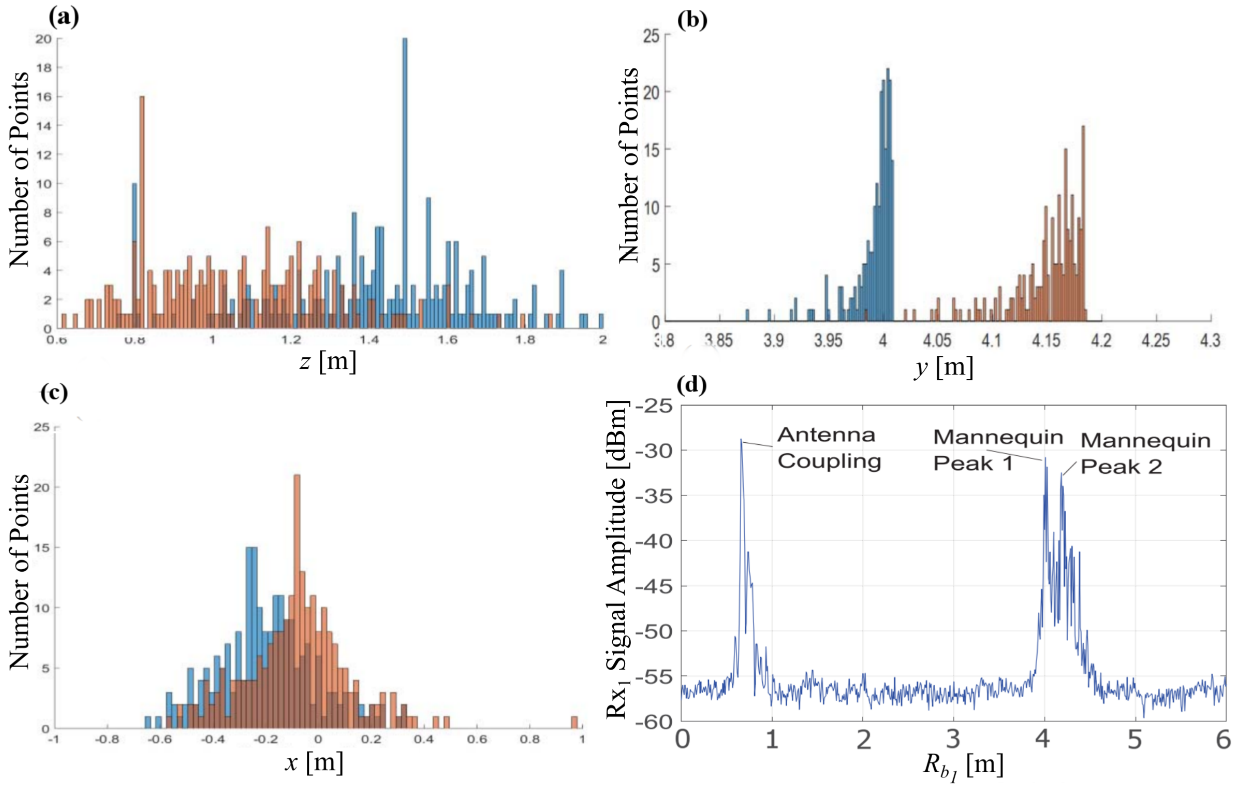

Fig. 5.7 Localisation of a mannequin using through trilateration. (a) Histogram of height (z) positions from trilateration. (b) Histogram of across-room (y) positions from trilateration. (c) Histogram of along-track (x) positions from trilateration. (d) Example range profile from a monostatic position.

It has the smallest range of 4.16 m for the quasi-monostatic receiver position (0, 0, 1.03) m and a greatest range of 4.24 m with the receiver at (0, - 0.70, 0.51) m.

As before, the histograms of the Cartesian coordinates recreated by these peak range values is shown in Figure 5.7. The bin sizes chosen were 2cm in x, 2mm in y, and 1cm in z. There is a stark contrast in the distributions of points in Figure 5.6 compared to 5.7. Although it is predicted that the RMS error of $\pm$(0.16,0.08, 0.35) m for the mannequin will be larger than the error at the sphere position, the peaks are even less well-defined than predicted for the mannequin. First, in z, Figure 5.7 shows significant overlap between the histograms of the z positions of the two peaks, the first between $z =$1.2m and $z =$1.8m high with a peak at 1.51m and the second between $z =$0.7m and $z =$1.3m with a peak at 0.81m. There are, however, a greater number of outliers, meaning there are a spread of points over the entire measured extent of $z \in [0.6, 2.0]$ m. As predicted, the extent in y is the smallest of the 3 axes, with the first peak at $y \in [3.96, 4.02]$ m and the second at $y \in [4.13, 4.18]$ m. Finally, in x the first peak is at -0.3m, and the second is at -0.1m. The mannequin is 0.5 m wide from one hand to another. The measurements thus give a useful indication of the range of positions over which returns are being seen, confirming that the returns come from multiple or extended scatterers on the mannequin. It is not immediately obvious that there are $n_{tg} = 2$ clear positions in 3D space which give rise to these peaks. The following discussion section will explore why this could be.

Discussion

The main issue highlighted in these experiments does not appear to be with the geometry or mathematics of trilateration, but with the n_{tg} scattering centres. The problem is how to pick the corresponding $R_{b_{i,j}}$ values which go in to (5.3). This can be broken down into two problems: the persistance of scattering centres at different aspect angles, and identifying that a peak in the 1^{st} range profile corresponds to the same j^{th} scattering centre in the i^{th} range profile (particularly when there are many scattering centres present).

First, let us consider the sphere. What is particularly interesting in this experiment is the distribution of the target's trilaterated positions in x. If a sphere is in the optical scattering region and the range resolution is much smaller than the radius of the sphere, it is more useful to consider facets along the sphere's surface rather than the sphere as a whole [13]. The sphere is considered to be a smooth, curved, metallic surface. As such, the returns will be specular. Even though it is fair to assume there is a single bright specular point of reflection, $n_{tg} = 1$, one would expect the point which gives the largest returns to change with Tx and Rx position. They will move across the surface of the sphere according to the point of specular reflection changing, as illustrated in 2D in Figure 5.8. Although the point of specular reflection for each of the Tx-Rx pairs are different, the bistatic range values can still be put into the trilateration equations. The reconstructed position is taken to be the position at which the ellipses overlap [27]. However, it is difficult to establish how much of this spread is coming from the physical scattering mechanisms of the surface as opposed to the calculated RMS error.

Although this is just an illustration, the intersection of the ellipses reveal that the reconstructed target position could align very closely with the surface of the sphere, even if the points of reflection are different. Therefore this process is not reconstructing the full extent of the target, but seems to do well at reconstructing the mean position of the sphere when considering multilateration over many Tx-Rx sites. A similar argument could be made to the curved torso of the mannequin to a lesser extent. For the mannequin, which has many depressions, edges, and corners in the surface, this pictoral explanation is insufficient. It is true that in the literature the RCS of the mannequin as a function of aspect angle appears more uniform due to the more diffuse reflections at these higher frequencies [113], and it is likely

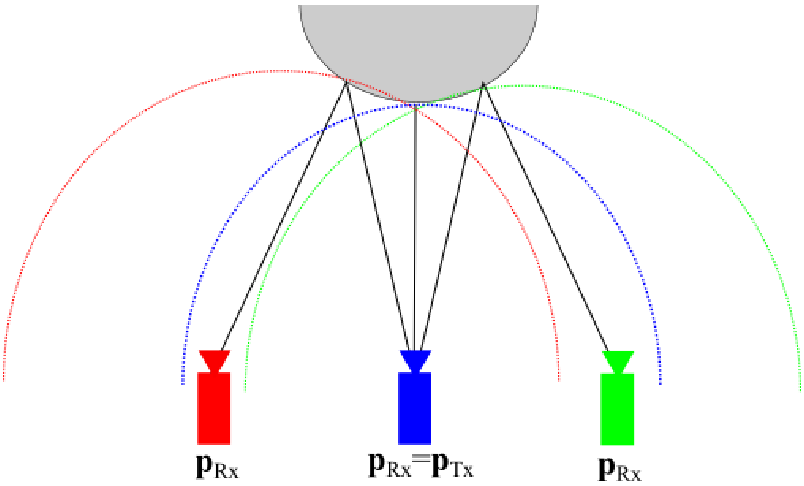

Fig. 5.8 Illustration of reflection from a sphere to multiple Rx sites.

that $n_{tg} >> 2$. This does not necessarily mean that the same scattering centres along the surface of the mannequin are giving bright reflections at every aspect angle. As such, the two peaks selected in the trilateration experiments with the mannequin are almost certainly not from the same two scattering centres from one Rx position to another. Effects of this can be seen in particular in the spread of target positions of the mannequin in x and z. In both directions, the spread in reconstruction of the mannequin is not only far greater than the sphere, but greater than the RMS error alone. These experiments do nonetheless verify that processes such as this can be used for position estimation, given the limits of physical scattering mechanisms.

These issues can be mitigated in a number of ways. The first is to reduce the distance between the Tx-Rx pairs, limiting the difference in aspect angle. The next is to use an antenna with a narrower beam, so that only a smaller subset of the n_{tg} scattering centres are illuminated in a given dwell. This also has the added benefit of increasing the antenna gain and hence the Rx power. Finally, if some of the localisation can be performed using mechanical scanning, the number of target coordinates which need to be estimated are decreased, reducing the number of range measurements required. Therefore in the next section, the 3D localisation process will be reduced into a more constrained form, where the TDoA algorithm is only applied in a 2D plane and the third dimension comes from other information.

5.3 Bilateration

This section is concerned with a more constrained version of the 3D ToA multilateration algorithm. Whereas section 5.2 dealt with localisation in 3D (x,y,z) from 3 or more range measurements in a more general distribution of Tx and Rx sites, shown in Figure 2.1a, here the focus is a set of Tx and Rx units colocated in x and y, and distributed in z. This is the Tx-Rx stack in Figure 2.1b. This section will focus on how to estimate a ground-range and height (x', z) position from 2 range measurements. The method which will be laid out is equivalent to the trilateration in the previous section, but applied to a 2D plane. The method used in this section is a variant of the one shown in [132].

5.3.1 Theory

The methods laid out in this section have a fundamental assumption that the 3D localisation problem can be approximated to be a set of 2D localisation problems. It relies upon another process to localise the target in azimuth, and then the ToA information from height offset receivers can be used to generate the elevation information. This is realised by treating a single angular bin in azimuth to be effectively a 2D ground-range height $(x'z)$ plane (2.3). This azimuth localisation could come from a number of different techniques, but here the focus is on scanning a highly directive beam pattern in azimuth. For reasons given in section 2.4, it is natural to consider a cylindrical polar coordinate system for this kind of localisation. First let us consider this treatment of a set of range-azimuth images as a set of $x'z$ planes. Consider a 2D imaging radar algorithm which localises a target in azimuth. This process generates a 2D polar image in $(R_{\mathrm{b_i}}, \theta)$. This algorithm could be mechanically scanning, beamsteering, beamforming, or many other 2D imaging processes. The azimuth resolution of such a process is $\delta\theta$, which is illustrated in Figure 5.9. A single target location, $\mathbf{p}$ is localised to be in the region $[\theta - \delta\theta, \theta + \delta\theta]$. As $x'^2 = x^2 + y^2 = x'^2 \sin^2\theta + x'^2 \cos^2\theta$, (5.9) shows that a change in θ has no bearing on the ground-range or bistatic range measurement because of the orthogonality of the cylindrical polar coordinate system.

$$R_{b_i} = \sqrt{x^2 + y^2 + (z - z_{\mathrm{Rx_i}})^2} + \sqrt{x^2 + y^2 + (z - z_{\mathrm{Tx_i}})^2} = \sqrt{x'^2 + (z - z_{\mathrm{Rx_i}})^2} + \sqrt{x'^2 + (z - z_{\mathrm{Tx_i}})^2} \quad (5.9)$$

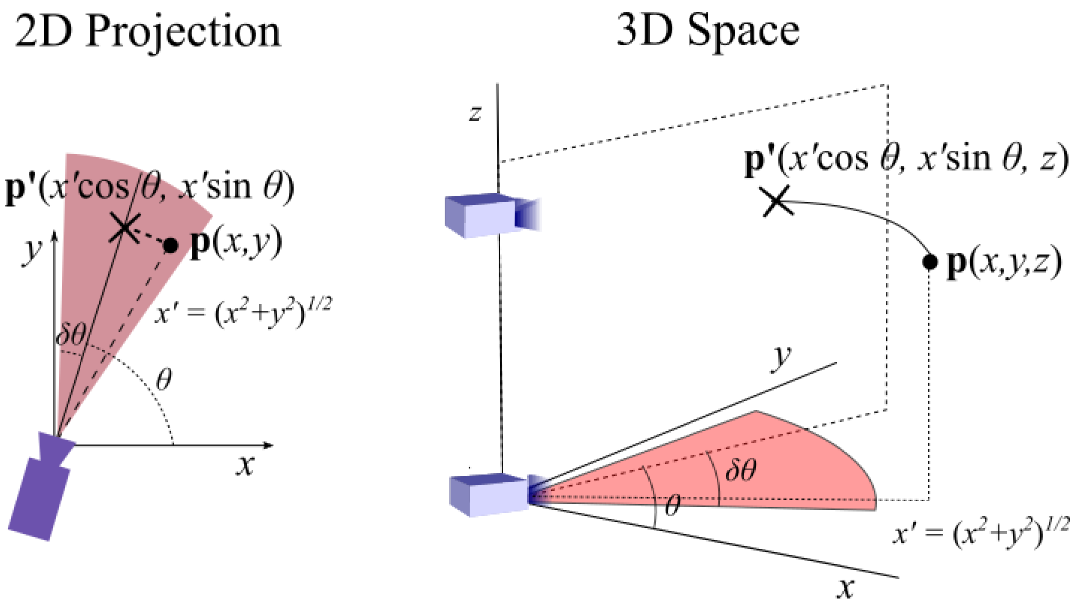

Fig. 5.9 Illustration of the narrow-beam assumption (localisation of points outside of $x'z$ plane). (left) 2D top-down view, and (right) 3D side view.

Therefore an offset in θ does not generate a difference in the ToA from height offset TxRx pairs. Similarly, θ is independent of z and z_{Rx}. If height offset receivers in the Tx-Rx stack measure multiple $(R_{\mathrm{b_i}}, \theta)$ image grids which are coaligned in azimuth, each image grid would place the target at the same azimuth position of θ, localising it to $[\theta - \delta\theta, \theta + \delta\theta]$. Therefore the extension of multiple aligned $(R_{\mathrm{b_i}}, \theta)$ image grids into a set of $x'z$ planes has no positive or negative effect on the systems ability to localise a target in azimuth. As was seen with trilateration in section 5.2, the only concern here should be ensuring that the system detects and localises a single scattering centre which can be found in multiple $(R_{\mathrm{b_i}}, \theta)$ image grids. This is expected to be less of an issue here due to smaller differences in aspect angle, but the range and azimuth resolution must be sufficient to pick out these multiple individual targets.

With this assumption in place, let us consider bilateration in the $x'z$ plane. As a multilateration problem, bilateration could be formulated similarly to how trilateration was laid out (5.3-5.6) [157, 158]. However, the problem is simplified here by reducing the number of dimensions. It is convenient to treat a pair of bistatic range equations as a set of simultaneous equations (5.9), and solve for x' and z. Here bilateration is considered for a 1Tx-2Rx system where $\mathbf{p}_{\mathrm{Tx}}$ is defined to be the origin, $\mathbf{p}_{\mathrm{Rx_1}} = (0, 0, z_{\mathrm{Rx_1}})$ and $\mathbf{p}_{\mathrm{Rx_2}} = (0, 0, z_{\mathrm{Rx_2}})$. The expression for x' and z from the two bistatic range values is given by (5.10) and (5.11) respectively.

$$x' = \pm \frac{\sqrt{-(R_{b_1}+z_{\mathrm{Rx}_1})(R_{b_2}+z_{\mathrm{Rx}_2})(R_{b_1}-z_{\mathrm{Rx}_1})(R_{b_2}-z_{\mathrm{Rx}_2})(R_{b_1}-R_{b_2}+z_{\mathrm{Rx}_1}-z_{\mathrm{Rx}_2})(R_{b_1}-R_{b_2}-z_{\mathrm{Rx}_1}+z_{\mathrm{Rx}_2})}}{2(R_{b_1}z_{\mathrm{Rx}_2}-R_{b_2}z_{\mathrm{Rx}_1})} \tag{5.10}$$

$$z = \frac{-R_{b_1}^2 R_{b_2} + R_{b_1} R_{b_2}^2 - R_{b_1} z_{\mathrm{Rx}_2}^2 + R_{b_2} z_{\mathrm{Rx}_1}^2}{2R_{b_1} z_{\mathrm{Rx}_2} - 2R_{b_2} z_{\mathrm{Rx}_1}} \tag{5.11}$$

This process is illustrated in Figure 5.10, where the ellipses in red and blue are the bistatic range ellipses of both Tx Rx pairs. Their point of intersection is the target position. As before, there is a sign ambiguity in x' due to the fact that the Tx and Rx units are not distributed along that axis [27].

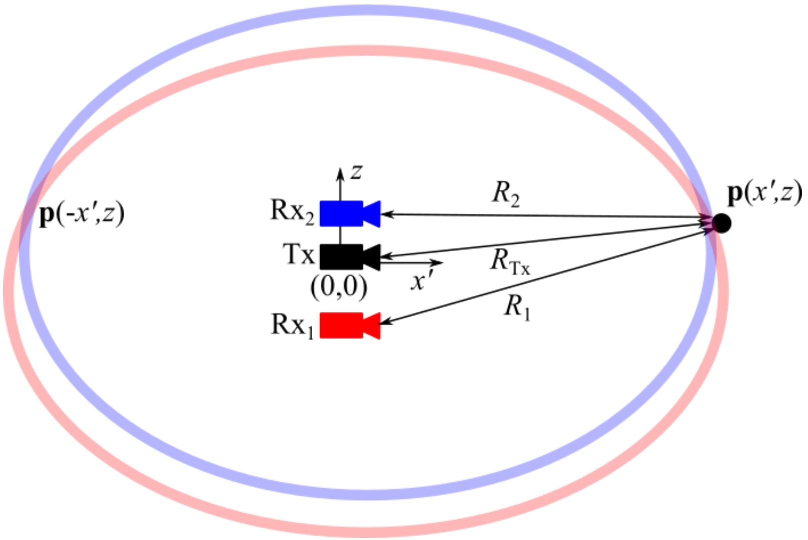

Fig. 5.10 Diagram of bilateration of a target using 1 Tx and 2 Rx in a 2D $x'z$ plane.

Here, an expression for the RMS error in x' and z is derived from (5.10) and (5.11) using (5.7). Again, because the Tx and Rx positions are known to the scale of mm, as the Tx and Rx heads lock together in position, it is assumed that the largest source of error is from range measurements. Here the typical geometry of an automotive scenario is used to provide a simple expression for the error term. Namely the facts that R_{b_i} is typically 3m or greater, $z_{\mathrm{Rx}_\mathrm{i}}$ is 0.3m or less, and the target lies directly ahead of the vehicle (within about 10° according to the beamwidth). Therefore $b_i = z_{\mathrm{Rx}_\mathrm{i}} - z_{\mathrm{Tx}}$, is at least an order of magnitude less than R_{b_i}, so for an integer $n \geq 2$; $b^n << R_b^n$. One may also assume that $|\varphi_{\mathrm{Tx}_\mathrm{i}}|$ lies in the region directly ahead of the vehicle, which has the lowest values of $|R_{b_1} - R_{b_2}|$. Therefore one can consider $R_{b_1} \approx R_{b_2} = R_{\text{Tx}}$.

The error in x', $\mathscr{D}x'$, is found directly through partial differentiation, and then applying both of the above assumptions. From this, the following expression is derived (5.12).

$$\mathscr{D}x' = \sqrt{\frac{z_{\text{Rx}_1}^2 + z_{\text{Rx}_2}^2}{(z_{\text{Rx}_1} - z_{\text{Rx}_2})^2}} R_{res} \tag{5.12}$$

The consequence of this is that for the region directly ahead of the Tx, the error in ground range is dependant on the range resolution, is independent of range, and is highly dependant on the separation of the receivers. Next let us consider the error in z. Similarly, $\mathscr{D}z$ is found directly through partial differentiation, and then applying both of the above assumptions. From this, the following expression is derived (5.13).

$$\mathscr{D}z = \frac{R_{\text{Tx}} R_{res}}{\sqrt{2}|z_{\text{Rx}_2} - z_{\text{Rx}_1}|} \tag{5.13}$$

The implications of this are that the height error should be highly dependant on the separation of the receivers, but also should increase radially from the transmitter (hence degrade reconstruction quality). In the following section, this theory will be tested at short range with a set of canonical targets.

5.3.2 Experimental Validation

The theory of bilateration was tested using a mechanically scanned setup in the TxRx stack setup in Figure 2.1. The setup is comprised of 1Tx-3Rx units, which can be seen as the black units in Figure 5.11. The positions and experimental parameters used here can be seen in Table 5.2. This is the radar system characterised in section 3, which will be used for the remainder of this thesis.

Due to the narrow azimuthal beamwidth, mechanically scanning this setup in azimuth at close range isolated a narrow region of space which generated the target azimuth position. The experiment was performed using a 2m long pipe which has six metal spheres attached to it. These spheres were placed at the heights given in Table 5.2 approximately equidistant along the pole. This was done so that the setup's ability to perform height finding through bilateration could be tested at short range for a set of different z

Parameter	Symbol	Value
Centre Frequency	f_c	290 GHz
Sweep Bandwidth	B	16 GHz
Azimuth Step Size	θ_s	0.5 °
Transmit power	$\mathrm{P}_{\mathrm{Tx_i}}$	0 dBm
Tx Height	z_{Tx}	1.19 m
Rx$_1$ Height	z_{Rx_1}	1.08 m
Rx$_2$ Height	z_{Rx_2}	1.23 m
Rx$_3$ Height	z_{Rx_3}	1.30 m
Range resolution	R_{res}	9.4 mm
Azimuthal Beamwidth	θ_{BW}	1.1° (3 dB)
Elevation Beamwidth	φ_{BW}	7.5° (3 dB)
Sphere Heights	z_j	0.75, 0.90, 1.11, 1.33, 1.50, 1.58 m
Sphere Ranges	x'_j	3.0 m to 4.0 m (measurement 1)
		3.5 m to 4.5 m (measurement 2)

Table 5.2 Experimental parameters of the bilateration setup.

positions. The plastic pipe on which the spheres were mounted was found to have a sufficiently low RCS to not be distinguishable from the noise floor.

A 2D scanned $(R_{\mathrm{b_i}}, \theta)$ image from Rx$_1$ can be seen in Figure 5.12, where the approximate coordinates of $x = R_{\mathrm{b_i}} \cos\theta$ and $y = R_{\mathrm{b_i}} \sin\theta$ are used to generate a 2D PPI image. The spheres can be seen lying in the line between (x, y) = (-1.0,3.5) m and (0.9,4.6) m. Each of these spheres appear like a point-like target in the image, except from the sphere at (-0.6, 3.8) m which appears to have a secondary scattering centre present. It is thought that this is from a small section which suspends the pole which is next to this sphere. The scattering centres at longer ranges in the image are from the walls and windows of the room.
Provided the falls on the far side of the room are range gated out, the system can isolate one point-like scattering centre (sphere) in a given angular position, i.e. $n_{tg} = 1$ for each bilateration problem. Peak fitting was a relatively simple process for this image, because each of the targets appears as a very small, bright, scattering centre above a flat noise floor. As can be seen in Figure 5.12, where the targets appear over 20 dB above the noise floor, and only occupy a few range cells in the radial direction. From similar images from each of the TxRx pairs, a bistatic range value was evaluated for the spheres at each azimuthal position from which the targets were visible. The result of bilateration can be seen in Figure 5.13a. The error bars around each point were evaluated from the RMS errors in x' (5.12) and z (5.13). The results of

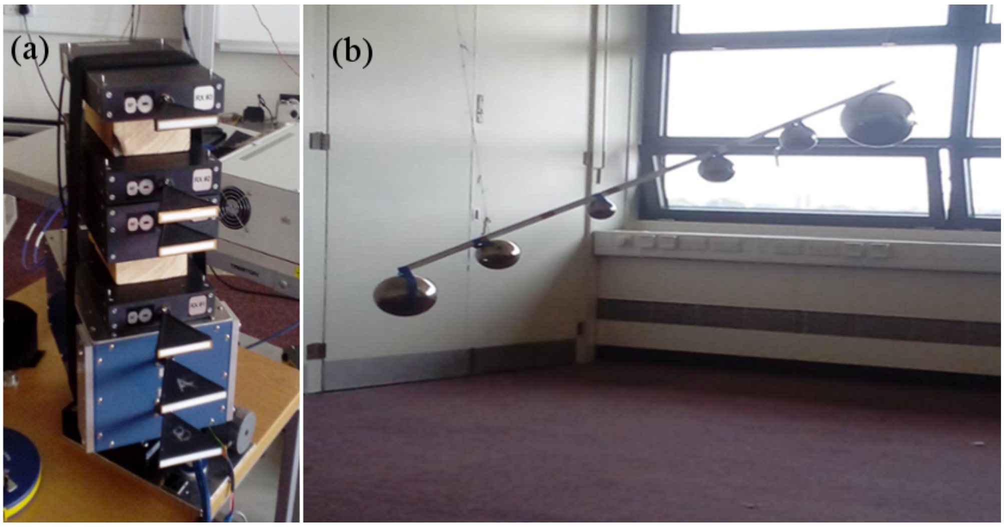

Fig. 5.11 Photos of the bilateration experiment. (a) 300GHz Tx and Rx units (black) mounted on a turntable. (b) Line of suspended spheres.

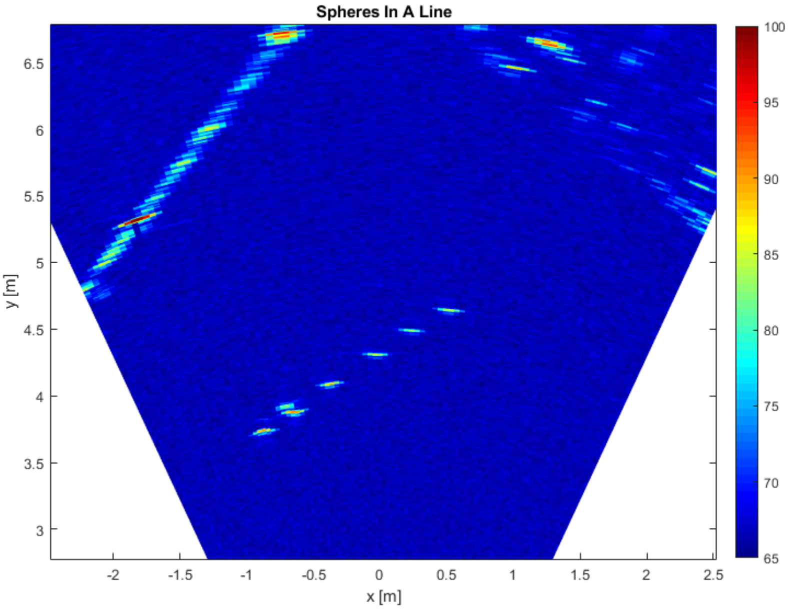

Fig. 5.12 2D radar scanned image of a a set of spheres in a line measured using Rx_1.

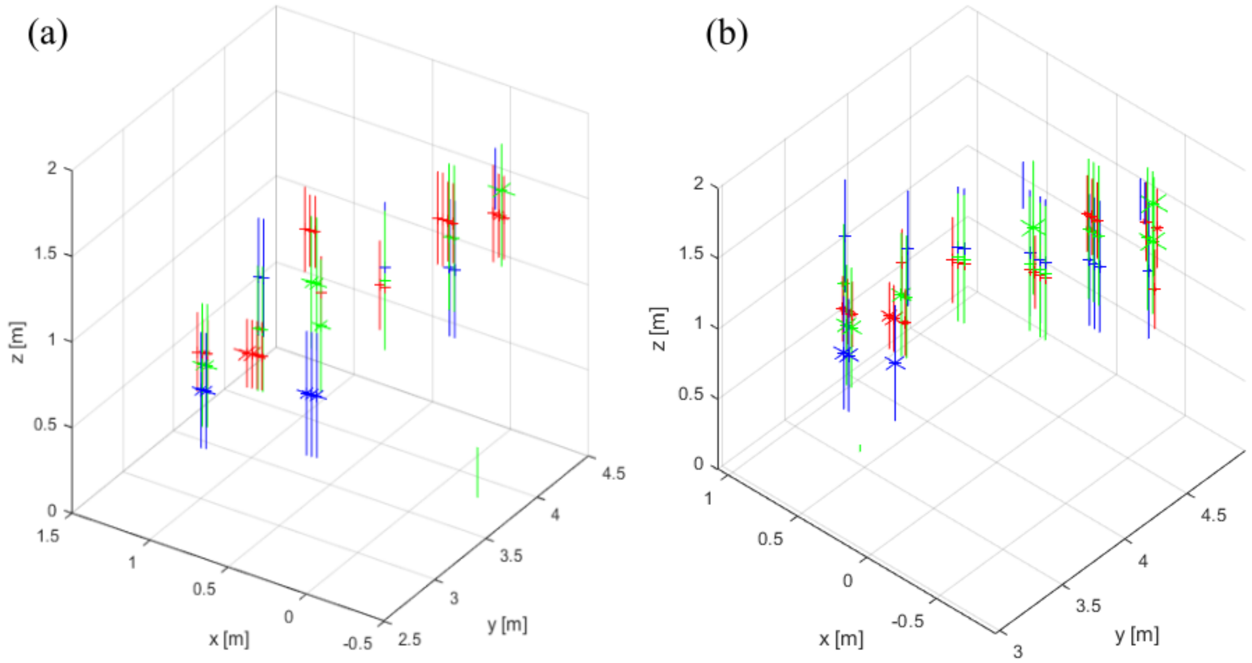

Fig. 5.13 3D positions of the spheres, Where the colours correspond to the pairs of Rx's used to bilaterate the target. (Red) Tx-Rx_1 and Tx-Rx_2, (green) Tx-Rx_1 and Tx-Rx_3, and (blue) Tx-Rx_2 and Tx-Rx_3. (a) Target ranges of 3.0 to 4.0 m, and (b) 3.5 to 4.5 m .

bilateration match the predicted heights of the spheres well, aside from the sphere which has the connector present (at x=0.5m), which complicated the selection of the bistatic range value of this sphere. This process was repeated for the same height positions of the spheres, but moved 0.5 m further from the TxRx stack. A very similar reconstruction was observed, as can be seen in Figure 5.13b.

Looking at the size of the error bars in each direction, the largest RMS error appears to be in the z direction, with an RMS error of ± 0.16 m (Rx_1,Rx_2), ± 0.11 m (Rx_1,Rx_3), ± 0.33 m (Rx_2,Rx_3). By contrast the RMS error in x and y was only ever a few cm. In this experiment, the Rx heads were locked in place with metal spacers of known lengths, so it was assumed that the position of the Tx and Rx heads are known exactly. In Figure 5.13b, the points reconstructed in z all appear to be within this RMS error of each other. In Figure 5.13a, there is a small departure from this in the third sphere from the left.

As the scan step in azimuth is smaller than the 3dB beamwidth of the antenna, one would predict that each of the targets can be seen in multiple azimuth bins, as in Figure 5.12. This can be seen in Figure 5.13 as points of the same colour appearing at a neighbouring position in the xy plane. For each of the Tx-Rx pairs, each sphere appears as a set of neighbouring points in the xy plane at the same position in z.

Although there is some variance between pairs of different Tx-Rx sites (shown as different colours), the results of each pair of Tx-Rx sites are very consistent from one azimuth position to another. This means that for a given target, not only is this procedure consistent, but it reconstructs the height of the target to be at the same position regardless if the true position of the sphere is outside of the azimuth cell being investigated. This appears to be true for each of the spheres.

5.4 Conclusion

The experiments detailed in this section confirm that multilateration is possible using a low-THz radar system; both in a constrained bilateration (height-finding) setup and as a triplet of Tx-Rx pairs selected from a large array of TxRx positions using a linear positioner. This process appears to give the finest resolution in the xy plane, with a coarser resolution in z which is highly dependant on the separation of the TxRx sites.

Major obstacles which need to be overcome with these kinds of multilateration algorithms are those of peak correspondence between multiple TxRx pairs, and different points of reflection. This is a feature which comes from using a distributed high resolution mm-wavelength radar, as very few targets can be thought of as point-like. Although the results of canonical targets such as spheres appear to work well for trilateration, it appears much more difficult for a mannequin. What is particularly reductionist is to assume that the many scattering centres present over the body of the mannequin can be reduced to two peaks. While it is relatively safe to assume that there is only one scattering centre present on a smooth metallic sphere for a single TxRx pair, this is far from true for a human. Although trilateration reconstructed two positions which correspond to the dominant scattering centres according to the literature, this is a far cry from a true 3D image of the mannequin. It is also particularly difficult in both cases to distinguish if the spread in values along each axis is from the resolution of the setup or from differences in the dominant scattering centre's position.

Reducing this 3D localisation problem to set of 2D localisation planes appears to be a sensible choice. For the same target distance, and very similar sweep bandwidths, the resolution delivered through bilateration with mechanical scanning was far better than that provided using the trilateration setup. It also appeared to be less effected by differences in the effects of physical surface scattering. What's more, the bilateration setup is far more practical. The setup is far more compact, and the positions of the Tx and Rx sites are already known relative to one another. For example, the case of using 6 nearby spheres is a complex correspondence problem, and using a purely trilateration based setup such as in section 5.2 requires many more TxRx sites than the 3 used in section 5.3. Indeed, although trilateration in this form does not require scanning and should in theory be much faster, the measurements would have to be time multiplexed which limits a lot of imaging scenarios practically. Bilateration using a mechanically scanned setup appears to excel at this kind of 3D reconstruction, even when correspondence issues such as the scattering centre near the sphere, are present. What's more, the resolution in xy was markedly improved by using this configuration. From here, the ToA imaging techniques used will use the scanned stack configuration, reconstructing a $x'z$ plane.

Chapter 6

Backprojection

This section details a method for converting a set of one dimensional range profiles (2.11) into a 3D image for the setup described in section 2. It demonstrates an alternative to multilateration which can produce an image in 3D space non-coherently, using time of arrival information as opposed to phase. As an imaging technique, the focus of this section is not to localise a point of reflection in 3D space, but instead to map out the entire space surrounding the vehicle. This is vital information for the system to determine both where is free space and where is occupied.
Some of the results of this section were previously published here [162, 163].

6.1 Background & Theory

A block diagram outlining the processing for backprojection is shown below in Figure 6.1. The diagram shows that the process of generating a range profile is much the same as in previous sections, but with an amplitude correction to a calibration target. This section will provide a background and theory of backprojection which will be used in this chapter, detailing how a 3D radar image can be generated from a set of range profiles.

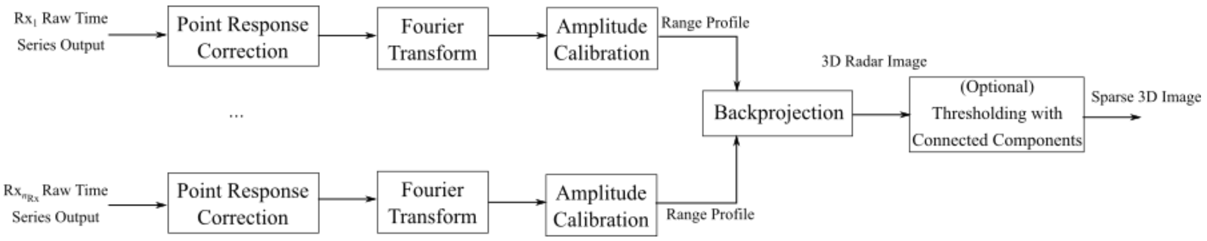

Fig. 6.1 Block diagram of backprojection.

First the general case (Figure 2.1a) is considered, and then the method is applied to the Tx-Rx stack specific case (Figure 2.1b) using the same data acquisition scheme as section 5.3. Introducing this topic requires a subtle change of notation. As in (2.6), the scene has n_{tg} point-like scattering centres present. The j^{th} scatterer has an RCS of σ_j at a position $\mathbf{p}_j$ where $j = 1,\ldots,n_{tg}$. This can be thought of as an RCS distribution in 3D space, $\sigma(x,y,z)$, where one can specify a particular (x,y,z) coordinate, $\mathbf{p}$, where $\sigma(\mathbf{p})$ is the RCS value of this distribution at $\mathbf{p}$. A scene which is free space aside from n_{tg} scattering centres is given by (6.1).

$$\sigma(\mathbf{p}) = \begin{cases} \sigma_j, \text{ for } \mathbf{p} \in \mathbf{p}_{j=1,\ldots,n_{tg}} \\ 0, \text{ otherwise} \end{cases} \tag{6.1}$$

This distribution is assumed to be real-valued in the $\mathbb{R}^3$ domain (x,y,z). Whereas in chapter 5, the focus was to estimate the value of $\mathbf{p}_j$ with the smallest possible uncertainty, the focus of the imaging algorithms is to reconstruct $\sigma(x,y,z)$ as accurately as possible. This means implicitly this process estimates $\mathbf{p}_j$ and σ_j, but also maps out the surroundings of the vehicle.

Backprojection in 3D has originally been developed for medical imaging and tomography, but since has been extensively used in Synthetic Aperture Radar (SAR) image formation [164]. Backprojection has been proven to be able to determine a distribution for both monostatic cases [165], and bistatic cases [166] from a set of one dimensional projections. For radars the set of range profiles are the projections (2.11), and the distribution of scattering coefficients $\sigma(x,y,z)$ is the distribution (6.1) [164].

As a note, the target returns in (2.6) can be defined in terms of (6.1). There is a return of (2.5) for every position, $\mathbf{p}$ and $\sigma(\mathbf{p})$ in (6.1), meaning the Rx has a return for every point in $\sigma(x,y,z)$. The descriptions of the target returns, and hence the range profile, are equivalent because there are only n_{tg} non-zero values of $\sigma(x,y,z)$. Thus the range profile can also be thought of as a sum of the returns from every value and position in $\sigma(x,y,z)$. As will be seen in the following discussion, the value of a cell in the range profile can be loosely thought of as defining the sum of these returns over the surface defined by a set value of $R_{\mathrm{b_i}}$, or more accurately, over the width of a range cell between $R_{\mathrm{b_i}}$ and $R_{\mathrm{b_i}} + R_{\mathrm{res}}$. In an abstract mathematical sense, it often makes more sense to define the problem in terms of continuous variables of Tx and Rx positions and bistatic range ($\mathbf{p}_{\mathrm{Tx}}$, $\mathbf{p}_{\mathrm{Rx}}$, and R_b), rather than talking about discrete sets of Tx-Rx sites and bistatic range ($\mathbf{p}_{\mathrm{Tx_i}}$, $\mathbf{p}_{\mathrm{Rx_i}}$, and R_{b_i}).

Although it is true that for the description in (6.1), the received signal will only have non-zero amplitude coming from n_{tg} points (2.18), there is almost guaranteed to be multiple degenerate distributions of $\sigma(x,y,z)$ which would yield the same set of range profiles (2.11) within the resolution and precision of a measurement setup. This will become more relevant in chapter 7. With all of this in mind, (6.2) reiterates the formulation of (2.10) used to define the range profile generated from a scene measurement from n_{tg} returns of the form defined in section 2 (2.6,2.11,2.18).

$$S_i(R_{b_i}) = \nu + \sum_{j=1}^{n_{tg}} S_i(R_{b_i}, \sigma_j, \mathbf{p}_j) = \nu + \int S_i(R_{b_i}, \sigma(\mathbf{p}), \mathbf{p}) \mathrm{d}\mathbf{p} \tag{6.2}$$

Let us consider why backprojection can offer a promising alternative to either trilateration in 3D for a general layout (Figure 2.1a and section 5.2), or bilateration in the (x', z) plane for the scanned Tx-Rx stack (Figure 2.1b and section 5.3). First, the system described in section 3 has a relatively low maximum range and a low SNR for the automotive radar conditions laid out in section 3.5. As will be seen, backprojection offers an additional integration gain to the signal amplitude compared to multilateration. This is because multilateration starts with detection on the range profile of each receiver independently before localising the target from using n_{Rx} range values. On the other hand, backprojection first integrates the signal of n_{Rx} receivers and then performs detection [8]. This means that backprojection is likely to have better SNR and hence a better target detection performance [4].

Secondly, the description of the scene given by $\sigma(x,y,z)$ is likely to be more useful than a set of target position estimates for many reasons. Autonomous cars must be as interested in mapping out free space, which are empty sections of road in which they can drive, as they are in obstructed space (containing targets) in which they cannot drive. Thus it is important to define regions where $\sigma(x,y,z) = 0$. Size, extent, and pose information is useful for collision avoidance, and characterising or identifying targets. Therefore it is important to define the entire region the target occupies, which means imaging regions where $\sigma(x,y,z) \neq 0$ as opposed to trying to perform a position estimate.

Next is the problem of correspondence which was highlighted in section 5.4. In short, how can the peaks in the range profile of one Rx be matched up to peaks in the range profile of another spatially separated Rx, and know with certainty that they come from the same scattering centre? This problem becomes particularly difficult for many peaks in close proximity to one another, as was seen with extended targets such as the mannequin in section 5.2.2. As will be shown, at no point in the Backprojection method does one need to find $\{R_{b_1,j},\ldots,R_{b_{n_{Rx}},j}\}$ (5.1), all known a priori to correspond to the jth scatterer, to localise the target as in (5.3).

The remainder of this section will go into the theory of backprojection, and how it can be applied to the setup in Figure 2.1.

Backprojection is often discussed in terms of a forwards and backwards transform. The forwards transform converts a spatial distribution into a set of measurable signals, and the backwards transform does the reverse of this. Many imaging problems can be described by a forward transform which converts the distribution into a set of surface or line integrals, known as projections. This is known as the Radon transform. The backwards transform converts these projections back into the original distribution, and is known as backprojection.

Let us now lay out the general case of bistatic backprojection for radar. $\mathscr{R}$ is defined to be the ellipsoidal Radon transform, such that $\mathscr{R}\sigma(x,y,z)$ is the ellipsoidal Radon transform of $\sigma(x,y,z)$. The ellipsoidal Radon transform converts a 3D distribution such as $\sigma(x,y,z)$, into its projections along each bistatic range ellipsoid (5.2). Geometrically the Radon transform is the surface integral of $\sigma(x,y,z)$ over the ellipsoid, $\mathbf{E}(R_b,\mathbf{p}_{\mathrm{Tx}},\mathbf{p}_{\mathrm{Rx}})$ (5.2). Instead of integrating over all $\mathbf{p}$ in (x,y,z) and using a δ function to select only $\mathbf{p} \in \mathbf{E}(R_b,\mathbf{p}_{\mathrm{Tx}},\mathbf{p}_{\mathrm{Rx}})$, one can replace the δ function in (6.3) with the surface integral. For our RCS distribution, $\mathscr{R}\sigma(x,y,z)$ is defined by a particular value of $\mathbf{p}_{\mathrm{Rx}}$, $\mathbf{p}_{\mathrm{Tx}}$, and R_b. The Radon transform occurs naturally by sampling a signal in range, rather than being a mathematical operation to perform.

$$\mathscr{R}\sigma(x,y,z) = \int_{-\infty}^{\infty}\int_{-\infty}^{\infty}\int_{-\infty}^{\infty}\sigma(x,y,z)\delta(\mathbf{p}\cdot\hat{\mathbf{n}} - R_b)d\mathbf{p} = \int_{\mathbf{E}(R_b,\mathbf{p}_{Tx},\mathbf{p}_{Rx})}\sigma(x,y,z)d\mathbf{E} \tag{6.3}$$

Where $\hat{\mathbf{n}}$ is the normal vector for the ellipsoid, $\mathbf{E}(R_b, \mathbf{p}_{\mathrm{Tx}}, \mathbf{p}_{\mathrm{Rx}})$ (6.4). The rightmost term of (6.4) specifically considers the one transmitter to n_{Rx} receivers case, with the Tx site as the origin.

$$\hat{\mathbf{n}} = \nabla\mathbf{E}(R_b, \mathbf{p}_{\mathrm{Tx}}, \mathbf{p}_{\mathrm{Rx}}) = \left[\frac{\partial\mathbf{E}}{\partial x}, \frac{\partial\mathbf{E}}{\partial y}, \frac{\partial\mathbf{E}}{\partial z}\right] = 4\left[\frac{(2x - x_{Rx_i})}{4R_{b_i}^2 + x_{Rx_i}^2}, \frac{(2y - y_{Rx_i})}{4R_{b_i}^2 + y_{Rx_i}^2}, \frac{(2z - z_{Rx_i})}{4R_{b_i}^2 + z_{Rx_i}^2}\right] \tag{6.4}$$

Let us now consider the inverse of this Radon transform. While the Radon transform converts a 3D distribution into its projections, its dual must do the opposite of this. The backprojection operator $\mathscr{R}^*$ is defined to be approximately the dual operator of $\mathscr{R}$. For the range profile in a specific configuration $S(R_{\mathrm{b}}, \mathbf{p}_{\mathrm{Tx}}, \mathbf{p}_{\mathrm{Rx}})$ (2.11), the backprojection operator is defined as follows (6.5).

$$\mathscr{R}^*|S(R_{\mathrm{b}}, \mathbf{p}_{\mathrm{Tx}}, \mathbf{p}_{\mathrm{Rx}})|^2 = \int_{-\infty}^{\infty}\int_{-\infty}^{\infty}|S(R_{\mathrm{b}}, \mathbf{p}_{\mathrm{Tx}}, \mathbf{p}_{\mathrm{Rx}})|^2 \mathrm{d}\mathbf{p}_{\mathrm{Tx}}\mathrm{d}\mathbf{p}_{\mathrm{Rx}} \tag{6.5}$$

Note that while (6.5) shows the mathematical sum of the signal from every Tx and Rx site, it is common to introduce a factor of $(n_{Tx}n_{rx})^{-2}$ to generate the mean of $\sigma(\mathbf{p})$. There are a number of implicit assumptions in using (6.3) and (6.5) in their raw form. Firstly, there is no way to collect and integrate an infinite number of range cells from infinite Tx-Rx positions. All backprojection imaging setups are merely an approximation of this, using as large a selection of useful $\mathbf{p}_{Tx}$ and $\mathbf{p}_{Rx}$ sites as possible. Second, a certain cell of a range profile does not perfectly represent the Radon transform, $\mathscr{R}\sigma(x,y,z)$ over $\mathbf{E}(R_b, \mathbf{p}_{Tx}, \mathbf{p}_{Rx})$. The radar has a characteristic point response in range, with a spread in R_b defined by the system parameters. Therefore the reconstruction of $\sigma(x,y,z)$ will not be a perfect reconstruction. All that is being considered at this stage is that the setup has a fine enough range resolution, R_{res}, to approximate $\mathscr{R}\sigma(x,y,z)$ and hence $\sigma(x,y,z)$ to a degree which is useful. The specific resolution of this is discussed later in this chapter, in section 6.3.

Next, there has to be some level of isotropy in $\sigma(x,y,z)$ with respect to $\mathbf{p}_{\mathrm{Tx}}$ and $\mathbf{p}_{\mathrm{Rx}}$. Like in multilateration, localisation only occurs in backprojection if $\sigma(\mathbf{p})$ is observable from a series of different $\mathbf{p}_{\mathrm{Tx}}$ and $\mathbf{p}_{\mathrm{Rx}}$

sites. As previously discussed in section 5, this by itself is a potential issue for any technique using a ToA approach in this way, and needs to be considered further later in this thesis. Next, this model does not consider the returns from positions in $\sigma(x,y,z)$ to interfere with each other. Therefore this model does not account for shadowing, or signals which have undergone multiple reflections. The signal must propagate from $\mathbf{p}_{\mathrm{Tx}}$ to some scattering centre $\mathbf{p}_j$ and then to a receiver at $\mathbf{p}_{\mathrm{Rx}}$.

Finally, the values of $\sigma(x,y,z)$ need to be detectable in $S(R_{\mathrm{b}},\mathbf{p}_{\mathrm{Tx}},\mathbf{p}_{\mathrm{Rx}})$. This does not necessarily require $P_{\mathrm{Rx}} >> P_N$ (2.18,2.12), but the estimate of σ from n_{Rx} measurements is subject to random variations from noise. Indeed, as the value of $\sigma(\mathbf{p})$ is estimated from the mean of n_{Rx} measurements of $\sigma(\mathbf{p},\mathbf{p}_{Tx_i},\mathbf{p}_{Rx_i})$ in AWGN, which is an unbiased estimator, in theory this technique will have a best possible performance set by the Cramer-Rao bound [167, 168]. This is slightly beyond the scope of this thesis, but what is considered here is that the signal must be distinguishable from any noise present (2.12). This puts constraints on both R_{b} due to losses due to propagation, and $\mathbf{p}_{\mathrm{Tx}}$ and $\mathbf{p}_{\mathrm{Rx}}$ in so much that $\mathbf{p}$ needs to be in the region illuminated by the Tx-Rx antenna patterns. Backprojecting a signal where $P_{\mathrm{Rx}} << P_N$ (2.18,2.12) is equivalent to just integrating more noise to the reconstruction, $\mathscr{R}\sigma(x,y,z)$.

The application of the backprojection operator will not generate a RCS distribution as a function of the angle of reflection. Instead it produces a matrix of scattered intensity coefficients which are averaged across the signals from each $\mathbf{p}_{\mathrm{Tx}}$ and $\mathbf{p}_{\mathrm{Rx}}$ position and are denoted as $\bar{\sigma}(x,y,z)$. This is equivalent to the normalized RCS of distributed clutter.

The formulation of (6.3) and (6.5) describes a system taking measurements at many $\mathbf{p}_{\mathrm{Tx}}$ and $\mathbf{p}_{\mathrm{Rx}}$ positions, but without changing orientation or scanning. Next, one must consider a mechanically scanned system, where a range-azimuth cell is taken at every $\mathbf{p}_{\mathrm{Tx}}$ and $\mathbf{p}_{\mathrm{Rx}}$ position. Applying (6.5) to the mechanically scanned TxRx stack described in section 2, (6.5) can be approximated as follows (6.6).

$$\mathscr{R}^*|S(R_{\mathrm{b}},\mathbf{p}_{\mathrm{Tx}},\mathbf{p}_{\mathrm{Rx}},\theta)|^2 = \int_0^{2\pi}\int_{-\infty}^{\infty}\int_{-\infty}^{\infty}|S(R_{\mathrm{b}},\mathbf{p}_{\mathrm{Tx}},\mathbf{p}_{\mathrm{Rx}},\theta)|^2 \mathrm{d}\mathbf{p}_{\mathrm{Tx}}\mathrm{d}\mathbf{p}_{\mathrm{Rx}}\mathrm{d}\theta_R \tag{6.6}$$

where θ_R is the orientation of the scanned radar stack. This is equivalent to integrating the returns from every Tx and Rx position every scan angle. There are some disadvantages of the formulation in equation (6.6). A non-isotropic azimuthal antenna pattern will not illuminate a target for $\theta_R \in [0,2\pi]$, and therefore the target will not appear in many of the azimuth positions and this process simply integrates extra noise. Most importantly, this method loses any localisation of the target which has been gained through scanning. Ultimately this is because the Radon Transform's purely ToA model of backprojection does not sufficiently describe radar phenomenology (6.3). Other than the range response, it ignores two major effects - antenna illumination and propagation loss. Let us consider the amplitude of a range cell to be the returns of each point in $\sigma(x,y,z)$ weighted by the path loss (2.16), beam pattern, and the limits defined by the range resolution (6.7). To express this succinctly, the 3D integration in Cartesian space in (6.3) has been replaced with the equivalent over the bistatic range shell (6.7), where the symbols carry their definitions from section 2.

$$|S(R_\mathrm{b},\mathbf{p}_\mathrm{Tx},\mathbf{p}_\mathrm{Rx},\theta_R)|^2 = \frac{n_c^2 P_T \lambda^2}{(4\pi)^3}\int_{R_b}^{R_b+R_{res}}\int_{\mathbf{E}(R_b,\mathbf{p}_{Tx},\mathbf{p}_{Rx})}\frac{G_{Tx}G_{Rx}\sigma(x,y,z)}{R_{Tx}^2 R_{Rx}^2}d\mathbf{E}dR_b \tag{6.7}$$

The full range profile (2.11,6.7) is sampled in units of R_{res}. For a range cell starting at R_b and ending at R_b+R_{res}, this is the volume integral of the region bound by $\mathbf{E}(R_b,\mathbf{p}_{Tx},\mathbf{p}_{Rx})$ and $\mathbf{E}(R_b+R_{res},\mathbf{p}_{Tx},\mathbf{p}_{Rx})$ (6.7). The total signal is a discrete set of weighted volume integrals across concentric ellipsoidal shells, corresponding to a specific bistatic range. To generate a continuous distribution of power to bistatic range, it is common practice to interpolate this set of volume integrals. This interpolation can take many forms, but only nearest neighbour interpolation is considered here. This interpolated form can be treated as a continuous set of iso-range ellipsoidal surface integrals (projections) of the form of S (6.5). Therefore one can apply the backprojection operator to generate a distribution of intensity of radar scattering coefficients in 3D space (x,y,z).

Looking at the form of (2.18), the next step to reconstruct $\sigma(x,y,z)$ would be to remove the effect of the antenna beam patterns (G_{Tx/Rx_i}) and general path loss (L) from the backprojected image. $L = L_a L_p L_i$ is used as a short hand for the path loss models from section 2.3.2, but specifically considering free space path loss here (2.16), as in (6.7). This is done in SAR imagery for a well-illuminated region by dividing by the path loss and beam patterns [164]. To perform this a weighted backprojection operator is used, $\tilde{\mathscr{R}}^*$, and the output image is taken to be approximately $\bar{\sigma}(x,y,z)$ (6.8).

$$\bar{\sigma}(x,y,z) = \tilde{\mathscr{R}}^* |S(R_b, \mathbf{p}_{\mathrm{Tx}}, \mathbf{p}_{\mathrm{Rx}}, \theta_R)|^2 = \int_0^{2\pi} \int_{-\infty}^{\infty} \int_{-\infty}^{\infty} |S(R_b, \mathbf{p}_{\mathrm{Tx}}, \mathbf{p}_{\mathrm{Rx}}, \theta_R)|^2 n_c^{-2} G_{Tx}^{-1} G_{Rx_i}^{-1} L^{-1} d\mathbf{p}_{\mathrm{Tx}} d\mathbf{p}_{\mathrm{Rx}} d\theta_R \tag{6.8}$$

The fact that (6.8) includes specific losses and gains for each Tx-Rx pair makes this method a general way of combining the returns of Rx modules with differing sensitivities and characteristics, as shown in section 3. What makes the method here ToA-based or "non-coherent" is that it is the signal envelope, $|S(R_b, \mathbf{p}_{\mathrm{Tx}}, \mathbf{p}_{\mathrm{Rx}}, \theta_R)|^2$ (6.8), being summed without using phase information. In this thesis $|S(R_b, \mathbf{p}_{\mathrm{Tx}}, \mathbf{p}_{\mathrm{Rx}}, \theta_R)|^2$ is evaluated through (nearest-neighbour) interpolation along the range axis, meaning this can be thought of as a ToA method. If another method of interpolation is used, it will be stated. The next section will take these theoretical methods and apply them to the setup used in section 5.3 to create an effective 3D imaging algorithm.

6.2 Implementation & Optimization

This section will consider how the general, purely ToA based backprojection from the previous section can be applied to the system from sections 3 and 5.3. Specifically, it considers the Tx-Rx stack in Figure 2.1b, which is being scanned as in Figure 5.9. What is so challenging about implementing (6.8) in this configuration from an engineering perspective is how to reconstruct a 3D image of the scene around a vehicle using so few Tx-Rx sites, and how to usefully use the narrow beam pattern. This is a far cry from a system with an infinite continuous variable of receiver position and scan angle, and so this infinite integral is approximated using a finite set of receiver and scan positions.

As before, the stack is comprised of n_{Tx} transmitters, and n_{Rx} receivers, which are scanned over n_θ azimuth positions. One can specify a set of $n_{\mathrm{TxRx}} = n_{\mathrm{Tx}} n_{\mathrm{Rx}}$ transmitter-receiver pairs. Looking at (2.18) and (6.7), to recover σ one has to remove the antenna gains and path loss. The weighted backprojection process (6.8) is approximated as follows (6.9). This is effectively a radiometric calibration process, which is an important step for Rx modules with different gains and losses.

$$\bar{\sigma}(\mathbf{p}) \approx n_{\text{TxRx}}^{-2} n_{\theta}^{-2} \sum_{i=1}^{n_{\text{TxRx}}} \sum_{k=1}^{n_{\theta}} |S_{i,k}(R_{b_i}(\mathbf{p}), \theta_{R_k})|^2 n_c^{-2} G_{Tx_{i,k}}^{-1} G_{Rx_{i,k}}^{-1} L_{i,k}^{-1} \tag{6.9}$$

Where the subscripts i,k refer to a measurement performed using the i^{th} Tx-Rx pair, where $i = 1,\ldots,n_{\text{TxRx}}$, and at the k^{th} azimuthal position, where $k = 1,\ldots,n_{\theta}$. In this discrete form, there is an integration over n_{TxRx} Tx-Rx pairs and n_{θ} azimuth positions, so it is assumed that there is a gain in power which is approximately $n_{\text{TxRx}}^2 n_{\theta}^2$ [148]. By contrast, if each Rx has the same G_i, L_i and noise figure, the noise is expected to have a gain in power of $n_{\text{TxRx}} n_{\theta}$, theoretically resulting in a gain in SNR of $n_{\text{TxRx}} n_{\theta}$ if the target has similar returns for each Rx and azimuth position. To recover σ, this is compensated for with a factor of $n_{\text{TxRx}}^{-2} n_{\theta}^{-2}$. Since y (2.1) is the bisector of the scan, $\theta_{R_k} = \frac{\pi}{2} + (k - \frac{n_s}{2})\theta_s$.

$G_{Tx_{i,k}}$ and $G_{Rx_{i,k}}$ are both functions of (θ,φ) (see Figures 3.7 and 3.8). Although theoretically correct for a well illuminated scene, weighting by $G^{-1}(\theta,\varphi)$ may not be the best choice, particularly for a scene with large variation in antenna illumination. The main problem arises in regions corresponding to a null ($G \rightarrow 0$) in the antenna pattern or regions far into the angular sidelobes. To generate a non-zero value of P_{Rx} (2.18) at these positions, $\sigma(x,y,z)$ must be very large, or theoretically infinite. As such, weighting by G^{-1} generates peaks in $\bar{\sigma}(\mathbf{p})$ which tend to infinity (6.9). More importantly, weighting by G^{-1} will allocate the highest $\bar{\sigma}(\mathbf{p})$ values to regions where the backscattered signal is almost certainly not coming from. At the same time, it would make little sense to integrate over all n_{θ} azimuth positions and lose the localisation from scanning (6.6).

Much like bilateration in section 5.3, the 3D imaging problem can be approximated to be a set of n_{θ} (x',z) planes. As can be seen in section 2.4, it is too computationally intensive to perform the processing required for (6.9) on a 3D Cartesian grid with increments less than R_{res} in x, y, and z, for an imaging scene with $x' \in [0,30]$ m or greater (approximately a 4000x4000x4000 point grid). However, with the setup in section 2, the 2D polar image of each receiver is already sampled in azimuth grid size θ_s. As in bilateration, each of the Tx-Rx pairs are positioned at $x = 0$, $y = 0$, and are coaligned in azimuth, meaning bilateration and backprojection will not generate additional azimuth information unless the setup is moved in the xy plane. Because of this, for a given azimuth cell, the 3D imaging volume is reduced from (x,y,z) into a 2D slice in the (x',z) plane defined by a set value of $\theta = \theta_R$. This is analogous to setting the beam patterns to (6.10), and equivalently for $G_{Rx_{i,k}}(\varphi,\theta)$.

$$G_{Tx_{i,k}}(\varphi,\theta) = G_{Tx_i}(\varphi)\delta(\theta_{R_k} - \theta) \tag{6.10}$$

In practice, most backprojection algorithms interpolate in both range and azimuth to map a measured range-azimuth image onto an image grid [8]. Here, (6.10) is equivalent to a set of n_θ (x',z) planes centred in the middle of each azimuth bin. Since the n_θ positions of (6.11) are the same n_θ positions in the scanned image, no interpolation in azimuth is necessary. This decreases the computational load of this process for three reasons. The number of grid points in the 3D imaging volume is greatly reduced by using cylindrical polar coordinates, there is no longer a need to interpolate in azimuth, and the second summation in (6.9) is removed (6.11). This effect is greatest at longer ranges where the cross-range extent of a range-azimuth cell increases (Figure 2.10).

Another effect to consider is the effect of the beam pattern in elevation. Much like the previous discussion about azimuthal beam patterns, weighting by G^{-1} will overcompensate for nulls in the beam pattern and allocate the highest highest values of $\sigma(x',\theta,z)$. These large variations in G^{-1} may disrupt the localisation from (6.9). (6.11) is the concise form of backprojection, where G is taken to be a constant value in elevation.

$$\bar{\sigma}(x',\theta,z) \approx n_{\mathrm{TxRx}}^{-2} \sum_{i=1}^{n_{\mathrm{TxRx}}} |S_i(R_b(x',z,b_i),b_i,\theta)|^2 n_c^{-2} G_{Tx_i}^{-1} G_{Rx_i}^{-1} L_i^{-1} \tag{6.11}$$

The factor of n_θ^{-2} has been removed, as there is no integration across the azimuth positions. The power compensation now accounts for an integration gain of approximately n_{TxRx}^2 in the signal power, resulting in a gain of n_{TxRx} in SNR. For the Tx-Rx stack in section 5.3, there is one major difference in the reconstruction performed here with 1 Tx - many Rx compared to conventional backprojection. $\sigma(\mathbf{p})$ of a target is dependant on the aspect angle it makes with the radar, and the reconstruction from backprojection creates an image from this distribution at a set of radar positions. (6.5) describes an RCS distribution averaged over every possible separate $\mathbf{p}_{\mathrm{Tx}}$ and $\mathbf{p}_{\mathrm{Rx}}$ site, so it is the average of the bistatic RCS of every point in $\sigma(x,y,z)$ from every Tx and Rx aspect angle. (6.5) with $\mathbf{p}_{\mathrm{Tx}} = \mathbf{p}_{\mathrm{Rx}}$ is similarly the monostatic RCS averaged over all aspect angles. For this setup, one can only measure the bistatic RCS from a single Tx site to many Rx sites. Hence what is reconstructed is the mean bistatic RCS of every point in $\sigma(x,y,z)$ averaged over a single angle of incidence and many angles of reflection. This highlights one potential weakness of this technique, and why there is a need for diffuse reflection from a target. If the transmitted power from this one angle of incidence is all scattered away from the Tx-Rx stack, there is no way of reconstructing $\sigma(x,y,z)$ for this target.

In the remainder of this section the margins of applicability of this technique are determined based on the physical constraints of an automotive radar. Three cases where this method breaks down are considered; when the point response in x' and z is too wide, when the narrow angle approximation is no longer valid, and when a target is no longer picked up by multiple receivers.

Let us first investigate what the ideal geometrical setup for the system is, and then what is physically realisable for our system using the layout described in section 2.

The Tx-Rx sites for an automotive radar must be distributed over the body of the vehicle. A Land Rover Discovery, for instance, occupies a height of $z \in [0.2, 2]$ which is used here. Our system has three receiver units. The region the antennas illuminate is taken to be narrow in azimuth. The values of x' of the mapped scene are between 3 and 100 m. If this system is to be mechanically scanned in azimuth, by far the most easily realisable configuration is the TxRx stack described in section 2.

Whether one considers bilateration or backprojection, the region a target is localised to by a range cell is the region bound by the ellipsoidal shell (5.2) between R_b and $R_b + R_{res}$. As such, the $x'z$ error considerations in this section are based on the same geometry as bilateration, while a discussion using the range response of the radar system is given in the next section. Let us consider the assumption that one can discretize the 3D space into $x'z$ slices. Each of the n_{Rx} range-azimuth (R_{b_i}, θ) images sample the space at the same n_θ azimuth positions, with the same beamwidth and scan step θ_s. Each Tx and Rx unit has a narrow azimuth antenna pattern that only illuminates a narrow region around θ_R. It is highly likely that a real target is not at the centre of the beam, and lies at a small distance either side of the $\theta = \theta_R$ plane. The target's azimuth position could lie anywhere between $[\theta_R - \theta_s, \theta_R + \theta_s]$. Due to the definition of x' (2.3) and the rotational symmetry and orthogonality of cylindrical polar coordinates (2.1), R_{b_i} is independent of θ. Examining the 2D $x'z$ planes, the $x'z$ intersection of $\mathbf{E}(R_{b_i},\mathbf{p}_{\mathrm{Rx}_i})$ with the plane $\theta = \theta_R$, appears the same as the $x'z$ intersection with $\theta = \theta_R \pm \theta_s$. Therefore the $x'z$ region bounded by $\mathbf{E}(R_{b_1},\mathbf{p}_{\mathrm{Rx}_1})$, $\mathbf{E}(R_{b_1}+R_{res},\mathbf{p}_{\mathrm{Rx}_1})$, $\mathbf{E}(R_{b_2},\mathbf{p}_{\mathrm{Rx}_2})$ and $\mathbf{E}(R_{b_2}+R_{res},\mathbf{p}_{\mathrm{Rx}_2})$ is the same in each case, and this assumption has no bearing on the estimate of (x',z).

No azimuth information is lost or gained through this assumption, as long as each of the receivers are picking up a signal from the same point. Therefore the narrow-angle approximation breaks down when the azimuth resolution cannot resolve two nearby targets in azimuth (which is the same as the 2D polar case), and not when a target lies outside of the $\theta = \theta_R$ plane. Unlike the 2D polar case, where the two targets may not be resolvable for a single Rx in the (R_{b_i},θ) image, with multiple Rx pairs the targets may be resolvable in z.

The assumption from section 5 that multiple receivers are receiving a signal from the same point, $\mathbf{p}$, is still true. $\mathbf{p}$ must be illuminated by each Tx and Rx antenna, and the RCS $\sigma(\mathbf{p})$ must be similar for the aspect angle of each Rx unit. This was touched upon in section 2.3.3. Backprojection does not necessarily require reflector coherence, where the reflected wave components are are mutually coherent and combine to yield a larger effective power than diffuse surface scattering [140]. However, the angle over which the scatterer is coherent is a useful metric of the range of angles over which the target response will be similar. In reality, the backscattered radiation will be a combination of diffuse and coherent scattering, and the angle may be larger than this due to the more uniform nature of diffuse scattering. In both cases, scattering mechanisms put a limiting maximum angle between the Tx and Rx (as in Figure 2.1) which cannot be exceeded (6.12). For the antenna illumination, the target must be within the main lobe beamwidth, φ_{BW} (6.12), and for scatterer coherence the difference in Rx positions must be within the scatterer coherence angle, φ_{SC} (6.12). This is illustrated in Figure 6.2.

$$|\varphi_{\mathrm{Tx}} - \varphi_{\mathrm{Rx}}| \leq \varphi_{SC} \quad |\varphi_{\mathrm{Tx}}| \leq \varphi_{BW} \quad |\varphi_{\mathrm{Rx}}| \leq \varphi_{BW} \tag{6.12}$$

The greatest variation in elevation occurs at short range (2.1), where this effect is most significant. φ_{BW} is a predictable quantity which can be measured from the antenna patterns, however it is more difficult

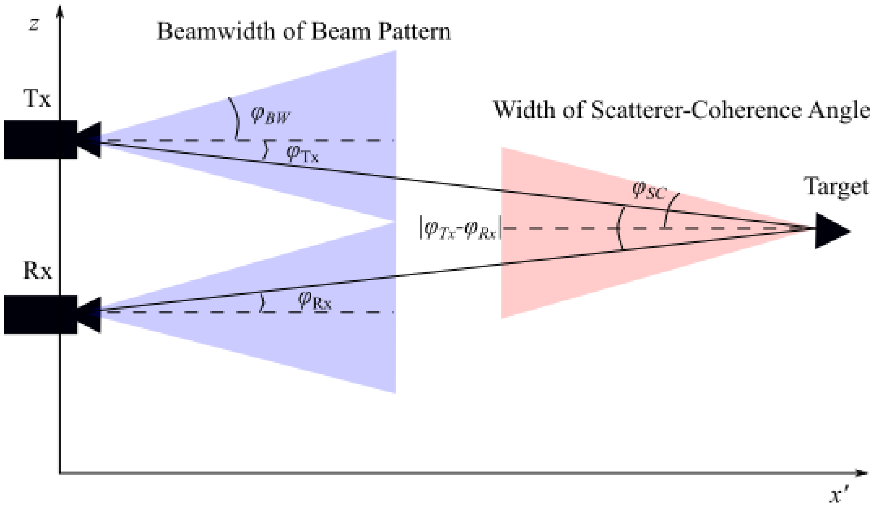

Fig. 6.2 Illustration of the elevation constraints for scatterer persistance.

to predict the persistence of a scattering centre between multiple receivers. φ_{SC} can vary from 5° for manmade objects at lower frequencies [169] up to 30° for a trihedral corner reflector [170].

With all of these considerations in mind, the general rule is as follows. At shorter ranges the receiver baselines must be restricted to maintain target illumination and similar target RCS values (6.12), whereas at longer ranges a larger baseline will be used to minimise the point response width in both x' (5.12) and z (5.13).

Before going into a more detailed look into the resolution and error of backprojection, let us use the RMSE from bilateration as a starting point of where this method might break down. Considering the short range case of $R_{\mathrm{Tx}} = 3$ m, $\varphi_{SC} \leq 5°$. The Rx units can be distributed in $z \in [z_{\mathrm{Tx}} - 0.3, z_{\mathrm{Tx}} + 0.3]$. For $n_{\mathrm{Rx}} = 3$, Rx heights of $b_1 = z_{\mathrm{Tx}} - 0.3$ m, $b_2 = z_{\mathrm{Tx}}$, and $b_3 = z_{\mathrm{Tx}} + 0.3$ m are considered. While this is a relatively small separation, so it has a larger error in both x' (5.12) and z (5.13), it is far more likely that a scattering centre will persist between each Rx image. Using these constraints with a range resolution of 8 mm, $\mathscr{D}x'$ = 6 mm for Rx_1 and Rx_3, and $\mathscr{D}x'$ = 8 mm for the other Rx pairs (5.12). In z this is $0.01R_{\mathrm{Tx}}$ and $0.02R_{\mathrm{Tx}}$ respectively (5.13), which is equivalent to a 1° and 2° elevation RMSE respectively.

For longer range where the degradation of RMSE is more important, one can use the full height extent of the vehicle $z \in [0.2, 2]$ m. Here $b_1 = 0.2$ m, $b_2 = 1.1$ m and $b_3 = 2.0$ m. With these constraints, $\mathscr{D}x'$ = 6 mm for Rx_1 and Rx_3, (5.12), and $\mathscr{D}x'$ = 8mm for the other Rx pairs. In height this is $0.003R_{\mathrm{Tx}}$ and $0.006R_{\mathrm{Tx}}$ respectively (5.13), which is equivalent to a 0.3° and 0.7° elevation RMSE respectively.

Backprojection is very flexible to system geometry, and additional performance may be available when distributing Tx-Rx pairs over the full body of the vehicle, but this section only considers the mechanically scanned vertically aligned stack.

This estimate only takes into account the region in x' and z bound by two range cells, and it does not take into account the range response of the system. In the following section, a resolution and error analysis will be performed using the radar system.

6.3 Resolution & Error

This section seeks to experimentally derive an expression for the error in x' and z for the image generated through backprojection (6.11). This will be compared with the error calculated by equations (5.12) and (5.13), and then it will be verified that this setup can resolve two targets which are near each other and only separated in z.

As the error in θ is a known quantity defined by mechanically scanning the antenna beam patterns, (which was investigated in section 4), it is not measured here. Instead the experiments in this section only consider the $x'z$ plane defined by $\theta_R = \theta(\mathbf{p}_{tgt})$, where $\mathbf{p}_{tgt}$ is the position of a canonical target, and $\theta(\mathbf{p}_{tgt})$ is target's azimuth position. This will be investigated using two common canonical radar targets - a sphere and a corner reflector.

Parameter	Value
Centre Frequency	290 GHz
Sweep Bandwidth	16 GHz
$\mathrm{P}_{\mathrm{Tx_i}}$	0 dBm
z_{Tx}	0 m (origin)
$z_{\mathrm{Rx_1}}$	0.06 m
$z_{\mathrm{Rx_2}}$	-0.36 m
$z_{\mathrm{Rx_3}}$	0.35 m
R_{res}	9.4 mm
Azimuthal Beamwidth	1.1° (3 dB)
Elevation Beamwidth	7.5° (3 dB)
Target Height (z)	z_{Tx}
x'_{Target}	2.8 m (corner)
	3.6 m (sphere)
x'_{add}	2.0 m
Target Range (x')	2.8 m to 4.8 m (corner)
	3.6 m to 5.6 m (sphere)

Table 6.1 Experimental parameters of the setup used to measure the resolution of backprojection in the ground-range height plane.

The setup is very similar to the one used in section 5.3. The exact parameters are given in Table 6.1, and the setup is illustrated in Figure 6.3, and corresponds to a typical configuration used - one monostatic Rx, and an Rx at both +0.35m and -0.35m from the Tx site. This setup is placed on a linear positioner as shown in Figure 6.3, with the target at a distance x'_{Target} =2.8 m which is directly ahead of the radar stack, such that $\theta_R = \theta(\mathbf{p}_{tgt}) = 0$. The linear positioner, which is 2.0 m long is used to introduce an additional distance x'_{add} to the target range, such that the target is a distance $x' \in [2.8, 4.8]$ m from the Tx-Rx stack. This will be used to investigate the point response of the system as a function of range in a controlled way.

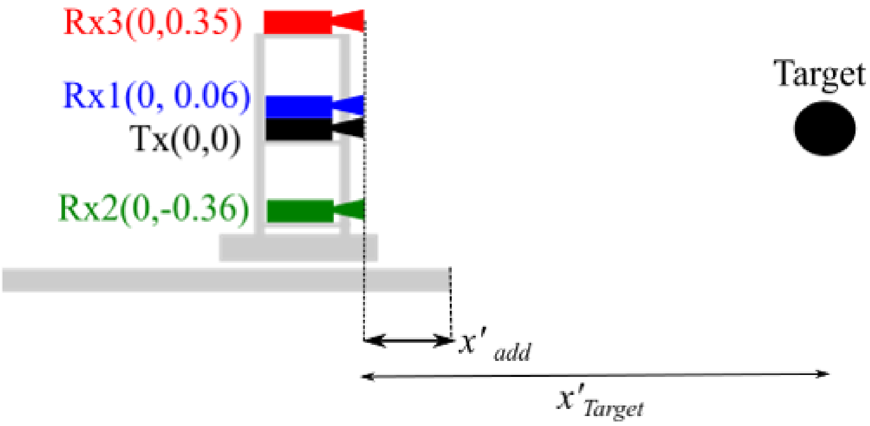

Fig. 6.3 Diagram of the experimental setup used to measure the resolution of backprojection in the ground-range height plane.

As before, the raw point response of the signal requires correction to use the quasi-bistatic setup. Therefore the correction from (3.2) is used. The goal of this section is to investigate the point response, and not to try and estimate the RCS (σ) of a sphere or corner reflector. Therefore no attempt is made here to convert from the raw amplitude, A_{IF} (2.7) after the point response correction (3.2), to the received amplitude A_{Rx} (2.18). Similarly, no attempt has been made to reweight by a constant antenna gain G or constants in the free space path loss (2.16) when the signal undergoes backprojection (6.11). The peak target amplitude found by $\text{Rx}_{1,2,3}$ have been set to the same maximum value to compensate for any differences in sensitivity between Rx units. All of these factors are constants of proportionality, which will effect the amplitude, but not the shape or spread of the point response.

In this section the reconstruction from backprojection $\bar{\sigma}(x', \theta_R = 0, z)$ (6.11) is considered for all possible cases of multiple Tx-Rx pairs. The system has 1 Tx and 3 Rx. Therefore there are 3 pairings with $n_{TxRx} = 2$, which are Rx_1 and Rx_2, Rx_1 and Rx_3, and Rx_2 and Rx_3. There is also the case of $n_{TxRx} = 3$, such that all 3 pairs are used; Rx_1, Rx_2, and Rx_3. All 4 of these cases are considered here. The reconstruction of a sphere which has been generated using all 3 Rx, and Rx_2 and Rx_3 can be seen in Figure 6.4. Two example (x', z) target positions have been shown here; (3.6,0.0) m and (5.5, 0.0)m. It is clear that there is an increase in the z extent of the sphere in the image at $x' = 5.5$ m compared with that at 3.6 m, which agrees with the form of (5.13). There is a much smaller difference in the x' extent of the sphere, though it is perhaps incorrect to think about the RMS error in x' and z as two separate quantities. The system can localise a target to some angle in elevation, which by definition is a function of x' and z simultaneously. However, as the system is dealing with a target at $z = z_{Tx}$, there is only a small variation in φ either side of z_{Tx}, and so the approximation that the elevation extent corresponds to an extent in z is a reasonably sound one. Using the linear positioner to generate a set of different target x' positions, the system was able to reconstruct the position and extent of the target as a function of target range. Let us now define the extent in z. The maximum in $\bar{\sigma}(x', \theta_R = 0, z)$ is σ_{max} and in these images is found at a height z_{Tx}. One can define z_1 to be the minimum z position where one can find $(\sigma_{max} - 6)$ dB, and z_2 as the maximum z position where one can find $(\sigma_{max} - 6)$ dB. The extent is $|z_1 - z_2|$, which for a power decrease of 6dB (0.25 in linear units)

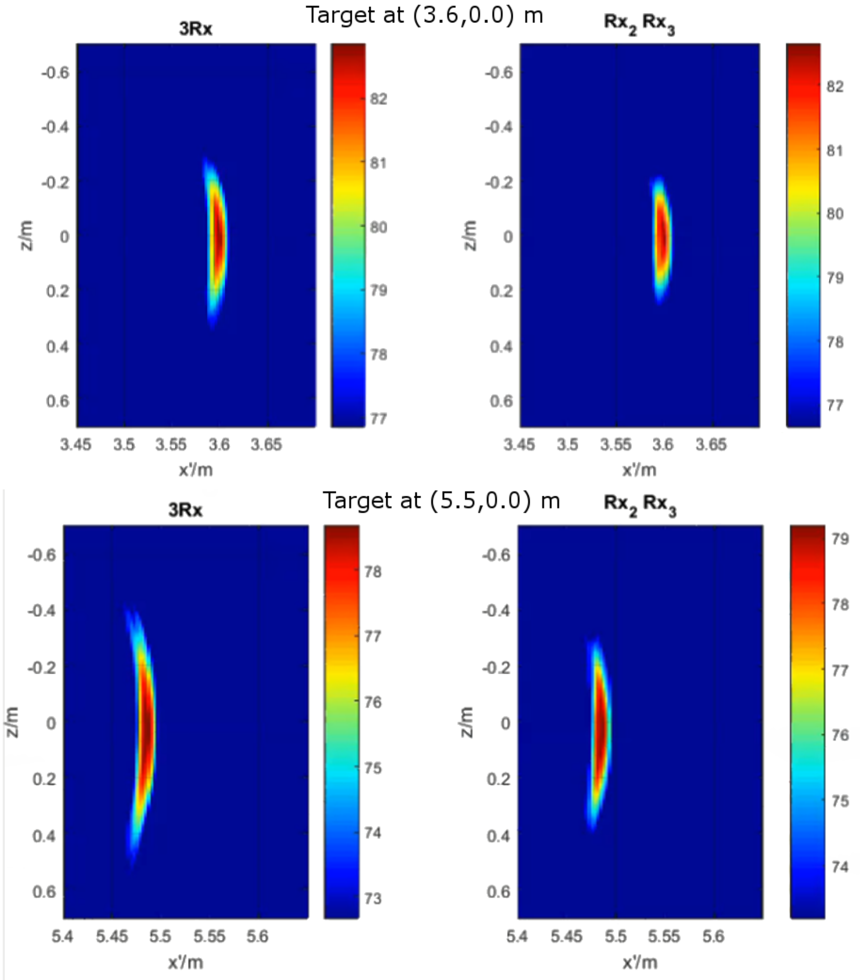

Fig. 6.4 $x'z$ reconstruction of a sphere at different target ranges using backprojection. (6.11)

of $\bar{\sigma}(x', \theta_R = 0, z)$ in z. Figures 6.5 and 6.6 show the 6dB height extent ($|z_1 - z_2|$) as a function of target range (x').

Alongside this, a simple simulation using these Tx, Rx, and target positions with an ideal sinc function (2.11) with unit amplitude and no noise present was performed, which was then backprojected (6.11). As predicted from the RMS z error (5.13), the target's extent in z increased radially, as can be seen by the linear distribution in Figures 6.5 and 6.6.

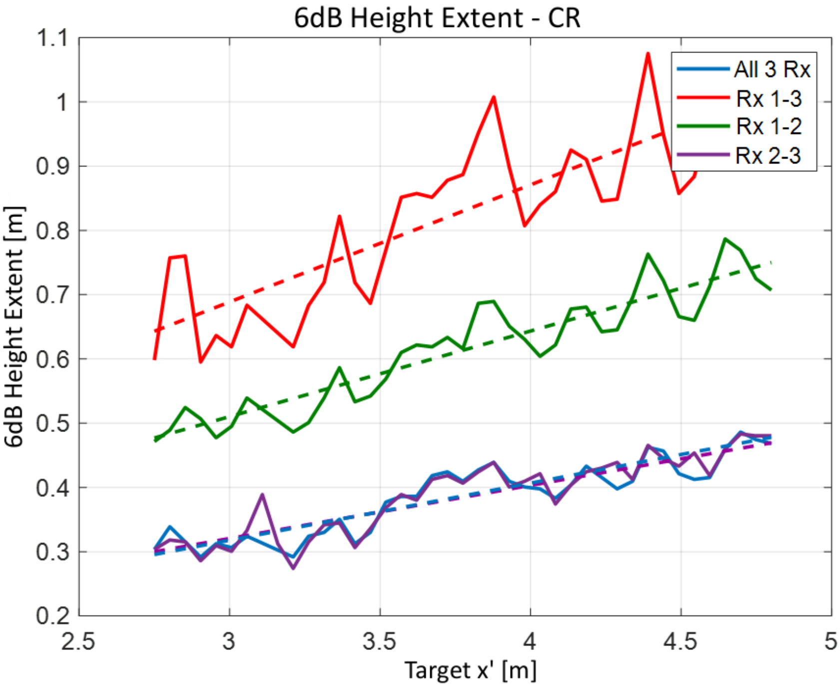

Fig. 6.5 6dB height extent of the corner reflector for different Rx groups and target ranges.

The gradients of the 6dB height extents of these distributions are shown in Table 6.2. This table includes $\mathscr{D}z$, the simulation, and the results of measurement. The 6dB spread of a target in height is an order of magnitude (just over 10x) larger than the RMS error predicted by (5.13). This is because $\mathscr{D}z$ is based on the region of space defined by a single range cell in both range profiles overlapping, and even a point-target does not appear as a single range cell. Typically even a single point will bridge into two range cells as predicted in section 5.1. Although they are slightly larger, the gradients measured in practice for the sphere and corner reflector are only $\leq 20\%$ larger than those predicted in simulations without noise and for a truly point-like target.

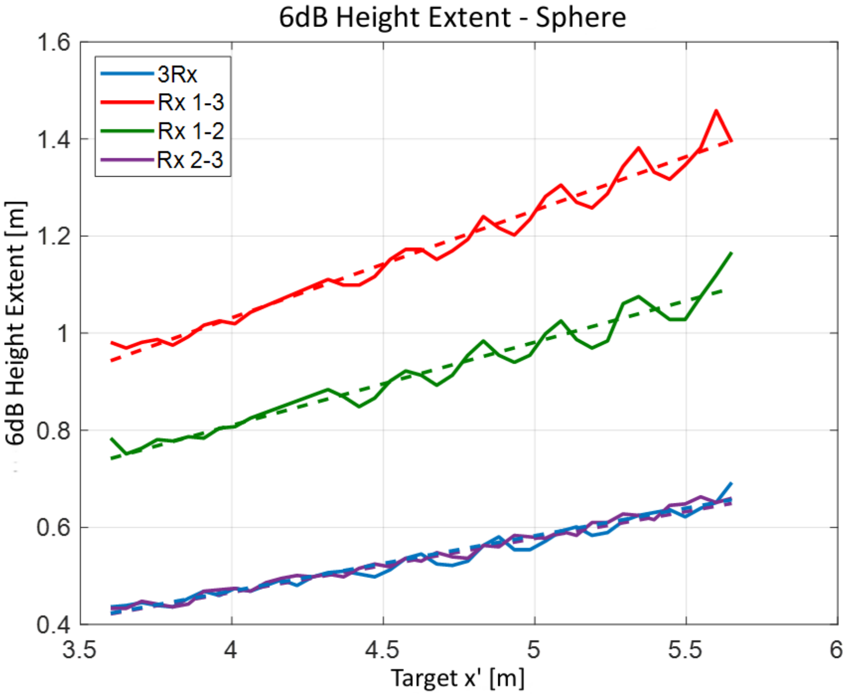

Fig. 6.6 6dB height extent of the sphere for different Rx groups and target ranges.

Rx	$\frac{\mathscr{D}z}{R_{\text{Tx}}}$	Simulation	Sphere	Corner
All 3	0.008	0.08	0.11	0.10
Rx$_2$, Rx$_3$	0.008	0.08	0.11	0.10
Rx$_1$, Rx$_2$	0.013	0.14	0.17	0.15
Rx$_1$, Rx$_3$	0.018	0.20	0.22	0.21

Table 6.2 6dB height extent per target range of canonical targets, generated using backprojection.

With the z extent in place, the remainder of this section will examine resolving two nearby point-like targets in z. Here there are two identical, small spheres separated in z. Although one could also consider the resolution of the system in x', if two identical targets are both placed at $z = z_{Tx}$ and $\theta_R = 0$, but with some offset in x' between them, the nearer of the two targets will occlude the other. Therefore the case for two targets offset in z is a far more realistic, measurable, and practical example.

The system was set up as before, but this time with sphere 1 at $z = -0.2$ m and sphere 2 at $z = 0.2$ m. The linear positioner was used to vary the target range along $x' \in [3.5, 5.5]$. In this situation, only the case of $n_{TxRx} = 3$, using all 3 Rx units is considered. This is because the theory of bilateration predicts that using $n_{TxRx} = 2$, the system will not be able to resolve the 2 spheres in z without introducing ghost targets into the reconstruction [27]. From Table 6.2, one can predict that the power drops from the maximum σ_{max} of each sphere, to (σ_{max}-6)dB at a position $z_{tgt} \pm 0.21$ m at $x' = 3.5$ m, and $z_{tgt} \pm 0.33$ m at $x' = 5.5$ m. From these predictions from experimental data, the spheres will no longer be outside of the 6 dB height extent of one another, and hence no longer be resolvable within a power of 6dB of one another somewhere in $x' \in [3.5, 4.0]$ m.

To show this, one can define the height profile of these targets to be the maximum of $\bar{\sigma}(x', z)$ along the z axis (6.11), i.e. $g(x'_{\text{tgt}}, z)$ is the maximum of $\bar{\sigma}(x', z)$ for a set value of z, for the reconstruction $\bar{\sigma}(x', z)$ performed at a target range x'_{tgt} (6.13). For a given target position, this is a distribution along z which shows the maximum returns in the image for that height (6.13). This is shown for two small metallic spheres in Figure 6.7 using the same experimental setup as before.

$$g(x'_{\text{tgt}}, z) = \max(\bar{\sigma}(x', z))|_{\mathbf{p}_{\text{tgt}} = (x'_{\text{tgt}}, z_{\text{tgt}})} \tag{6.13}$$

The results of Figure 6.7 do not reflect the predictions perfectly for a couple of reasons. First, $\bar{\sigma}$ of sphere 1 is larger than that of sphere 2. This appears to be due to some short range effects for $x' \leq 4$m where the spheres are not fully illuminated by the beam of each Rx unit. Next, based on the distribution in Figure 6.7, the spheres are just separable to within 6dB at a range of 5.5 m, which is further than predicted from Table 6.2. What is encouraging is that the system is able to resolve the 2 true targets from a situation which should yield 2 additional ghost targets using bilateration, which cannot be seen in $\bar{\sigma}(x', z)$.

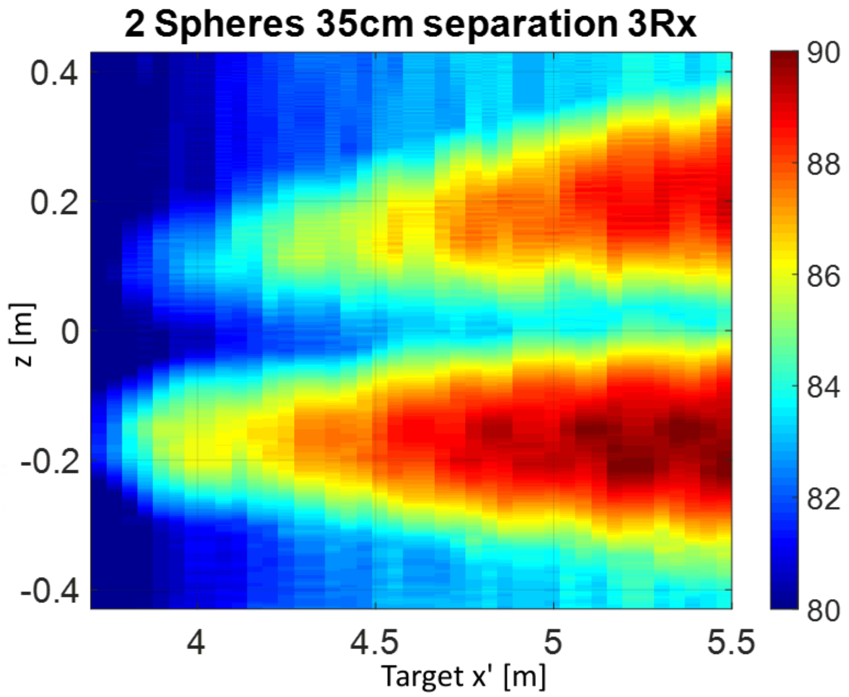

Fig. 6.7 Height profile of the backprojection reconstruction of two spheres as a function of target range.

This section has examined the resolution and error in x' and z for the proposed method of backprojection. The next section will examine how to best use this image ($\bar{\sigma}(x', \theta_R, z)$), by applying thresholds to remove the noise from the reconstruction while leaving the target reconstructions.

6.4 Connected Components

The aim of this section is to explain the final step in Figure 6.1, which converts the 3D image generated using backprojection into a readable plot. This will be used to generate the 3D plots in the remainder of this chapter. Backprojection in the form of (6.11) generates a non-zero RCS for every point in the 3D Cylindrical polar grid (Figure 2.1), but the majority of these points will correspond to free space, $\sigma(\mathbf{p}) = 0$ (6.1), where no object is present, but $\bar{\sigma}(\mathbf{p}) \neq 0$ (6.11) for all $\mathbf{p}$. Because of this, processing is required to remove these extraneous data points and leave only the points corresponding to radar targets. For simplicity, at this stage only methods which are not computationally intensive are considered.

Practically there are two additional factors one must consider. The signal is corrupted with noise (2.12) and backprojection has a finite point spread function (6.11). Therefore there are two kinds of extraneous points which need to be removed; the background noise, and sidelobes of backprojection. Assuming that the noise level of the radar is relatively flat, removing background noise can be performed by applying a threshold to the image [4]. By contrast, the sidelobes are most prominent when the amplitude of the signal from a highly reflective (bright) cell of at each receiver (2.11) is highest in a range cell, and when backprojected (6.11), this bright signal is added to every point on this bistatic range ellipsoid (5.2). Therefore every point on this ellipsoid has a large amplitude, even when most points still correspond to free space.

The two-stage thresholding procedure proposed here to combat this is fairly simple; threshold out the background noise, and then select only the points with the highest amplitude for each remaining target to remove the sidelobes. This is shown below in Algorithm 6.1. This procedure is performed independently for every $x'z$ plane (Figure 2.1) in the cylindrical polar grid. The standard definition [171] of Connected Components (CC) are used here, where a CC is defined in the $x'z$ plane to be a unique set of points which all have an amplitude greater than the applied threshold, where one can define a path between any two points in the set which passes through only adjacent connected points above the threshold. Two adjacent points are connected if either the edges or corners of their grid cells touch (8-connectivity). This is illustrated in Figure 6.8.

The connected component detector assigns each point an integer label, m, which allocates the connected component to which it belongs. The entire process is performed as follows:

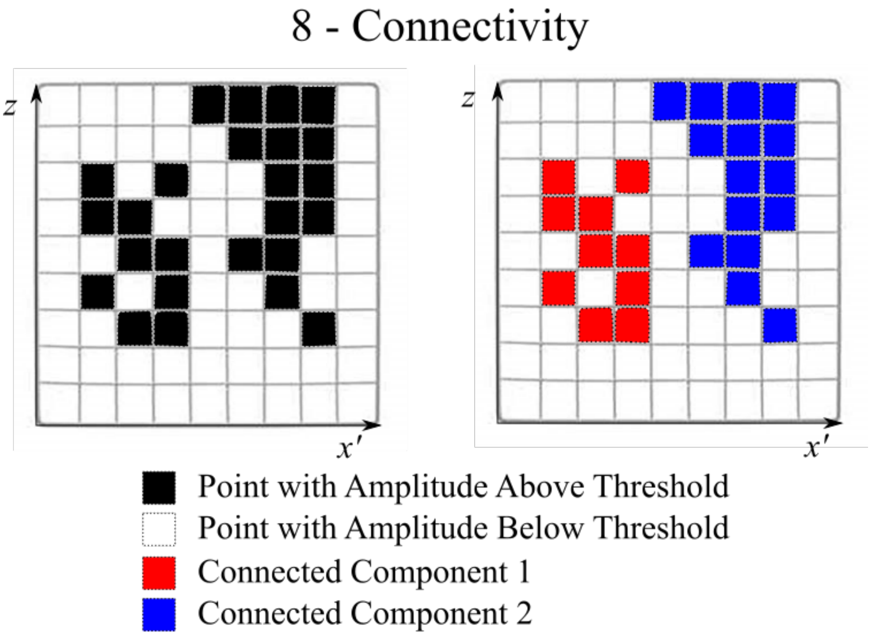

Fig. 6.8 Diagram of connected components in the $x'z$ plane.

The coordinates of the thresholded image are then converted from cylindrical polar to 3D Cartesian coordinates using (2.1) as described in section 2.

This section has presented a simple multi-stage thresholding system which can be used to remove the noise and sidelobes from the reconstruction $\bar{\sigma}(x,y,z)$ (6.11). The next section will apply these ideas practically at short range for a series of targets which an autonomous vehicle is likely to encounter.

Algorithm 6.1 : Connected Components Algorithm

```
• Initialize the label as $m = 0$.
• Apply a threshold to the $x'z$ image $\bar{\sigma}(x', \theta = \theta_R, z)$.
• While there are unlabelled points with $\bar{\sigma}$ greater than the threshold:
    – Find the next unlabelled point greater than the threshold.
    – Apply a flood-fill of $m$ to label the points which are in this CC.
    – Increase $m$ by 1.
• $n_{obj} = m$, then reset $m = 0$.
• For $m$ from values 0 to $n_{obj}$:
    – Find the CC labelled $m$.
    – Find the maximum amplitude $\sigma_{max}$ in this CC.
    – Apply a threshold of $(\sigma_{max} - 6)$dB to this CC.
    – Set amplitudes below this threshold to 0.
```

6.5 Short Range Imaging

In this section the backprojection method developed in this chapter will be applied to imaging common automotive objects at short range. This section is laid out as follows: section 6.5.1 details the experimental setup used, section 6.5.2 shows how a calibration is performed using this setup, and finally section 6.5.3 shows the results of the experiments.

6.5.1 Experimental Setup

To test the ability of this system to perform 3D images at short range for a series of common automotive objects, a set of objects were mounted on a turntable x' =3.8 m from the TxRx stack. This setup is shown in Figure 6.9, with the parameters shown in Table 6.3. Practically the system is implemented using the backprojection formulation of (6.11), using n_{TxRx}=3 and $80 \leq n_\theta \leq 120$ depending on the $x-y$ extent of the target. The measurements presented here were taken in laboratory conditions at the University of Birmingham using the 300GHz LFMCW radar from section 3. This uses a wide elevation beam pattern and 3 receiver positions hope to obtain a coarse resolution in height, compared to a narrow beam pattern in azimuth scanned in $\theta_s = 0.25^o$ steps which will generate a much finer resolution in azimuth. The use of a turntable allowed the imaging of the target from a series of different azimuth aspect angles, θ_{tgt}.

Table 6.3 Parameters used for short range imaging of targets on a turntable.

System		Topology	
Centre Frequency	290GHz	n_{TxRx}	3
Sweep Bandwidth	20GHz	n_θ	80-120
Transmitted Power	0dBm	z_{Tx}	0.70m (z=0)
Chirps Per Dwell	10	z_{Rx}	0.40, 0.78, 0.94 m
Dwell Time	11ms	θ_s	0.25°
Chirp Pattern	Repeated Up Chirps	R_{Res}	7.5mm
Azimuthal Beamwidth	1.0-1.1°(3dB)	l	2.6 mm
	1.4-1.5° (6dB)		
Elevation Beamwidth	6.2-7.0°(3dB)		
	8.8-9.1° (6dB)		

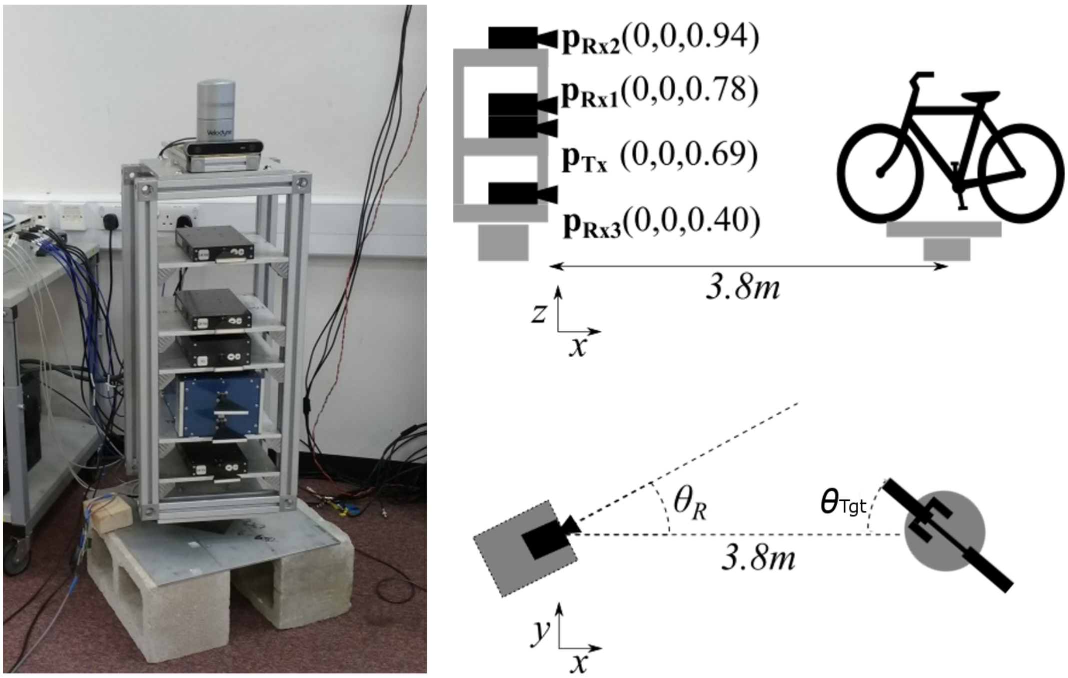

Fig. 6.9 Setup used for short range imaging of targets on a turntable. (left) Photograph of setup, and xz (top right) and xy (bottom right) diagrams of setup.

6.5.2 Calibration

This section performs a point response correction and radiometric calibration, as in section 3.2, which is used for the results in the remainder of this chapter. Here a method to correct the digitised signal is laid out, which is a signal of the form of (2.7) which has been affected by the system's components' non-ideal responses. There are two causes of distortion which are considered here. The first is that in order to achieve a quasi-bistatic setup, signal cables must be used to connect the transmitters and receivers to a control box. These cables introduce internal reflections and can be a source of non-linearities which degrade the point response of the system. This was previously described in section 3.2. The second is that the amplitude of the signal from each receiver (2.7) should be calibrated with respect to a known reference target.

The first part of this calibration makes use a method laid out in section 3.2 [145]. One can consider the signal to be approximately the ideal signal (2.7), multiplied by an infinite series of many different internal reflections, I_{ref_i} (3.2). Therefore one can evaluate this series by fitting a signal (s_{ideal}) with linear phase to a reference target (s_{ref}) which is known to be both bright and point-like, as in [145]. This must be done independently for each receiver which each have a unique set of internal reflections.

To reconstruct the RCS of each point, the amplitude of the signal must be converted from the form of A_{IF_i} (2.7) to A_{Rx_i} (2.6). To generate this correction a reference target is used with the known RCS, σ_{ref} at the known position, $\mathbf{p}_{\mathrm{ref}}$. One can evaluate the total corrected signal amplitude as in (6.14).

$$q_i = \frac{A_{\mathrm{Rx}_i}(\sigma_{\mathrm{ref}}, \mathbf{p}_{\mathrm{ref}})}{A_{\mathrm{IF}_i}(\sigma_{\mathrm{ref}}, \mathbf{p}_{\mathrm{ref}})} \tag{6.14}$$

The configuration of the hardware remains largely the same independent of θ_R, so this compensation can be mixed with the signals taken at any position to generate the useful signal S_{Rx_i} in (6.15). Here, the Blackman window (W) has been chosen due to its low sidelobe level [133].

$$S_i(R_b) = q_i \mathscr{F}\left(W s_{\mathrm{IF}_i}(t) \circledast \tilde{I}_{\mathrm{ref}_i}\right) \tag{6.15}$$

where $\tilde{I}_{\mathrm{ref}_i}$ is derived as in section 3.2. To calibrate this system the instrument response correction and overall amplitude of the range profile must be derived from a known, bright, canonical target. For calibration a trihedral triangular corner reflector with side length d =4 cm and RCS $\sigma_{\mathrm{ref}} = 20.6$ dBsm (6.16), is placed at $\mathbf{p}_{\mathrm{ref}} = (4.6, 0.1, z_{Tx})$ m. Using the method described in section 3.2 and [145]. Each Rx is placed in a quasi-monostatic position ($b_{1,2,3}$ = 4 cm) and a mechanically scanned image is formed ($|S_i(R_{b_i}, \theta)|^2$). The range profile at the azimuth position with the largest return from the reference target is considered here.

$$\sigma_{CR} = \frac{4\pi d^4}{3\lambda^2} \tag{6.16}$$

The point response has been sharpened considerably as can be seen in Figure 6.10. Leaving $q_i = 1$ in Figure 6.10 to emphasize that the energy reflected from the corner reflector has been focused into a a sharper peak $|S_i(R_b)|^2$ (6.15) is shown in blue, and the uncorrected signal (equivalent to $|S_i(R_b)|^2$ with $\tilde{I}_{\mathrm{ref}_i} = 1$) (6.15) is shown in red. This correction has resulted in a 5.7 dB peak power increase from 110.9 dBarb (uncorrected) to 115.6 dBarb (corrected) with comparable noise floors.

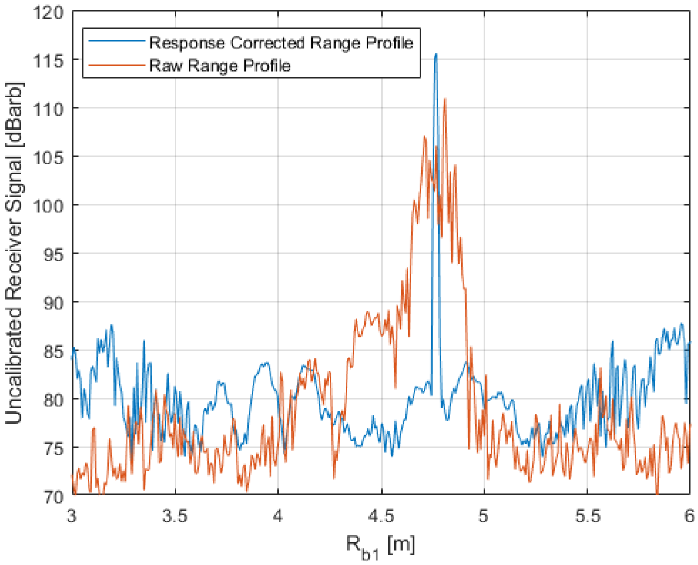

Fig. 6.10 The range profile of the reference corner reflector, with and without the instrument response correction.

The path loss is proportional to $R_{\mathrm{Tx}}^{-2}R_{Rx1}^{-2}$, which is -54.5 dB, (note that constant terms such as 4π can be ignored as this generates a single constant to correct the amplitude of the range profile). The target aspect angles are $\theta_{\mathrm{Tx}} = \theta_{Rx1} = 0°$ in Figure 3.7, $\varphi_{\mathrm{Tx}} = 0°$ and $\varphi_{Rx1} = -0.5°$ in Figure 3.8. Using the normalised values of the beam patterns this gives a gain of -0.2 dB. The final consideration is the integration of n_{Rx} receivers through backprojection (6.11). The gain in power is going to be somewhere between n_{Rx} = 4.8 dB and n_{Rx}^2 = 9.6 dB, but as in (6.11) it is likely to be on the higher end of this range [148] so it is taken to be approximately 9.6 dB.

The maximum value in the corrected range profile is $|S_i(R_b)|^2$ =115.6 dBarb. Using the amplitude correction as in (6.9), this gives a total amplitude correction of q_i^2 = 20.6 -115.6 + 0.2 -54.5 = -149.5 dB. This process is repeated for each of the receivers in turn. The integration gain of n_{Rx} is removed from the final backprojected image (6.11).

To test the calibration, the system was then configured as in Table 6.3. The 3D reconstruction of the corner reflector shown in Figure 6.11 matches the expected value well. It has a peak value of σ of 21 dBsm at $(x', z) = (4.8, 0)$ m. The observed roll-off is an artifact of backprojection, and lies approximately along the intersections of $\mathbf{E}(R_{b_{1,2,3}}, \mathbf{p}_{\mathrm{Rx}_{1,2,3}})$ (5.2). These have a total 6 dB spread of 0.7 m in height and 0.1 m in ground-range. From Table 6.2, one would predict a 6dB height spread of 0.6 m for the similar setup in section 6.3. For comparison, the largest RMS predicted errors are $\mathscr{D}z$ = 0.09 m (5.13), and $\mathscr{D}x'$ = 0.01 m here (5.12). To test this process on a simple canonical target, a metallic corner reflector of side length of 4cm was placed at (x', z) = (5.1,0.6) m. Figure 6.11 shows a 2D $x'z$ slice of $\bar{\sigma}(x', \theta_R = \theta(\mathbf{p}_{tgt}), z)$. This is before a threshold or connected components has been applied. The extent in z shows that without some form of additional processing, it is not obvious what regions of $\bar{\sigma}(x', \theta_R, z)$ correspond to free space and what corresponds to a target. The full cylindrical polar reconstruction of $\bar{\sigma}(x', \theta_R, z)$ after thresholding is shown in Figure 6.12. $|S_i(R_{b_i}, \theta)|^2$ (6.15) is shown as a black and white image at ground height, and $\sigma(x,y,z)$ (6.11) after thresholding is shown in colour. A larger roll-off of 10 dB (rather than 6dB) from the maxima of the target's connected component (σ_{max}) is taken to illustrate the point response of the system while just thresholding out the background noise, as described in section 6.4. This appears to give a 10dB z extent of 0.8 m for the reference target.

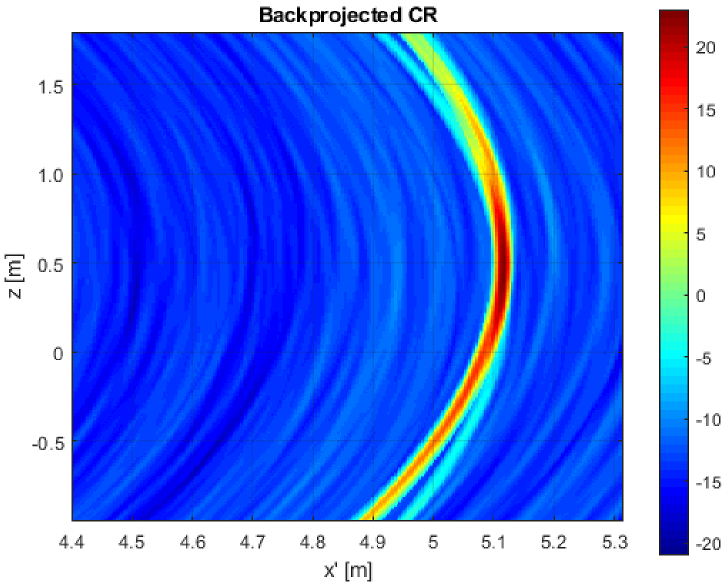

Fig. 6.11 Corner reflector. 2D $x'z$ slice of 3D Backprojected image.

The full 3D image is shown in Figure 6.12. At either side of the corner reflector in azimuth, there are regions where the target is poorly localised. This is because the target is now only visible in one Tx-Rx pair. Although the target is visible in each Rx when $\theta_R = \theta(\mathbf{p}_{tgt})$, at some orientations it is only detectable for the monostatic receiver (Rx$_1$) - with the lowest associated loss, L_i. What's more, in section 3 the monostatic receiver was also found to have the best sensitivity, and hence could detect a target with a

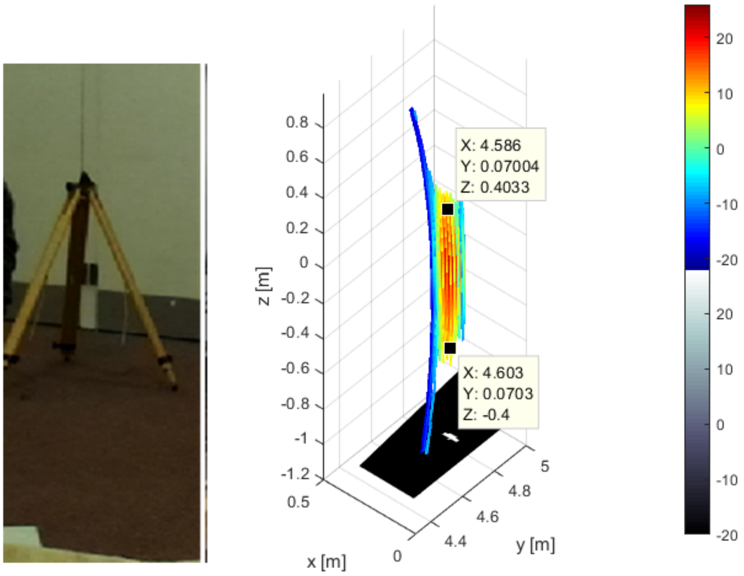

Fig. 6.12 (left) photo of corner reflector. (right) 3D image of corner reflector in colour, with 2D radar image superimposed at ground height.

lower received amplitude (2.18). Each Rx has a different noise power, and so $S_i(\sigma_{tgt}, \mathbf{p}_{tgt})$ (6.15) of the same target disappears below the noise floor (2.12) at different θ_R values for each Rx.

In this section, it has been demonstrated how the calibration of the system can be performed, and the 3D image corresponding to a reference target has been produced. In the following section, a set of objects which appear frequently in the automotive environment will be imaged in the same way using the calibration derived here.

6.5.3 Results

In this section a series of different common road objects will be used as targets for the short range 3D imaging setup described in Table 6.3 and shown in Figure 6.9. These targets will be positioned at $x' = 3.8$ m one at a time, and will include a traffic cone, a pole, a child mannequin (pedestrian), and a bike.

All of these targets are placed at the same xy position, and so the point response can be predicted. From Table 6.2, one can predict that the 6dB z extent for a point-like target or scattering centre should be 0.4 m. From the beam pattern parameters in Table 3.2, one can predict that the 3 and 6 dB widths in θ_R for these targets from mechanically scanning should be 1.1° and 1.5° respectively. These are cross-range extents of 0.07 m and 0.1 m respectively, which is perpendicular to x' in the xy plane.

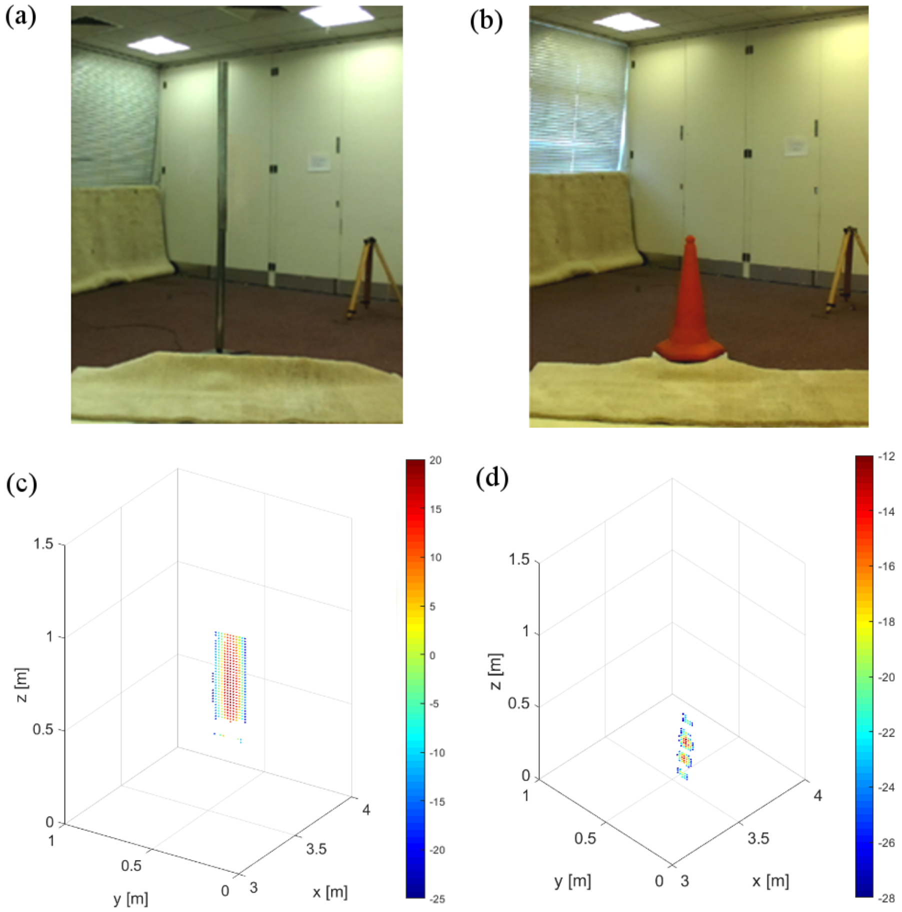

Fig. 6.13 (a) Photograph of pole. (b) Photograph of traffic cone. (c) 3D reconstruction of pole. (d) 3D reconstruction of traffic cone.

First let us consider the 3D reconstruction of $\bar{\sigma}(x', \theta_R, z)$ (6.11) after thresholding for the cone and pole. The traffic cone (Figure 6.13b and 6.13d) appeared as a peak of maximum RCS $\sigma =$-12 dBsm. The height extent of this target was observed to be $z \in [0.04, 0.47]$ m. This agrees with the predicted z extent of 0.4m well. The reconstruction at every value of θ_{tgt} was near-identical, as there is rotational symmetry of the target about the z axis. Because the base is an angular object without this symmetry, the lower scattering centre was unlikely to come from the corner between the turn-table and the base of the cone which varies with aspect angle. If there are indeed two separate scattering centres present, it appears that the lower is from the corner between the base and inner cone, and the upper is from the main body of the cone. The pole (Figure 6.13a and 6.13c) appeared as a single peak with maximum $\sigma =$ 19dBsm. The 6dB height extent of the target was from $z \in [0.46, 0.93]$ m. This RCS value is much brighter than the cone, both due to the higher relative permeability of the metal pole [172], and that the pole occupies a height of $z = z_{Tx}$. This is what one would predict from specular reflection of a pole, where the point of brightest reflection for each receiver is the midpoint in height between the transmitter and receiver. This does highlight one issue with height profiling a smooth metallic object, which was predicted in section 2.3.3. The pole was connected to the ground, yet did not have a 6dB height extent approaching its physical extent of $z =\in [0, 2]$ m. If the goal is to reconstruct the full extent of a target, this suggests that further work should be done to characterise cylindrical or planar objects which yield specular reflections. The reconstruction at every value of θ_{tgt} was near-identical due to the rotational symmetry of the pole around the z axis.

Next a child mannequin is considered. The 3D reconstruction, $\bar{\sigma}(x', \theta_R, z)$ (6.11), can be seen in Figure 6.14b and c.

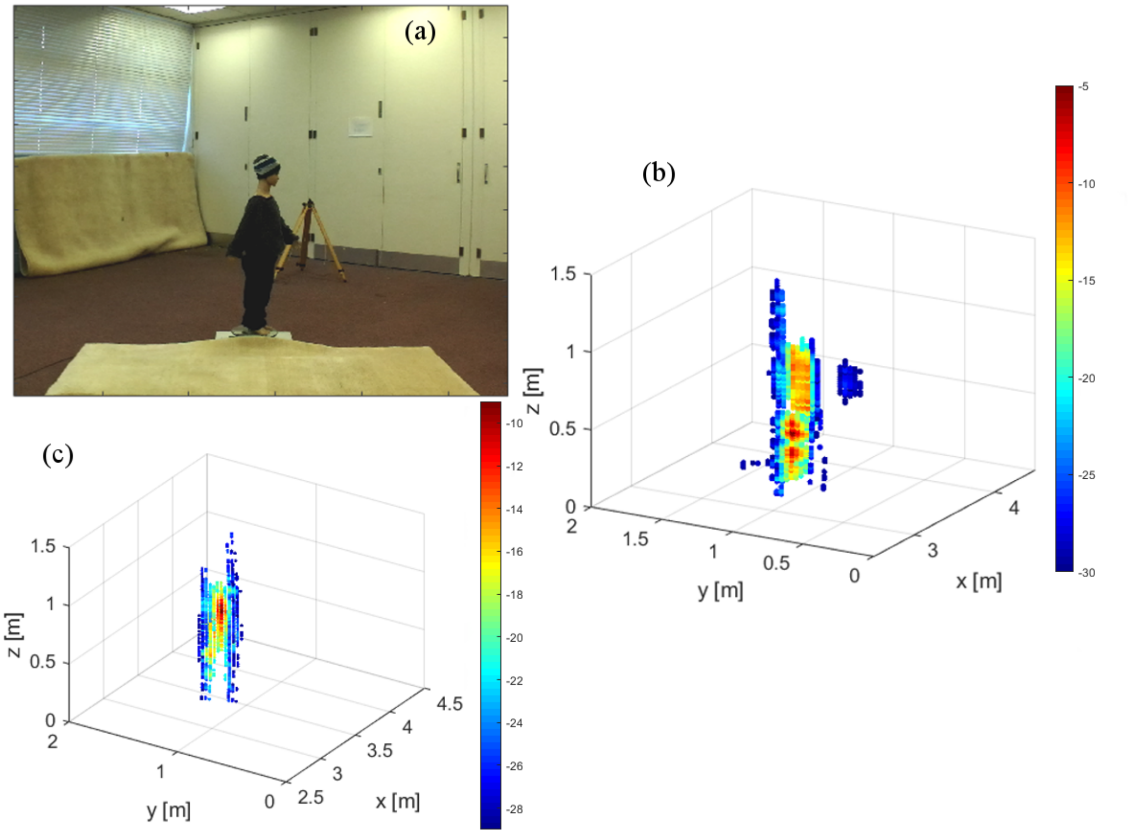

Fig. 6.14 (a) Photograph of side-facing mannequin. (b) 3D reconstruction of side-facing mannequin. (c) 3D reconstruction of front-facing mannequin.

The main body of the mannequin appears to occupy $z \in [0, 0.95]$ m, with multiple bright scattering centres with a peak RCS of σ = -12 to -8 dBsm along the body. The height of the brightest returns of both the child and pole appeared to be around the Tx height, as this is the point of the bright specular reflection. These are in good agreement with the measured RCS of this child mannequin which is -9 ± 2.4 dBsm [113]. Looking at Figure 6.14b, there appears to be 3 main scattering centres present. The legs with σ = -8 dBsm at (x, y, z) = (3.4,1.0,0.3), the torso with σ = -10 dBsm at (3.4,1.0,0.6), and the outstretched arm with σ = -25 dBsm at (3.5,0.8,0.3). The RCS values of the mannequin's legs and torso are close to mannequin RCS values from section 5.2. Each of these targets has the predicted 0.4 m extent in z, aside from the arm, which has a much smaller value of σ, and much of the 6dB spread was likely thresholded out. As expected, the outstretched arm is far dimmer, with a peak RCS of σ = of -25 dBsm. The RCS of the arm seems like an underestimate due to the fact that the arm was only picked up by two receivers. On top of this, this value then undergoes the correction from integrating over $n_{\mathrm{Rx}} = 3$ receivers of - 9.6 dB, which seems to underestimate the brightness of the arm further. In contrast, Figure 6.14c does not show the arm. It does show returns over $z \in [0,1]$ m, again, but this time it is shown as a single dominant scattering centre of RCS $\sigma =$ -8 dBsm at (x,y,z) = (3.4,1.1,0.6). This is consistent with the torso from Figure 6.14b, but it appears that at this θ_{tgt} the torso and the legs are no longer resolvable within 6dB, and so the thresholding procedure is not showing both scattering centres.

What is encouraging about this result is the fact that one can not only identify the position of the target in 3D, but can also identify some pose information (such as the outstretched arm) through this procedure.

Finally a bike was mounted on the turntable. The 3D reconstruction, $\bar{\sigma}(x', \theta_R, z)$ (6.11), can be seen in Figure 6.15b,c, and d. The bike is 1.5m long from the front of the front wheel to the back of the rear wheel. The bike is referred to as front facing at $\theta_{\mathrm{tgt}} = 90°$ when the 1.5 m length of the bike is parallel to the $x'z$ plane at $\theta_R = \theta(\mathbf{p}_{tgt})$, and side facing when the 1.5 m length is perpendicular to this at $\theta_{\mathrm{tgt}} = 0°$ and $\theta_{\mathrm{tgt}} = 180°$.

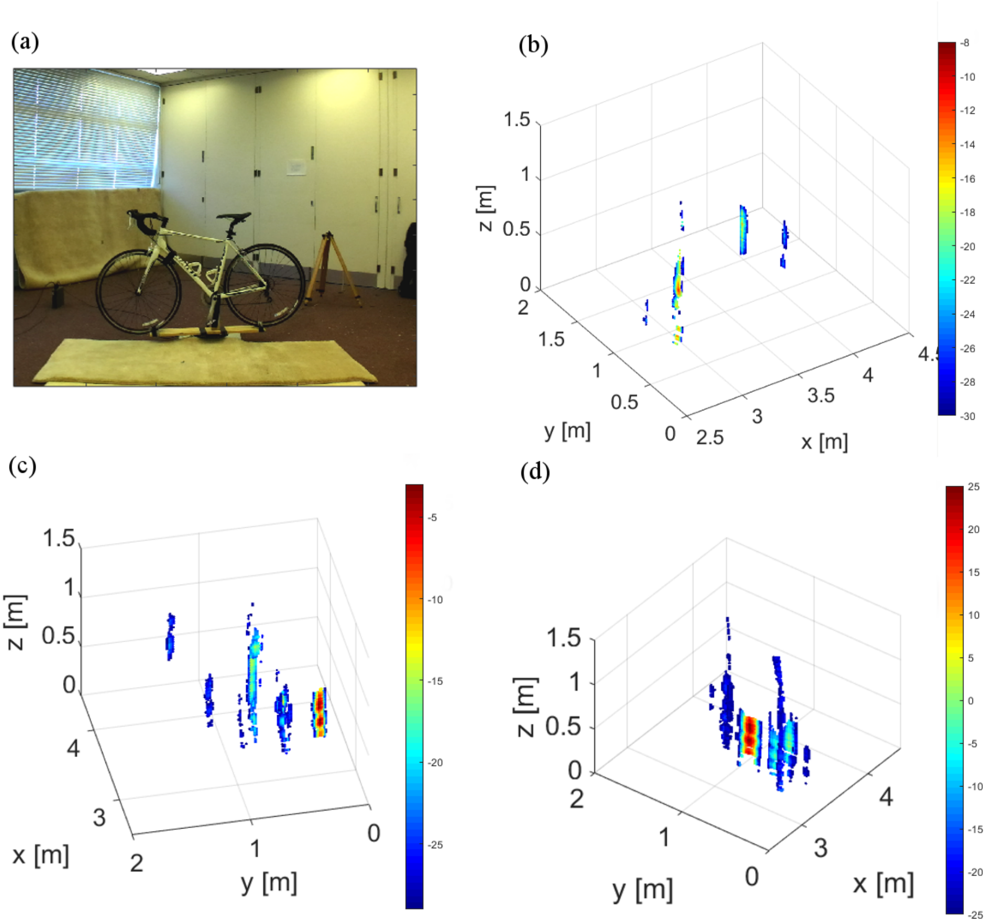

Fig. 6.15 (a) Photograph of bike ($\theta_{\mathrm{tgt}} = 0°$). (b) 3D reconstruction of front-facing bike ($\theta_{\mathrm{tgt}} = 90°$). (c) 3D reconstruction of side-facing bike ($\theta_{\mathrm{tgt}} = 0°$). (d) 3D reconstruction of side-facing bike ($\theta_{\mathrm{tgt}} = 180°$).

As predicted, when side-facing (Figure 6.15c,d), the bike appeared as a long extended target with a xy extent of 1.5m. The bike is a complicated object with many scattering centres present. Here it will be discussed in terms of 4 main parts of interest; the seat, the handlebars, the wheels and the chainring. In Figure 6.15b the seat and its surrounding structure appears as a peak with RCS $\sigma = -18$ dBsm at (x, y, z) = (3.6, 0.7,0.7) m , and in Figure 6.15c with RCS $\sigma = -16$ dBsm at (x, y, z) = (3.6, 0.9,0.7) m.

The handlebars appear in Figure 6.15c and d as a structure with peak RCS of around $\sigma = -20$ dBsm at $z = 0.8$ m. Although they are a similar size, the seat is a metallic object with many corners and clips, while the handlebars are less angular and are wrapped in polymer. When considering the wheels, most of these peaks when side facing are at heights of $z \in [0.1, 0.6]$ m which correspond to positions of metal clips within the wheels and chain of the targets. Each of these features are relatively consistent with what one would expect from the physical layout of the bike.

At θ_{tgt}=180° (Figure 6.15d) a bright flash was visible with $\sigma = 25$dBsm and z =0.33 m. This bright spot was only observed when the chainring was facing the radar stack. The chainring is a metallic structure with many corners, so it was assumed that it would have a large RCS. Figure 6.15b shows the bike when front-facing, when the majority of the body and the inside of the wheels are occluded by the front of the bike. The chassis of the bike is still illuminated and occupies a height extent for most peaks of $z \in [0.45, 0.9]$ m, though the scattering centres of the wheels are no longer visible. These variations in scattering centres at varying aspects can not only tell us whether the bike is side or front-facing, but with the presence of the bright flash of the wheel grating one can estimate the direction in which the bike is heading.

This section has examined a close-range 3D imaging scenario for a set of objects which are common in road environments. The reconstructions showed a high level of detail, but also showed a lot of variation with aspect angle. This is useful for classification and pose estimation, but these objects must be able to be detected, imaged, and tracked in a dynamic scene. The next section will examine a slightly more realistic scenario where there are pedestrians moving slowly through a scene, and the radar is itself moving in a stop-and-go configuration.

6.6 Walking Pedestrians

These measurements are designed to emulate a slightly more realistic scenario than the turntable images in section 6.5. Namely, pedestrians walking as a vehicle moves past them. To achieve this, a series of different sensors were mounted on a linear positioner to incrementally move the sensor stack. The stack and the motion of the sensors and actors are shown in Figure 6.16.

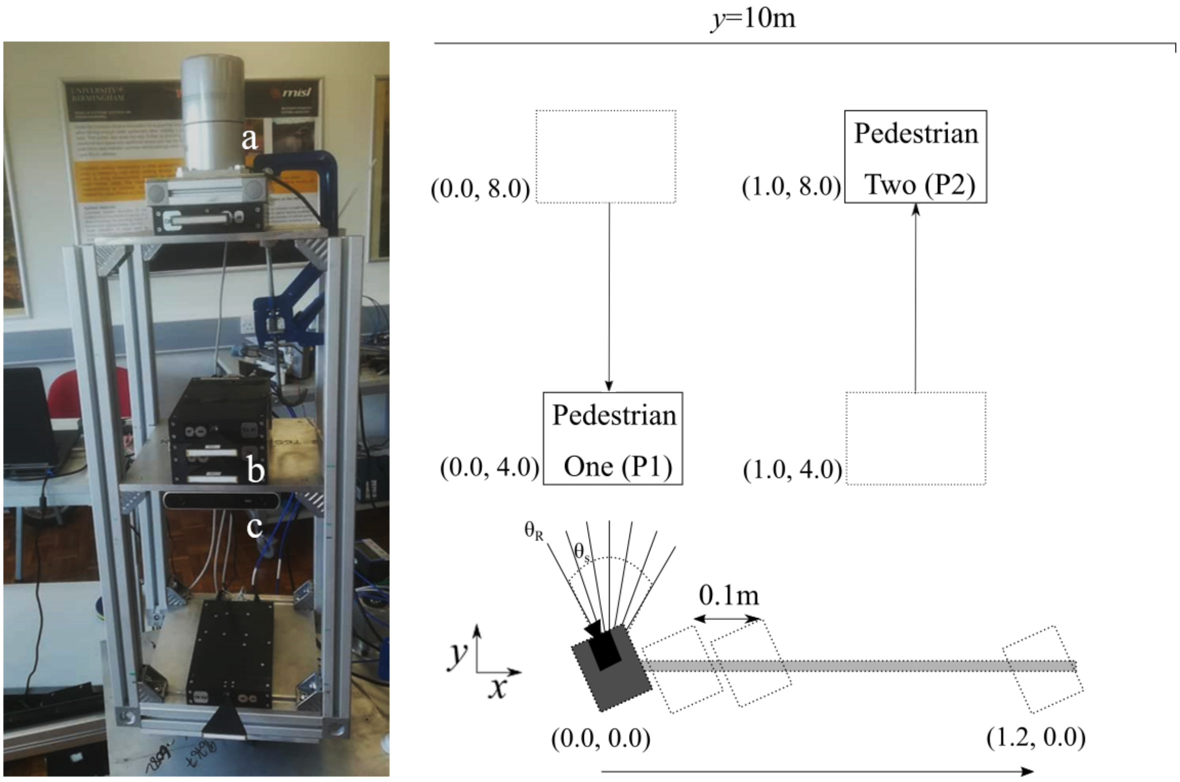

Fig. 6.16 (left) Photograph of experimental setup. (a) Velodyne 32 beam lidar, (b) 300GHz radar transmitter, (c) ZED stereo camera. (right) Diagram of the position of the sensor stack and pedestrians, with positions given as (x,y).

A ZED stereo camera[173] and Velodyne 32 beam lidar [61] were used to compare the performance of such a system to current common high-resolution industry sensors. The 300GHz radar was mounted with the receivers vertically separated in a way which can generate a significant TDoA between receivers to perform 3D imaging. The parameters used can be seen in Table 6.4. Given that each of these sensors were positioned at $x = x_{stack}$, $y = 0$, vertically on top of each other, coregistration was a simple case of adding

System		Topology	
Centre Frequency	290GHz	z_{ZED}	1.0m
Sweep Bandwidth	18GHz	z_{Vel}	1.6m
Transmitted Power	0dBm	z_{Tx}	1.12m
Chirps Per Dwell	10	z_{Rx_1}	1.05m
Dwell Time	11ms	z_{Rx_2}	1.32m
Chirp Pattern	Repeated Up Chirps	z_{Rx_3}	1.76m
Azimuthal Beamwidth	1.0-1.1°(3dB)	x_{stack}	0-1.2m
	1.4-1.5° (6dB)	x_s	0.1 m
Elevation Beamwidth	6.2-7.0°(3dB)	θ_s	0.25°
	8.8-9.1° (6dB)	θ_R	-25.0° to 25.0°

Table 6.4 Parameters used in experiment to image walking pedestrians.

z_{ZED},z_{Vel} and z_{Tx} to the heights of their respective sensor images. The 3D images of the stereo video and lidar systems were generated using in-built procedures from the manufacturers.

Using a linear positioner, x_{stack} was varied from 0 to 1.2 m in steps of x_s, so that a scan was taken at 12 equally spaced x_{stack} positions. At the same time, pedestrian 1 (P1) moved from (x,y) = (0.0,4.0) m to (0.0, 8.0) m in 12 approximately equal steps, as pedestrian 2 (P2) moved from (1.0,8.0) m to (1.0, 4.0) m. At each of the 12 positions, the pedestrians were stationary and a range-azimuth image was generated through mechanically scanning the stack, with a range profile taken at each θ_R position (2.11). The 3D reconstruction $\bar{\sigma}(x',\theta_R,z)$ (6.11), was then performed as before.
The images of two pedestrians walking can be seen in Figure 6.17. In the subsequent figures the left hand side (a),(d),(g) shows the photos taken by the left camera of the ZED stereo camera. The central images (b),(e),(h) show the radar 3D image $\bar{\sigma}(x',\theta_R,z)$ (6.11) after thresholding, superimposed with the coregistered 3D lidar pointclouds in black. The reconstruction from the ZED stereo camera generated from the disparity map between the left and right cameras can be shown on the right hand side (c),(f),(i). At positions 1, 5 and 10, the y position of the pedestrian one was found to be 8.0m, 6.3m, and 4.7m respectively. The second pedestrian follows the opposite path, and was found to be at 4.0m, 5.7m, and finally 7.3m.

For both pedestrians the brightest returns appear to be coming from the torso. This may be due to it having the largest RCS or due to it generating bright specular returns (being close to $z = z_{Tx}$), however returns appear to be visible from most of the pedestrians body, allowing us to visualise a height profile of

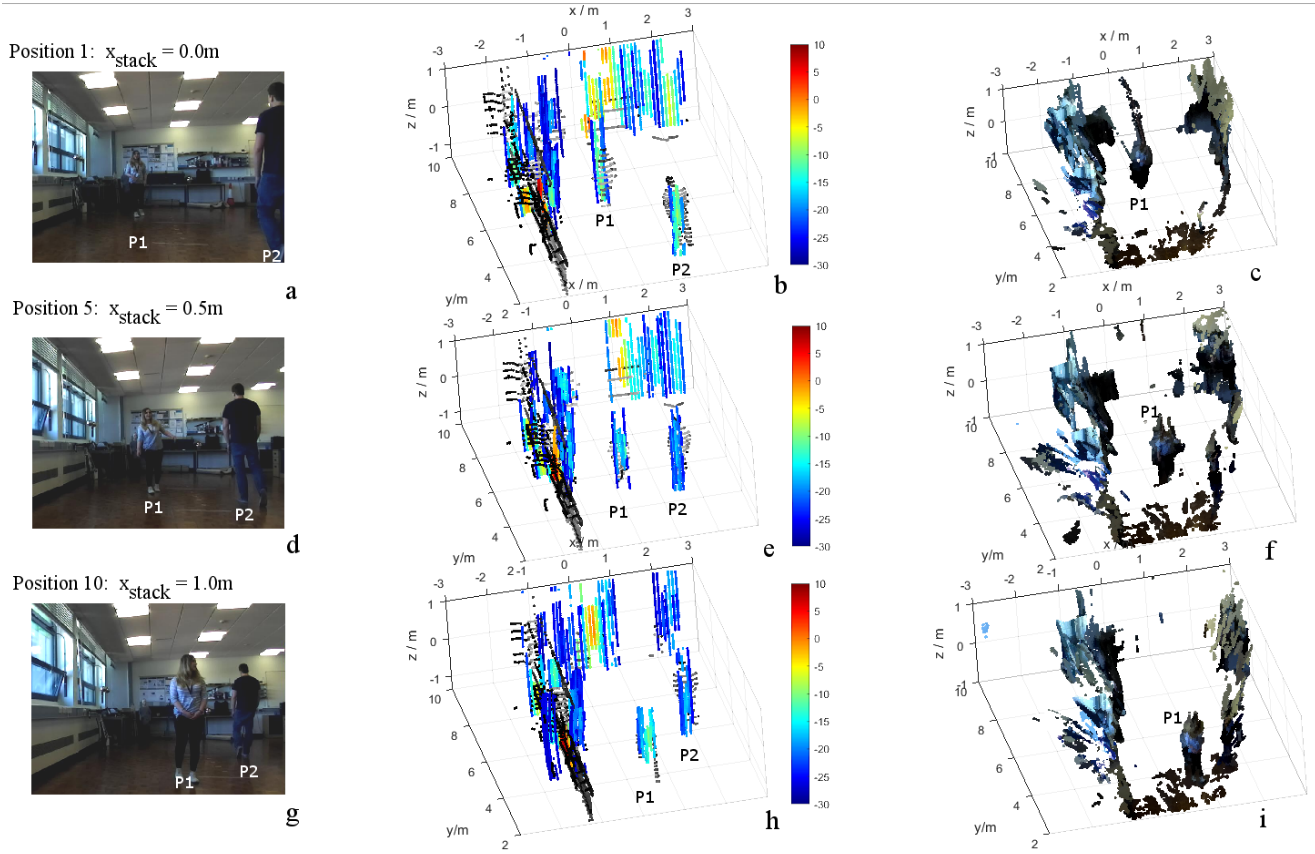

Fig. 6.17 3D Images of two walking pedestrians. (a,d,g) photographs, (b,e,h) 3D radar reconstructions (colour) and lidar point cloud (black), and (c,f,i) stereo video reconstruction.

the pedestrians. The peak RCS of the pedestrians and the mannequin are very similar, with a peak of $\sigma =$ -7 ± 3 dBsm. This is a slight overestimate of the RCS of an adult pedestrian or a mannequin which lie between $\sigma =$-8.6 dBsm [113] for an adult, and $\sigma =$-9 ± 2.4 dBsm for the child mannequin, but this is reasonably consistent with the findings of sections 5.2.2 and 6.5.3. There was clear variation present in the radar intensity of different sections of the back wall, in the plane y = 10 m. The peak return at (x,y) = (1.0,10.0) m with σ = 5 dBsm corresponds to a metal corner shelf bracket. There was clear variation present in the radar intensity of different sections of the back wall (in the plane y = 10 m). Although the wall is visible as a large planar object, there is clear evidence of shadowing from the pedestrians on the back walls (at x=-0.5m, x=0m and x=1.5m at positions 1,5,10 respectively) when the pedestrians are obscuring the radar and lidar images. Here no points are observed in any of the three sensor images. At position 10 (Figure 6.18g,h,i), P1 shadows the corner bracket. This is to be expected, and should not greatly impact path planning for obstacle avoidance.

Good agreement can be seen in the positions of the pedestrians in all three sensors. For both pedestrians the brightest returns appear to be coming from the torso of the pedestrians which are at transmitter height (the point of specular reflection), however returns are visible from most of the pedestrians body, allowing us to generate a height profile of the pedestrians.

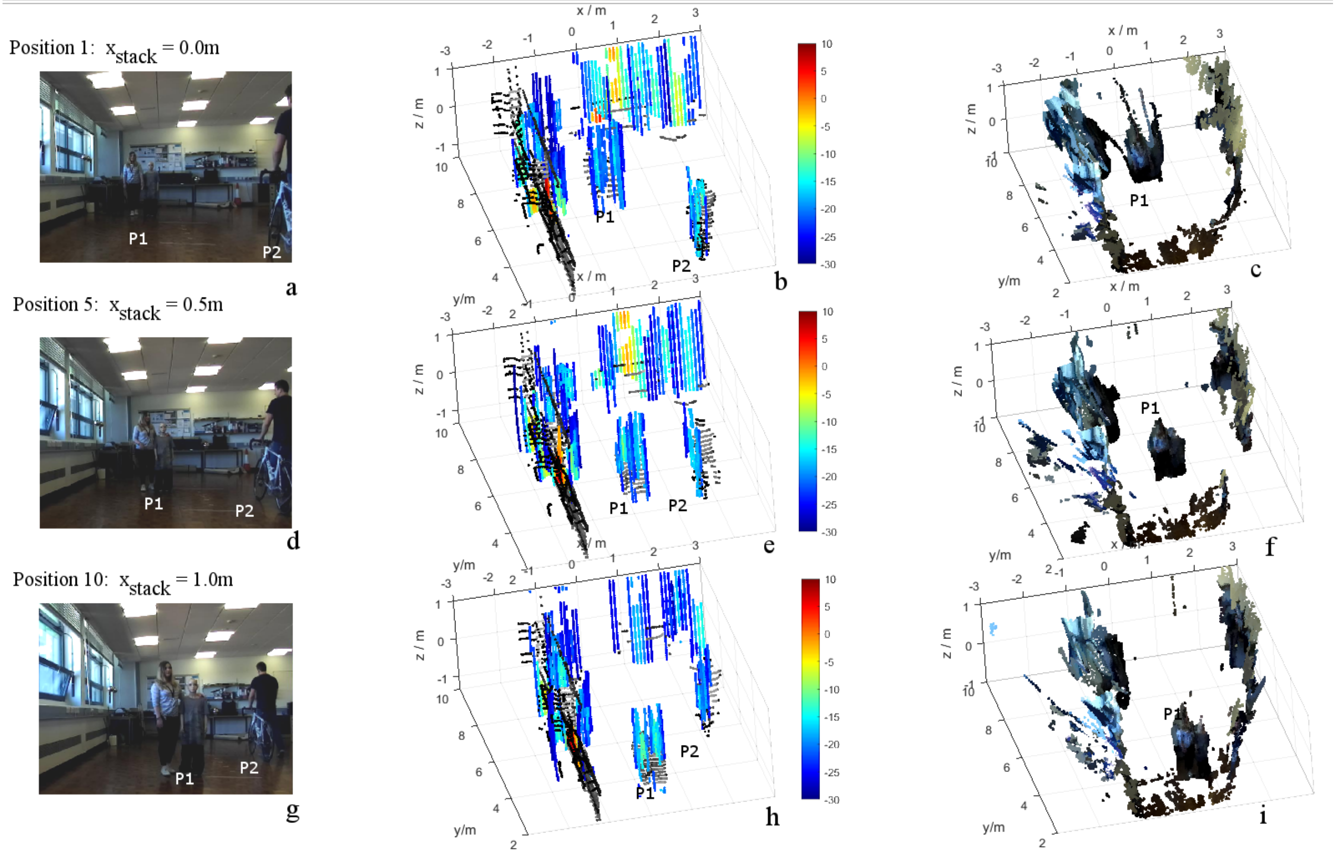

Fig. 6.18 3D Images of two pedestrians walking with objects. (a,d,g) photographs, (b,e,h) 3D radar reconstructions (colour) and lidar point cloud (black), and (c,f,i) stereo video reconstruction.

To demonstrate the resolution performance of this system, and its ability to distinguish vulnerable road users (in this case a parent and child, and dismounted cyclist), both pedestrians were given additional objects to hold. These images can be seen in Figure 6.18. Pedestrian one walked with a child mannequin and pedestrian two wheeled along a bicycle. In each of the images, the object the pedestrians were holding were clearly distinguishable from the body of the pedestrians, meaning that the system is likely to be capable of distinguishing between different kinds of pedestrians, which may improve the results of classification in the future. The position of these objects were consistent between the radar, lidar, and stereo camera.

From the analysis of imagery one can make four important conclusions. (i) radar imagery allows not only rough estimation of the height, but also highlight the shape of the objects, as expected due to predominantly diffuse scattering at 300 GHz. (ii) the ability to highlight the shape leads to appearance of resolved targets. In Figure 6.17 (d) and 6.18 (d) the intensity map of pedestrian with child mannequin appears as two clusters with lower intensity of returns at the interface between them, though they were tightly attached. However, these targets are distributed in xy, so it is likely that a lot of these resolution capabilities are coming from the azimuth resolution of the system. (iii) the proposed thresholding approach offers a rudimentary method of image segmentation with separation between passable free space (no elevated objects) and obstacles, at least at the shown distances. (iv) the reconstructions are comparable between the radar, lidar, and stereo camera in 3D space.

This section has demonstrated that this setup and technique is capable of performing 3D images of actors moving through a scene. In the next section the setup will be mounted in a vehicle, taken out on to the road, and some important use cases are examined where height information is essential for a vehicle navigating a scene.

6.7 Vehicle Based Imaging

In this section, the setup will be mounted on a vehicle and taken out on the road. This setup will be used to measure some everyday scenes in which the vehicle needs height information to be able to safely navigate. In this section a low bridge, an arm barrier, and an entrance to a multi-storey car park are considered.
For these measurements a series of different sensors were mounted in the trunk of a land rover discovery and were powered from the car's battery using an inverter. Because of the size of the equipment, the set up had to be mounted in the boot of the land rover. There was no other position on the vehicle where the setup could be mounted without moving or obscuring the driver's vision. As in section 6.6, a ZED stereo camera and Velodyne 32 beam lidar were taken to compare the performance of such a system to current common high-resolution industry sensors. The 300GHz radar was mounted in a stack as shown in Figure 6.19, with the receivers vertically separated to generate a significant TDoA between receivers to perform 3D imaging. For comparisons with automotive radars in lower frequency bands, an LFMCW radar with a centre frequency of 77GHz, a lower bandwidth, and a higher output power (but otherwise, the same operating parameters) was mounted in the radar stack. The parameters used for these measurements are shown in Table 6.5. With the additional radar, not all of the equipment could be mounted in the stack at $x=0, y=0$, and so the lidar was positioned at an offset x position.
In this section, 5 sensor outputs are going to be displayed. First will be the photo taken by the ZED camera [173], this time without a stereo video reconstruction. Next will be the lidar point cloud generated by the velodyne lidar, which will be displayed as a pointcloud in black [61]. Next are the 2D range-azimuth images of the 300 GHz radar and the 79GHz radar. The 79GHz image is the raw $S_i(R_b, \theta_R)$ image which is a series of range profiles with no point response correction, (2.11), whereas the 300 GHz image has undergone a point correction as in section 6.5.2. This is shown without reweighting A_{IF} (2.7). This signal is the corrected $S_i(R_b, \theta_R)$ (6.15) with $q_i = 1$. Finally, the reconstruction $\bar{\sigma}(x', \theta_R, z)$ (6.11) is shown in 3D after having undergone the thresholding procedure from section 6.4.

An object which a vehicle is likely to have to navigate is a low-bridge, such as the one shown in Figure 6.20. The bridge can be split into 3 radar targets; the section attached to the ground (annotated as a), the suspended section (b), and the metal corners connecting them (c). The setup is positioned such that the

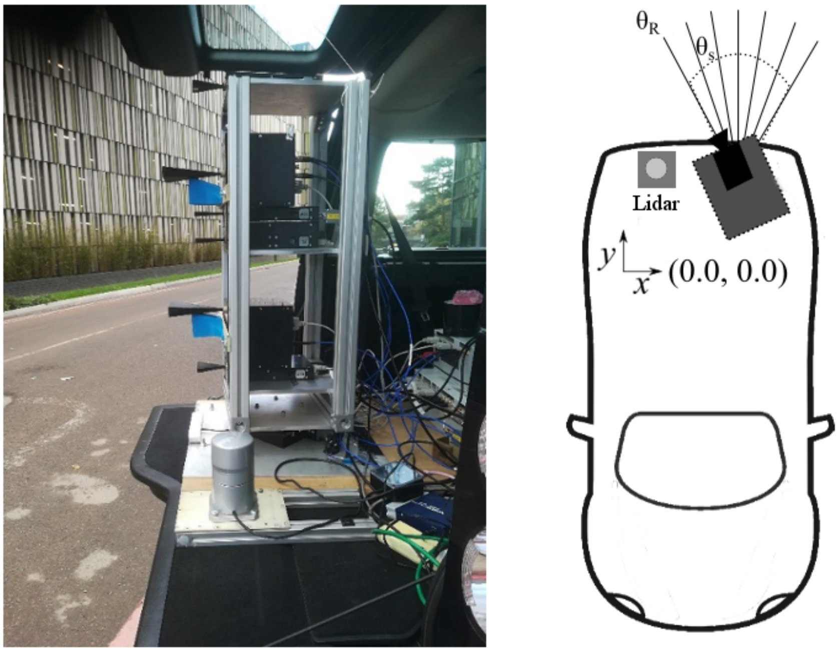

Fig. 6.19 (left) Photograph and (right) top-down *xy* diagram of vehicle-borne experimental setup.

facade of the bridge is at a position of $y = 12m$. At this range, from Table 6.2 one would predict a 6dB z extent of the point response to be between 1.1 and 1.3m, though this is an extrapolation from target ranges of 3.5m to 5.5 m and may not be accurate.

The bottom of the suspended section of the concrete bridge is at $z = 3.0$m from the ground (z=0), and the top of the bridge is at $z = 4$m. There is no obvious differences between sections a, b, and c in the 79 and 300GHz 2D radar images, $S_i(R_b, \theta_R)$ (6.15), aside from a 5dB decrease in signal power in the

Table 6.5 Parameters used for vehicle-borne 3D road imaging.

System		Topology	
Centre Frequency	77GHz, 290GHz	z_{ZED}	0.9m
Sweep Bandwidth	5GHz, 16GHz	$z_{Velodyne}$	0.9m
Transmitted Power	13dBm, 0dBm	$x_{Velodyne}$	-0.4m
Chirps Per Dwell	10	$z_{Rx_{1,300GHz}}$	1.05m
Dwell Time	11ms	$z_{Rx_{2,300GHz}}$	1.32m
Chirp Pattern	Repeated Up Chirps	$z_{Rx_{3,300GHz}}$	1.76m
Azimuthal Beamwidth	1.0-1.1°(3dB)	$z_{Rx_{79GHz}}$	1.55m
	1.4-1.5° (6dB)	$z_{Tx_{300GHz}}$	1.39 m
Elevation Beamwidth	6.2-7.0°(3dB)	$z_{Tx_{79GHz}}$	1.14 m
	8.8-9.1° (6dB)	θ_s	0.25°
		θ_R	-25.0° to 25.0°

range-azimuth 300GHz image between a and b. In the 3D image; section a appeared as a variety of different scattering centres at heights of $z \in [0.0, 4.0m]$ with RCS of σ =0 to 5dBsm. Section b appeared as centres of heights of $z \in [2.9, 4.1]$ m, and RCS of σ = -5 to 0 dBsm. Section c appeared as single bright scattering centres of 6dB height spread of $z \in [2.6, 3.4]$ m, and RCS of σ = 15dBsm. As the point response in z is predicted to be around 1m, one cannot say with certainty if $\bar{\sigma}(x', \theta_R, z)$ of sections b and c was coming from one or more scattering centres. However, the reconstruction of section a occupies a z extent roughly 3 times larger than this, and so one can say that reflections came from scattering centres over the surface of the rough wall. The results of this section suggest that this approach is clearly able to determine which sections of the bridge are safe for a vehicle to pass under.

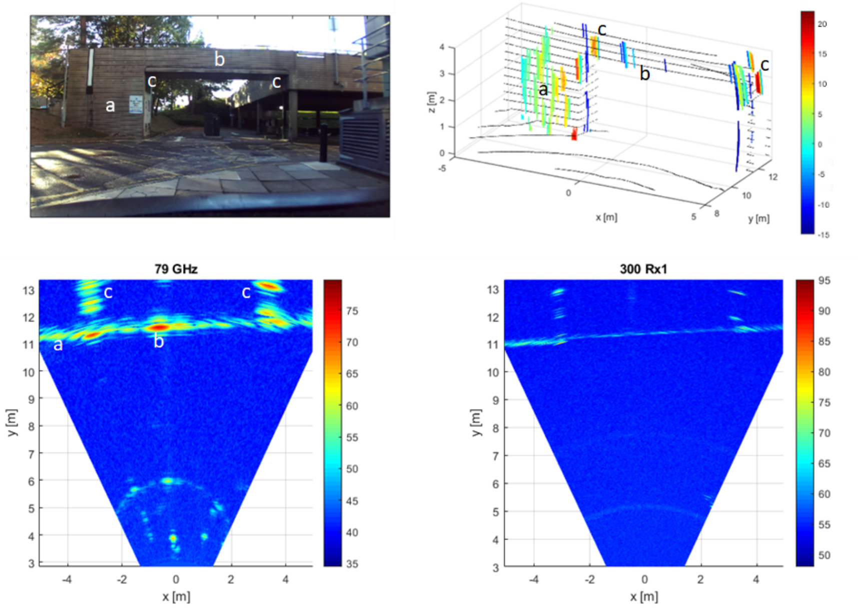

Fig. 6.20 Low Bridge: (top left) Zed Image, (top right) 3D reconstruction, (bottom left) 79GHz image, (bottom right) 300GHz image.

Another object of interest may be an arm barrier used to control entry of vehicles, such as the one shown in Figure 6.21. Here interesting sections of the images are annotated; the grassy verge (a), the arm (b), and the body of the arm restrictor (c). The velodyne lidar has 32 beams over an elevation field of view of 40° [61]. This is approximately 1.25° between beams, or $z = 0.26$m at a range of 12m. The arm of the barrier has a similar physical z extent, and hence may only be picked up by one vertical lidar beam. At this range, from Table 6.2 one would again predict a 6dB z extent of the point response to be between 1.0 and 1.7m at the furthest range. In contrast with the lidar, this obstacle appears reasonably bright in the 300GHz and 79GHz radar images. Although much of the information of section a has been thresholded out of the 3D radar image, the 2D radar images show a great deal of surface texture information. The centres which have been reconstructed in the 3D image of RCS of $\sigma \leq$ -6dBsm and $z \in [1.0, 2.3]$ m, are in keeping with the velodyne image. The arm (b) appears as a single scattering centre of RCS of $\sigma = 5$ dBsm, and height spread of $z \in [0.4, 1.7]$ m. The sign and body of the arm restrictors (c) appear as multiple different scattering centres of heights $z \in [1.2, 2.1]$ m, and RCS of $\sigma =$ -15dBsm. Even with the large extent in z, one can therefore successfully tell that these obstacles are impassable for the vehicle.

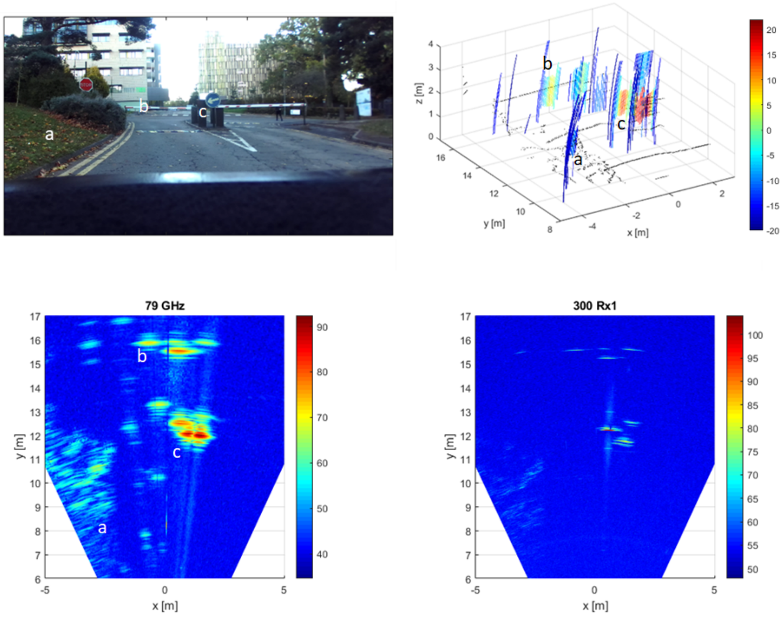

Fig. 6.21 Arm Barrier: (top left) Zed Image, (top right) 3D reconstruction, (bottom left) 79GHz image, (bottom right) 300GHz image.

Finally, this section considers the entrance to a multi-storey car park. This scene shows 3 overhead objects which appear relatively bright in a radar image in Figure 6.22. The facade of the entrance is in th plane $y = 12m$. At this range, from Table 6.2 one would again predict a 6dB z extent of the point response to be between 1.1 and 1.3m at the furthest range. For the height restrictor at $y = 6$ m, it should be half of this (approximately 0.6m). A parking height restrictor (a), the entrance to a building (b), and a metal frame with light fittings (c). The height restrictor had 3 main scattering centres (from left to right), the hanging sign (RCS of σ = -5dBsm, height of $z \in [1.6, 2.3]$ m, the point where the radar is normal to the surface (specular reflection) (σ =10dBsm,$z \in [2.4, 2.9]$ m), and the corner of the frame (σ =10dBsm, $z \in [1.8, 2.5]$ m). By contrast, the rougher bricks which make up the entrance to the car park (b) gave reflections across the entire surface of heights of $z \in [1.9, 3.3]$ m. Finally the fixtures (c) had 3 metal sections each with reconstructed heights of $z \in [1.9, 3.1]$ m, and RCS of $\sigma = 15$dBsm. Again, one can therefore tell that each of these obstacles can be driven under safely.

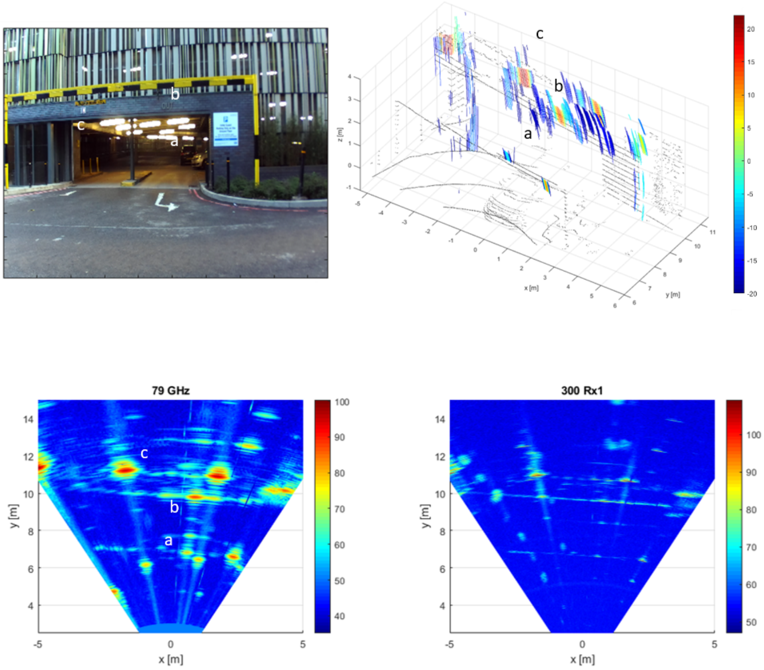

Fig. 6.22 Height Restrictor: (top left) Zed Image, (top right) 3D reconstruction, (bottom left) 79GHz image, (bottom right) 300GHz image.

The following section will conclude this chapter with a discussion of the experimental results.

6.8 Discussion of Results and Conlusion

This section has proposed that backprojection is a suitable method for augmenting a set of n_{Rx} scanned range-azimuth images into a 3D cylindrical polar image. The experiments in this section demonstrate how versatile this technique is to a variety of different setups, being demonstrated for short range imagery, actors moving slowly through a scene, and some key 3D road scenes. The predictions of the error and resolution of the system from section 6.3 at short range seemed to accurately estimate the observed height extent of the reconstructions at longer ranges for the moving pedestrians and the real road scenes (sections 6.6 and 6.7). There was also a very good agreement of the reconstructed RCS values of common road objects, such as the pedestrians between experiments. This means that this technique appears to be predictable and repeatable.

These measurements have been performed at ranges less than 20 m due to the low SNR, large data size, and the azimuth resolution of this demonstrator. The low SNR of the system is a limit from the current technology readiness level of low-THz radar rather than being a fundamental problem. At longer ranges the azimuth resolution will be improved with the ongoing development of azimuth refinement techniques such as SAR [130] and DBS [174]. The data size is more of an algorithm design issue, and there will be ways of optimising the backprojection process. One could, for example, look at detection before integrating over the n_{Rx} receivers. Although this would yield a lower gain, it would allow the process to eliminate regions which are known before hand to be only noise and exclude them from the reconstruction $\bar{\sigma}(x', \theta_R, z)$ (6.11).

The versatility of this process is one of the main strengths of backprojection. Compared to the multilateration in section 5, backprojection has some key advantages. Firstly, it gives some kind of extent of the target. Even if this may not correspond to the true surface of a target, the extent of the target in (x', θ_R, z) does convey the RMS error of the point response of the system. Also, multilateration relies on a threshold or peak fitting to detect the presence of a target in each range profile. By thresholding after backprojection, low-amplitude peaks which may have been filtered out from thresholding can still be integrated and can still assist the system in localising the target in 3D. Backprojection also intrinsically comes with a method of resolving which targets are real and which are ghosts. Much in the same way that multi-lateration for many Tx-Rx pairs will reconstruct multiple targets at the site of a real target and few at the site of a ghost target, a real target will appear brighter than the ghost targets as more Tx-Rx pairs will integrate the peak signal amplitude onto this position. While multilateration requires some kind of statistical test to cluster the reconstructed positions together, in theory, backprojection should reproduce a single target position which is much brighter than any of the ghosts.

This being said, backprojection in this form is not without its problems. Firstly, it is much more computationally intensive. Next, unlike multi-lateration, where the absence of a target in the range profile of a receiver simply meant that a target is not detected, if a range profile with no targets present is integrated, this is equivalent to simply adding more noise into the 3D reconstruction. Rather than a non-visible target just being a missed detection, it actively degrades the reconstruction of the other receivers by raising the noise floor of the $x'z$ image. Linked to this idea is the fact that each receiver has a different sensitivity. Therefore the SNR of a target depends on which Tx-Rx pairs detect the target. This should effect the choice of threshold in the connected components thresholding outlined in section 6.4.

There are also some fundamental questions in terms of the system response, including its RMS error and resolution, which need to be carefully considered. First of all, the connected component threshold procedure. Although this process worked well in giving a positional estimate of the target, is there a correct roll-off from the peak amplitude to consider? Is a target definitely inside the 3/6/10dB extent of the reconstructed peak, and is the region above and below this definitely free space? The method used here was only intended to generate a more easily readable image, and should not be taken seriously as an occupancy mapping technique. Much like thresholding, it does provide some rudimentary capabilities of segmenting which regions have no visible targets in them and which do. This is, however, poorly defined compared to methods which truly consider the system response (such as probabilistic models or compressive sensing models).

Building on this, the next section is going to explore whether or not it is possible to remove the large extent in x' and z from the image to try and create an image which more accurately reconstructs the RCS distribution of the world around it without the sidelobes of backprojection. With this, it is hoped that the technique will be able to reconstruct the full 3D profile of extended objects and achieve some degree of super resolution. This will be performed with an investigation into compressive sensing.

Chapter 7

Compressive Sensing

In the previous section, backprojection was presented as a flexible 3D imaging algorithm for low-THz automotive radar, however, it is not without its drawbacks. The most crucial of these is that the reconstruction of the target is a radar image with noise, and a broad point response in elevation. This makes it difficult to tell with any certainty what part of the image is a target and which is free space, which is a fundamental requirement for route guidance. This chapter will explore two algorithms which could improve upon this, based on compressive sensing and orthogonal matching pursuit (OMP). These kinds of techniques are often discussed as super-resolution algorithms, which is a concept which will be detailed later in this chapter. As can be seen below in the block diagram in Figure 7.1, these methods naturally generate a sparse image and do not require thresholding or post-processing of the 3D radar image.

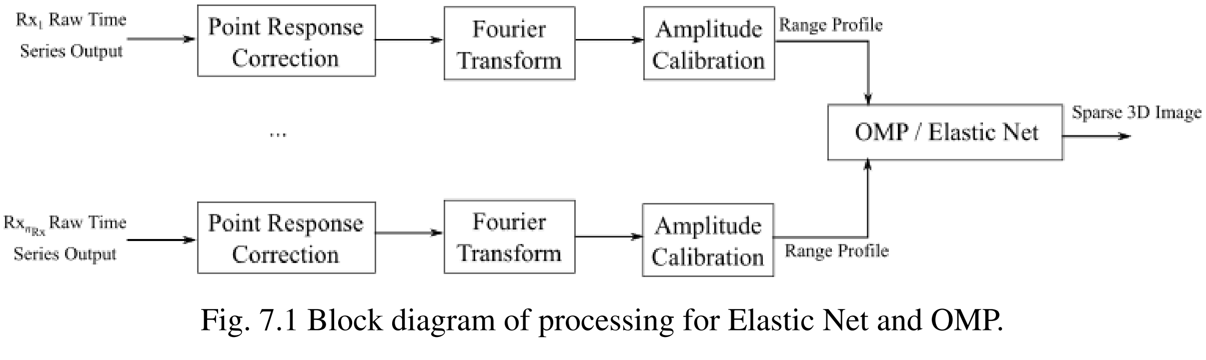

Fig. 7.1 Block diagram of processing for Elastic Net and OMP.

The chapter is laid out as follows. First, section 7.1 will introduce the notation of l_p norms required for this section. Section 7.2 will set up the radar imaging problem from the previous chapter as a linear inverse problem, as required by these algorithms. Section 7.3 then explores how this can be implemented in the radar system. Sections 7.4 and 7.5 define the orthogonal matching pursuit (OMP) and convex optimisation algorithms respectively. Section 7.6 tests these algorithms for a variety of SNR levels through simulations. Section 7.7 then performs both procedures experimentally, before section 7.8 provides a discussion of these results. Finally conclusions and further work are formulated.

Some of the results of section 7.7 were published in [175].

7.1 Lp Norms

This section will describe what is meant by different l_p norms of a vector. In signal processing, their primary use is as tools for generating solutions to under-determined mathematical problems (a topic known as regression [176]). These will be particularly important for a discussion of convex optimisation later in this chapter. Here, an l_p norm is defined for a generic vector, $\mathbf{x}$, which has n_x elements. The l_p norm is defined by some value, $p \in [0, \infty]$. l_p norms have a standard definition which is given by (7.1).

$$||\mathbf{x}||_p = \left(\sum_i^{n_x} x_i^p \right)^{\frac{1}{p}} \tag{7.1}$$

Although there are infinite l_p norms, five of the most commonly used ones are described in Table 7.1.

l_p	Description
l_0	Number of non-zero elements in the array.
l_1	Manhattan or taxi-cab norm, sum of absolute values of the array.
l_2	Euclidean norm, the total RMS values of the array.
l_∞	Maximum norm, the absolute maximum value of the array.
l_{TV}	Total variation, the sum of all gradients along the array.

Table 7.1 Summary of commonly used l_p norms.

That being said, there are two caveats to this list, which mean that the l_0 and l_{TV} norms are not l_p norms in a strict sense. The first being that the l_0 norm does not obey the property of homogeneity, where $||a\mathbf{x}||_p = a||\mathbf{x}||_p$ for a constant $a \geq 0$. The second being that the Total Variation (TV) norm does not match the normal form of (7.1), and instead TV-norms are defined as some variant of (7.2).

$$||\mathbf{x}||_{TV} = \sum_{i=2}^{n_x} |x_i - x_{i-1}| \tag{7.2}$$

At this stage it is worth noting which l_p norms are concave and convex. The l_p norm is convex if $p \geq 1$, as defined by to the triangle inequality [177]. This is illustrated in Figure 7.2, which shows a diagram of the l_p norm of $\mathbf{x}$ for a 2-element vector.

Finally this section will consider the meaning of a constraint such as $l_p(\mathbf{x}) \leq a$. For the list in Table 7.1, using this constraint means setting a particular property to be less than a. For example, for $p = 0$, this means that there must be a or fewer non-zero elements in $\mathbf{x}$. Depending on the exact equation, introducing a constraint on l_{TV} can smooth or denoise the signal, l_0 can enforce a level of sparsity, and l_1, l_2 and l_∞ are used to limit the total amplitude of the elements of $\mathbf{x}$. Section 7.5 will explore this further.

This section has introduced l_p norms. The following section will set up the imaging scenario as a linear inverse problem, in which we can use these definitions.

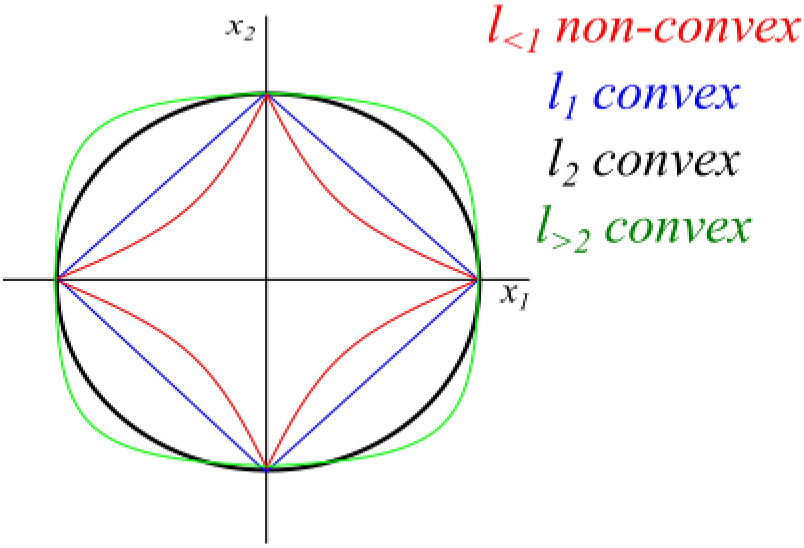

Fig. 7.2 Illustration of the l_p norms of two variables; x_1 and x_2.

7.2 Radar as a Linear Inverse Problem

In this section radar imaging problem from section 6.1 will be set up as a linear inverse problem, using the same definition of $\sigma(x,y,z)$ (6.1) as before. An inverse problem is any mathematical problem which tries to reconstruct a set of causes from a set of observed effects, which in this context means reconstructing the RCS distribution from a series of different range profiles. All the techniques in this thesis (in fact, all radar imaging techniques in general) are an attempt to solve underdetermined inverse problems - mathematical problems where the number of unknowns being solved for is greater than the number of known values. In the context of 3D imaging, physical 3D space is an infinite continuum of reflectivity coefficients, which are being measured and approximated from a finite set of digitised signals from a limited number of Tx Rx pairs.

As touched on in section 6.1, $\sigma(x,y,z)$ is taken to be free space apart from n_{tg} positions. But even for free space with a canonical target, which is known to have a small n_{tg}, the reconstruction from backprojection in section 6.3 showed $\bar{\sigma}(x,y,z)$ with all points as non-zero from noise or the point response of the system. This chapter examines some techniques which use the assumption that n_{tg} is far smaller than the number of voxels in $\bar{\sigma}(x,y,z)$, to create a better approximation of $\sigma(x,y,z)$.

What is unique about the algorithms in this chapter is that they require this to be formulated into a linear form as in (7.3).

$$\mathbf{s} = \mathbf{A}\mathbf{y} + \nu \tag{7.3}$$

Where the desired scene information is set up as a single vector, $\mathbf{y}$, of size n_y by 1. All of are observed signals are combined into a single vector, $\mathbf{s}$, which has size 1 by n_s. $\mathbf{A}$ is the measurement matrix which maps the amplitude of a pixel in $\mathbf{y}$ to a response in $\mathbf{s}$, of size n_s by n_y. It is assumed that the signal has been corrupted by AWGN which is described by the noise vector ν. $\mathbf{s}$ will be formed from the radar range profiles S_i (2.11), and $\mathbf{y}$ will be formed from $\sigma(x,y,z)$ (6.1). The exact way this is done is explored in section 7.3. Although a set of range profiles is being considered here, this description is very general, and this observed signal could just as well be in the time domain or be a spectrogram. Correspondingly the image grid does not need to be an evenly spaced grid per se. What is of the most importance is that there is a single measurement matrix, **A**, which maps the value of a given cell in **y** to its corresponding distribution in **s**.

There are some subtleties to this model. If a compressive sensing framework is going to applied to this, this model needs to meet the required levels of sparsity, isometry, and incoherence. Sparsity is perhaps the easiest to understand - if this process is expected to reconstruct K non-zero points in **y**, there needs to be more than K measurements in **s**. Using the description from chapter 6, this requires that for $K = n_{tg}$ points where $\sigma(x,y,z) \neq 0$, there must be greater than n_{tg} range cells observing the space in (x,y,z). As shown in section 7.1, if the l_0 norm of **y** is K (7.1), $||\mathbf{y}||_0 = K$, then the array has K non-zero elements. Another way to express this is that **y** is K-sparse.

The next is that this mapping using **A** should obey the restricted isometry property (7.4).

$$(1-\delta_s)||\mathbf{y}||_2 \leq ||\mathbf{A}\mathbf{y}||_2 \leq (1+\delta_s)||\mathbf{y}||_2 \tag{7.4}$$

Where $\delta_s \in (0,1)$ is a constant. Most compressed sensing recovery algorithms are defined to recover the sparsest solution to $\mathbf{s} = \mathbf{A}\mathbf{y}$, if **A** acts sufficiently close to an isometry [178]. Finally is the property of incoherence, which put simply, means that the rows of **A** must not be able to sparsely represent the columns of **A**, and vice versa [179]. Therefore the value at one cell in **y** should not influence the value at another cell.

This section has defined what a linear inverse problem is, and how the radar imaging problem can be expressed this way. The following section will look at how this can be implemented for the 3D imaging scenario.

7.3 Implementation

This section looks at how to implement the 3D imaging scenario from chapter 6 as a linear inverse problem. This formulation is going to be applied to the 2D imaging scenario in the $x'z$ plane, with the scanned Tx-Rx stack setup from section 5.3 and chapter 6.

The goal of the techniques in this section is to reconstruct a radar image matrix $\sigma(x', \theta = \theta_R, z)$ (6.1) from the set of range profiles S_i (2.11), when each Tx-Rx pair are coaligned at some scan angle θ_R. The way this is formulated into a linear inverse problem is illustrated in Figure 7.3.

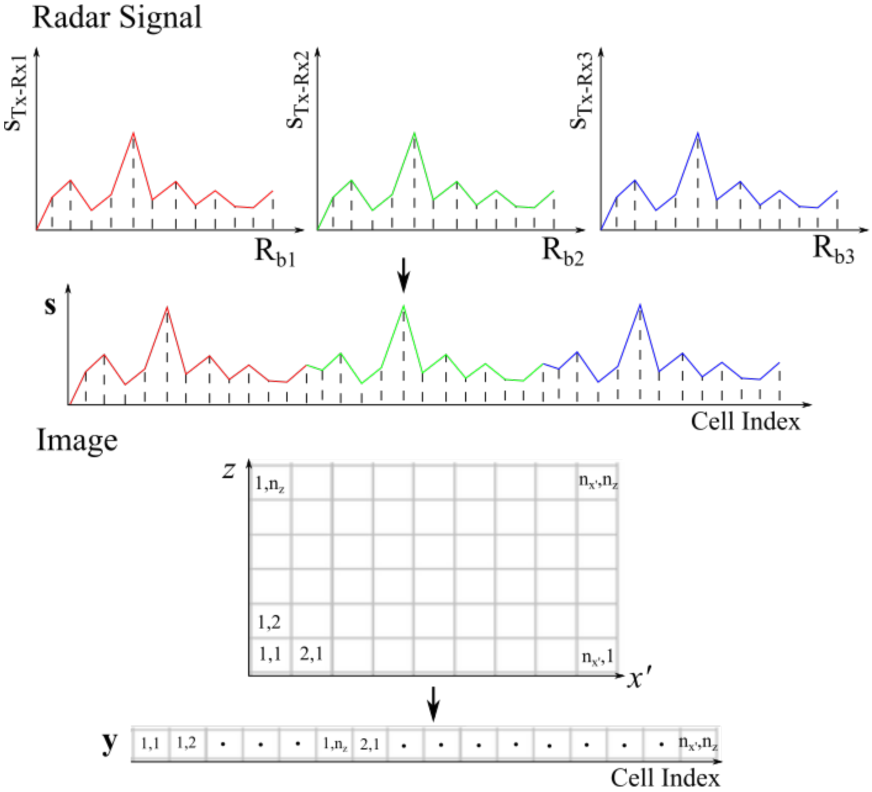

Fig. 7.3 Setting up the $x'z$ imaging problem from multiple range profiles as a linear inverse problem. (top) concatenating the range profiles, and (bottom) reshaping the $x'z$ image.

For the reconstruction in (x', z), the region has a smallest bistatic range R_{min_i} and largest range R_{max_i} for the i^{th} Tx-Rx pair (2.2). Where $i = 1, \dots, N_{TxRx}$. The signal vector, $\mathbf{s}$, is formed through concatenating the range profiles of each Tx-Rx pair which are measuring the scene at $\theta = \theta_R$ (7.5).

$$\mathbf{s} = \left[S_1(R_{min_1}), \ldots, S_1(R_{max_1}), S_2(R_{min_2}), \ldots, S_{N_{TxRx}}(R_{max_{N_{TxRx}}})\right] \tag{7.5}$$

The desired scene to be reconstructed, $\sigma(x', z)$, is reshaped from a 2D matrix into a single 1D vector, $\mathbf{y}$. The results of section 3.4 confirm that the noise present is additive and white, and so ν is a suitable description for the radar system.

In the formulation of backprojection in chapter 6, if the range profile of each Rx had undergone an amplitude correction (6.15) the backprojection operator estimated the mean RCS of a target (6.11). By contrast, many of the techniques used in this chapter apply constraints to $\mathbf{y}$ to achieve some kind of enhanced resolution, but in doing so greatly vary the amplitude of the reconstruction. Therefore the RCS values of $\mathbf{y}$ (7.3) will not be anything like the RCS values of (6.11). The images in this chapter are typically either normalised with respect to a maximum value of $\mathbf{y}$, or are left with uncalibrated Rx amplitudes, so as if $q_i = 1$ in (6.15).

The interesting part of this formulation is how to design the matrix $\mathbf{A}$ which maps the values of $\mathbf{y}$ onto $\mathbf{s}$. At first glance, the best approximation appears to be (2.11) where the amplitude of the signal is defined by (2.18). But this introduces the same problem of antenna patterns as weighting by G^{-1} had before (6.9), in that the nulls create singular regions in the reconstruction, which breaches the restricted isometry property (7.4). If one uses (2.18) and (6.7) to define the measurement matrix, $\mathbf{A}$, inverting $\mathbf{A}$ to generate $\mathbf{A}^{-1}\mathbf{s}$ is equivalent to using backprojection operator (6.11).

Largely speaking, the approximations used for the backprojection technique in sections 6.1-6.3 are the same as those used here. Firstly, a major assumption is that the backscattered radiation from $\sigma(x', z)$ is approximately isotropic. This was important for backprojection, but it becomes even more relevant here, as will be seen later in this chapter. Another point of interest is that the elements of $\mathbf{y}$ do not interact with one another, much like scattering centres in $\sigma(x', z)$ did not interact with one another. There are therefore some effects which both formulations ignore, which includes shadowing and multipath signals, which are dependant on the existence of other scattering centres in an image. Indeed, although one could use the flat earth model of propagation loss (2.17), this implicitly assumes that there is a plane of asphalt at $z = 0$m. Finally there is the question about the grid itself. Although it is true that there is no need for any one particular grid setup if the mapping between $\mathbf{y}$ and $\mathbf{s}$ meets the criteria of section 7.2, it does introduce a number of additional considerations. The surface area of an ellipsoid increases radially, and so the number of points in the $x'z$ grid which lie in the ellipsoidal shell (5.2) between R_b and $R_b + R_{res}$ is variable. Depending on the region in the $x'z$ plane, and the values of R_b chosen, a range cell may correspond to no points in the image, or a great many points in the image. This can be mostly fixed by range gating S_i between R_{min_i} and R_{max_i} which will remove the range cells with no points $\mathbf{p} \in \mathbf{E}(R_{b_i}, \mathbf{p}_{Rx_i})$. However, there is no guarantee that this formulation can be considered as an isometry (7.4).

This section has introduced how to form the backprojection imaging problem into a linear inverse problem, the following section will look at how to solve this equation using OMP. The measurement matrix $\mathbf{A}$ used in this chapter is dependant on a number of features of OMP and compressive sensing. Therefore the measurement matrix used is defined in the following section within the context of OMP.

7.4 Matching Pursuit

This section lays out a matching pursuit algorithm, using the assumption that $\sigma(x', \theta = \theta_R, z)$ has n_{tg} non-zero values. Using an integer $K \approx n_{tg}$, this means that it is taken that $\sigma(x', \theta = \theta_R, z)$ (6.1), and hence $\mathbf{y}$ (7.3), is K-sparse. There is a very simple way to ensure that $\mathbf{y}$ is K-sparse, and that is to only introduce K non-zero points into the array one by one. This approach belongs to the family of algorithms called basis pursuit or matching pursuit, which iteratively introduce non-zero values into $\mathbf{y}$ by examining the discrepancies between $\mathbf{Ay}$ and $\mathbf{s}$. Specifically, this section examines the application of the Orthogonal Matching Pursuit algorithm (OMP) to this linear inverse problem [180].

For this process to work, the mutual coherence, μ, of $\mathbf{A}$ must be small for it to be considered orthogonal [181]. This is given by (7.6). Assuming its columns are normalised, a matrix can be considered incoherent if $(n_s n_y)^{-\frac{1}{2}} \leq \mu \leq 1$ [181]. Typically the diagonal elements of $\mathbf{A^T A}$ are ignored in this discussion.

$$\mu = \max |\mathbf{A^T A}| \tag{7.6}$$

There is an easy way for $\mathbf{A}$ to satisfy this constraint for the imaging scenario in this section. If one considers the discretised form of the backprojection operator with nearest neighbour interpolation (6.11), ignoring discussions of beam patterns and path loss this can be set up as (7.7). For a position (x', z), the corresponding column in $\mathbf{A}$ will only have relatively few non-zero values. These will occur at the bistatic range indices whose ellipsoids overlap at (x', z). Therefore in $\mathbf{A^T A}$, the vast majority of values will also be zero, and the only level of mutual coherence will come from the regions of overlap of these ellipsoids. μ will satisfy the incoherence criterion as long as the image grid of (x', z) does not drastically oversample the ground-range and height axes to the resolution of (5.12) and (5.13). One must be careful with this effect, however, as if the $x'z$ grid dramatically undersamples the range profiles, then $\mathbf{A}$ no longer satisfies the restricted isometry property (7.4). Therefore one must choose a range gate and a suitable grid size to satisfy both of these criteria.

$$\mathbf{A}(x', z, R_{b_i}) = \begin{cases} 1, & \left|\sqrt{x'^2+z^2}+\sqrt{x'^2+(z-z_{Rx_i})^2}-2R_{b_i}\right| \leq 2R_{\text{res}} \\ 0, & \text{otherwise} \end{cases} \tag{7.7}$$

A point of note here is correlated values of **s** according to **A**. There is an underlying correlation for this setup, both in range and between Rx signals which is explained here. According to the range profile model (6.7), at a bistatic range R_{b_i}, the imaging algorithm has a known maximum power $S_i(R_{b_i})$ which it can distribute between points in the region bound by the ellipsoids $\mathbf{E}(R_{b_i})$ and $\mathbf{E}(R_{b_i}+R_{res})$ (5.2). Therefore the measurement matrix based on this (7.7) means that the choice of values in **y** between $\mathbf{E}(R_{b_i})$ and $\mathbf{E}(R_{b_i}+R_{res})$ effect one other, and are hence correlated. Similarly, (7.7) is designed for an isotropic RCS distribution, **y**, and so if one Rx detects a scattering centre, it is assumed that the other Rx sites also detect this scattering centre. There is therefore also some correlation in **s** for the region defined by $S_1(R_{min_1}),\ldots,S_1(R_{max_1})$, and $S_2(R_{min_2}),\ldots,S_2(R_{max_2})$ and so on (7.5).

Now that the measurement matrix has been set up, the OMP algorithm can be employed. This method introduces an additional non-zero point into the image **y**, one at a time, by examining which point it could introduce to minimise the residuals. The residuals are defined by an l_2 norm (7.8).

$$h(\mathbf{s},\mathbf{A},\mathbf{y}) = ||\mathbf{s}-\mathbf{A}\mathbf{y}||_2 \tag{7.8}$$

A simplified version of [180] is shown in Algorithm 7.1.

This procedure will produce a set of n non-zero values in **y** which are represented in the set Γ. The reason this is performed rather than re-weighting non-zero indices in **y** with each iteration, is that the latter is not guaranteed to produce a sparse solution.

The algorithm above is a greedy algorithm, because for each loop (steps 2-6), it seeks to deliver the maximum decrease in h (7.8) for the introduction of an additional point into **y**. Typically greedy algorithms such as this are fast, and tend towards a solution of **y** which is a local minimum of h, but may not necessarily be the global minimum. In other words, the solution which delivers the best dh for $n = 1$, then

Algorithm 7.1 : Orthogonal Matching Pursuit

```
1. Initialise the problem with all $\mathbf{y}$ values as 0, and with an iterator $n = 1$. An empty atomic index set $\Gamma$ will be used to introduce non-zero values into $\mathbf{y}$.
2. Calculate the residuals with $\Gamma$ as the non-zero values in $\mathbf{y}$: $h = \sqrt{\mathbf{s}^2 - (\mathbf{A}\mathbf{y})^2}$
3. Find the index which solves the optimisation problem: $i = \text{argmax}|h|$
4. Solve the least square problem to generate a non-zero index at position $i$: $\gamma_i = \text{argmin}_i||\mathbf{s} - \mathbf{A}\mathbf{y}||$
5. Augment $\Gamma$ to include $\gamma_i$: $\Gamma = \Gamma \cup \gamma_i$
6. If the stopping criteria have not been met, return to step 2, and increase $n$ by 1.
```

$n = 2, \ldots, n = K$, may not reconstruct the best possible $\mathbf{y}$ with K non-zero points. In the context of OMP, it has been shown that it approximates the best solution relatively well [182].

The final consideration to using this algorithm is the stopping point in step 6 above. One of the simplest ways is to predefine K visible scattering centres in $\mathbf{y}$ are present in a scene, and to stop when $n = K$. Of course, this is highly unrealistic, because the exact value of $K = n_{tg}$ is almost certainly unknowable a priori for any given scene. Another idea could be to look at how the residuals, h (7.8), change with each iteration. Once the number of iterations have been reached for while the residuals are no longer decreasing $,\frac{\Delta h}{\Delta n} \geq 0$, this is a natural last resort stopping point. The noise of the signal, ν, may help define a more useful stopping point here. Below the noise power of the signal (2.12), the amplitude of the signal is no longer clearly deterministic. Therefore one could define a threshold, such that the amplitude of the point described by γ_i is greater than this threshold.

This section has defined the OMP algorithm which will be applied to radar imaging in the $x'z$ plane. The next section will explore a convex optimisation method which will be explored alongside this.

7.5 Convex Optimisation

This section will explore convex optimisation as an alternative to the OMP method outlined in the previous chapter. Thanks to the development of convex optimisation solvers [183, 184], there is an alternative to the matching or basis pursuit introduction of scattering centres into $\mathbf{y}$. These solvers are versatile tools for solving linear equations of the form of (7.3). The same definitions of $\mathbf{s}, \mathbf{A}$, and $\mathbf{y}$ are used here as were used for OMP (7.3,7.5,7.7).

It is important to detail why one should consider a solver as opposed to a greedy algorithm, such as OMP [182]. When OMP introduces a point γ_i into $\mathbf{y}$ at a step $n = i$, this voxel in the image remains constant for the iterations $n = i + 1, \ldots, K$. This is ultimately why the solution of $\mathbf{y}$ does not get readjusted to find the best solution with K non-zero points.

Solvers on the other hand typically operate using some kind of coordinate descent algorithms, like many modern machine learning or optimization algorithms [185]. With every iteration, every point in $\mathbf{y}$ is iteratively reweighted and adjusted to come closer and closer to the value of $\mathbf{y}$ which best fits some kind of constraint equation. The stopping point is instead defined by some minimum tolerance on the constraint equation. This means that typically these algorithms are slower, but are more likely to reach the global best solution to $\mathbf{y}$. What constitutes a constraint equation and how to set one up for the radar imaging problem is considered here.

Typically most constraint equations find the minimum l_2 error, like the residuals h for OMP (7.8), but with an additional l_p norm used to find a solution with another property, such as sparse solutions of $\mathbf{y}$. Another consideration is the utility of these l_p norms (7.1). Namely, does the l_p norm provide a tractable and stable solution to $\mathbf{y}$? This ultimately comes down to whether these functions are concave or convex. Many linear, quadratic, and second-order cone programs make use of assumptions based on the fact that these distributions are convex, which are used to solve these problems quickly and effectively. Some widely used examples of such solvers are l_1 magic [186] and CVX [187]. Therefore $p \geq 1$ distributions are the easiest to solve, but as we will see below, they have some undesirable attributes.

Two of the most commonly used algorithms with l_p constraints used in statistics are Lasso [176] and Ridge-Regression [188]. These make use of a l_1 and l_2 norm regularisation term respectively. The way in which these l_p normalisation processes work is illustrated in Figure 7.4, which is taken from [189]. Consider the under-determined equation $g(x)$ in Figure 7.4. Any point along the line $g(x)$ is a valid solution to the linear inverse problem for the two variables, $\mathbf{x} = (x_1,x_2)$. One way to select a single solution on the line $g(\mathbf{x}) = 0$ is to find the point which minimises the l_1 norm, P, and the the l_2 norm, Q. P has one non-zero value, whereas Q has both x_1 and x_2 being non-zero. Due to its shape matching the triangle inequality between convex and concave, the l_1 norm has been proven to be able to approximate the sparsest solution [189], which is the solution with the smallest l_0 norm. On the other hand the l_2 norm is almost guaranteed to generate a non-sparse solution. The difficulty in finding a sparse solution to $\mathbf{x}$, is that finding the solution with the smallest l_0 norm is not a directly solvable quantity. Combined with the fact that $p \geq 1$ norms are the most easily solvable, the l_1 norm combines the best of both worlds - a solution which is easily solvable and is likely to be sparse. This idea is extended into higher-dimensional space, for signals with many variables ($\mathbf{y}$), rather than just two ($\mathbf{x}$).

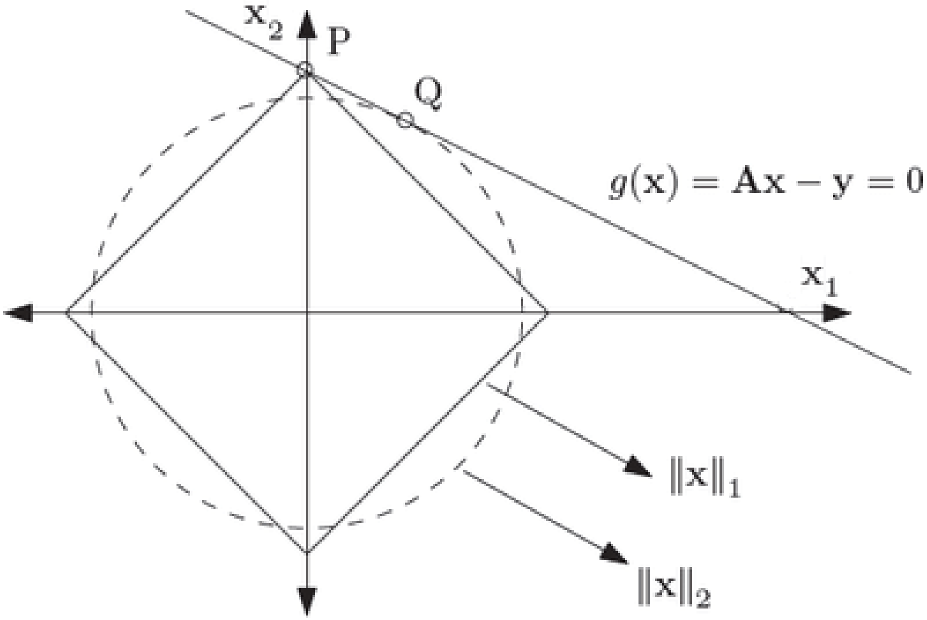

Fig. 7.4 Illustration of l_1 and l_2 norms applied to an under-determined linear equation for two variables; x_1 and x_2.

The imaging problem can be considered much like Figure 7.4, but for n_y unknowns instead of 2. This is shown in (7.9). The system of equations is trying to find the best least-squares (l_2) solution of $||\mathbf{s} - \mathbf{A}\mathbf{y}||_2$ subject to an additional constraint placed on $\mathbf{y}$, which keeps $||\mathbf{y}||_p$ under a certain value, ς. The example shown in Figure 7.4 is the smallest value of ς which generates the solution closest to $||\mathbf{s}-\mathbf{A}\mathbf{y}||_2 = 0$.

$$\underset{\mathbf{y}}{\operatorname{argmin}} ||\mathbf{s}-\mathbf{A}\mathbf{y}||_2 \quad \text{subject to} \quad ||\mathbf{y}||_p \leq \varsigma \tag{7.9}$$

Although this is the purest way of formulating this problem, it is not necessarily the easiest one to solve computationally. An alternative way of setting this up is to introduce a hyperparameter, $\lambda \propto \varsigma^{-1}$. This allows us solve a single equation (7.10).

$$\underset{\mathbf{y}}{\operatorname{argmin}} \left(||\mathbf{A}\mathbf{y}-\mathbf{s}||_2 + \lambda ||\mathbf{y}||_p \right) \tag{7.10}$$

It is also possible to consider multiple constraints at once, as can be seen below. One of the most widely used formulations of this is Elastic Net (7.11) which finds the solution of **s** with the minimum l_2 error, but subject to constraints to both the l_1 and l_2 norms of **y** [190]. This formulation includes Lasso and Ridge regression as special cases (7.11).

$$\underset{\mathbf{y}}{\operatorname{argmin}} \left(||\mathbf{A}\mathbf{y}-\mathbf{s}||_2 + \lambda \left(\alpha ||\mathbf{y}||_1 + \frac{1-\alpha}{2} ||\mathbf{y}||_2 \right) \right) \tag{7.11}$$

The hyperparameters λ and α tune the amount of regularisation, and the proportion of l_1 vs l_2 regularisation respectively. Tuning the value of λ is equivalent to deciding the amplitude of noise and artefacts which can remain in **y**, (the higher the value of λ, the lower the noise level in the reconstruction). Lasso ($\alpha = 1$) excels at generating sparse solutions, but handles correlated values in **y** poorly, whereas ridge regression ($\alpha = 0$) does the opposite of this. Therefore a combination of both techniques is used here to generate a solution which is sparse enough to map out free space, but not over-sparse such that extent information of targets is lost.

$$\underset{\lambda \in \mathbb{R}, \alpha \in [0,1]}{\operatorname{argmin}} \quad ||\mathbf{A}\mathbf{y}(\lambda,\alpha)-\mathbf{s}||_2 \tag{7.12}$$

The value of these hyperparameters are chosen through cross-validation of the solution of $\mathbf{y}$ generated from (7.11) in the formulation below (7.12). α has a relatively small domain to search through compared to λ which has an infinite domain. The largest value of λ to undergo cross-validation is found as the value which just zeros all coefficients of $\mathbf{y}$, and is decreased from this value (which as it is the sparsest values, is likely to be the point of interest). The only exception to this process is that one must avoid the global minimum of this function (7.12) which occurs at $\lambda = 0$, where the solution is by definition the one which minimises the l_2 error. Instead we are looking for local minima in the hyperparameter space which generates a sparse solution.

This section has outlined Elastic Net as an alternative to OMP, and detailed how it can be applied to the radar imaging problem. In the next section these techniques will be applied in simulations of a target at short range, and tested using different target SNRs.

7.6 Simulations

In this section, OMP and Elastic Net are applied in simulations to test their ability to reconstruct a target at short range. These techniques are understood to be highly sensitive to the SNR of the target, and so through simulations the SNR can be varied for a point target at the same position.

These simulations make use of $n_{\text{TxRx}} = 5$ Tx-Rx modules, which each take one measurement of a single point target at $\mathbf{p}_{\text{tg}_1}$ = (5.0, 0.3) m. The full list of parameters are shown in Table 7.2. The target is taken to have a return of unit amplitude in each range profile, and the SNR is variable.

Table 7.2 Parameters used in the simulations of compressive sensing techniques.

Parameter	Value
Sweep Bandwidth	18 GHz
Target Amplitude A_{IF}	1
SNR	20, 10, 6 dB
n_{TxRx}	5
$\mathbf{p}_{\text{TxRx}_{1,2,3,4,5}}$	(0, 0), (0, 0.15), ... , (0, 0.60) m
$\mathbf{p}_{\text{tg}_1}$	(5.0, 0.3) m
TxRx Separation	0.04 m
R_{Res}	8.3mm

For both OMP and Elastic Net, the signal was formed into a single signal vector (7.5), which is shown below in Figure 7.5a. Backprojection can be applied to the range profiles in Figure 7.5a, which can be used to generate the image in Figure 7.5b. These specifically show the case for SNR = 20 dB. This can be used as a benchmark to compare the image generated using OMP and Elastic Net. It is known that $n_{tg} = 1$, but this response has a broad point response in z, and this response may be improved if one assumes some level of sparsity in the image.

Let us first consider the reconstruction using Elastic Net, which are shown in Figure 7.6. The residuals (7.8) are shown as a function of the hyperparameter, λ, in Figure 7.6a. The residual error (7.8) appears

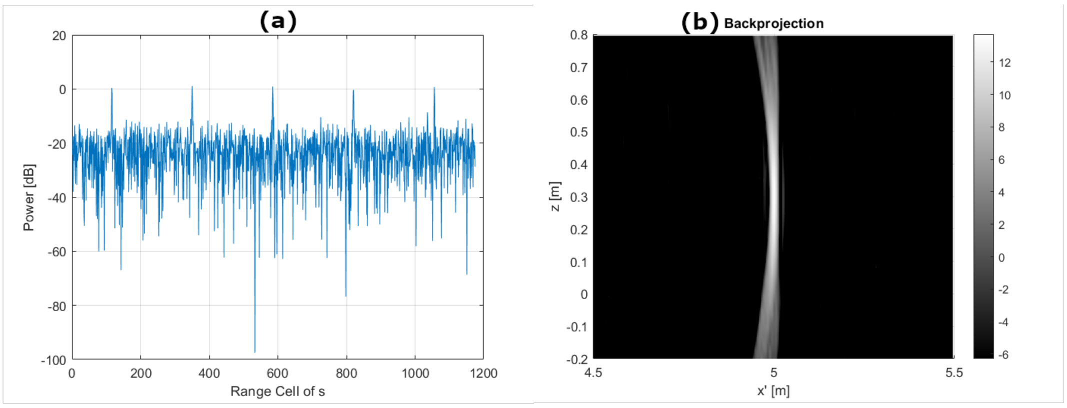

Fig. 7.5 Signal vector for 5 Tx-Rx modules for an SNR of 20 dB.

higher for lower SNRs - the higher the comparative noise level, the higher the residual error. Looking at (7.11), when $\lambda \to 0$, the solver naturally tries to minimise the l_2 residual error (7.8) without additional constraints. Therefore it is unsurprising that smaller λ give a smaller residual error. However, the reconstruction using smaller λ is noisy and not sparse. Therefore the values of λ used to generate the reconstructions in Figure 7.6b-d is $\lambda \approx 0.1$, which is the value of λ which was chosen just before the error plateaus.

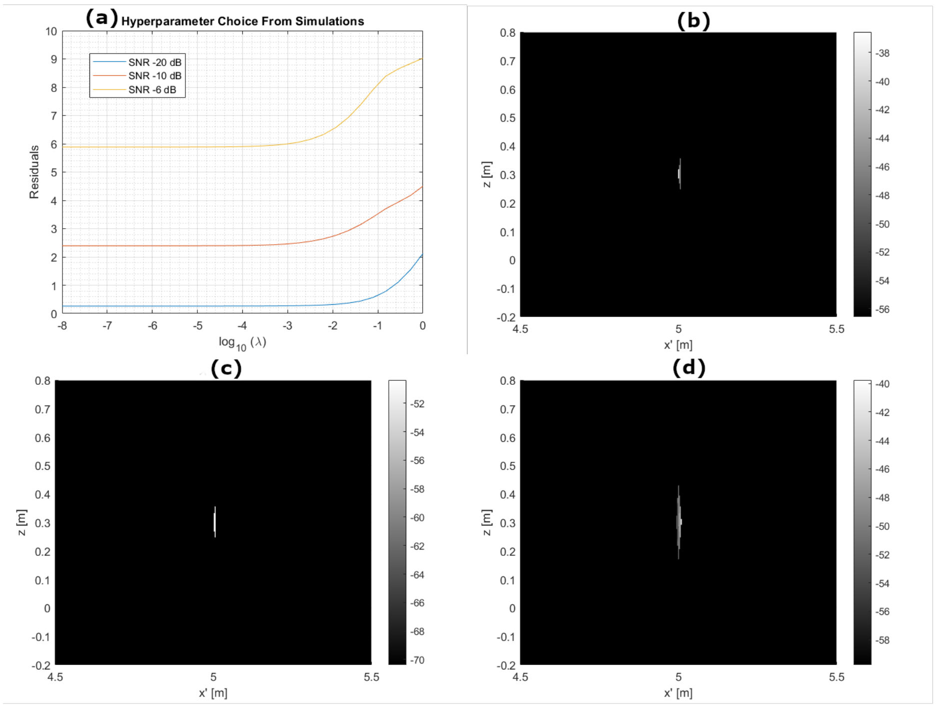

Fig. 7.6 Simulations of Elastic Net. (a) Hyperparameter selection. Image reconstruction for an SNR of (a) 6 dB, (b) 10 dB, (c) 20 dB.

Let us examine what these residual errors look like for OMP, which are shown in Figure 7.7. The residuals shown in Figure 7.7a are much higher for lower SNRs, as was seen for Elastic Net in Figure 7.6a. What is particularly interesting for OMP is how each successive point introduced into the image changes the residual error, which is shown in Figure 7.7b. For the higher SNR cases, the first point introduced into the image has a large change in the residuals, and then the subsequent points have a much smaller impact. Introducing the first point scatterer into the image greatly reduces the residuals, and subsequent points are less important. On the other hand, for the SNR of 6 dB this difference is less pronounced.

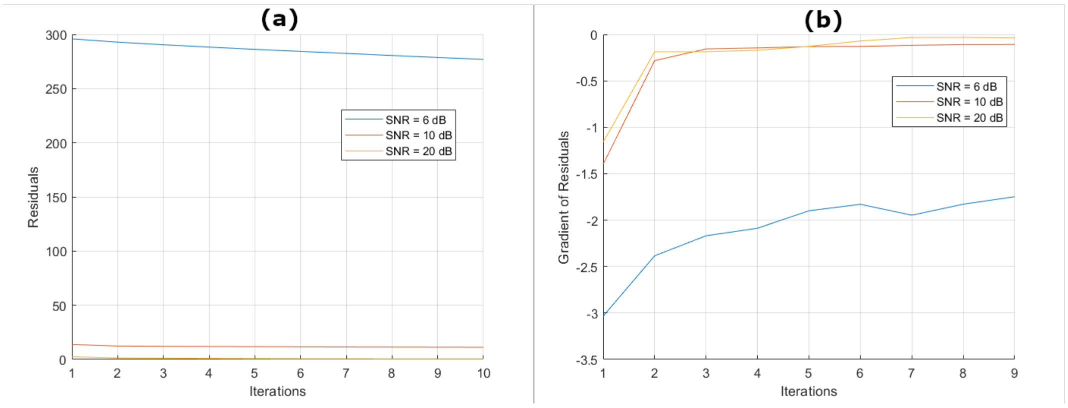

Fig. 7.7 Residuals for OMP. (a) total residuals, (b) change in residuals per point introduced.

The reconstructions along the z axis for OMP, convex optimisation, and backprojection are shown in Figure 7.8. In each case the first 10 points for the OMP reconstruction are shown, and $\lambda = 0.1$ in each case. For OMP, the highest noise in Figure 7.8a, the brightest point is at the target location, and the other 9 points are randomly distributed in the noise. By contrast, in Figure 7.8c, the first point is the same, but the other 9 points are centrally clustered around the target position. For Elastic Net, this is just reconstructed as a point target at the target position for a low SNR, and for a higher SNR this generates a set of clustered points around the target.

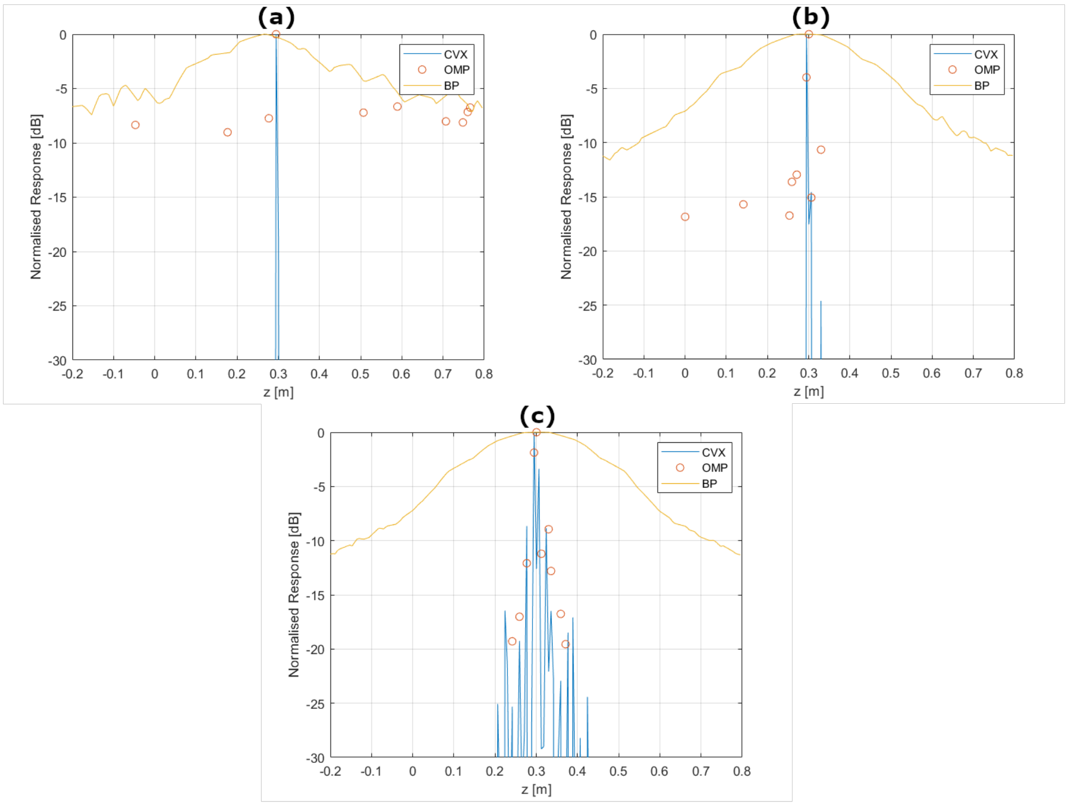

Fig. 7.8 Height profile from OMP, Elastic Net, and Backprojection. SNR of (a) 6 dB, (b) 10 dB, (c) 20 dB.

This section has investigated how the point response of OMP and Elastic Net compare for different SNRs through simulation. The following section will detail the experimental investigations into these methods.

7.7 Experimental Validation

This section will detail the experimental implementation of both OMP and Elastic Net into real-world 3D imaging scenarios.

Ideally, one would use the same radar data as the experiments in section 6 to test these algorithms, but there was one glaring issue with using the implementation as discussed in section 7.3. This came from concatenating n_{Rx} range profiles into the vector $\mathbf{s}$ (7.3). Because each Rx module has a different loss, L_i, after calibration to a reference target, it appeared as though each Rx had a significantly different noise floor (see Table 3.3). This is shown in Figure 7.9, as the range profiles of each Rx which are measuring a 4cm corner reflector, using the setup from section 6.3. In this figure, the indices 1-1400 correspond to Rx_1, 1400-2800 to Rx_2, and 2800 onwards to Rx_3. In this figure, the mean amplitude of the noise of Rx_3 (2.12) is approximately the same as the peak amplitude of the CR in Rx_2 (2.18). The signal in orange $\mathbf{s}$, where the Rx signals are the raw output of the process described by section 3.2, with no compensation as if $q_i = 1$ (6.15). The blue curve shows the case where each range profile S_i (2.11) has been normalised with respect to a corner reflector.

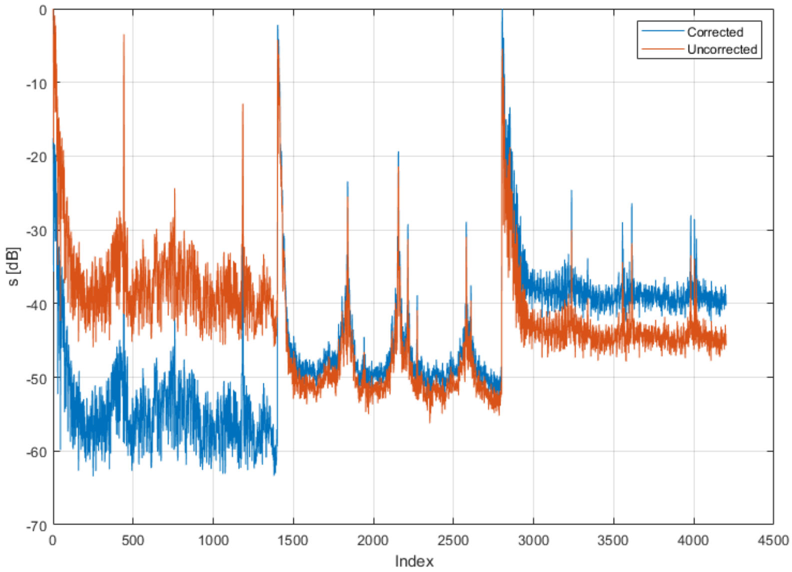

Fig. 7.9 Signal vector $\mathbf{s}$ of a corner reflector from the concatenation of the range profiles of each Rx.

It was shown in the previous section that both OMP and Elastic Net were highly dependant on the SNR of the system, but the SNR was the same for each Rx in the simulations. For the resultant signal in blue, Rx_1 has the lowest SNR and Rx_3 has the highest SNR which matches the measurements in section 3.4. Although there is no longer a large disparity between the received power from the corner reflector between the three receivers, one now has to deal with the fact that $\mathbf{s}$ has multiple distinct regions with different noise figures.

This is problematic for a number of reasons. First, OMP (Algorithm 7.1) and Elastic Net (7.11) both use the SNR (2.12). OMP uses it to define the stopping criteria, and Elastic net uses it to define the hyperparameter λ. With a variable noise floor in $\mathbf{s}$, it is difficult to define these features reliably. Next, the isotropy assumption which underpins $\mathbf{A}$ (7.7) means that the signal of each Rx in $\mathbf{s}$, is correlated such that $S_1(R_{min_1}),\ldots,S_1(R_{max_1})$ and $S_2(R_{min_2}),\ldots,S_2(R_{max_2})$ (and so on) are correlated. Therefore if there is a peak in $S_1(R_{min_1}),\ldots,S_1(R_{max_1})$ at a set value of R_{b_1}, but the noise floor has a similar amplitude in $S_2(R_{min_2}),\ldots,S_2(R_{max_2})$ for all R_{b_2}, then a point scatterer could be placed at any location along $\mathbf{E}(R_{b_1},\mathbf{p}_{\text{Rx}_1})$ (5.2), which would disrupt the reconstruction.

With this in mind, the experiments are split into two separate cases. In section 7.7.1, a single Rx unit is used to recreate the simulations in the previous section. A signal is taken from different Rx positions and time multiplexed. In section 7.7.2, all 3 Rx units are used. In these measurements, the results of OMP and Elastic net will be compared with bilateration and backprojection.

7.7.1 Single Rx

This section covers the results of measurements for a time multiplexed system. To test the three algorithms the TxRx height finding setup was mounted on a linear positioner, with carpet placed on the floor to prevent ground reflections. This is shown in Figure 7.10, and the parameters used are shown in Table 7.3. Due to the available number of transmitters and receivers, it uses a single Tx Rx setup. The multiple positions are generated through time multiplexing the signals from a set of static Tx Rx sites. There are three fundamental abilities these techniques should impart to this system. To be able to reconstruct the position of a simple target, to resolve the position of two nearby simple targets, and to be able to estimate

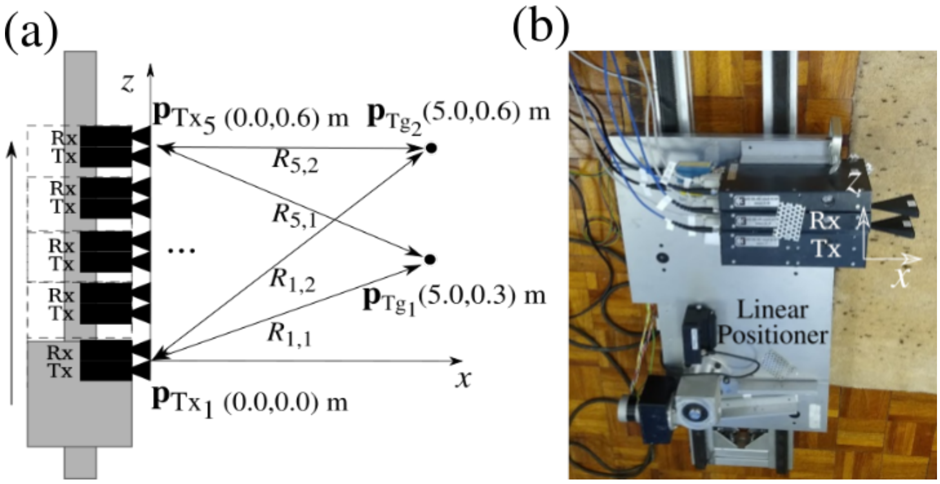

Fig. 7.10 (a) Diagram and (b) picture of experimental setup of the radar on a linear positioner.

the extent of an extended target. To test these abilities the system has been setup to measure a single corner reflector (CR), two CRs separated in z, and an extended rough metal suitcase. To exemplify this process, $n_{TxRx} = 5$ has been used here.

The targets and the Tx-Rx sites were all aligned in a single plane, which is considered to be the $x'z$ plane, so positions are given as $\mathbf{p} = (x', z)$ in this section. These experiments consider 5 TxRx monostatic positions denoted $\mathbf{p}_{\mathrm{TxRx}_{1,\ldots,5}}$, and 2 target positions denoted $\mathbf{p}_{\mathrm{tg}_1}$ and $\mathbf{p}_{\mathrm{tg}_2}$.

Table 7.3 Parameters used in the experimental comparison of compressive sensing techniques.

System	
Sweep Bandwidth	18GHz
Chirps Per Dwell	30
Dwell Time	33 ms
Noise Figure	13dB
Chirp Pattern	Repeated Up Chirps
Elevation Beamwidth	1.0°(3dB), 1.4° (6dB)
Azimuthal Beamwidth	7.0°(3dB), 8.8° (6dB)
Topology	
n_{TxRx}	5
$\mathbf{p}_{\mathrm{TxRx}_{1,2,3,4,5}}$	(0, 0), (0, 0.15), ... , (0, 0.60) m
$\mathbf{p}_{\mathrm{tg}_1}$	(5.0, 0.3) m
$\mathbf{p}_{\mathrm{tg}_2}$	(5.0, 0.6) m
TxRx Separation	0.04 m
R_{Res}	8.3mm

The experiments consider 3 scenarios; a single corner reflector (CR), two CRs separated in z, and an extended rough metal suitcase. The first scenario is a trihedral CR of side length of 4 cm placed at $\mathbf{p}_{\mathrm{tg}_1}$, shown in Figure 7.15. The scene should appear as a single point target at $\mathbf{p}_{\mathrm{tg}_1}$. The second scenario was two trihedral CRs of side length of 3 cm, placed at $\mathbf{p}_{\mathrm{tg}_1}$ and $\mathbf{p}_{\mathrm{tg}_2}$. The scene should appear as two point targets at $\mathbf{p}_{\mathrm{tg}_1}$ and $\mathbf{p}_{\mathrm{tg}_2}$. The third scenario was a rough metal plate with a length of 30 cm. This was placed with its centre at $\mathbf{p}_{\mathrm{tg}_1}$ with its largest side running parallel to the z axis.

The remainder of this section will consider 4 subsections. First, the calibration of OMP and Elastic net will be performed to define OMP's stopping point and λ. Then the following 3 subsections will consider the CR, two CRs, and the extended rough metal suitcase respectively.

Calibration

This section shows how the processing is set up, and how the hyperparameters and stopping point are defined for the algorithms, in a similar way to the simulations in section 7.6.

First, Figure 7.11 shows the vector $\mathbf{s}$ for the corner reflector at $\mathbf{p}_{\mathrm{tg}_1}$, which has been generated by concatenating $S_i(R_{min_i}),\ldots,S_i(R_{max_i})$ for $i = 1,\ldots,5$. As expected, when one compares Figure 7.9 and 7.11 the noise floor in this experiment appears relatively flat throughout $\mathbf{s}$. The image, $\mathbf{y}$, will be reconstructed from this using the measurement matrix $\mathbf{A}$ (7.7), using OMP (Algorithm 7.1) and Elastic Net (7.11).

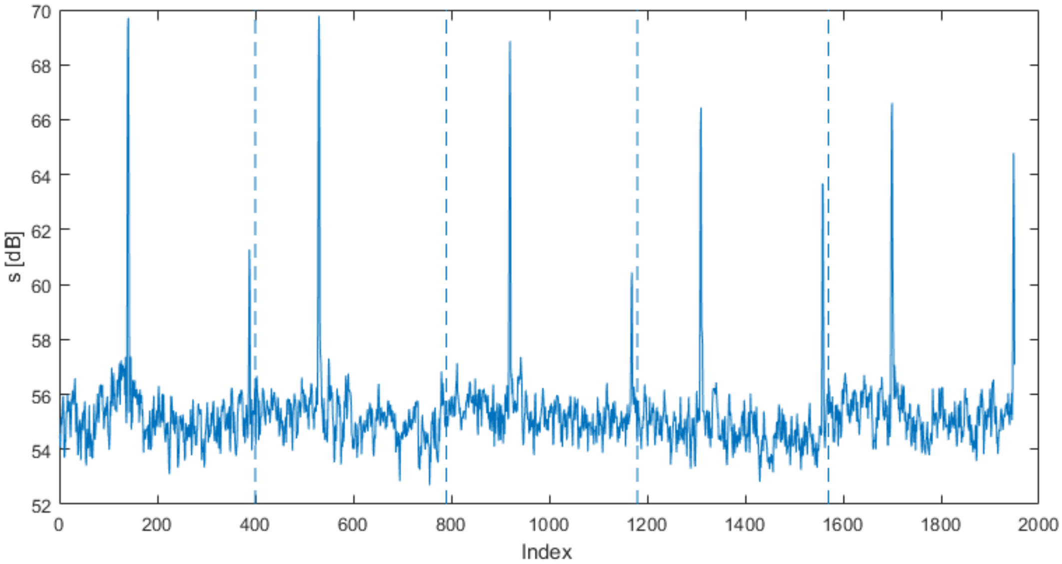

Fig. 7.11 s generated from 5 TxRx sites for a corner reflector.

Next the stopping point for OMP is considered, which is the final step in Algorithm 7.1. Figure 7.12 shows the change in residuals (7.8) from OMP for each of the three different target setups. Specifically, Figure 7.12 shows the change in residuals, h (7.8), per iteration of OMP, $\frac{dh}{dn}$, as in the simulations in Figure 7.7b. For the CR, one would predict that there is a single non-zero peak in the image which is surrounded by free space. There is a single large value of Δh for the first iteration, and then the subsequent change in residuals are much lower. This is consistent with Figure 7.7b. As one would predict, the magnitude of $\frac{dh}{dn}$ is monotonically decreasing, as the fit of $||\mathbf{Ay}-\mathbf{s}||_2$ should improve with each iteration. It is obvious from this distribution, that using $\frac{\Delta h}{\Delta n} \geq 0$ is not a good criterion to choose a stopping point, as it fits a very large number of points compared to the number of targets. The result of Figure 7.12 suggests that fitting a single point target into **y** has the largest impact on the residuals, which is consistent with what one expects from the scene.

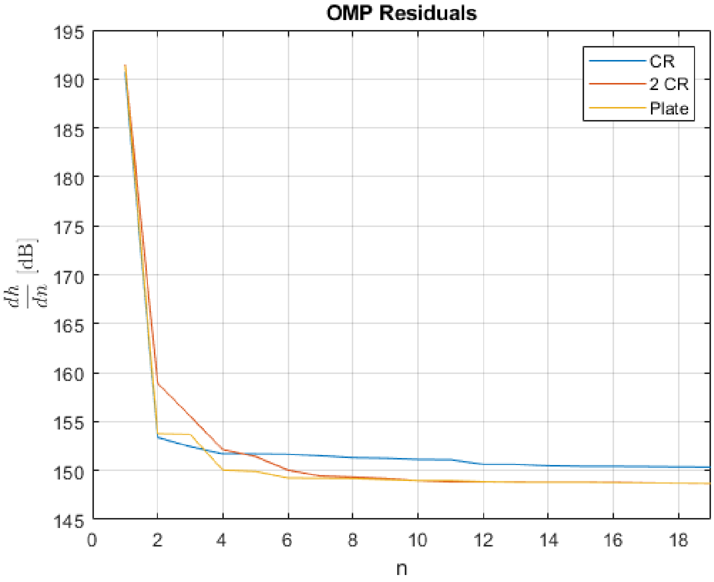

Fig. 7.12 Residuals from applying OMP to image the corner reflector.

Each of the residuals have a peak change for the $n = 1$, and reach a near constant level by $n = 6$. For the CR, it reaches within a couple of dB of this background value by $n = 2$. For the pair of CRs, the first two points have by far the greatest impact, but there is some non-ideal behaviour which means that it does not reach the background value until $n = 4$. It therefore seems reasonable to define the end point as when $n = K = 4$ for OMP in these experiments.

Next an example of tuning the hyperparameters for a canonical reference target is shown. In the simulations this is Figure 7.6a. Note that the maximum value of **s** is not 1 here, and so the required degree of regularisation is different. Figure 7.13 shows the l_2 error (7.12) used to tune the value of λ for $\alpha = 0.9$ (7.11). $\log(\lambda) \geq 2.5$ yields solutions with too high a degree of regularisation. The solution generated is sparse, but the l_2 error is large. $\log(\lambda) \leq 1$ is a region with insufficient regularisation, with many non-zero points and higher l_2 error for lower λ. The minimum at $1 \leq \log(\lambda) \leq 2.5$ yields solutions which are both sparse and have the minimum l_2 error. Therefore this value of λ and α will be used for these experiments. Cross-validation in this way was very computationally expensive and slow compared to the other algorithms. If Elastic Net is to be used in this way, **A** must be computed ahead of time and the domain of λ must be limited with a prior estimate before performing imaging.

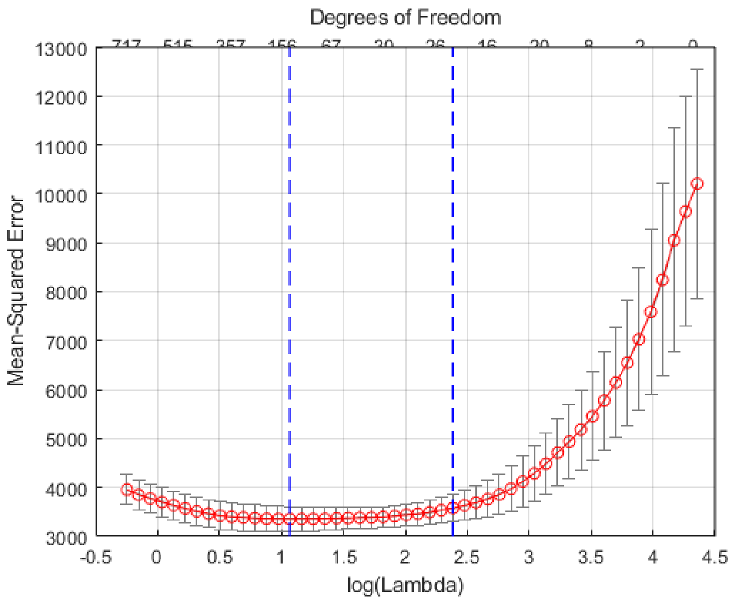

Fig. 7.13 l_2 error for the reconstruction of a corner reflector using Elastic Net as a function of λ.

Corner Reflector

This subsection shows the reconstruction of a single CR. For comparison, bilateration and backprojection have been implemented alongside this as described in chapters 5.3 and 6 respectively. The result of backprojection, $\sigma(x',z)$ (6.11) has been normalised with respect to its maximum value.

The first reconstruction was of a trihedral CR of side length of 4 cm. This was placed at a position of (5.0,0.3) m. The rest of the scene was kept empty. Both OMP and Elastic net are expected to reconstruct the scene well, as there should only be a single point target at $\mathbf{p}_{tg_1}$. It is therefore a sparse scene, with few correlated values in $\mathbf{y}$. The reconstruction of $\mathbf{y}$ from OMP and Elastic Net is shown in Figure 7.14. Elastic net has reconstructed the target as two pixels at (5.0,0.28) m and (5.0,0.31) m respectively. Whereas OMP has reconstructed a single pixel at (5.0,0.31) m. Both have successfully mapped out the free space of the scene, and placed the target to be at $\mathbf{p}_{tg_1}$.

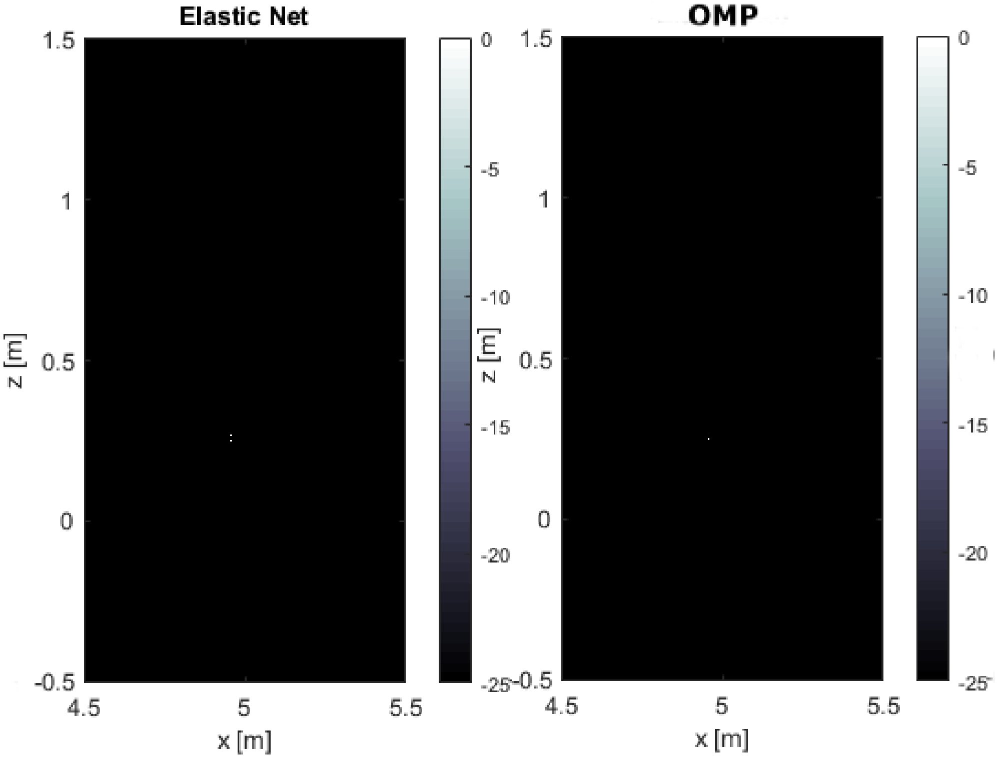

Fig. 7.14 Reconstruction of a corner reflector by (left) Elastic Net and (Right) OMP.

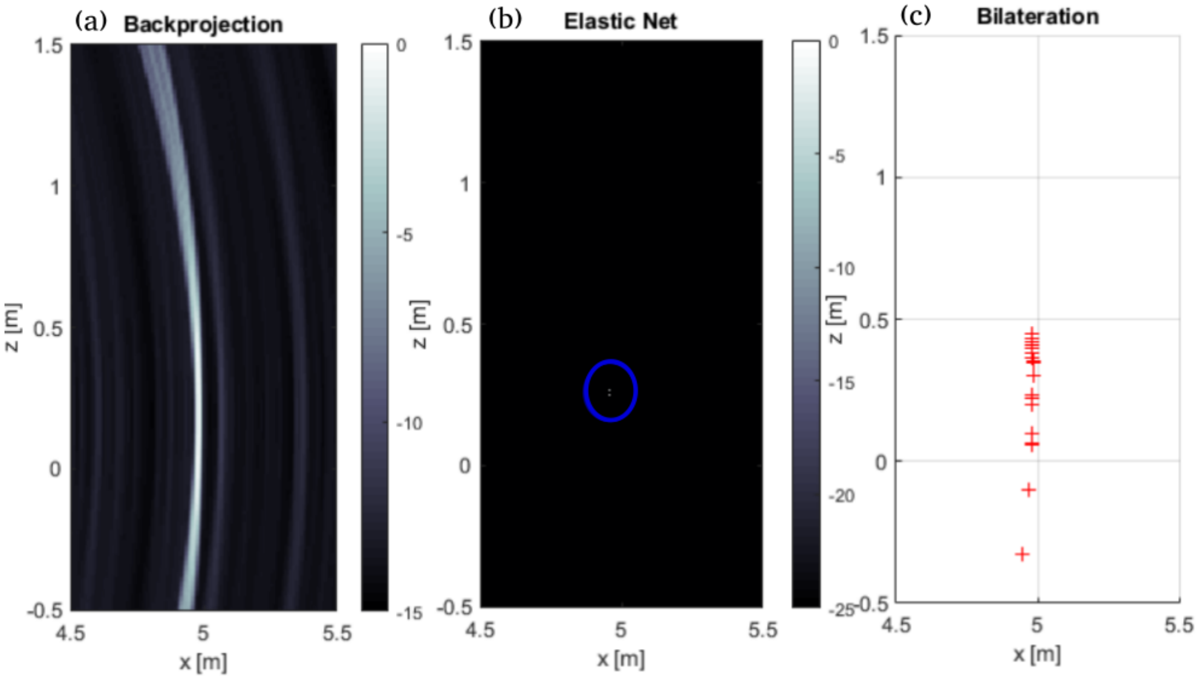

Fig. 7.15 CR at (5.0,0.3) m. Reconstructions from backprojection (left), Elastic Net (centre), and bilateration (right).

The reconstructions from bilateration, backprojection and elastic net are shown alongside one another in Figure 7.15. A blue circle has been added to the result of Elastic Net to highlight the target position. The majority of points from bilateration are clustered between (4.9,0.1) m and (5.0,0.5) m, with few outliers. Although the centre of this distribution is the true position of the target, there is a high variance in target position. Backprojection also obtains the correct peak position of (5.0,0.3) m, though it has a poor resolution in height with a very wide roll-off in elevation.

Let us now consider the point response of each function in height. Figure 7.16 shows the height profile of each technique. For backprojection and compressive sensing this is the maximum value of the radar image at each z position. For bilateration this is the z positions of the reconstructed target positions. Figure 7.16 shows that each of the methods are consistent in placing the corner reflector at $z = 0.3$ m. Bilateration has a cluster of points at this height, but with some outliers at $z = -0.1$ m and $z = 0.6$ m. Backprojection is a broad peak with a maximum value at $z = 0.3$m and a 3 dB extent in height of around 0.6 m. Although the peak is in the correct position, the resolution is reasonably poor. Finally elastic net reconstructs one dominant scattering centre at $z = 0.3$ m, with two other points which are at least 20 dB

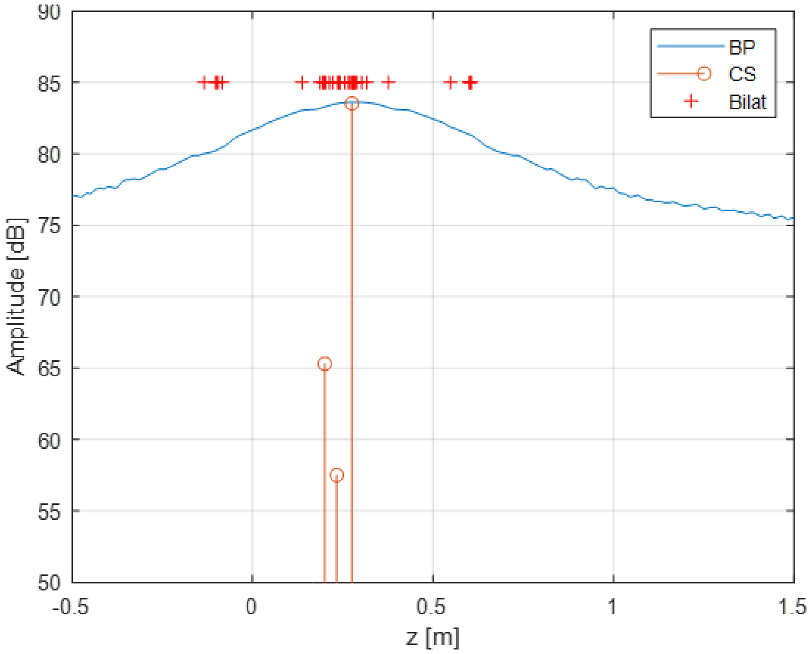

Fig. 7.16 Height profile from backprojection, Elastic Net and bilateration for a CR at (5.0,0.3) m.

lower in amplitude. Compressive sensing appears to give the most accurate reconstruction of the target, and importantly, appears to give the best representation of free space around the target. However, this may simply be due to the the l_1 regularisation term enforcing a sparse solution to $\mathbf{y}$. Therefore investigation needs to be performed to test if compressive sensing does give a better resolution than backprojection, so the following sections will examine Elastic Net's ability to resolve two targets in height and to reconstruct the surface of an extended target.

Two Corner Reflectors

The second reconstruction was of two trihedral CR of side length of 4 cm. As before, bilateration and backprojection have been implemented alongside this as described in chapters 5.3 and 6 respectively. Where $\sigma(x', z)$ (6.11) has been normalised with respect to its maximum value. These was placed at a position of (5.0,0.3) m and (5.0,0.6) m. The rest of the scene was kept empty. This time there are more correlated values in $\mathbf{y}$ because there are are two targets at nearby bistatic ranges (2.2). It is still a sparse scene, with few non-zero values in $\mathbf{y}$. The reconstruction of $\mathbf{y}$ from OMP and Elastic Net is shown in Figure 7.17. Elastic net has reconstructed the targets as two clusters of pixels, with brightest returns centred at (5.0,0.35) m and (5.0,0.6) m. OMP on the other hand has reconstructed this as 3 pixels at (5.0,0.65) m, (5.0,0.35) m, and (5.0,0.8) m. Elastic net appears to have reconstructed a better representation of the scene geometrically, but this is especially true in terms of the target amplitudes. Both targets have the same RCS, so both should have a normalised amplitude of around 0 dB. This is true for Elastic net, but not OMP. However, both have successfully mapped out the free space of the scene, and placed targets at $\mathbf{p}_{tg_1}$ and $\mathbf{p}_{tg_2}$.

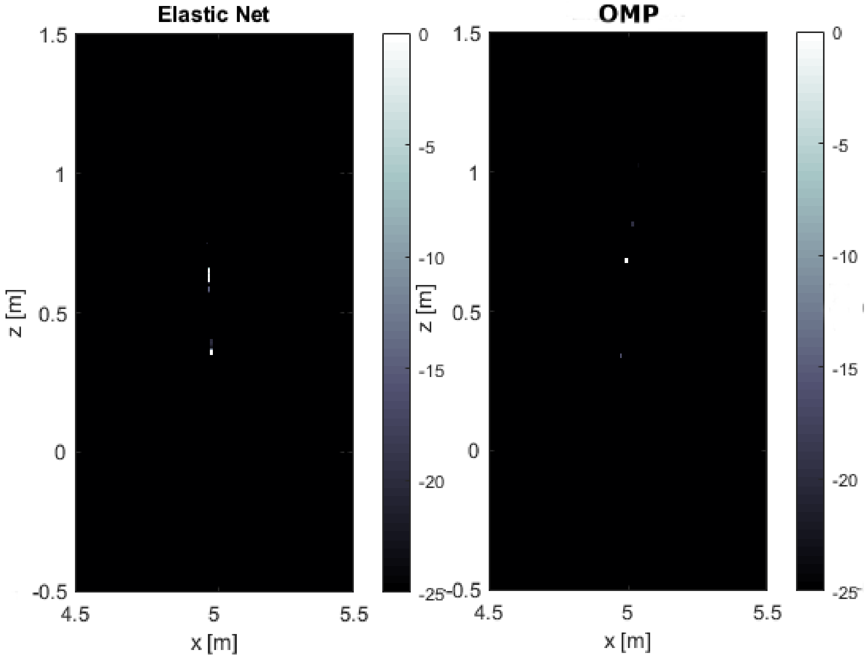

Fig. 7.17 Reconstruction of two corner reflectors by (left) Elastic Net and (Right) OMP.

The reconstructions from bilateration, backprojection and elastic net are shown alongside one another in Figure 7.18. Blue circles have been added to the result of Elastic Net to highlight the target positions. The majority of points from bilateration are clustered between (4.9,0.2) m and (5.0,0.8) m. There are more points present and more outliers and ghost targets in Figure 7.18 due to the fact that there are twice the number of CRs. Many of these points will be ghost targets where one receiver detects one CR and the other detects the other CR. It is not obvious how many CRs are present in the scene from inspection. Backprojection does not easily resolve the two CRs, but appears to have a much broader spread in elevation with a peak at (5.0,0.5) m.

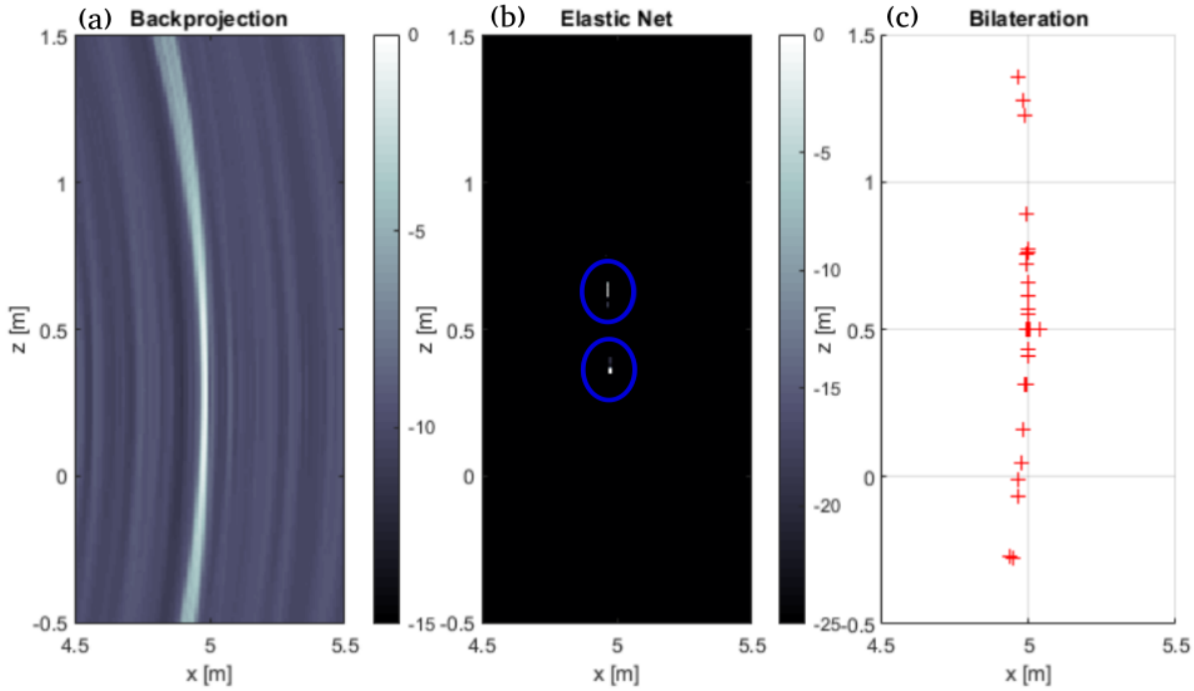

Fig. 7.18 CRs at (5.0,0.3) m and (5.0,0.6) m. Reconstructions from backprojection (left), Elastic Net (centre), and bilateration (right).

Suitcase

The final reconstruction was of a suitcase of side length of 30 cm. As before, bilateration and backprojection have been implemented alongside this as described in chapters 5.3 and 6 respectively. Where $\sigma(x', z)$ (6.11) has been normalised with respect to its maximum value. This was laid at a position so that its length occupied (5.0,0.3) m to (5.0,0.6) m. The rest of the scene was kept empty. In this scene there are many correlated values in **y** because the suitcase is an extended object with many scattering centres along its surface (2.2). The reconstruction of **y** from OMP and Elastic Net is shown in Figure 7.19. Elastic net has reconstructed the target as a spread of pixels between (5.0,0.3) m and (5.0,0.6) m as expected. OMP on the other hand has reconstructed this as 3 pixels at (5.0,0.4) m, (5.0,0.6) m, and (5.0,0.6) m. In this respect, Elastic net appears to give a better profile reconstruction of an extended target.

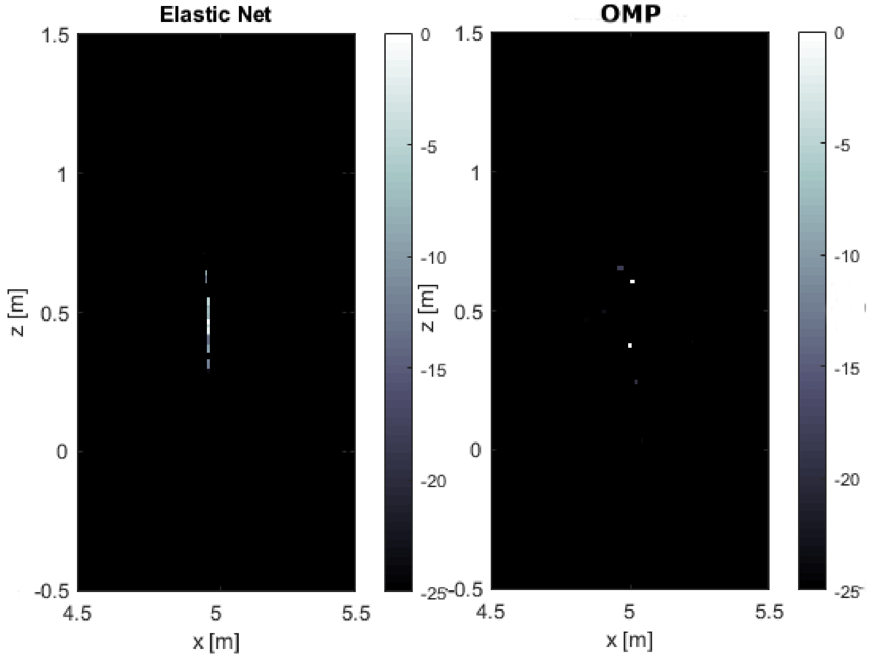

Fig. 7.19 Reconstruction of a flat plate by (left) Elastic Net and (Right) OMP.

The reconstructions from bilateration, backprojection and elastic net are shown alongside one another in Figure 7.18. A blue rectangle has been used to highlight the true profile of the suitcase. There is good agreement between the reconstructions from bilateration and elastic net, with a large cluster of points between (4.9,0.1) m and (4.9,0.5)m, and a separate cluster at (4.9,0.6) m. Both approximately capture the 0.3 m extent of the plate, but elastic net does so with fewer outliers and less variation in position. Backprojection, however, does not allow us to distinguish the extent of the target from the point spread function.

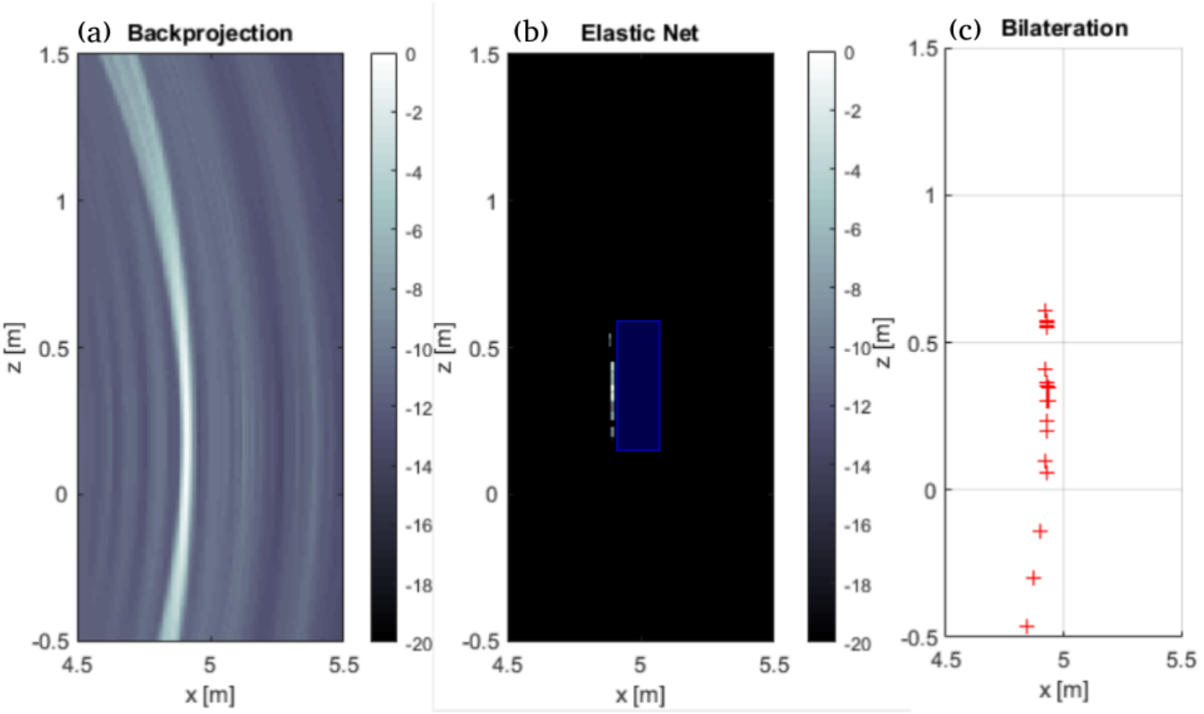

Fig. 7.20 30cm long metal suitcase at (5.0,0.3) m. Reconstructions from backprojection (left), Elastic Net (centre), and bilateration (right).

In general each of the algorithms were able to localise the targets, but did so with varying degrees of success. Both backprojection and bilateration had some uncertainties in their reconstructions; due to variance in position and ghost targets for bilateration, and due to the large point spread function in elevation for backprojection. OMP showed strong and fast performance in reconstructing a point target, but did not provide the ability to resolve multiple nearby targets or an extended surface well. The most encouraging results were from elastic net, which appeared to deconvolve the reconstruction from the instrument response and leave the expected target in each of the scenes. The use of l_1 regularisation for super-resolution became particularly clear in resolving two separated CRs where backprojection alone can not. Further work is needed to prove that techniques such as this can truly reconstruct the full extent of a target, and what is the minimum spacing and number of Tx Rx positions required to capture the true extent of real world complex extended objects.

This section has shown how OMP and Elastic Net can be applied to the Tx-Rx stack to achieve an enhanced resolution in the $x'z$ plane. The following section provides a brief investigation into if these techniques can be applied to the multiple Rx configuration used previously in chapters 5.3 and 6.

7.7.2 Multiple Rx

This section considers how this could be implemented in the multi-receiver stack used throughout this thesis. This was touched on at the start of section 7.7, but this section seeks to demonstrate why using the Rx stack setup proves difficult for OMP and Elastic Net.

The most fundamental challenge in this section is how to handle a signal with such drastically different sensitivities, which are treated as having different noise figures. The instrument response is expected to be the same for each Rx, but after compensation for L_i, the mean noise power of each of them varies (see Table 3.3). It has been shown in the previous section that the definitions of $\mathbf{s}, \mathbf{A}$, and $\mathbf{y}$ (7.3,7.5,7.7) are appropriate for reconstructing a target if ν has a constant mean power. So how does the existing framework handle a variable mean noise power?

First let us consider Elastic Net. Elastic Net removes the noise from the image using the parameter λ (7.10). Figure 7.21 shows the l_2 norm error as a function of λ (7.12). The previous cross-validation in Figure 7.13 shows a minimum, with an over-sparse solution for higher λ and the opposite for lower λ. However, Figure 7.21 does not show such a pattern. The solution generated has the minimum error for between 0-7 non-zero pixels in the radar image, and every additional point introduced generates a larger l_2 error. λ controls both the l_1 and l_2 regularisation, and so the larger value of λ also limits the amplitude of the pixels within $\mathbf{y}$ (7.11). Indeed, the best fit appears to be when Elastic Net introduces as few non-zero indices, and with the smallest amplitudes into $\mathbf{y}$ as possible. This means that this is not a good representation of the scene.

Finally let us apply OMP to the imaging of a corner reflector in section 6.5.2. The reconstruction from OMP is shown next to that of backprojection in Figure 7.22. The image on the right is Figure 6.12, but without normalising the amplitude of each Rx, as if $q_i = 1$ (6.15). Unlike Figure 7.12, there was not a characteristic drop off in h with an increrase in n (7.8). Therefore, the stopping point of $K = 4$ was used as in section 7.7.1 for Algorithm 7.1. While backprojection appears as a single target with a significant spread in z, the result of OMP is a consistently a single point at the predicted position in $x'z$. However, there are a lot of points corresponding to noise in Figure 7.22a. Without the distribution of $\frac{dh}{dn}$, it is difficult to separate the target from the noise using OMP alone. There is a large different in amplitude for the

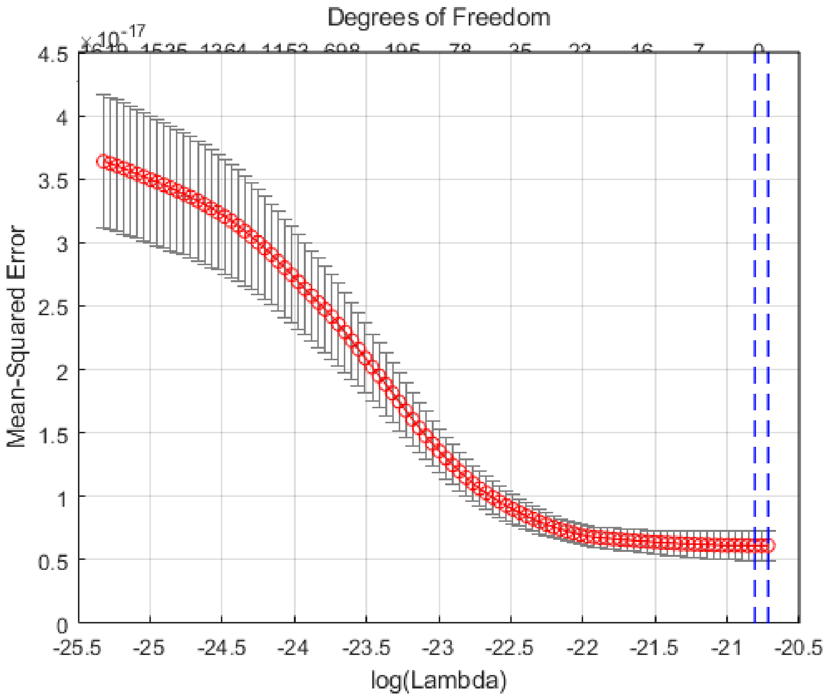

Fig. 7.21 Residuals from the corner reflector using the three receivers with different noise figures.

targets compared with the noise, so a threshold could still probably remove these points. There is still a spread in azimuth present, which comes from the 2D $x'z$ plane model as described in section 2. Therefore it does seem possible to use OMP as a fast way of reconstructing **y**, but it is questionable if the results will be anything near as good as those in section 7.7.1.

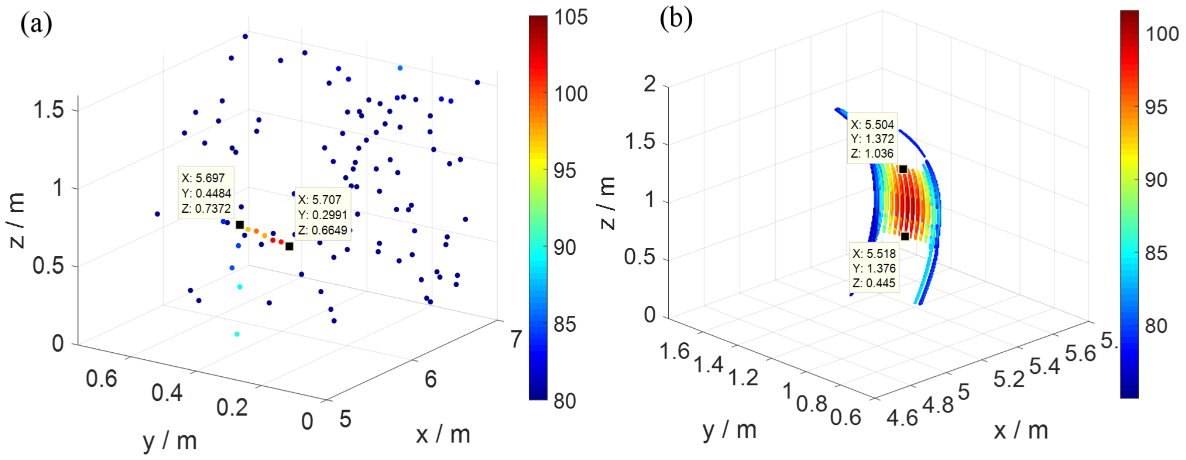

Fig. 7.22 (a) Reconstruction of CR using OMP. (b) Reconstruction of CR using Backprojection.

7.8 Discussion

In general the imaging techniques proposed using OMP and Elastic Net offer a promising alternative to backprojection and bilateration to generate 3D images from height-offset Tx-Rx pairs. A major challenging aspect of this is the quality of the data, and in particular, the role of noise in these reconstructions. It was verified through simulations that these procedures can reconstruct a point target with variable SNR values between 20 dB and 6 dB, and so these methods are suitable even in high levels of noise. The difficulty of using multiple Rx units was discussed in section 7.7.2, but in general even for one Rx unit the SNR of this radar is reasonably low. This is because the noise figure is very high for low-THz radars currently, as seen in section 3.4, which is why these algorithms required a process to handle the image de-noising (e.g. a threshold for bilateration, and connected component thresholding for backprojection).

Compressive sensing's main promising features for this application are that it can deconvolve the image from the point response of the radar while denoising the image. These algorithms perform this first aspect well enough, creating clear single-pixel sparse point responses from canonical radar targets such as Figure 7.14. However, although these algorithms reconstructed the brightest points in the image well, such as the specular returns of the plates in Figure 7.19, or the position of a single corner reflector in Figure 7.14, further work is needed to conclusively say if any of the lower amplitude diffuse returns could be seen. Therefore in the future, with higher available SNR values, systems such as these may be able to reconstruct the surface of an object in this way, but for now the technology readiness level might not allow for this.

When using a single TxRx pair with time multiplexing in section 7.7.1, each of the ToA imaging algorithms were able to localise the targets, but did so with varying degrees of success. Both backprojection and bilateration had some uncertainties in their reconstructions; due to variance in position and ghost targets for bilateration, and due to the large point spread function in elevation for backprojection. The most encouraging results were from elastic net, which appeared to deconvolve the reconstruction from the instrument response and leave the expected target in each of the scenes. Although the use of elastic net for super-resolution algorithms is well-established, it is still particularly encouraging to see this technique resolve two separated CRs where backprojection alone can not. OMP also successfully performed these tasks, but with slightly different reconstructions. However, OMP handled the reconstruction of the flat plate poorly. It is likely due to the fact that the greedy matching pursuit algorithm does not iteratively reweight its reconstruction like Elastic Net does, and hence it handled nearby correlated values poorly. Further work is needed to prove that techniques such as this can truly reconstruct the full extent of a target, and what is the minimum spacing and number of Tx Rx positions required to capture the true extent of real world extended objects, when random surface scattering is such a complex process.

Chapter 8

Conclusions & Further Work

8.1 Conclusion

This project has detailed the development of 3D ToA imaging algorithms using low-THz radar for the application of automotive radar. It started by estimating the 3D position of simple targets at short ranges in controllable conditions, extended these capabilities to 3D imaging of the scene in variable real world conditions, and finally applied super resolution techniques to accurately reconstruct the 3D shape and extent of extended targets.

The novel contributions of this work are as follows. First, it was demonstrated experimentally that a multi-receiver 300 GHz radar can perform 3D target localisation in a variety of different configurations using ToA information. This then built upon previous work, considering not only target ToA position estimation, but a 3D radar imaging of the target. A novel method of modified backprojection was proposed which built up a 3D image of the target from multiple sets of range profiles without the use of phase information. This was then demonstrated experimentally both on moving actors and on real-world road scenes. To improve the resolution of these imaging techniques, new imaging frameworks were proposed using compressive sensing and orthogonal matching pursuit algorithms, which were demonstrated both in simulations and experimentally, which greatly improved the resolution of the 3D low-THz radar image.

A summary of the advantages and disadvantages of each technique can be seen below in Table 8.1.

Technique	**Advantages**	**Disadvantages**
Raster Scan	Fine angular resolution. Least amount of signal processing. Few or no assumptions.	Very long measurement time (minutes). Large amounts of data. Limited FOV per chirp. No integration between Rx units.
Trilateration	Can monitor wide FOV at a time. No need for scanning (shortest measurement time). Short processing time.	Low transmitted power is not focused by wide beam pattern. More ambiguity in target correspondence between Rx pairs. Cannot reconstruct a height profile / 3D image of a target. Target requires detection before integration between Rx units. Large setup.
Bilateration	Energy focused towards target in narrow azimuth beam. Less ambiguity in target correspondence. Short processing time.	Requires scanning to obtain azimuth information. Cannot reconstruct a height profile / 3D image of a target. Target requires detection before integration between Rx units.
Backprojection	Generates a 3D reconstruction of the scene. Energy focused towards target in narrow azimuth beam. Additional gain through integration of multiple Rx units. Thresholding provides a rudimentary form of scene segmentation.	Scanning. Broad system response (low resolution) in elevation. Image includes regions of noise. Moderately long processing time.
Orthogonal Matching Pursuit	Those of Backprojection. Provides a reconstruction of the scene with the broad point response removed (deconvolution). Guaranteed sparsity.	Scanning. Moderate processing time. Strict assumptions about the sparsity of the scene. Image is not reweighted each iteration - may not tend to best global solution.
Convex Optimisation	Those of backprojection. Provides a reconstruction of the scene with the broad point response removed (deconvolution). Image is iteratively reweighted - more likely to approximate the best global solution.	Scanning. Long processing time, (Limited) Assumptions about the sparsity of the scene,

Table 8.1 Summary of the advantages and disadvantages of each 3D localisation and imaging technique.

The remainder of this section will break down the key findings of chapter 3 onwards.

The characterisation of the system confirmed multiple things. First that the range resolution of the system can be sub-cm, and the azimuth beamwidth was sufficiently narrow to deliver highly detailed imagery. However, it raised some issues in the fact that the noise figure of the multiple receivers were high, and the sensitivity varied from receiver to receiver. What's more, the use of the local oscillator cables from the control box to the Rx units degraded the system response in range and needed compensating for. Ultimately it was shown that the system was sufficient for short-range imaging applications, such as SRR, but the low output power and technical issues made current demonstrators unsuitable for longer range imaging.

Raster scanned imagery was then performed using this system. These images were very highly detailed and reconstructed the structure and extent of highly complicated targets. These produced levels of information very similar to their stereo video and lidar counterparts, but the time taken to perform a full raster scan took typically around a minute, which is insufficient for automotive applications.

ToA localisation through multilateration was then put forward as an alternative to interferometry and other height finding systems. This technique demonstrated the ability to determine the position of simple targets with trilateration in 3D, and to determine a more constrained version of bilateration height finding in 2D. It was clear that techniques like this have limited utility when it comes to creating a 3D image of a target, but should be considered as a method of extracting the mean height of the target. If the goal of this radar technique is to determine if the scattering centre ahead is a speed-bump or an overhead bridge, this is probably sufficient. However, it does not provide anything like the 3D images created by electro-optical sensors. With this in mind, the focus of these techniques were then changed to 3D imaging.

Backprojection was applied to generate 3D imagery. With this setup, mechanically scanning in azimuth was used to perform the azimuth localisation, and the elevation localisation was generated from the TOA of multiple Tx-Rx pairs which were offset in height. This technique was applied to many scenes, from 3D images of road actors at short range up to mapping complex real-world road scenes in a vehicle. The resolution of these images were somewhat limited, especially when compared to the earlier raster scanned images. Backprojection was able to generate highly detailed images of road objects, detect and image actors moving through a scene, and reconstruct road scenes where height information was essential for route guidance. However, the point response in elevation was very broad. This made it difficult to determine what points in the image came from the object itself, and what was an artefact of backprojection. There were multiple pairs of receivers, despite the fact that only one pair were needed to localise a target in 2D. What's more, the majority of the space surrounding the vehicle will not be a scattering centre. Therefore the image is sparse and underdetermined, which makes it an ideal candidate for compressive sensing.

Two algorithms were tested which can loosely be thought of as compressive sensing; Elastic net, and orthogonal matching pursuit. Both were used as a method to simultaneously deconvolve the image from the wide point spread function to generate a height profile, and to remove the noise. It proved to be effective in reconstructing a point like target, two nearby point like targets, and gave an estimate of the position and extent of a flat plate. A major limitation in using l_p normalisation as a constraint was that the noise figure of one Rx was far larger than another, and the reconstruction was limited by the largest noise figure.

This project demonstrated that low-THz radar can generate 3D imagery through the use of height-offset receivers using amplitude and range information alone. At the simplest level, multilateration can be used to obtain a height estimate of the target, and more complex imaging techniques can be used to convert a set of range profiles into a 3D image.

8.2 Further Work

The techniques designed to be used in the low-THz band are likely to become more relevant as the band is developed. The low-THz band is still an emerging radar application. This means that the band requires more development from a hardware standpoint to increase the output power and SNR, among other things. With an increased transmit power, the low-THz band can be used not only for SRR and other short range applications, but can be applied to LRR and various other disciplines. The techniques here are appropriate for 3D imaging for SRR, but they need rethinking for longer ranges. For one, constraining the imaging problem into 2D cross sections as the setup is scanned in azimuth is no longer appropriate at long ranges when the region illuminated by the beam in azimuth corresponds to a large cross range extent with many targets occupying it. There is also a trade-off in Tx-Rx spacing in that the larger spacing gives a better elevation resolution, but the target's returns must be visible in the Rx beam. The resolution also degrades with target range. Therefore it is likely that the system should use different Rx spacings depending on the target range. What this means is that setups with multiple different Tx-Rx baselines must be experimented with to give smaller separations which are more appropriate for short range 3D imaging, and larger separations which are more appropriate for long range imaging.

The equipment available for this project has been a single transmitter to three receiver system. Therefore the experimental setups have either been a direct 1Tx-3Rx measurement or time multiplexed measurements with 1Tx-1Rx measured at a time. None of the algorithms developed throughout this project are dependent on this specific configuration, and they are flexible to the number and separation of Tx and Rx units. Therefore work should be done in determining how best to use a greater number of Tx and Rx units.

The focus of the work performed here has been how to generate height information for height separated Tx and Rx units, and it has been taken for granted that the target can be localised in azimuth. Any 3D imaging algorithm used will need to obtain a sufficiently fine azimuth resolution. It is fully possible to use a TOA imaging algorithm along both directions, but it may not be the best choice, as shown in section 5. One could for example make use of multiple height separated linear arrays which generate azimuth information from using phased array techniques and generate elevation information from TOA techniques. Indeed, variants of MIMO could be used along each axis to further improve this resolution.

Another consideration needs to be whether or not radar can be used to reconstruct the true extent of an object as opposed to a specular point of reflection, which has been one of the main claims of low-THz radar. Raster scanning was proven to perform this in section 4, and compressive sensing showed some ability of doing this in section 7. The raster scans only illuminate a very small region of a target at a time, and so this has a very fine angular resolution and can estimate the surface extent of an object successfully. However, this means that whenever the radar is illuminating one direction, it is not monitoring all other directions. In the case of TOA algorithms, including compressive sensing here, the combined aperture of the radar was of a similar size to the extent of the target being reconstructed. For more limited sized apertures, this is unlikely to be possible. This is also partially a question of the SNR of these systems, because reconstructing the extent of an object involves receiving the low amplitude diffuse reflections from the full extent of a target.

Once a fully 3D automotive radar is available, a major research application will have to be the sensor fusion between the 3D radar data and existing electro-optical systems. It is hoped that the higher resolution, 3D imagery, and more optical nature of low-THz radar will make it more feasible to explore new avenues of sensor fusion. For example, if current automotive radar provides a robust but low resolution range-azimuth estimate of a target, it may be more suitable to aid the electro-optical sensors by extracting a small set of parameters of a radar target (its position, velocity, and RCS). Instead, if the radar data were to be 3D and comparable in detail to that provided by the electro-optical sensors, then this would open up other modalities of sensor fusion.

References

[1] T. K. Sarkar, M. Salazar Palma, and E. L. Mokole, “Echoing Across the Years: A History of Early Radar Evolution,” *IEEE Microwave Magazine*, vol. 17, pp. 46–60, Oct. 2016.

[2] P. Z. Peebles, *Radar principles*. A Wiley-Interscience publication, New York, NY: Wiley, 1998. OCLC: 833158540.

[3] I. T. Union, “Nomenclature of the frequency and wavelengh bands used in telecommunications,” *ITU-R V.431-8*, p. 5, Aug. 2015.

[4] M. I. Skolnik, *Introduction to radar systems*. New York: McGraw-Hill, 2d ed ed., 1980.

[5] M. A. Richards, J. Scheer, W. A. Holm, and W. L. Melvin, eds., *Principles of modern radar*. Raleigh, NC: SciTech Pub, 2010.

[6] M. I. Skolnik, “Millimeter and submillimeter wave applications,” tech. rep., DTIC Document, 1970.

[7] M. A. Richards, “A Beginner’s Guide to Interferometric SAR Concepts and Signal Processing,” Sept. 2007.

[8] Y. K. Chan and V. C. Koo, “An introduction to synthetic aperture radar (SAR),” *Progress In Electromagnetics Research B*, vol. 2, pp. 27–60, 2008.

[9] IEEE, “IEEE Standard Letter Designations for Radar-Frequency Bands,” *IEEE Std 521-1984*, pp. 1–8, Nov. 1984.

[10] F. Norouzian, E. G. Hoare, E. Marchetti, M. Cherniakov, and M. Gashinova, “Next Generation, Low-THz Automotive Radar – the potential for frequencies above 100 GHz,” in *2019 20th International Radar Symposium (IRS)*, pp. 1–7, June 2019.

[11] J. Wenger, “Automotive radar - status and perspectives,” in *IEEE Compound Semiconductor Integrated Circuit Symposium, 2005. CSIC ’05.*, pp. 4 pp.–, Oct. 2005.

[12] T. A. Milligan, *Modern antenna design*. Hoboken, N.J: IEEE Press : Wiley-Interscience, 2nd ed ed., 2005.

[13] J. A. Ogilvy, *Theory of wave scattering from random rough surfaces*. A. Hilger, 1991.

[14] A. G. Stove, “Linear FMCW radar techniques,” *IEE Proceedings F - Radar and Signal Processing*, vol. 139, pp. 343–350, Oct. 1992.

[15] B. Willetts, M. Gashinova, A. Stove, and C. C. Constantinou, “Distinguishing surfaces with different roughness characteristics by using a wideband device at 300 GHz,” in *2017 18th International Radar Symposium (IRS)*, pp. 1–8, June 2017.

[16] L. Daniel, D. Phippen, E. Hoare, A. Stove, M. Cherniakov, and M. Gashinova, “Multi-height radar images of road scenes at 150 GHz,” in *2017 18th International Radar Symposium (IRS)*, pp. 1–7, June 2017.

[17] I. Getting, “SCR-584 radar and the Mark 56 naval gun fire control system,” *IEEE Aerospace and Electronic Systems Magazine*, vol. 5, pp. 3–15, Oct. 1990.

[18] M. H. Woodring, “The SCR-268 Radar,” *Electronics*, vol. 18, pp. 100–109, Sept. 1945.

[19] A. I. Leonov and K. I. Pomichev, “Monopulse Radar,” tech. rep., Foreign Technology Division, June 1972.

[20] R. S. Phillips, “SIMULTANEOUS LOBING SYSTEM,” *United States Patent Office*, vol. US2682656, Oct. 1946.

[21] D. D. Howard, “High Range-Resolution Monopulse Tracking Radar,” *IEEE Transactions on Aerospace and Electronic Systems*, vol. AES-11, pp. 749–755, Sept. 1975.

[22] P. Molchanov, S. Gupta, K. Kim, and K. Pulli, “Short-range FMCW monopulse radar for hand-gesture sensing,” in *2015 IEEE Radar Conference (RadarCon)*, pp. 1491–1496, May 2015.

[23] U. Nickel, “Overview of generalized monopulse estimation,” *IEEE Aerospace and Electronic Systems Magazine*, vol. 21, pp. 27–56, June 2006.

[24] R. Mailloux, “Antenna array architecture,” *Proceedings of the IEEE*, vol. 80, pp. 163–172, Jan. 1992.

[25] U. Nickel, “Fundamentals of Signal Processing for Phased Array Radar,” *Research Institute for High-Frequency Physics and Radar Techniques(FHR), Research Establishment for Applied Science (FGAN)*, p. 23, Sept. 2006.

[26] J. Li and P. Stoica, “MIMO Radar with Colocated Antennas,” *IEEE Signal Processing Magazine*, vol. 24, pp. 106–114, Sept. 2007.

[27] M. Compagnoni, R. Notari, F. Antonacci, and A. Sarti, “A comprehensive analysis of the geometry of TDOA maps in localization problems,” *Inverse Problems*, vol. 30, p. 035004, Mar. 2014.

[28] D. G. Macfarlane, H. M. Odbert, D. A. Robertson, M. R. James, H. Pinkerton, and G. Wadge, “Topographic and Thermal Mapping of Volcanic Terrain Using the AVTIS Ground-Based 94-GHz Dual-Mode Radar/Radiometric Imager,” *IEEE Transactions on Geoscience and Remote Sensing*, vol. 51, pp. 455–472, Jan. 2013.

[29] P. Phu, H. Aumann, and J. E. Piou, “Multipath height finding in the presence of interference,” in *2007 IEEE Antennas and Propagation Society International Symposium*, pp. 2025–2028, June 2007.

[30] G Pietrzyk, P Samczyriski, A Gorzelakzyk, and K Kulpa, “Real-time Implementation of Doppler Beam Sharpening Technique with Simple Motion Estimation,” in *First European Radar Conference, 2004. EURAD.*, (Amsterdam, The Netherlands), Oct. 2004.

[31] On-Road Automated Driving (ORAD) committee, “Taxonomy and Definitions for Terms Related to Driving Automation Systems for On-Road Motor Vehicles,” Tech. Rep. J3016_201806, SAE International, June 2018.

[32] A. Dunoyer and I. Ci, “ADAPTIVE CRUISE CONTROL SYSTEMS,” *United States Patent Office*, vol. US 20040193354A1, p. 5, 2004.

[33] W. Luo and S. V. Samuel, “Automatic reverse brake assist system,” *United States Patent Office*, vol. USOO8738264B1, p. 7, May 2014.

[34] B. B. Litkouhi, “LANE DEPARTURE WARNING AND ASSIST SYSTEMUTILIZING ACTIVE MATERLALS,” *United States Patent Office*, vol. US008111147B2, Feb. 2012.

[35] M. Lynberg, “NHTSA: Automated Vehicles for Safety,” text, National Highway Traffic Safety Administration, Sept. 2017.

[36] Tesla, “Upgrading Autopilot: Seeing the World in Radar,” in *https://www.tesla.com/en_GB/blog/upgrading-autopilot-seeing-world-radar*, Tesla Inc, Sept. 2016.

[37] J. D. Lee, D. V. McGehee, T. L. Brown, and D. Marshall, “Effects of Adaptive Cruise Control and Alert Modality on Driver Performance,” *Transportation Research Record*, p. 8, 1980.

[38] D. H. Schittenhelm, “Advanced Brake Assist – Real World effectiveness of current implementations and next generation enlargements by Mercedes-Benz,” Tech. Rep. 13-0194, Daimler AG, May 2013.

[39] E. Edmonds, “Americans Steer Away from Autonomous Parking,” in *AAA Newsroom. https://newsroom.aaa.com/tag/self-parking-cars/*, AAA, Sept. 2015.

[40] S. Sternlund, J. Strandroth, M. Rizzi, A. Lie, and C. Tingvall, “The effectiveness of lane departure warning systems—A reduction in real-world passenger car injury crashes,” *Traffic Injury Prevention*, vol. 18, pp. 225–229, Feb. 2017.

[41] R. Krueger, T. H. Rashidi, and J. M. Rose, “Preferences for shared autonomous vehicles,” *Transportation Research Part C: Emerging Technologies*, vol. 69, pp. 343–355, Aug. 2016.

[42] T. Litman, “Implications for Transport Planning,” tech. rep., Victoria Transport Policy Institute, Jan. 2020.

[43] S. Hörl, F. Ciari, and K. W. Axhausen, “Recent perspectives on the impact of autonomous vehicles,” *Institute for Transport Planning and Systems*, 2016.

[44] K. Yang, S. I. Guler, and M. Menendez, “Isolated intersection control for various levels of vehicle technology: Conventional, connected, and automated vehicles,” *Transportation Research Part C: Emerging Technologies*, vol. 72, pp. 109–129, Nov. 2016.

[45] S. E. Shladover, D. Su, and X.-Y. Lu, “Impacts of Cooperative Adaptive Cruise Control on Freeway Traffic Flow,” *Transportation Research Record: Journal of the Transportation Research Board*, vol. 2324, pp. 63–70, Jan. 2012.

[46] D. J. Fagnant, K. M. Kockelman, and P. Bansal, “Operations of Shared Autonomous Vehicle Fleet for Austin, Texas, Market,” *Transportation Research Record: Journal of the Transportation Research Board*, vol. 2563, pp. 98–106, Jan. 2016.

[47] M. Bertoncello and D. Wee, “Ten ways autonomous driving could redefine the automotive world,” in *McKinsey & Company: Automotive & Assembly. https://www.mckinsey.com/industries/automotive-and-assembly/our-insights/ten-ways-autonomous-driving-could-redefine-the-automotive-world*, June 2015.

[48] G. Njobelo, T. Sando, S. Sajjadi, E. Mtoi, E. E. Ozguven, and J. Sobanjo, “Safety Evaluation of the Advanced Stop Assist System in Connected Vehicle Environment,” *Transportation Research Record: Journal of the Transportation Research Board*, vol. 2672, pp. 47–57, Dec. 2018.

[49] L. Martinez, “Urban Mobility System Upgrade How shared self-driving cars could change city traffic,” tech. rep., OECD / International Transport Forum, Paris, 2015.

[50] D. for Transport, “RAS50001: Reported Road Casualties Great Britain: 2016,” in *https://www.gov.uk/government/statistical-data-sets/reported-drinking-and-driving-ras51*, Department for Transport, 2017.

[51] J. Horne and L. Reyner, “Vehicle accidents related to sleep: a review,” *Occupational and Environmental Medicine*, vol. 56, pp. 289–294, May 1999.

[52] D. for Transport, “RAS51011: Reported drink drive accidents and casualties, by month,” in *https://www.gov.uk/government/statistical-data-sets/reported-drinking-and-driving-ras51*, Department for Transport, 2019.

[53] I. T. U, “Recommendation ITU-R M.2057-1: Systems characteristics of automotive radars operating in the frequency band 76-81 GHz for intelligent transport systems applications,” Tech. Rep. ITU-R M.2057-1, International Telecommunications Union, Jan. 2018.

[54] D. for Transport, “General rules, techniques and advice for all drivers and riders (103 to 158) - The Highway Code - Guidance - GOV.UK,” Aug. 2019.

[55] “Rover Group Ltd: Discovery workshop manual,” 1996.

[56] N. Baker, “Prevention of bridge strikes - A good practice guide for passenger transport operational staff,” Tech. Rep. NR/CE/GPG/005, Network Rail, Apr. 2012.

[57] P. Schyter, “Radiometry and photometry in astronomy. http://stjarnhimlen.se/comp/radfaq.html#10,” 2006.

[58] J. Hecht, “Lidar for Self-Driving Cars | Optics & Photonics News : https://www.osa-opn.org/home/articles/volume_29/january_2018/features/lidar_for_self-driving_cars/.”

[59] R. Szeliski, *Computer vision: algorithms and applications, Ch.11.* Springer Science & Business Media, 2010.

[60] K. Muller, P. Merkle, and T. Wiegand, “3-D Video Representation Using Depth Maps,” *Proceedings of the IEEE*, vol. 99, pp. 643–656, Apr. 2011.

[61] I. Velodyne Acoustics, “Velodyne’s HDL-64E: A High Definition Lidar Sensor for 3D Applications,” tech. rep., Velodyne Acoustics, Inc., Oct. 2007.

[62] T. Gaisecker and P. Amon, “Riegl’s versatile VUX-1 laser scanning engine for multiple kinematic applications,” tech. rep., Riegl Laser Measurement Systems, 2016.

[63] Innoviz, “InnovizPro | Solid State Lidar Sensors: https://innoviz.tech/innovizpro.”

[64] L. Eldada, “Solid State LiDAR Sensors: The Future of Autonomous Vehicles,” in *IS&T Intenational Symposium on Electronic Imaging Sciene and Technology*, 2019.

[65] J. Hu, R. Hu, Z. Wang, Y. Gong, and M. Duan, “Kinect depth map based enhancement for low light surveillance image,” in *2013 IEEE International Conference on Image Processing*, pp. 1090–1094, Sept. 2013.

[66] A. Geiger, P. Lenz, C. Stiller, and R. Urtasun, “Vision meets robotics: The KITTI dataset,” *The International Journal of Robotics Research*, vol. 32, pp. 1231–1237, Sept. 2013.

[67] G. Pandey, J. R. McBride, and R. M. Eustice, “Ford Campus vision and lidar data set,” *The International Journal of Robotics Research*, vol. 30, pp. 1543–1552, Nov. 2011.

[68] Riegl, “Datasheet for RIEGL’s VUX-1HA: http://www.riegl.com/uploads/tx_pxpriegldownloads/Datasheet-RIEGL _vux-1HA_2019-09-02.pdf,” Sept. 2019.

[69] J. D. Gammell, C. H. Tong, and T. D. Barfoot, “Blinded by the Light: Exploiting the Deficiencies of a Laser Rangefinder for Rover Attitude Estimation,” in *2013 International Conference on Computer and Robot Vision*, (Regina, SK, Canada), pp. 144–150, IEEE, May 2013.

[70] W. Sun, Y. Hu, D. G. MacDonnell, C. Weimer, and R. R. Baize, “Technique to separate lidar signal and sunlight,” *Optics Express*, vol. 24, p. 12949, June 2016.

[71] C. Visvikis, T. L. Smith, M. Pitcher, and R. Smith, “Study on lane departure warning and lane change assistant systems,” *Transport Research Laboratory*, p. 128, Nov. 2008.

[72] L. Daniel, D. Phippen, E. Hoare, A. Stove, M. Cherniakov, and M. Gashinova, “Low-THz Radar, Lidar and Optical Imaging through Artificially Generated Fog,” in *International Conference on Radar Systems (Radar 2017)*, (Belfast, UK), Institution of Engineering and Technology, 2017.

[73] W. Maddern, G. Pascoe, C. Linegar, and P. Newman, “1 year, 1000 km: The Oxford RobotCar dataset,” *The International Journal of Robotics Research*, vol. 36, pp. 3–15, Jan. 2017.

[74] P. Wang, X. Huang, X. Cheng, D. Zhou, Q. Geng, and R. Yang, “The ApolloScape Open Dataset for Autonomous Driving and its Application,” *IEEE Transactions on Pattern Analysis and Machine Intelligence*, pp. 1–1, 2019.

[75] D. Barnes, M. Gadd, P. Murcutt, P. Newman, and I. Posner, “The Oxford Radar RobotCar Dataset: A Radar Extension to the Oxford RobotCar Dataset,” *arXiv:1909.01300 [cs, eess]*, Sept. 2019. arXiv: 1909.01300.

[76] M. Meyer, G. Kuschk, and A. GmbH, “Automotive Radar Dataset for Deep Learning Based 3D Object Detection,” in *2019 16th European Radar Conference*, p. 4, Oct. 2019.

[77] D. Anguelov, C. Dulong, D. Filip, C. Frueh, S. Lafon, R. Lyon, A. Ogale, L. Vincent, and J. Weaver, “Google Street View: Capturing the World at Street Level,” *Computer*, vol. 43, pp. 32–38, June 2010.

[78] Techweb, “Baidu Panorama: Real World Baidu Map is at your fingertips. http://www.techweb.com.cn/ news/2013-09-03/1321393.shtml,” Sept. 2013.

[79] S. Wang, M. Bai, G. Mattyus, H. Chu, W. Luo, B. Yang, J. Liang, J. Cheverie, S. Fidler, and R. Urtasun, “TorontoCity: Seeing the World with a Million Eyes,” *arXiv:1612.00423 [cs]*, Dec. 2016. arXiv: 1612.00423.

[80] C. B. Insights, “40+ Corporations Working On Autonomous Vehicles. https://www.cbinsights.com/research/ autonomous-driverless-vehicles-corporations-list/,” Mar. 2020.

[81] Tesla, “Model X Owner’s Manual,” tech. rep., Tesla Inc, May 2020.

[82] A. G. Stove, “Obstacle detection radar for cars,” *Electronics Communication Engineering Journal*, vol. 3, pp. 232–240, Oct. 1991.

[83] H. H. Meinel, “Evolving automotive radar — From the very beginnings into the future,” in *The 8th European Conference on Antennas and Propagation (EuCAP 2014)*, pp. 3107–3114, Apr. 2014.

[84] M. Schneider, “Automotive Radar – Status and Trends,” in *GeMiC 2005*, (Ulm, Germany), p. 4, 2005.

[85] J. Dickmann, J. Klappstein, M. Hahn, M. Muntzinger, N. Appenrodt, C. Brenk, and A. Sailer, “"Present research activities and future requirements on automotive radar from a car manufacturer´s point of view",” in *2015 IEEE MTT-S International Conference on Microwaves for Intelligent Mobility (ICMIM)*, pp. 1–4, Apr. 2015.

[86] Y. Xiao, F. Norouzian, E. Marchetti, S. Cassidy, E. Hoare, M. Cherniakov, and M. Gashinova, “Transmissivity Through Automotive Bumpers at mm-wave and Low-THz Frequencies,” in *2019 20th International Radar Symposium (IRS)*, pp. 1–6, June 2019.

[87] I. T. U, “RECOMMENDATION ITU-R P.676-3 ATTENUATION BY ATMOSPHERIC GASES,” Tech. Rep. ITU-R P.676-3, International Telecommunications Union, Aug. 2019.

[88] J. Wenger and S. Hahn, “Long Range and Ultra-Wideband Short Range Automotive Radar,” in *2007 IEEE International Conference on Ultra-Wideband*, pp. 518–522, Sept. 2007.

[89] A. Kawakubo, S. Tokoro, Y. Yamada, K. Kuroda, and T. Kawasaki, “Electronically-Scanning Millimeter-Wave RADAR for Forward Objects Detection,” in *SAE 2004 World Congress & Exhibition*, (Sherbrooke, Canada), pp. 2004–01–1122, Mar. 2004.

[90] NXP, “76 GHz to 81 GHz car RADAR transceiver: https://www.nxp.com/docs/en/data-sheet/TEF810XDS.pdf,” 2019.

[91] INRAS, “Radar evaluation board: http://www. inras.at/en/ products/ radarbook.html,” tech. rep., Inras GmbH, Oct. 2019.

[92] T. Instruments, “mmWave Sensors for Automotive Applications | Overview | http://www.ti.com/sensors/mmwave/awr/overview.html,” Oct. 2019.

[93] G. Davies and E. Linfield, “Bridging the terahertz gap,” *IOP Physics World*, vol. 17, no. 4, 2004.

[94] G. P. Williams, “Filling the THz gap—high power sources and applications,” *Reports on Progress in Physics*, vol. 69, pp. 301–326, Feb. 2006.

[95] W. Li, G. LingYu, C. QingGong, and P. ShuSheng, “Application of NUFFT to Terahertz FMCW 3-D imaging,” in *2016 IEEE International Conference on Microwave and Millimeter Wave Technology (ICMMT)*, vol. 2, pp. 952–954, June 2016.

[96] R. Arusi, Y. Pinhasi, B. Kapilevitch, D. Hardon, B. Litvak, and M. Anisimov, “Linear FM radar operating in the Tera-Hertz regime for concealed objects detection,” in *2009 IEEE International Conference on Microwaves, Communications, Antennas and Electronics Systems*, pp. 1–4, Nov. 2009.

[97] K. B. Cooper, R. J. Dengler, N. Llombart, B. Thomas, G. Chattopadhyay, and P. H. Siegel, “THz Imaging Radar for Standoff Personnel Screening,” *IEEE Transactions on Terahertz Science and Technology*, vol. 1, pp. 169–182, Sept. 2011.

[98] A. Badolato, G. Rubio-Cidre, L. Úbeda Medina, J. Grajal, B. Mencia-Oliva, A. Garcia-Pino, B. Gonzalez-Valdes, and O. Rubiños, “A 300 GHz imaging radar for standoff anomaly detection,” in *2015 9th European Conference on Antennas and Propagation (EuCAP)*, pp. 1–5, May 2015.

[99] T. Spreng, S. Yuan, V. Valenta, H. Schumacher, U. Siart, and V. Ziegler, “Wideband 120 GHz to 140 GHz MIMO radar: System design and imaging results,” in *2015 European Microwave Conference (EuMC)*, pp. 430–433, Sept. 2015.

[100] S. Kueppers, H. Cetinkaya, and N. Pohl, “A compact 120 GHz SiGe:C based 2 × 8 FMCW MIMO radar sensor for robot navigation in low visibility environments,” in *2017 European Radar Conference (EURAD)*, pp. 122–125, Oct. 2017.

[101] J. Li and P. Stoica, eds., *MIMO radar signal processing*. Hoboken, NJ: J. Wiley & Sons, 2009. OCLC: ocn228632694.

[102] I. T. Union, “Intelligent transport systems (ITS) usage,” tech. rep., International Telecommunications Union, Nov. 2018.

[103] F. Norouzian, E. Marchetti, M. Gashinova, E. Hoare, C. Constantinou, P. Gardner, and M. Cherniakov, “Rain Attenuation at Millimeter Wave and Low-THz Frequencies,” *IEEE Transactions on Antennas and Propagation*, vol. 68, pp. 421–431, Jan. 2020.

[104] F. Norouziari, E. Marchetti, E. Hoare, M. Gashinova, C. Constantinou, P. Gardner, and M. Cherniakov, “Low-THz Wave Snow Attenuation,” in *2018 International Conference on Radar (RADAR)*, pp. 1–4, Aug. 2018.

[105] F. Norouzian, R. Du, E. Marchetti, M. Gashinova, E. Hoare, C. Constantinou, P. Gardner, and M. Cherniakov, “Transmission through uniform layer of ice at low-THz frequencies,” in *2017 European Radar Conference (EURAD)*, pp. 211–214, Oct. 2017.

[106] R. Du, F. Norouzian, E. Marchetti, B. Willetts, M. Gashinova, and M. Cherniakov, “Characterisation of attenuation by sand in low-THz band,” in *2017 IEEE Radar Conference (RadarConf)*, pp. 0294–0297, May 2017.

[107] S. Sabery, F. Norouzian, P. Gardner, E. Hoare, M. Cherniakov, and M. Gashinova, “Signal Reduction by Tree Leaves in Low- THz Automotive Radar,” in *2018 48th European Microwave Conference (EuMC)*, pp. 1445–1448, Sept. 2018.

[108] F. Norouzian, R. Du, M. Gashinova, E. Hoare, C. Constantinou, M. Lancaster, P. Gardner, and M. Cherniakov, “Signal reduction due to radome contamination in low-THz automotive radar,” in *2016 IEEE Radar Conference (RadarConf)*, pp. 1–4, May 2016.

[109] F. Norouzian, R. Du, E. G. Hoare, P. Gardner, C. Constantinou, M. Cherniakov, and M. Gashinova, “Low-THz Transmission Through Water-Containing Contaminants on Antenna Radome,” *IEEE Transactions on Terahertz Science and Technology*, vol. 8, pp. 63–75, Jan. 2018.

[110] S. V. Hum, “University of toronto: ECE422 Radio and Microwave Wireless Systems - lecture 20,” 2016.

[111] E. Marchetti, L. Daniel, E. G. Hoare, F. Norouzian, M. Cherniakov, and M. Gashinova, "Radar Reflectivity of a Passenger Car at 300 GHz," in *2018 19th International Radar Symposium (IRS)*, pp. 1–7, June 2018.

[112] E. Marchetti, S. Cassidy, F. Norouzian, E. G. Hoare, M. Cherniakov, and M. Gashinova, "Automotive Targets Characterization in the Low-THz Band," in *2019 20th International Radar Symposium (IRS)*, pp. 1–6, June 2019.

[113] E. Marchetti, R. Du, F. Norouzian, E. G. Hoare, T.-Y. Tran, M. Cherniakov, and M. Gashinova, "Comparison of pedestrian reflectivities at 24 and 300 GHz," in *2017 18th International Radar Symposium (IRS)*, pp. 1–7, June 2017.

[114] E. Marchetti, R. Du, F. Norouzian, E. G. Hoare, M. Cherniakov, M. Gashinova, and T.-Y. Tran, "Radar reflectivity and motion characteristics of pedestrians at 300 GHz," in *2017 European Radar Conference (EURAD)*, pp. 57–60, Oct. 2017.

[115] D. Jasteh, E. G. Hoare, M. Cherniakov, and M. Gashinova, "Experimental Low-Terahertz Radar Image Analysis for Automotive Terrain Sensing," *IEEE Geoscience and Remote Sensing Letters*, vol. 13, pp. 490–494, Apr. 2016.

[116] L. Daniel, D. Phippen, E. Hoare, M. Cherniakov, and M. Gashinova, "Image Segmentation in Real Aperture Low-THz Radar Images," in *2019 20th International Radar Symposium (IRS)*, pp. 1–8, June 2019.

[117] A. Bystrov, E. Hoare, M. Gashinova, M. Cherniakov, and T.-Y. Tran, "Experimental Study of Rough Surface Backscattering for Low Terahertz Automotive Radar," in *2019 20th International Radar Symposium (IRS)*, pp. 1–7, June 2019.

[118] A. Laribi, M. Hahn, J. Dickmann, and C. Waldschmidt, "Vertical Doppler beam sharpening goes self parking," in *2018 IEEE Radar Conference (RadarConf18)*, pp. 0383–0388, Apr. 2018.

[119] A. Laribi, M. Hahn, J. Dickmann, and C. Waldschmidt, "A performance comparison of RELAX and MODE for multipath height finding," in *2017 18th International Radar Symposium (IRS)*, pp. 1–10, June 2017. ISSN: 2155-5753.

[120] F. Diewald, J. Klappstein, F. Sarholz, J. Dickmann, and K. Dietmayer, "Radar-interference-based bridge identification for collision avoidance systems," in *2011 IEEE Intelligent Vehicles Symposium (IV)*, pp. 113–118, June 2011.

[121] A. Laribi, M. Hahn, J. Dickmann, and C. Waldschmidt, "A new height-estimation method using FMCW radar Doppler beam sharpening," in *2017 25th European Signal Processing Conference (EUSIPCO)*, (Kos, Greece), pp. 1932–1396, IEEE, Aug. 2017.

[122] O. Frey, C. L. Werner, I. Hajnsek, and R. Coscione, "A Car-Borne SAR System for Interferometric Measurements: Development Status and System Enhancements," in *IGARSS 2018 - 2018 IEEE International Geoscience and Remote Sensing Symposium*, (Valencia), pp. 6508–6511, IEEE, July 2018.

[123] O. Frey, C. L. Werner, U. Wegmuller, A. Wiesmann, D. Henke, and C. Magnard, "A car-borne SAR and InSAR experiment," in *2013 IEEE International Geoscience and Remote Sensing Symposium-IGARSS*, pp. 93–96, IEEE, 2013.

[124] S. Melo, E. Marchetti, S. Cassidy, E. Hoare, B. Antonella, M. Gashinova, and M. Cherniakov, "24 GHz Interferometric Radar for Road Hump Detections in Front of a Vehicle," in *The 19th International Radar Symposium IRS 2018, Bonn, Germany*, June 2018.

[125] T. Instruments, "Imaging Radar Using Cascaded mmWave Sensor Reference Design (Design Guide: TIDEP-01012)," 2019.

[126] Arbe, "Phoenix Imaging Radar: https://arberobotics.com/product/," Oct. 2019.

[127] M. Caris, S. Stanko, A. Wahlen, R. Sommer, J. Wilcke, N. Pohl, A. Leuther, and A. Tessmann, "Very high resolution radar at 300 GHz," in *2014 11th European Radar Conference*, pp. 494–496, Oct. 2014.

[128] S. Palm, R. Sommer, A. Tessmann, and U. Stilla, "Ultra-High Resolution Imaging of Facades and Vertical Infrastructure by Carborne SAR and Airborne CSAR," *ISPRS Annals of Photogrammetry, Remote Sensing and Spatial Information Sciences*, vol. IV-2/W7, pp. 129–136, Sept. 2019.

[129] S. Palm, R. Sommer, and U. Stilla, "Mobile Radar Mapping—Subcentimeter SAR Imaging of Roads," *IEEE Transactions on Geoscience and Remote Sensing*, vol. 56, pp. 6734–6746, Nov. 2018.

[130] S. Gishkori and B. Mulgrew, "Azimuth Enhancement for Automotive SAR Imaging," in *2018 International Conference on Radar (RADAR)*, pp. 1–5, Aug. 2018.

[131] S. Gishkori, L. Daniel, M. Gashinova, and B. Mulgrew, "Imaging for a Forward Scanning Automotive Synthetic Aperture Radar," *IEEE Transactions on Aerospace and Electronic Systems*, vol. 55, pp. 1420–1434, June 2019. Conference Name: IEEE Transactions on Aerospace and Electronic Systems.

[132] S. Shishanov, A. Bystrov, E. G. Hoare, A. Stove, M. Gashinova, M. Cherniakov, T.-Y. Tran, and N. Clarke, "Height-Finding for Automotive THz Radars," *IEEE Transactions on Intelligent Transportation Systems*, vol. 20, pp. 1170–1180, Mar. 2019.

[133] F. J. Harris, "On The Use of Windows For Harmonic Analysis WIth The Discrete Fouriter Transform," *Proceedings of the IEEE*, vol. 66, Jan. 1978.

[134] C. A. Balanis, *Antenna theory: analysis and design*. Hoboken, New Jersey: Wiley, fourth edition ed., 2016.

[135] W. C. Jakes, ed., *Microwave mobile communications*. An IEEE Press classic reissue, New York, NY: IEEE Press [u.a.], nachdr. ed., 1995. OCLC: 249569885.

[136] A. W. Rihaczek, *Principles of high-resolution radar*. Los Altos, California: Peninsula Publishing, 1985. OCLC: 859629845.

[137] P. Beckmann and A. Spizzichino, *The scattering of electromagnetic waves from rough surfaces*. The Artech House radar library, Norwood, MA: Artech House, 1987.

[138] T. Balz, H. Hammer, and S. Auer, "Potentials and limitations of SAR image simulators – A comparative study of three simulation approaches," *ISPRS Journal of Photogrammetry and Remote Sensing*, vol. 101, pp. 102–109, Mar. 2015.

[139] C.-Y. Hsieh, A. Fung, G. Nesti, A. Sieber, and P. Coppo, "A further study of the IEM surface scattering model," *IEEE Transactions on Geoscience and Remote Sensing*, vol. 35, pp. 901–909, July 1997.

[140] A. Ferretti, C. Prati, and F. Rocca, “Permanent scatterers in SAR interferometry,” *IEEE Transactions on Geoscience and Remote Sensing*, vol. 39, pp. 8–20, Jan. 2001.

[141] D. Wright, M. Gashinova, L. Daniel, S. Gishkori, and B. Mulgrew, “Circular Imaging and Phase Error Correction of 300GHz Radar Data,” in *Radar 2019*, (Toulon, France), p. 4, 2019.

[142] E. 1, “Millimeter wave components and systems, waveguide antennas, standard gain horns, MM wave radars - ELVA-1: http://elva-1.com/.”

[143] V. G. Nebabin and D. K. Barton, *Methods and techniques of radar recognition*. Boston: Artech House, 1995.

[144] F. Norouzian, R. Du, M. Gashinova, E. Hoare, C. Constantinou, P. Gardner, and M. Cherniakov, “Monostatic and bistatic reflectivity measurements of radar absorbers at low-THz frequency,” in *2016 European Radar Conference (EuRAD)*, pp. 117–120, Oct. 2016.

[145] S. L. Cassidy, “Compensating For Point Response Degradation In A High Resolution FMCW Imaging Radar,” in *2019 20th International Radar Symposium (IRS)*, pp. 1–8, June 2019.

[146] J. Dunlop and D. G. Smith, *Telecommunications engineering*. London: Chapmann & Hall, 3. ed., reprint ed., 1995. OCLC: 174550911.

[147] R. E. Collin, *Antennas and radiowave propagation*. McGraw-Hill series in electrical engineering, New York: McGraw-Hill, 1985.

[148] M. A. Richards, “Noncoherent Integration Gain, and its Approximation,” tech. rep., Georgia Institute of Technology, 2010.

[149] E. Li and K. Sarabandi, “Low grazing incidence millimeter-wave scattering models and measurements for various road surfaces,” *IEEE Transactions on Antennas and Propagation*, vol. 47, pp. 851–861, May 1999.

[150] A. J. Gatesman, T. M. Goyette, J. C. Dickinson, J. Waldman, J. Neilson, and W. E. Nixon, “Physical scale modeling the millimeter-wave backscattering behavior of ground clutter,” in *Aerospace/Defense Sensing, Simulation, and Controls* (W. R. Watkins, D. Clement, and W. R. Reynolds, eds.), (Orlando, FL), pp. 141–151, Sept. 2001.

[151] D. Phippen, L. Y. Daniel, M. Gashinova, A. G. Stove, and M. Cherniakov, “Trilateration of Targets Using a 300GHz Radar System,” in *International Conference on Radar Systems (Radar 2017)*, (Belfast, UK), p. 4, 2017.

[152] H. Rohling, “Radar CFAR Thresholding in Clutter and Multiple Target Situations,” *IEEE Transactions on Aerospace and Electronic Systems*, vol. AES-19, pp. 608–621, July 1983.

[153] L. Wang, J. Tang, and Q. Liao, “A Study on Radar Target Detection Based on Deep Neural Networks,” *IEEE Sensors Letters*, vol. 3, pp. 1–4, Mar. 2019.

[154] T. Mathworks, “Signal Processing Toolbox Reference Manual 2019b,” Sept. 2019.

[155] J. A. Hogbom, “Aperture Synthesis with a non-regular distribution of interferometer baselines,” *Astronomy and Astrophysics Supplement Series*, no. 15, pp. 417–426, 1974.

[156] V. S. Chernyak, *Fundamentals of multisite radar systems: multistatic radars and multiradar systems*. Amsterdam, The Netherlands: Gordon and Breach Science Publishers, 1998. OCLC: ocm40570465.

[157] W. Hereman and W. S. Murphy, "Determination of a Position in Three Dimensions Using Trilateration and Approximate Distances."

[158] A. Noroozi and M. A. Sebt, "Target Localization from Bistatic Range Measurements in Multi-Transmitter Multi-Receiver Passive Radar," *IEEE Signal Processing Letters*, vol. 22, pp. 2445–2449, Dec. 2015.

[159] Vivatech, "Millimeter Wave Product Catalogue," tech. rep., VivaTech Consulting S.A.R.L., 2013.

[160] G. T. Ruck, *Radar cross section handbook.* Los Altos, Calif.: Peninsula Publishing, 1970. OCLC: 223980949.

[161] M. Chen and C.-C. Chen, "RCS Patterns of Pedestrians at 76¿ 77 GHz," *IEEE Antennas and Propagation Magazine*, vol. 56, no. 4, pp. 252–263, 2014.

[162] D. Phippen, L. Daniel, E. Hoare, M. Gashinova, and M. Cherniakov, "3D Images of Pedestrians at 300GHz," in *2019 20th International Radar Symposium (IRS)*, pp. 1–10, June 2019.

[163] D. Phippen, L. Daniel, E. Hoare, M. Gashinova, and M. Cherniakov, "3D Images of Elevated Automotive Radar Targets at 300GHz," in *2019 International Radar Conference (RADAR)*, (TOULON, France), pp. 1–5, IEEE, Sept. 2019.

[164] A. Doerry, E. E. Bishop, and J. A. Miller, "Basics of Backprojection Algorithm for Processing Synthetic Aperture Radar Images.," Tech. Rep. SAND2016-1682, Sandia National Laboratories, Feb. 2016.

[165] D. Finch, S. K. Patch, and Rakesh, "Determining a Function from Its Mean Values Over a Family of Spheres," *SIAM J. Math. Analysis*, vol. 35, pp. 1213–1240, 2004.

[166] J. Zhu, S. W. Lee, Y. Ye, S. Zhao, and G. Wang, "X-ray transform and 3D Radon transform for ellipsoids and tetrahedra," *Journal of X-Ray Science and Technology*, vol. 12, Sept. 2004.

[167] J. A. Johnson and M. L. Fowler, "Cramer-Rao lower bound on doppler frequency of coherent pulse trains," in *2008 IEEE International Conference on Acoustics, Speech and Signal Processing*, (Las Vegas, NV), pp. 2557–2560, IEEE, Mar. 2008.

[168] A. Dogandzic and A. Nehorai, "Cramer-Rao bounds for estimating range, velocity, and direction with an active array," *IEEE Transactions on Signal Processing*, vol. 49, pp. 1122–1137, June 2001.

[169] C. Chen and H. C. Andrews, "Multifrequency Imaging of Radar Turntable Data," *IEEE Transactions on Aerospace and Electronic Systems*, vol. AES-16, pp. 15–22, Jan. 1980.

[170] P. Corona, G. Ferrara, F. D'Agostino, C. Gennarelli, and G. Riccio, "An improved physical optics model for the evaluation of the field backscattered by triangular trihedral corner reflectors," in *Electrotechnical Conference, 1996. MELECON '96., 8th Mediterranean*, vol. 1, pp. 534–537 vol.1, May 1996.

[171] M. B. Dillencourt, H. Samet, and M. Tamminen, "A general approach to connected-component labeling for arbitrary image representations," *Journal of the ACM*, vol. 39, pp. 253–280, Apr. 1992.

[172] A. Elhawil, L. Zhang, J. Stiens, C. D. Tandt, N. A. Gotzen, G. V. Assche, and R. Vounckx, "A Quasi-Optical Free-Space Method for Dielectric Constant Characterization of Polymer Materials in mm-wave Band," in *IEEE/LEOS Benelux*, (Brussels), p. 5, 2007.

[173] Stereolabs, "ZED Camera Product Page from Stereolabs: https://www.stereolabs.com/. oct 2019."

[174] L. Daniel, S. Cassidy, D. Phippen, E. Hoare, A. Stove, M. Cherniakov, and M. Gashinova, "Doppler Beam Sharpening for Angular Refinement at 150 GHz – Initial Experimentation," in *2018 19th International Radar Symposium (IRS)*, pp. 1–7, June 2018.

[175] D. M. Phippen, L. Y. Daniel, E. Hoare, M. Cherniakov, and M. S. Gashinova, "Compressive sensing for automotive 300GHz 3D imaging radar," in *2020 IEEE Radar Conference (RadarConf20) (RadarConf20)*, (Florence, Italy), Sept. 2020.

[176] R. Tibshirani, "Regression Shrinkage and Selection Via the Lasso," *Journal of the Royal Statistical Society: Series B (Methodological)*, vol. 58, pp. 267–288, Jan. 1996.

[177] J. Belk, "Bard college: Real Analysis II, Math 461," 2016.

[178] J. D. Blanchard, C. Cartis, and J. Tanner, "Compressed Sensing: How Sharp Is the Restricted Isometry Property?," *SIAM Review*, vol. 53, pp. 105–125, Jan. 2011.

[179] R. G. Baraniuk, "Compressive Sensing [Lecture Notes]," *IEEE Signal Processing Magazine*, vol. 24, pp. 118–121, July 2007.

[180] T. T. Cai and L. Wang, "Orthogonal Matching Pursuit for Sparse Signal Recovery With Noise," *IEEE Transactions on Information Theory*, vol. 57, pp. 4680–4688, July 2011.

[181] T. T. Do, L. Gan, N. H. Nguyen, and T. D. Tran, "Fast and Efficient Compressive Sensing Using Structurally Random Matrices," *IEEE Transactions on Signal Processing*, vol. 60, pp. 139–154, Jan. 2012.

[182] J. Tropp, "Greed is Good: Algorithmic Results for Sparse Approximation," *IEEE Transactions on Information Theory*, vol. 50, pp. 2231–2242, Oct. 2004.

[183] M. Grant and S. Boyd, "CVX: Matlab Software for Disciplined Convex Programming | CVX Research, Inc. http://cvxr.com/cvx/."

[184] S. P. Boyd and L. Vandenberghe, *Convex optimization*. Cambridge, UK ; New York: Cambridge University Press, 2004.

[185] S. J. Wright, "Coordinate descent algorithms," *Mathematical Programming*, vol. 151, pp. 3–34, June 2015.

[186] E. Candes and J. Romberg, "l1-magic : Recovery of Sparse Signals via Convex Programming," tech. rep., Caltech, 2005.

[187] S. R. Becker, E. J. Candès, and M. C. Grant, "Templates for convex cone problems with applications to sparse signal recovery," *Mathematical Programming Computation*, vol. 3, pp. 165–218, Sept. 2011.

[188] A. E. Hoerl and R. W. Kennard, "Ridge Regression: Biased Estimation for Nonorthogonal Problems," *Technometrics*, vol. 12, pp. 55–67, Feb. 1970.

[189] K. Usman, H. Gunawan, Faculty of Mathematics and Natural Sciences, Institut Teknologi Bandung, A. B. Suksmono, and School of Electrical and Informatics Engineering, Institut Teknologi Bandung, "Compressive Sensing Reconstruction Algorithm using L1-norm Minimization via L2-norm Minimization," *International Journal on Electrical Engineering and Informatics*, vol. 10, pp. 37–50, Mar. 2018.

[190] H. Zou and T. Hastie, "Regularization and variable selection via the elastic net," *Journal of the Royal Statistical Society: Series B (Statistical Methodology)*, vol. 67, pp. 301–320, Apr. 2005.

Appendix A

Publications

The following is a list of publications related to the PATHCAD project in which the author of this thesis is a (co-)author. This list is correct at the time of writing, Tuesday 1^{st} June, 2021.

1. L. Daniel et al., ‘Doppler Beam Sharpening for Angular Refinement at 150 GHz – Initial Experimentation’, in 2018 19th International Radar Symposium (IRS), Jun. 2018, pp. 1–7, doi: 10.23919/IRS.2018.8448091.

2. L. Daniel, D. Phippen, E. Hoare, M. Cherniakov, and M. Gashinova, ‘Image Segmentation in Real Aperture Low-THz Radar Images’, in 2019 20th International Radar Symposium (IRS), Jun. 2019, pp. 1–8, doi: 10.23919/IRS.2019.8768106.

3. D. Phippen, L. Daniel, E. Hoare, A. Stove, M. Cherniakov, and M. Gashinova, ‘3D Images of Overhead Objects at 300GHz’, presented at the RADAR 2019, Toulon, France.

4. D. Phippen, L. Daniel, E. Hoare, M. Gashinova, and M. Cherniakov, ‘3D Images of Pedestrians at 300GHz’, in 2019 20th International Radar Symposium (IRS), Jun. 2019, pp. 1–10, doi: 10.23919/IRS.2019.8768144.

5. L. Daniel, D. Phippen, E. Hoare, A. Stove, M. Cherniakov, and M. Gashinova, ‘Low-THz Radar, Lidar and Optical Imaging through Artificially Generated Fog’, presented at the International Conference on Radar Systems (Radar 2017), Belfast, UK, 2017, doi: 10.1049/cp.2017.0369.

6. D. Phippen, L. Y. Daniel, M. Gashinova, A. G. Stove, and M. Cherniakov, ‘Trilateration of Targets Using a 300GHz Radar System’, presented at the International Conference on Radar Systems (Radar 2017), Belfast, UK, 2017.

7. L. Daniel, D. Phippen, E. Hoare, A. Stove, M. Cherniakov, and M. Gashinova, ‘Multi-height radar images of road scenes at 150 GHz’, in 2017 18th International Radar Symposium (IRS), Jun. 2017, pp. 1–7, doi: 10.23919/IRS.2017.8008165.

8. D. M. Phippen, L. Y. Daniel, E. Hoare, M. Cherniakov, and M. S. Gashinova, “Compressive sensing for automotive 300GHz 3D imaging radar,” in2020 IEEE Radar Conference (RadarConf20), Florence, Italy, Sept. 2020.